Design, Implementation and First Results of the Neutrino Triggered Target of Opportunity Program with the IceCube Neutrino Telescope

D I S S E R T A T I O N

zur Erlangung des akademischen Grades

doctor rerum naturalium
(Dr. rer. nat.)
im Fach Physik

eingereicht an der
Mathematisch-Naturwissenschaftlichen
Fakultät I
Humboldt-Universität zu Berlin

von
Dipl.-Phys. Robert Franke

Präsident der Humboldt-Universität zu Berlin:
Prof. Dr. Jan-Hendrik Olbertz

Dekan der Mathematisch-Naturwissenschaftlichen
Fakultät I:
Prof. Stefan Hecht PhD

Gutachter:
1. Dr. Elisa Bernardini
2. Prof. Dr. Marek Kowalski
3. PD Dr. Alexander Kappes

Tag der mündlichen Prüfung: 03.11.2014

Abstract

Active Galactiv Nuclei (AGN) and galactic objects like e.g. supernova remnants are promising candidates for the sources of the high-energy cosmic rays. The detection of high-energy neutrinos from these objects would be a strong hint for the acceleration of protons or heavier nuclei. No source of high-energy astrophysical neutrinos has been identified up to now. From the observation of AGN with TeV γ-rays it is known that their emission is highly variable. Models predict that also the neutrino emission should show that variability. If time-dependent neutrino emission would be detected it would be desirable to have simultaneous data for different messengers (neutrinos and photons) and energy ranges, to learn as much as possible about the emission mechanism. However, due to the small field of view and the low duty cycle of the TeV γ instruments, not all interesting sources can be continuously monitored.

This work describes the development and the first results of a system, that analyses data of the IceCube neutrino telescope online at the South Pole, in order to send alerts to the TeV telescopes MAGIC and VERITAS in case a statistically interesting cluster of neutrinos is detected from an monitored source. This program is termed the Neutrino Triggered Target of Opportunity program (*NToO*). The catalog of sources monitored during the first year of operation contained 109 objects in the northern sky ($\delta > 0$). The system has been continuously operated since March 2012 and has sent five alerts between May 2012 and May 2013. One alarm issued on 9 November 2012 resulted in a follow-up observation by the VERITAS telescopes. No significant TeV-γ flux has been detected. Improvements to the IceCube online analysis are described that will further improve the sensitivity of the *NToO* in the near future.

Zusammenfassung

Die Kerne aktiver Galaxien (AGNs) und einige galaktische Objekte wie z.B. Supernovaüberreste gelten als vielversprechende Kandidaten für die Quellen der hochenergetischen kosmischen Strahlung. Der Nachweis der Emission von hochenergetischen Neutrinos von diesen Objekten wäre ein starker Hinweis für die Beschleunigung von Protonen oder schwereren Kernen. Bisher wurde jedoch keine Punktquelle hochenergetischer Neutrinos identifiziert. Durch die Beobachtung aktiver galaktischer Kerne mit γ-Strahlung im TeV-Bereich ist bekannt, dass die Emission von AGNs zeitlich extrem variabel ist. Modelle sagen vorher, dass auch die Neutrinoemission diese Variabilität aufweist. Um im Falle der Detektion zeitabhängiger Neutrinoemission von AGNs möglichst viel über den Emissionsmechanismus zu lernen, ist es entscheidend, Daten verschiedener Energiebereiche und Botenteilchen (Neutrinos und Photonen) zur Verfügung zu haben. Durch das beschränkte Gesichtsfeld und den geringen Duty-Cycle der TeV-γ Instrumente, können diese jedoch nicht alle potentiell interessanten Quellen lückenlos überwachen.

Diese Arbeit beschreibt die Entwicklung und die ersten Resultate eines Systems, dass Daten des Neutrinoteleskops IceCube direkt am Südpol analysiert, um Alarme an die TeV-Teleskope MAGIC und VERITAS zu senden, falls eine erhöhte Neutrinoemission eines überwachten Objekts detektiert wird. Der Katalog überwachter Objekte, der im ersten Jahr dieses Programms aktiv war, umfasste 109 Objekte in der nördlichen Himmelshemisphäre ($\delta > 0$). Das System befindet sich seit März 2012 kontinuierlich Betrieb und hat von Mai 2012 bis Mai 2013 fünf Alarme generiert. Ein Alarm am 9.November 2012 resultierte in einer Folgebeobachtung durch die VERITAS-Teleskope. Es wurde kein signifikanter γ-Fluss im TeV-Bereich detektiert. Weiterhin werden Verbesserungen der IceCube Online-Analysemethode beschrieben, die die Sensitivität des vorgestellten Programms in naher Zukunft weiter verbessern werden.

Contents

1. Introduction

Finding the sources of the constant stream of high-energy particle hitting the Earth's atmosphere, the so called cosmic rays, has been the defining question of the young field of astroparticle physics. Reaching energies of up to about 10^{20} eV their acceleration environments must be among the most active and violent regions in the universe. As the high-energy component of the cosmic rays consists of protons and heavier nuclei, the particles are deflected in the inter- and intra-galactic magnetic fields on their way to Earth. Hence they do not point back to their sources! Other messengers need to be employed to identify the acceleration environments.

Starting in the 1990's Imaging Atmospheric Cherenkov Telescopes (IACTs) identified sources of high-energy γ-rays, reaching energies of up to several TeV. Active Galactic Nuclei (AGN) are the most abundant class of sources identified by these instruments. One characteristic of the high-energy γ-radiation from AGNs is their tremendous flux variability of up to one order of magnitude and time scales ranging from days down to several minutes. However, the observation of the electromagnetic radiation alone can not constrain the environmental conditions enough to explain the acceleration process. Competing models invoking either leptonic or hadronic acceleration processes often fit to the observational evidence equally well. However, neutrinos of high energies (> TeV) are produced in sizeable numbers only in environments where hadronic acceleration takes places. Hence the detection of neutrino point sources would greatly aid in identifying the sources of the cosmic rays!

The detection of high-energy neutrinos from an astrophysical object would prove that hadrons are accelerated to very high energies in the object. However, we will learn the most about the acceleration environment by combining observations using different messengers (the so-called multi-messenger approach). The IceCube Neutrino Observatory is the worlds biggest and most sensitive high-energy neutrino telescope. After its completion in 2011 it has reached a sensitivity that would allow it to detect the flares of very active objects in their highest flux states (like the AGNs Markarian 421 and Markarian 501), assuming that the neutrino flux is comparable to the γ-ray flux. Offline searches for time-dependent fluxes with the IceCube detector are performed since several years. In the case a source is detected by these means, the possibility to combine the neutrino data and the high-energy γ-ray observations is most likely lost. Cherenkov telescopes have a small field of view of only several square-degrees and a small duty cycle ($\sim$ 10%). To solve this problem, a target of opportunity program based on an online analysis of the neutrino data could alert TeV instruments and ensure that follow-up observations of potential neutrino flares are performed. A program based on this idea was tested in 2006 by the AMANDA neutrino telescope in collaboration with the MAGIC observatory (see [ABG+08]). The program presented in this work is an evolution of this idea. A list of target sources is continuously monitored for statistically significant clusters of neutrinos in an online neutrino analysis directly at the South

Pole. If a potentially flaring source is identified a request for a γ-ray follow-up observation is sent to the partner experiments MAGIC and VERITAS.

The combination of neutrino data with γ-ray observations does not only increase the chance of understanding the source characteristics but might also increase the statistical significance of the neutrino observations. The detection of high-energy neutrinos is very challenging due to their small cross section and the unavoidable background of atmospheric neutrinos. The detection of TeV γ-ray flare in coincidence with a marginally significant cluster of neutrinos could also help to establish the discovery of a neutrino point source.

The Neutrino Triggered Target of Opportunity (*NToO*) presented in this work provides the unique opportunity to obtain valuable data on sources of high-energy neutrinos in their high flux state, simultaneously with a neutrino instrument and high-energy γ-rays.

2. High-Energy Astroparticle Physics

This chapter gives an introduction into the field of high-energy astroparticle physics. Section 2.1 introduces the high-energy cosmic rays, their discovery, their spectrum and possible acceleration mechanisms. The special properties of photons and neutrinos as cosmic messengers are briefly discussed in Sec. 2.2. Active Galactic Nuclei and their high-energy emissions are then described in Sec. 2.3. Other sources of high-energy radiation are briefly presented in Sec. 2.4. Finally, Imaging Atmospheric Cherenkov Telescopes, an important class of instruments for the detection of high-energy γ-rays, are introduced in Sec. 2.5.

2.1. High-Energy Cosmic Rays

2.1.1. Energy Spectrum

In 1912 the Austrian physicist Victor F. Hess discovered during balloon flights that the electrical conductivity of the atmosphere increases above an altitude of 1000 m until at an altitude of 5000 m it reaches several times the value measured at ground [Hes65]. Hess's explanation was that "a radiation of very high penetrating power enters the atmosphere from above", causing ionization. For this discovery he was awarded the Nobel Prize in Physics in 1936. The term "cosmic rays" for these particles impinging on the atmosphere was coined by Robert A. Millikan and was quickly adopted in the scientific community. Coincidence measurements carried out by Pierre Auger in 1938 showed that cosmic rays can produce particle showers in the atmosphere (see [AEM+39]), proving that they can reach energies above 10^6 GeV. During the century that passed since Hess's discovery, a lot of measurements were performed improving our understanding of cosmic rays.

The spectrum of particles hitting the Earth's atmosphere extends over a very wide range of energy (see Fig. 2.1). Particles with an energy somewhat more than 10^{20} eV have been observed [Hil06]. For energies below 10^5 GeV the cosmic ray flux is strong enough to be analyzed with sophisticated detectors aboard balloons and satellites. Therefore, its composition can be easily measured directly in that energy range. The deduced relative element abundances are similar to their general occurrence in the universe with the exception of hydrogen and helium [Sta03]. Non-hadronic particles (electrons, positrons and photons) only represent a very small fraction of the primary cosmic ray flux. In this work the term cosmic rays will be used for the hadronic component only. At higher energies (above 10^5 GeV) ground based experiments, relying on the observation of the induced air showers, only give indirect measurements of the cosmic ray composition. A further complication for the measurement of the primary cosmic ray composition is the limited knowledge of hadron cross sections above 10^6 GeV, as these have to be extrapolated from lower

energy accelerator measurements. These cross sections, however, are important to understand the air shower development in detail. The knowledge about high-energy hadron cross sections will be greatly improved by the LHC experiments LHCf [Tri12] and TOTEM [Lf09, TAA+12].

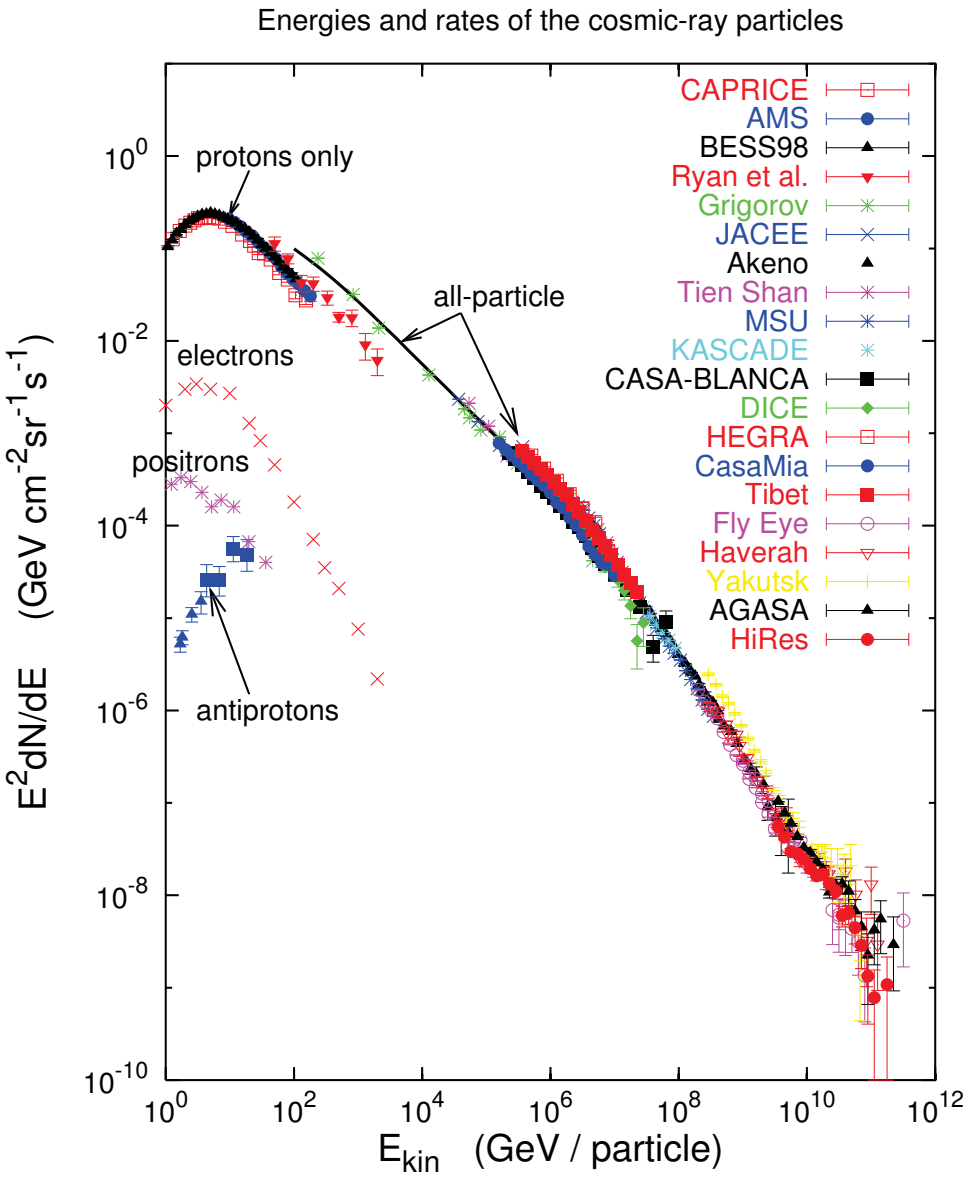

Figure 2.1.: *Measurements of the energy spectrum of primary cosmic rays up to energies of* 10^9 GeV. *Plot taken from [Hil06], assembled by T. Gaisser. The flux has been multiplied by* E^2 *in order to make small features better visible.*

Ever since the discovery of high-energy cosmic rays, scientists also tried to understand the shape

of the cosmic ray energy spectrum. Between about 10 GeV primary energy up to about $10^{15.5}$ eV the flux can be parametrized by a pure power law with $dN/dE \propto E^{-2.7}$. This implies that the flux in every decade of energy is about a factor of 50 lower than in the decade before. Above $10^{15.5}$ eV the spectrum steepens a little to $dN/dE \propto E^{-3.0}$ for three decades in energy. This change in the slope is termed the "knee". The spectrum flattens again to $dN/dE \propto E^{-2.7}$ at an energy of about $10^{18.5}$ eV (termed the "ankle"). At an energy somewhat above 10^{20} eV the flux then becomes too low to be measured. It has been argued, that the "knee" of the cosmic ray spectrum marks the transition point from galactic sources to extragalactic ones. Hillas, however, refutes that and claims the spectrum might be a superposition of different sources already at lower energies [Hil06]. There are several experimental hints that the "knee" is caused by a charge-dependent cutoff in the maximum energy of accelerated particles (see [Hoe12] for a summary).

For a more detailed analysis of the cosmic ray spectrum see [Gai04] and [Sta03].

GZK Effect Shortly after the discovery of the 2.7 K cosmic microwave background radiation by Penzias and Wilson in 1965 [PW65], Kuzmin, Zatsepin [ZK66] and Greisen [Gre66] predicted that the cosmic ray spectrum would end just below 10^{20} eV because the high-energy nuclei would interact with the photons of the microwave background via the Δ-resonance and thus loose energy during their propagation. This feature of the cosmic ray spectrum is called the Greisen-Zatsepin-Kuzmin (GZK) cutoff. It is especially important for neutrino experiments as it is a guaranteed source of a diffuse high-energy neutrino flux through the decay of the Δ-resonance:

$$\begin{aligned} p + \gamma &\to \Delta^+ \\ &\to n + \pi^+ \\ &\to n + \nu_\mu + \mu^+ \\ &\to n + \nu_\mu + \bar{\nu}_\mu + \nu_e + e^+ \,. \end{aligned} \tag{2.1}$$

Due to the GZK effect the range of a particle with an energy of 10^{20} eV is approximately 13 Mpc [Sta03]. Hypothetical sources that produce particles with energies larger than 10^{20} eV therefore have to be located in the local galaxy cluster to be detectable. The Pierre Auger Collaboration has recently reported on a strong suppression of the cosmic ray flux above 4×10^{19} eV that could be interpreted as the GZK cutoff [CP11].

Source Identification Charged particles propagating through the universe are deflected by inter- and intra-galactic magnetic fields. Therefore, their reconstructed arrival directions do not point back to their sources. However, at the highest energies (above a few tens of EeV), for nearby sources (closer than a few tens of Mpc) the deflection in the magnetic fields becomes so small, that clustering of events around sources can be reported. This clustering has been detected by the Pierre Auger Observatory (see [PAA+07, PAA+08a, Pie08]). The available statistics does not yet allow the identification of individual extragalactic sources.

At lower energies, where galactic sources are believed to dominate the spectrum, sources can

not be identified using the cosmic rays themselves. However, secondary particles (photons and neutrinos) produced in the acceleration process, could be used to pinpoint the galactic sources. Recently the Fermi collaboration reported the clear identification of π^0-decay signatures in two supernova remnants (SNRs), IC 443 and W44 [AAA+13d]. The existence of high-energy pions is a proof of hadronic acceleration in these sources (see Sec. 2.3.5). This further strengthens the argument that SNRs are the sources of the galactic cosmic-ray component.

The detection of high-energy neutrinos from an astrophysical object would unambiguously prove that hadrons are accelerated to very high energies in that environment. Thus neutrinos are critically important to identify the sources of high-energy cosmic rays.

2.1.2. Air Showers

High-energy particles hitting Earth's atmosphere will initiate a reaction (either electromagnetic or hadronic) in the upper layers of the atmosphere, sharing their energies between these secondary particles. The produced particles are going to react or decay themselves, giving rise to further particles. The developing particle cascades are called cosmic-ray air showers. Their development is a very complex interplay of hadronic and electromagnetic reactions and decay processes in an inhomogeneous medium. A fully analytical description of these showers is thus not possible, and one often has to rely on Monte Carlo simulations to model them. Cosmic ray air showers are, however, of special interest for neutrino experiments as the neutrino and muon components of these showers form the major background for a search for cosmogenic neutrinos.

Muons are the most penetrating component of cosmic-ray air showers. They are mainly produced in the decay of charged pions and kaons. The decay of mesons containing charm quarks plays only a minor, but not yet fully understood role [RNTN07]. Therefore their decay contributes to the systematic uncertainty in the search for a diffuse high-energy astrophysical neutrino flux (see e.g. [AAA+11a]).

Charged pions can either decay weakly via

$$\begin{aligned} \pi^{\pm} &\rightarrow \mu^{\pm} + \nu_{\mu}/\bar{\nu}_{\mu} \\ &\rightarrow e^{\pm} + \nu_{e}/\bar{\nu}_{e} + \nu_{\mu}/\bar{\nu}_{\mu} \end{aligned} \tag{2.2}$$

or undergo further hadronic interactions. The decay length of the pion is given by $l_d = \gamma_{\pi^{\pm}} \cdot 780\,\mathrm{cm}$ with γ being the Lorentz factor. Therefore, high-energy pions almost exclusively interact, as their decay length becomes large due to their γ-factor. Low-energy pions decay into muons and neutrinos. The probability for a decay also depends on the altitude as an interaction is much more likely in denser, lower regions of the atmosphere. Interacting charged pions give rise to pions with lower energies. This process continues until the energies involved are so low, that almost all particles decay. The photons produced in the decay of neutral pions initiate electromagnetic sub-showers. The resulting atmospheric muon flux at sea level as a function of the zenith angle θ

can then be approximated by

$$\frac{dN_\mu}{dE_\mu} \approx \frac{0.14\,E^{-2.7}}{\mathrm{cm\,s\,sr\,GeV}} \left(\frac{1}{1 + \frac{1.1 E_\mu \cos\theta}{115\,\mathrm{GeV}}} + \frac{0.054}{1 + \frac{1.1 E_\mu \cos\theta}{850\,\mathrm{GeV}}} \right) \tag{2.3}$$

for muons with $E_\mu > 100\,\mathrm{GeV}/\cos\theta$ [BAB+12]. The two terms represent the contribution from kaon and pion decay, respectively. Equation 2.3 ignores the contribution from charm decay and heavier flavors which only contribute significantly at the highest energies ($> 10^6$ GeV). Further details on the development of cosmic ray air showers can be found in [Sta03].

Monte Carlo simulations and analytical calculations show that the number of high-energy muons from a single cosmic ray air shower in an underground detector is almost Poissonian but has a long tail [Gai04]. These quasi-parallel muons (a so-called muon bundle) can mimic a single muon of higher energy. Muon bundles form a major background for the search for high-energy neutrinos above the horizon (with primary energies above ~ 1 PeV).

Using the Earth as a filter by looking for upward-going events it is possible to reduce the background of misreconstructed down-going atmospheric muons to a negligible level. The flux of atmospheric neutrinos (see Fig. 2.2) from cosmic ray air showers forms the background in such a search for astrophysical neutrinos in neutrino telescopes.

2.1.3. The Origin of Cosmic Rays

What are the astrophysical environments that produce the observed cosmic rays with extremely high energies? This is the fundamental question in cosmic ray physics that is still unanswered to date. Even more puzzling is the simple power law which describes cosmic rays over an extremely wide range of energies. In order to speculate on possible sources of origin of high-energy cosmic rays it is first necessary to understand what physical mechanisms could accelerate charged particles to these energies.

This section is only going to discuss so-called bottom-up scenarios where charged particles are accelerated to the high energies that have been observed. Alternative top-down scenarios also exist, where the high-energy particles originate from the decay of super-heavy exotic particles. These models, however, require extensions to the Standard Model of particle physics and are severely constrained by measurements [PAA+08b].

Fermi Acceleration

One proposed acceleration mechanism for charged particles in astrophysical environments is the so-called Fermi acceleration [Fer49]. Two variants of this mechanism exist, first- and second-order Fermi acceleration, termed after the dependence of the acceleration efficiency on the velocity ($\beta = v/c$) of the involved accelerating medium (e.g. a shock front or a moving interstellar cloud). Other proposed acceleration mechanisms involve for example the strong electric and magnetic fields close to the surface of pulsars.

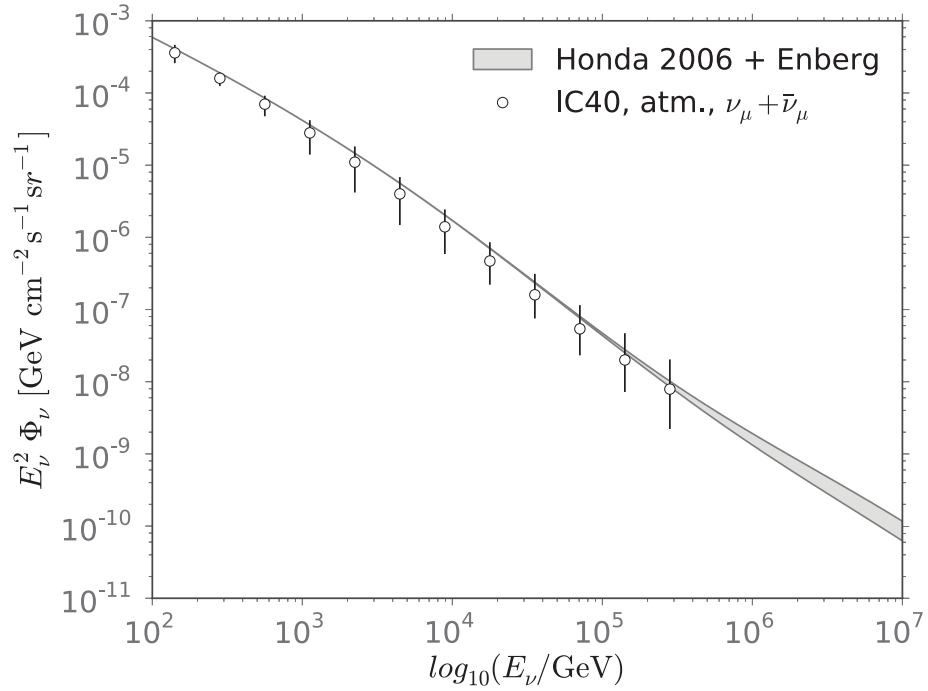

Figure 2.2.: *Atmospheric muon neutrino energy spectrum. The error bars show the $\nu_\mu + \bar{\nu}_\mu$ energy spectrum measured with the IceCube detector in its 40-string configuration averaged over the zenith region from 97° to 180° [AAA+11b]. The shaded area depicts the sum of theoretical predictions for the conventional (see [HKK+07]) and prompt (see [ERS08]) $\nu_\mu + \bar{\nu}_\mu$ flux averaged over the zenith region from 90° to 180°. The theoretical uncertainty in this plot stems entirely from the uncertainty on the prompt flux component. The uncertainty does, however, not include the uncertainties from the primary cosmic ray spectrum and composition which may be a factor of 2 or more [Gai12].*

Second-order Fermi Acceleration Second order Fermi acceleration takes place, when charged particles are scattered on moving interstellar magnetized plasma clouds. As the directions of the movement of the clouds are randomly distributed, this process is very inefficient and thus probably not the source of high-energy cosmic radiation. It has, however, been argued that second order Fermi acceleration might play a role in the further acceleration of high-energy particles from other sources (e.g. supernova remnants) [NOP07].

First-order Fermi Acceleration Fermi acceleration of first order happens at shock fronts, e.g. resulting from supernova explosions or in jets of Active Galactic Nuclei (see Sec. 2.3). The scenario is depicted in Fig. 2.3.

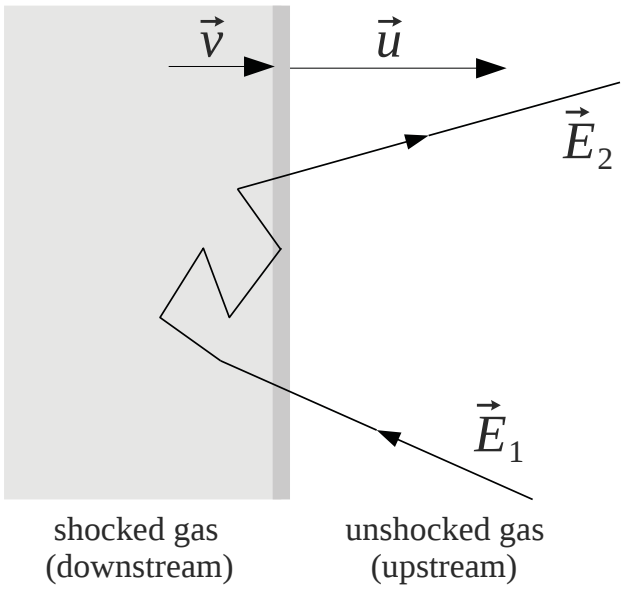

Figure 2.3.: *First-order Fermi acceleration in the rest-frame of the unshocked gas. The shock front moves with velocity* **u***, the shocked gas behind the front with* **v***, where* $|\mathbf{v}| < |\mathbf{u}|$.

The energy gain per crossing ΔE of a particle with energy E can be written as:

$$\frac{\Delta E}{E} \approx \beta = \frac{3}{4} u \,. \tag{2.4}$$

Provided that a magnetic field exists on both sides of the shock region the particle can be rescattered and cross the shock boundary multiple times. If a constant escape probability P is assumed the resulting energy spectrum is given by

$$\frac{\mathrm{d}N}{\mathrm{d}E} = \frac{\mathrm{d}N}{\mathrm{d}E}(E_0) \cdot \left(\frac{E}{E_0}\right)^{1+\ln P/\ln\left(1+\frac{3}{4}\frac{u}{c}\right)} = \frac{\mathrm{d}N}{\mathrm{d}E}(E_0) \cdot \left(\frac{E}{E_0}\right)^{\alpha} \,. \tag{2.5}$$

Making additional, realistic, assumptions on the input spectrum $\frac{\mathrm{d}N}{\mathrm{d}E}(E_0)$ it can be shown that the resulting energy spectrum has a spectral index $\alpha \approx -2.2 \cdots -2.0$. This is compatible with the observed cosmic ray spectral index of $\alpha = -2.7$ if the energy loss in the interstellar medium is taken into account.

Several astrophysical environments exist that could provide suitable conditions for first-order Fermi acceleration. Shock fronts are present e.g. in supernova remnants (SNRs), gamma-ray bursts (GRBs), active galactic nuclei (AGNs) and micro-quasars.

Supernova remnants have been shown to be very effective particle accelerators by observing their TeV γ-emissions (see e.g. [AAA+04]). Considerations of the total power output of all supernovae

in our galaxy in comparison to the cosmic ray energy density show that supernova remnants may be the major source of cosmic rays with galactic origin [GS64, Aha04]. Recently the Fermi Gamma-ray Space Telescope showed evidence that π^0-decay is responsible for the gamma-ray spectrum of two SNRs (IC 443 and W44) thereby proving that these objects accelerate protons to very high energies [TA+13].

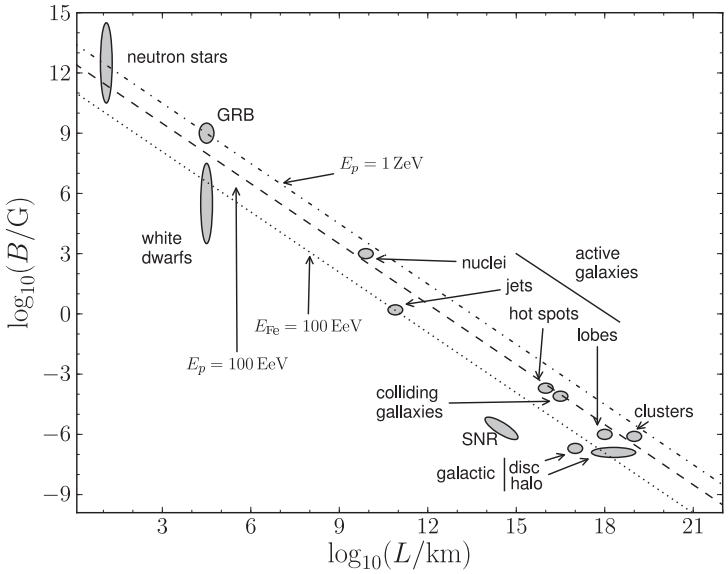

Figure 2.4.: *Hillas plot, showing for different astrophysical environments, their typical sizes (x-axis) and magnetic fields (y-axis). The maximum energy to which a particle of charge z can be accelerated in this environment can be calculated using Eq. 2.6. The three lines highlight the regions that can accelerate protons to 10^{21} eV (dash-dotted line), protons to 10^{20} eV (dashed line) or iron nuclei to 10^{20} eV (dotted line). All astrophysical environments with bigger dimensions or higher magnetic field than marked by the respective line provide the conditions to achieve that acceleration. The plot shows that AGNs are prime candidates for the acceleration of ultra high-energy cosmic rays (e.g. in their nuclei or in hot spots in the jets) and thus are also favored environments for extragalactic neutrino production. Plot taken from [Pan11], data from [BEH09]*

Hillas Condition

In order to estimate the maximum energy to which a particle can be accelerated in a certain astrophysical environment a simple model can be employed. A particle with energy E and charge z in a homogeneous magnetic field B moves with a gyro-radius $R_{\mathrm{gyro}} = E/Bz$. Therefore, the

particle can be accelerated to a maximum energy

$$E_{\max} = zBR \tag{2.6}$$

in a region of size R before its gyroradius becomes too big to be confined in the magnetic field. This equation is called the Hillas condition. Using typical values and estimates for the magnetic field and the size of the acceleration region, the so-called Hillas plot (see Fig. 2.4) is obtained. It shows the maximum energy a particle can reach in different astrophysical environments.

2.2. High-Energy Radiation from Cosmic Objects

2.2.1. Photons as Cosmic Messengers

In comparison to charged cosmic rays, photons have the advantage to point back to their source as they are not deflected by magnetic fields. In environments that accelerate protons and heavier nuclei to very high energies also a considerable flux of high-energy photons could be produced. This connection between the primary cosmic ray flux and high-energy photons is discussed in more detail in Sec. 2.3.5 in the light of hadronic emission models for Active Galactic Nuclei. Therefore, high-energy photons could be a prime messenger to search for the sources of high-energy cosmic rays. In the past years a multitude of discoveries was made with a new generation of Cherenkov telescopes. However, for photon energies above several hundred GeV the cosmos becomes less transparent[1]. Photons with these energies can be lost via a reaction with the Extragalactic Background Light (EBL)

$$\gamma_{\mathrm{HE}} + \gamma_{\mathrm{Background}} \rightarrow e^+ + e^- \,. \tag{2.7}$$

This reaction absorbs photons from TeV γ-ray sources. The resulting attenuation of TeV γ-rays can be used to measure and constrain the amount of Extragalactic Background Light (see [AAB+06b, MR07]). Up to now no extragalactic photons with energies above 10^{13} eV have been detected, higher energies would only be observable for nearby objects [NS02]. Therefore, EBL absorption can put a strong limit on the exploration of extragalactic objects with very high-energy γ-rays. On the other hand, the observation of high-energy γ-rays can also be used to constrain the EBL. Nearby objects, although not strongly influenced by photon absorption on the EBL, might be too dense to allow high-energy photons to escape or the photons might be reabsorbed in interstellar clouds on their way to Earth.

[1] Several models exist, that predict a conversion of photons into a hypothetical light, weakly interacting particle, called the axion. This particle is postulated to solve the strong CP problem. As it does not interact via the electromagnetic force it could, like the neutrino, travel large distances in the universe without absorption. In order to be detected at the Earth the axion would need to convert back into a photon.

2.2.2. Neutrinos as Cosmic Messengers

Neutrinos have several unique properties that make them suited as cosmic messengers. As they interact only via the weak force they are not influenced by inter- or intragalactic magnetic fields and therefore point back to their origin. Their very small cross section with matter enables them to escape very dense astrophysical environments, where e.g. photons can be trapped. The small neutrino interaction cross section, however, also makes neutrinos hard to detect. To facilitate neutrino detection, huge detection volumes are required (see 4). This great effort is justified as neutrinos allow to answer questions that can hardly be answered by other means. As neutrinos in non-negligible amounts can only be produced by hadronic interactions a neutrino detection from a cosmic object would unquestionably prove that protons are accelerated at this source (see Sec. 2.3.5). It is important to note that in addition to the neutrino flux also high-energy photons are produced in hadronic emission models. Depending on the production environment these photons can escape and could be detected at the Earth. This tight linkage between high-energy neutrinos and photons is the prime motivator for the multi-messenger approach applied in this work.

2.3. Active Galactic Nuclei

Active Galactic Nuclei (AGN) are located at the center of a specific type of galaxy. About 3 % of all galaxies are classified as active. Their main feature is a very strong electromagnetic emission over a very wide range of frequencies from radio to TeV γ-rays. These galaxies are the most luminous persistent sources of electromagnetic radiation in the universe. The driving engine of these emissions is believed to be a massive black hole in the center of the galaxy. The accretion of matter onto this black hole is a very effective process to convert matter into energy and is thus able to power the strong emissions.

Active Galactic Nuclei are prime candidates to be the source of ultra high-energy cosmic rays with energies above 10^{15} eV as they fulfill the Hillas condition (see Sec. 2.1.3) and exist within the GZK horizon (see Sec. 2.1.1). Thus these objects are also of very high interest to neutrino telescopes.

Active Galactic Nuclei have several key components, though not all of them are present in every AGN:

- a massive central black hole ($10^6 < M_{\mathrm{BH}}/M_\odot < 10^9$)
- an accretion disk
- jets on one or both sides of the accretion disc
- a broad-line emission region
- a narrow-line emission region
- a molecular/dust torus around the central region

Almost all AGNs where the host galaxy could be resolved are housed by large elliptical galaxies.

In the following section the characteristic features of AGNs and their connections to AGN models are described. It follows mainly the overviews given in [RB07] and [Lon11].

2.3.1. Classification

AGNs show a very large variety of phenomena, from low energy radio emissions with photon energies $<10^{-6}$ eV to high energy γ-ray emission with photon energies >1 TeV. As it is hard to obtain full spectral coverage, the classification of Active Galactic Nuclei in one frequency range often does not agree with the classification in another one. However, several identifiable classes exist that will be described shortly.

Quasars

Quasars (Quasi Stellar Radio Sources) were the first type of Active Galactic Nuclei identified. They show a featureless spectrum with an ultraviolet excess, outshining their host galaxy. About 10 % of all quasars are radio loud (ratio of fluxes at $f = 5\,\mathrm{GHz}$ and the optical B band $F_5/F_\mathrm{B} \gtrsim 10$). All quasars show a strong flux variability over the full spectrum. Their total power output reaches from $10^{46}\,\mathrm{erg\,s^{-1}}$ to $10^{49}\,\mathrm{erg\,s^{-1}}$.

The object 3C 273 was the first identified quasar in 1962. It was observed as a point-like radio source. After the precise determination of its position with the Lunar occultation technique (see [Haz76]), an optical counterpart could be identified [HMS63]. Its spectrum showed a redshift of 0.158 which proved that the source was located outside of the Milky Way. It has been estimated that more than 10^6 quasars exist in the universe [PMY+12].

Radio galaxies

Radio galaxies are unusually radio-bright galaxies with luminosities $L_\mathrm{radio} \geq 3 \times 10^{41}\,\mathrm{erg\,s^{-1}}$. They are in most cases identified as large elliptical galaxies. The source of the radio emission might be either the nucleus of the galaxy or two areas displaced several kpc from the nucleus perpendicular to the galactic disc, the so-called radio lobes. In a lot of cases jets of highly ionized plasma connect the lobes to the nucleus. Depending on the position of the highest radio emission, radio galaxies are divided into two classes named after B. L. Fanaroff and J. M. Riley (see [FR74]):

- Fanaroff-Riley type I, which is brightest close to the center of the galaxy. The spectrum is also harder in the center than closer to lobes. This type is generally more powerful than Fanaroff-Riley type II galaxies.
- Fanaroff-Riley type II, which have their highest brightness in the jets connecting the galaxy to the radio lobes. Often the jets show bright spots with elevated emission, so-called hot spots.

Seyfert Galaxies

Seyfert galaxies are radio-quiet spiral galaxies with very bright cores showing emission lines from highly ionized atoms. The temperatures to achieve that degree of ionization can not be reached in star atmospheres. Some Seyfert galaxies are in the process of merging with another galaxy and a significant fraction seems to be interacting with a close companion. The brightest Seyfert galaxies achieve a brightness comparable to weak quasars.

Blazars

Blazars are the type of AGN that has been observed most numerously up to the highest energies. They show a very high radio brightness, a flat radio spectrum and a mainly featureless, non-thermal optical spectrum with a high degree of polarization [RB07]. Furthermore they exhibit high X-ray and γ-ray brightness. Fluxes in all wavelength show fast variability. Two subclasses of blazars are usually distinguished:

- Flat Spectrum Radio Quasars (FSRQs), that show strong, broad emission lines and
- BL Lac objects, that show a featureless optical spectrum.

2.3.2. Phenomena

Central Black Hole

The central black hole of an AGN has a mass M_{BH} in the range of $10^6 < M_{\mathrm{BH}}/M_\odot < 10^9$ and therefore a Schwarzschild radius R_{S} of $6R_\odot < R_{\mathrm{S}} < 6 \cdot 10^3 R_\odot$. Interestingly, the mass of the black hole is not correlated to the luminosity of the host galaxy or the radio loudness of the AGN. It could, however, be shown that the velocity dispersion of central stars and the bulge luminosity provide good approximations of the black hole mass. The spin of the black hole is believed to be connected to the production of jets (see below).

The accretion rate of a black hole is limited by the Eddington limit, which is reached when the radiation pressure from the heated infalling matter balances the gravitational force of the Black Hole. That maximum luminosity is given by

$$L_{\mathrm{Edd}} \approx 3 \cdot 10^{13} \left(\frac{M_{\mathrm{BH}}}{10^9 M_\odot} L_\odot \right) \tag{2.8}$$

under the assumption that the infalling matter consists purely of ionized hydrogen gas and the thermal radiation is emitted isotropically. Assuming a conversion efficiency of matter to radiated energy of $\frac{L}{\dot{M}c^2} = 0.1$ (see [Tho74]), the mass inflow required to sustain the Eddington luminosity can be written as

$$\dot{M}_{\mathrm{Edd}} \approx 22 \left(\frac{M_{\mathrm{BH}}}{10^9 M_\odot} \right) M_\odot \,\mathrm{yr}^{-1} \,. \tag{2.9}$$

This shows that even the brightest quasars, with a power output of $10^{48}\,\mathrm{erg\,s^{-1}}$ and a mass $M_{\mathrm{BH}} = O(10^9 M_\odot)$, can be powered with the accretion of only a few tens of solar masses ($1\,M_\odot c^2 = 1.8 \cdot 10^{54}$ erg) per year!

Accretion Disk

The accretion of gas onto the black hole leads to the formation of a rotating, geometrically thin, optically thick disk of hot material (several 10^3 K). The angular momentum transport in outward direction leads to velocity dispersion between different disc radii which heats the disk. It is interesting to note that the mass of the central black hole and the temperature of the accretion disk are inversely correlated ($T \sim M_{\mathrm{BH}}^{-1/4}$). This leads to the effect that e.g. micro quasars (neutron stars in our Milky Way that accrete matter from an accompanying massive object) are brightest in X-ray energies whereas AGNs are brightest in blue or UV frequencies (the so-called "big blue bump" in the AGN spectrum). The thermal spectrum of the disk is very broad as the disk temperature decreases with increasing distance to the black hole. The plasma in the accretion disk is accompanied by a confined magnetic field. An overview over the physics of accretion discs is given in [Pri81] and [FKR92].

Jets

Approximately 10 % of all AGNs show a collimated outflow of highly energetic plasma from their center with a high bulk Lorentz factor (up to 30). That outflow can be stable over distances of up to 100 kpc. Depending on the angle under which the jet is observed it can appear to move superluminally. This, however, is just a geometrical effect. The mechanism of the formation and acceleration of jets are not entirely understood (see e.g. [CR$^+$04a]). Two different classes of models are generally discussed. The first class of models invokes complex magnetohydrodynamics in the accretion disc alone, whereas the second class is based on the interaction of the magnetic fields confined in the accretion disc with the angular momentum of the black hole (see e.g. [Mei03]).

The observation of polarized synchrotron emission from the jets implies the presence of free electrons and an ordered magnetic field. When the jet develops it sweeps up gas from the surrounding medium and a shock develops. This could provide the conditions suitable for the acceleration of particles to very high energies via the mechanism of Fermi acceleration (see Sec. 2.1.3).

Connected to the phenomenon of the jets are the so-called "radio lobes", large, roughly symmetrical volumes often at the end of both jets that are very prominent on radio maps. Some lobes also show spots of elevated emission ("hot spots") at their boundaries [Urr94]. Observations with the Chandra satellite show correlated variation of the X-ray and radio emission from the jets [HLK$^+$11]. This implies that the emission in both wave bands is produced by the same underlying mechanism which is believed to be synchrotron emission from the high energy electrons (responsible for the radio emission) and photons that gained energy from these high energy electrons through inverse Compton scattering [RB07].

Broad Line Region

Very broad, permitted emission lines can be observed in the optical spectra of Seyfert I galaxies and quasars. Their most likely source are gas clouds orbiting the central region whose atoms are photo-ionized by the central continuum emission from the accretion disc. In many Seyfert galaxies a correlation of the central continuum emission with the broad line emission could be observed. As the line widths are too big to be of thermal origin they must be caused by Doppler broadening due to movement of the gas clouds in the central potential. This implies cloud velocities of up to 10^4 km/s.

Narrow Line Region

In addition to the broad emission lines also narrow lines can be observed in AGN spectra. They are caused by so-called forbidden transitions and thus originate from a collisionless gas with a low density ($10^2 - 10^4\,\mathrm{cm}^{-3}$). The collisionless environment allows sufficient population of the long-lived source energy levels in order to make these strongly suppressed transitions detectable. The thermal broadening of the lines indicates gas temperatures of 10 000 to 25 000 K. The morphology of this narrow-line emission regions is asymmetric, it is mostly observed in two cones perpendicular to the accretion disk.

Molecular Torus

Quasar spectra often show a bump in the infrared part of the spectrum that originates from the thermal emission of a molecular or dust torus around the central region. From the spectrum a temperature of 20 to 80 K can be inferred. The matter in the torus absorbs high energy radiation from the central region and re-emits it as infrared light.

2.3.3. Unified Models

Unified AGN models try to explain the different observational characteristics with different viewing angles on the AGN. The claim is, that intrinsically all AGNs are similar but appear different depending on what components are visible.

The distinction between Seyfert I and II galaxies from optical and infrared observations is explained by the viewing angle on the molecular torus. If the torus is observed from the side it obscures the high-energy emission from the nucleus. Therefore these galaxies appear much less luminous in X-rays.

Similarly the different characteristics of AGNs in the radio band can be explained by the observers line of sight with respect to the jet. In quasars the jet is close to the line of sight and the resulting relativistic beaming leads to an elevated high-energy flux. Non-quasar radio galaxies, on the other hand, have a jet that lies in the plane of the sky and are therefore less luminous radio emitters. The general radio loudness is connected to the magnitude of the spin of the central black hole.

Galaxies that contain a faster spinning Black Hole are louder than slower spinning ones as they have stronger jets.

The canonical picture of a blazar is that the jet is seen head on. Therefore, the strongly boosted radiation from the jet obscures all other features of the galaxy. Blazar fluxes show a very fast variability due to changes in Doppler factor ($\gamma \sim 10$) of the jet caused e.g. by density variations in the intergalactic medium that the jet moves through.

A first unified model of the diverse AGN phenomena was proposed in [UP95]. Figure 2.5 shows the different AGN components and their visibility under different viewing angles in the current unified AGN schema.

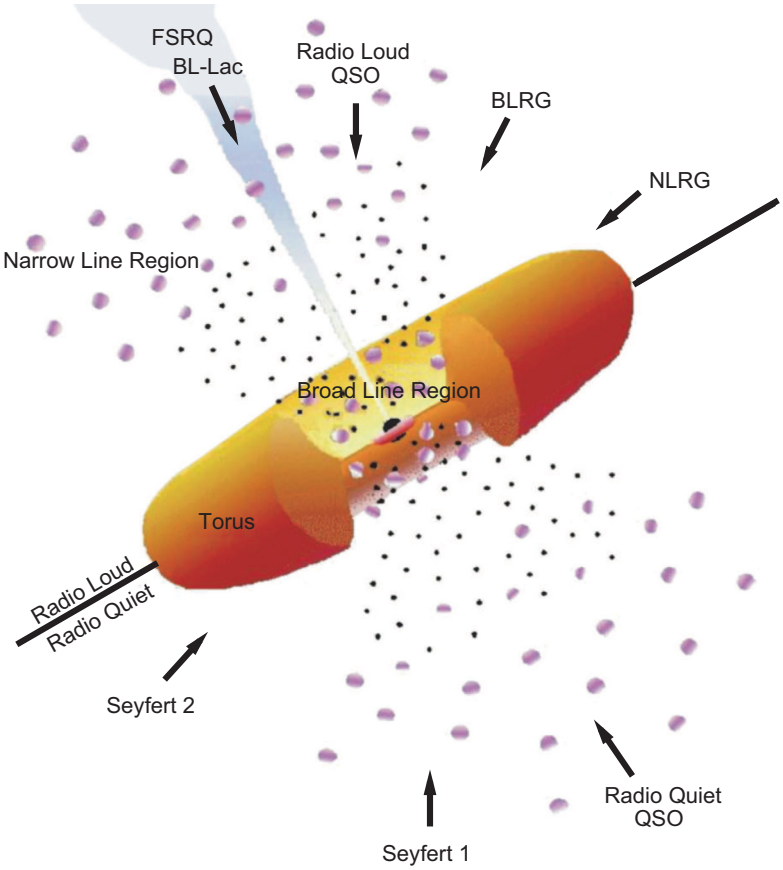

Figure 2.5.: *Unified model of active galactic nuclei (AGN). The electromagnetic emissions observed from these objects depend on the orientation of our line of sight to the jet and the accretion disk of the super-massive black hole in the AGN center. Plot taken from [Ack07].*

2.3.4. Cosmological Importance

It is generally believed that the energy dumped into the intergalactic medium by AGNs had a big impact on the structure formation in the universe. The heating of the intergalactic gas slowed the growth of very large scale structures.

As quasars are observable up to very high redshifts they are a very useful tool for cosmological studies. Their emitted light passes through hydrogen clouds at different redshifts on its way to Earth. Each such cloud absorbs light in a different part of the spectrum due to their different redshifts. Thus the same absorption lines from the Hydrogen Lyman-α series shows up multiple times (the so-called Lyman-α forest). From the presence of certain lines, of their width and strength, the distribution of hydrogen gas and the degree of its ionization over the history of the universe can be inferred.

2.3.5. High-Energy Emission from AGNs

Active Galactic Nuclei where among the first objects detected with Imaging Air Cherenkov Telescopes. The closest known blazar, Markarian 421 (at a redshift of $z = 0.03$), was detected by the Whipple telescope in 1992 [PAC+92]. Subsequently the flux measured from Markarian 421 showed very strong variability down to timescales of several minutes (see e.g. [G+96]). A long term TeV light curve of this object is shown in Fig. 2.6. The extremely fast variability requires a very compact emission region and significant Doppler boosting. Other AGNs that were discovered later show similar flux variability (e.g. PKS 2155-304 [AAB+07], M 87 [AAA+12e] and Markarian 501 [AAA+07b, BBB+12]), though none has been covered as extensively as Markarian 421.

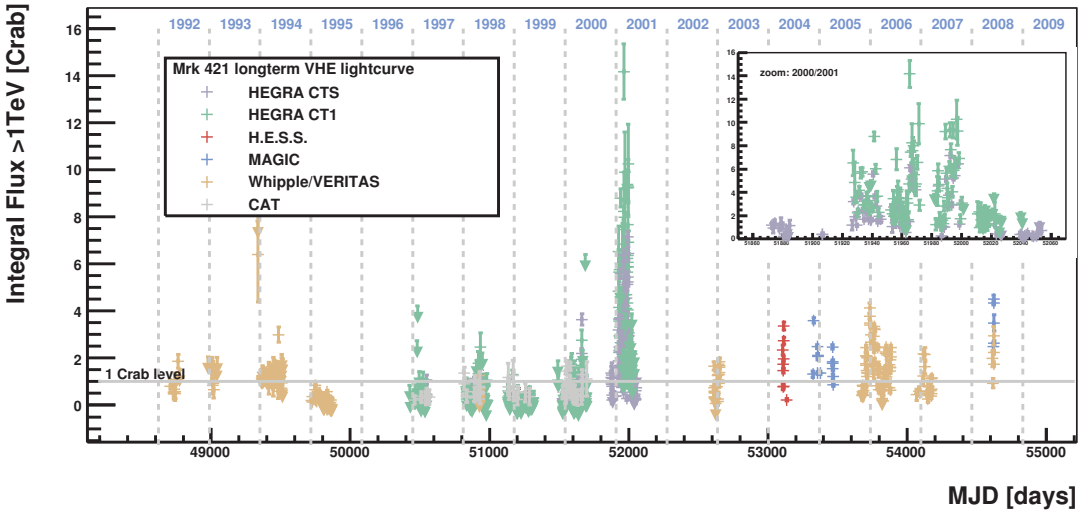

Figure 2.6.: *Markarian 421 longterm* TeV *light curve. Plot taken from [TBS+10].*

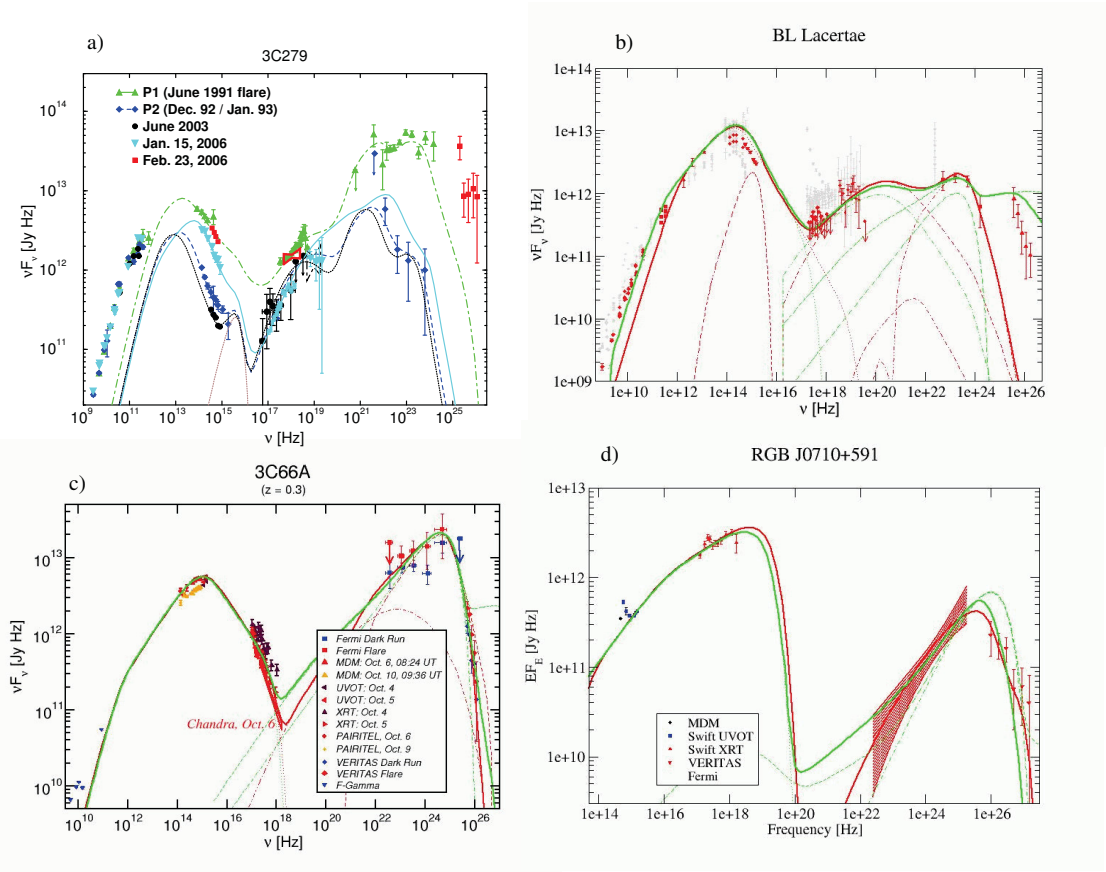

Figure 2.7.: *Spectral energy distributions and fit of leptonic and hadronic emission models for four different subclasses of blazars. Fig. a) shows the FSQR 3C279, the lines depict single-zone leptonic models fitted to the SED in different flux states. Fig. b) shows the low-frequency peaked BL Lac, Fig. c) shows the intermediate-frequency peaked BL Lac 3C66A and Fig. d) the high-frequency peaked BL Lac RGB J0710+591. In Figures b), c) and d) the red line shows a fit of a single-zone leptonic model, green lines show a fit of a single-zone lepto-hadronic model to the data. Figure taken from [Böt12].*

The spectral energy distributions (SEDs) of AGNs consist of two broad components (see Fig. 2.7). The low-energy peak, in the radio-UV or X-ray energy range, is generally believed to be caused by synchrotron radiation of relativistic electrons. The high-energy peak, whose origin is still debated, ranges from X-ray to TeV energies. The fact that the inferred isotropic luminosities for the high-energy emission would be extremely high, together with the very fast high-energy variability suggests that the emission originates from the relativistic jet that is closely alligned with our line of sight [BRZ13]. If the jet with a velocity $\beta = v/c$ is oriented with an angle θ_{obs}

with respect to our line of sight this results in a Doppler boosting with a Doppler factor

$$\mathcal{D} = \frac{\sqrt{1-\beta^2}}{1-\beta\cos\theta_{\mathrm{obs}}}\,. \tag{2.10}$$

It is important to note that the observed flux density S_{f} is boosted according to

$$S_{\mathrm{f}} = \mathcal{D}^3 S'_{\mathrm{f}} \tag{2.11}$$

where S'_{f} is the flux density in the co-moving frame [RB07]. Hence reasonable jet velocities lead to a very strong boosting of the observed flux (e.g. $D \simeq 10$ for $\beta = 0.98$ and $\theta_{\mathrm{obs}} = 1°$).

Two different classes of models have been put forward to explain the observed spectral energy distributions. The first class of models, so-called leponic models, assumes that the emission originates from high energy electrons and their interaction with either self-generated synchrotron radiation or the surrounding radiation field. The second class of models are hadronic models that try to explain the observed spectral features with the interaction of high energy protons or neutrons with the surrounding radiation field (photo-hadronic models) or ambient matter. As hadron interactions (e.g. via decay of $\pi^{\pm}$) also produce electrons and positrons, a full description must consider also these leptonic processes, at least if the acceleration and target region are identical [Rei12]. Thus hadronic models are actually lepto-hadronic models. Historically, however, the name hadronic model is more frequently used.

Leptonic Models

In leptonic AGN emission models the observed radiation over the entire SED is dominated by leptons (electrons and positrons). Any protons that might be present in the jet are not energetic enough to contribute significantly to the radiative output. The low-energy peak is explained by non-thermal synchrotron radiation of the accelerated electrons. The high energy photons in the second bump in the SED originate from Compton scattering of either the synchrotron photons on the accelerated electrons (so-called synchrotron self-Compton radiation) or external photons on the electron population. Possible external target photons could come from the accretions disk radiation, the broad line region (i.e. reprocessed radiation from the accretion disk) and infrared radiation from the molecular torus.

Observed flares from BL Lac objects (e.g. Markarian 421 and Markarian 501) show acceleration of particles to tens of TeV within a couple of minutes. The fast evolution of these flares can usually be best described with synchrotron self-Compton models. The fast cooling times of the accelerated electrons due to synchrotron radiation allow for a quick rise and fall of the flux level. In a simple single zone synchrotron self-Compton model a clear correlation between the synchrotron photons and the high-energy photons would be expected.

Flat spectrum radio quasars (FSRQs), on the other hand, show flux variations on the timescales of hours, with peak energies in the 10 to 100 GeV range. Models used to describe their emission usually employ an additional external Compton component in addition to the synchrotron self-Compton emission.

Hadronic Models

In the hadronic models protons in addition to electrons are accelerated to ultrarelativistic energies. While the low-energy peak in the SED is also believed to be due to synchrotron radiation from the primary electrons, the high-energy component is dominated by proton synchrotron radiation, photons from π^0 decay, synchrotron and Comptom emission from charged meson decay products and electromagnetic cascades due to $\gamma\gamma$ pair production [BRZ13].

One particular hint for hadronic emission are flares that are observed in the TeV energy range but are not accompanied by an X-ray outburst as would be expected in a purely leptonic model. These so-called "orphan" flares have been observed e.g. from 1ES 1959+650 on 4 June 2002 (see [KHH+04, DBB+05, TKH03]). Explaining these flares with either hadronic or leptonic acceleration models is challenging, but harder for leptonic models [RBP05, KT06].

Modelling of blazar SEDs with leptonic models also shows that the total energy in pairs and magnetic field is much less than the radiative power in the comoving frame ($L_{\mathrm{rad}}/\Gamma^2$). Energy conservation requires the presence of hadrons, however it is unclear if they are cold or ultrarelativistic [Rei12].

Proton-Proton Interactions In the first class of hadronic models secondary particles produced in proton-proton interactions in dense target materials are responsible for the observed high energy photon emissions via the production and decay of pions:

$$p + p \rightarrow \begin{cases} pp\pi^0 \text{ , fraction } 2/3 \\ pn\pi^+ \text{ , fraction } 1/3 \end{cases} \tag{2.12}$$

The charged pions decay and produce photons and neutrinos:

$$\pi^0 \rightarrow \gamma\gamma \tag{2.13}$$
$$\pi^+ \rightarrow \mu^+\nu_\mu \rightarrow e^+\nu_e\bar{\nu}_\mu\nu_\mu \tag{2.14}$$
$$\pi^- \rightarrow \mu^-\bar{\nu}_\mu \rightarrow e^-\bar{\nu}_e\nu_\mu\bar{\nu}_\mu \tag{2.15}$$

One example is the channeled blast-wave model that considers a blast wave caused by accelerated hadronic matter sweeping through the surrounding medium or interacting with ambient gas clouds that interact with the jet. The observed variability in the γ flux could then be explained by density variations in the interstellar gas. This models easily explains the very fast variability time scales on the time scale of minutes observed e.g. in Markarian 421, as the emission basically follows the density variations of medium that the jet moves through [PS00b, PS00a]. The channeled blast-wave model also predics correlation between the X-ray emission and the TeV γ-emission, a feature often observed in AGNs [BHG+09].

Photo-Hadronic Interactions The second class of hadronic models does not require the existence of dense target materials but rather considers interactions of the highly relativistic

protons with photons either produced in synchrotron processes by the accompanying electrons or from external sources. The possible sources of the external photon field are the same as discussed in the leptonic class of models. The observed high-energy primaries are produced via photo-meson production, e.g. via the Δ-resonance (see Eq. 2.1). Other decay modes as well as other resonances can produce high-energy neutrons that can escape or transport large amounts of energy very far from the black hole region. Furthermore, protons resulting from decays of these neutrons could form the ultra high-energy cosmic rays.

The energy deposited in photons and neutrinos depends on the spectral shape of the target photon field. The fraction of the primary proton energy dumped into photons and neutrinos increases from about 10 % for a steep target spectrum to about 25 % for a very flat target photon spectrum [Rei12]. In each case the ratio of energies deposited in photons and neutrinos is around unity! However, the flatter the target photon field the more multi-pion production processes become dominant [MRE+99]. Therefore, the average energy per photon (neutrino) as a fraction of the primary proton energy decreases from 6 % (4 %) in steep target photon fields to less than 1 % in very hard target photon fields [Rei12]. To fully describe the processes in an environment with photo-hadronic processes, the energy loss of muons and charged pions via synchrotron radiation prior to to their decay would need to be modeled as well (besides the processes involving electrons and positrons). This implies that hadronic models are usually considerably more complex then purely leptonic acceleration models.

Flat Spectrum Radio Quasars are especially interesting candidates for photo-hadronic production due to the strong target photon field produced in the broad line region. It is, however, argued that the flux of ambient photons in the Broad Line Region is so high that e^+e^- pair production from $\gamma\gamma$ interactions starts to play a major role, so the source would be essentially opaque to photons with energies > 30 GeV. Alternative models discuss a re-collimation of the jet further away from the black hole, outside the broad line region where the ambient photon flux is substantially reduced [TBG+11].

Distinguishing Emission Models

Two main classes of observations might be able to distinguish between leptonic and hadronic models for specific AGNs. The detection of high-energy neutrinos from a source would unequivocally prove that protons are accelerated to very high energies in this object. The detailed study of flare behaviours, especially the time structure and the spectral evolution in different γ energy regimes could also help to constrain the model space. However, the discussion e.g. in [BRZ13] shows, that even small changes in model parameters can lead to substantial changes in the time lag behaviour between different photon energy regimes.

2.3.6. Neutrino Production in AGNs

Section 2.3.5 discussed hadronic emission models in the light of observed γ spectral energy distributions and flare behavior. However, it has also been already pointed out that hadronic

emission models predict the production of neutrinos through the decay of charged mesons (mainly $\pi^{\pm}$ and $K^{\pm}$).

It has been speculated that active galactic nuclei are sources of high-energy neutrinos since a long time (see e.g. [Eic79, SDSS91, SDSS92]). Using very generic assumptions on the magnetic field in the jet and energy spectrum of charged pion decay, in [HZ97] a ν_μ flux from the AGN Markarian 421 is derived:

$$\frac{\mathrm{d}N_\nu}{\mathrm{d}E_\nu} \sim \frac{5 \times 10^{-17} \mathrm{cm}^{-2}\,\mathrm{s}^{-1}}{E_\nu}\,. \tag{2.16}$$

A good overview over different neutrino emission models for different classes of blazars, FSRQs and radio-quiet AGNs is given in [Bec08]. For different detected TeV γ flares the resulting neutrino fluxes are calculated under the assumption of a $1:1$ correlation between the neutrino and photon fluxes. It can be concluded that for the strongest flares observed to date (e.g. from Markarian 421) the produced neutrino flux is close to the sensitivity of current generation neutrino telescopes!

2.4. Other Sources of High-Energy Radiation

This section briefly discusses two galactic source classes of very high energy γ-radiation that are also likely to exhibit some degree of hadronic acceleration. Object like gamma-ray burst, while likely candidates for hadron acceleration, are probably much more short-lived than the flare search presented in this work is designed to detect. Hence they will not be discussed here.

Supernova Remnants An exploding supernova creates a shock wave that moves through the surrounding interstellar medium. The shock wave continuously slows down as it sweeps up material. The shock wave is assumed to be a very efficient area for first order Fermi acceleration (see Sec. 2.1.3). Hence supernova remnants (SNRs) are believed to be the major source of galactic cosmic rays. This connection was already proposed in 1934 by W. Baade and F. Zwicky [RB07]. The recent detection of the π^0-decay signature in two SNRs supports the thesis that they are efficient hadron accelerators [TA$^+$13].

Microquasars A microquasar can be pictured as a small version of a quasar. They are a special class of X-ray binary systems, where a stellar-mass black hole or a neutron star accretes matter from a companion star. Like in quasars an accretion disk and often also a pair of radio jets forms. The flux from the radio jets is highly variable. The accretion disk is much hotter than in quasars (see Sec. 2.3.2), hence its thermal emission is concentrated in X-rays. A small number of microquasars have also been detected as high-energy γ-emitters (see e.g. [AAA$^+$06] for the first such discovery).

2.5. Imaging Atmospheric-Cherenkov Telescopes

The program presented in this work sends alerts to Imaging Atmospheric-Cherenkov Telescopes (IACTs) for follow-up observations. This sections briefly describes how these instruments work and gives information about the MAGIC and VERITAS telescopes.

Mode of Operation IACTs detect photon induced air showers by means of the Cherenkov effect (see Sec. 3.2.3). Highly relativistic charged particles in the air showers produce Cherenkov light. Due to the interplay between the emission geometry and the altitude dependent index of refraction the Cherenkov light flash ($\sim$ 10 ns duration) is mainly concentrated in a light pool with a diameter of $\sim$ 120 m on the ground. A telescope located inside the light pool can reflect the light into an array of sensors from where it can be read out. Figure 2.8 depicts the mode of operation.

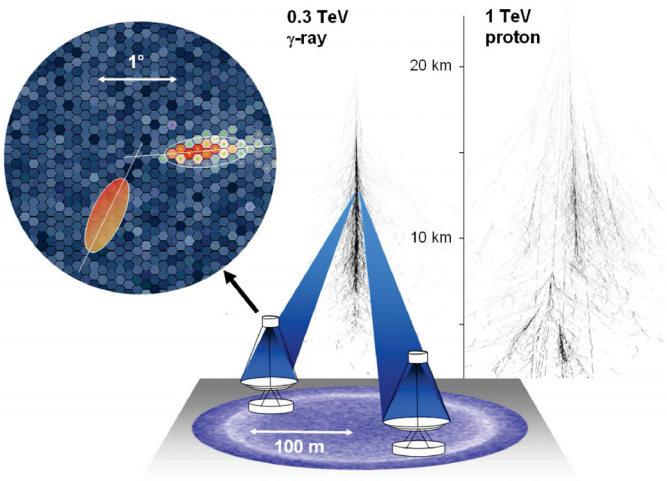

Figure 2.8.: *Schematic of the mode of operation of Imaging Atmospheric-Cherenkov Telescopes. Cherenkov light emitted from highly relativistic charged particles in air showers forms a light pool. The light is reflected into a pixelated array of sensors from where it can be read out electronically. The image can be parametrized to separate hadron induced showers (depicted on the right) from γ induced showers (depicted on the left). By placing two or more telescope about* 100 *m apart the stereoscopic observation of the shower greatly improves the accuracy of the reconstruction of the shower direction. Picture taken from [HH09]*

By analyzing the shape of the elliptical image of the air shower it is possible to discern hadron induced showers from the sought after photon induced (electromagnetic) showers. Due to photohadronic interactions hadron induced showers contain a number of electromagnetic sub showers that lead to a "fuzzier" image in the camera. State of the art methods employ advanced machine learning methods like random forests in order to achieve the γ-hadron separation.

By placing two or more IACTs so close together that they can see the same light pool, the reconstruction of the shower direction is improved.

The MAGIC Telescopes The MAGIC (Major Atmospheric Gamma-Ray Imaging Cherenkov) telescope array is located at 28° 45′ 43″ N, 17° 53′ 24″ W at an altitude of 2200 m on the Canary island of La Palma. The MAGIC array consists of two telescopes, placed 85 m apart, each with a primary mirror of 17 m diameter [CGSf09]. The primary telescope structure is made out of carbon fiber, to reduce the overall weight in order to achieve fast movements to any point in the sky in less than 40 s. After a recent upgrade of the camera and readout electronics of the first telescope (MAGIC I) the array achieves a sensitivity of 0.71 % ± 0.02 % of the Crab Nebula flux ($\frac{\mathrm{d}N}{\mathrm{d}E\,\mathrm{d}t\,\mathrm{d}A} = 3.2 \cdot 10^{-11} \left(\frac{E}{\mathrm{TeV}}\right)^{-2.4}$ $\mathrm{TeV}^{-1}\mathrm{cm}^{-2}\mathrm{s}^{-1}$) after 50 hours of observation. The angular resolution for γ-induced events (68 % containment) is $\lesssim 0.1°$ for $E_\gamma > 250\,\mathrm{GeV}$. The energy resolution in this energy regime is 18% [SCC+13]. A speciality of the MAGIC telescopes is the ability to take data also under moderate moonlight conditions.

The VERITAS Telescopes The VERITAS (Very Energetic Radiation Imaging Telescope Array System) telescopes are located at 31° 40′ 30″ N, 110° 57′ 8″ W near Tucson (Arizona) in the USA. The array consists of four 12 m telescopes with 499 pixel PMT cameras. It is fully operational since 2007, to optimize the array geometry one telescope was repositioned in 2009, an update of the photomultipliers in all cameras in 2012 to high quantum-efficiency PMTs (> 32%) reduced the low-energy threshold and improved the low energy sensitivity. The VERITAS array can detect a γ-ray flux of 5% of the Crab Nebula flux after 1 hour of observations with a significance of $5\,\sigma$ [Nf11, Kf13].

3. Neutrino Propagation and Detection

This chapter deals with propagation of neutrinos and the various methods to detect neutrinos. Section 3.1 explains the phenomenon of neutrino flavor oscillations. The different available methods to detect neutrinos in different energy regimes are described in Sec. 3.2. Finally, in Sec. 3.3, several methods to identify potential astrophysics point sources of neutrinos are discussed.

3.1. Neutrino Flavor Oscillations

The weak flavor of a detected neutrino can be different from its flavor at the production site. This effect is called neutrino flavor oscillation and is mediated by the non-diagonal mixing matrix of neutrino mass eigenstates to weak eigenstates. Therefore, the neutrino flavor ratio at the detection site can be markedly different from its production ratio!

The treatment of neutrino oscillation in this section follows mostly [AS09]. It is important to note that the derivation given here is an approximation as it assumes a plane-wave description of the propagation of the neutrino mass eigenstate m_i. However, a full wave packet treatment of the problem yields the same results! The first experimental hint for neutrino oscillations was obtained by R. Davis by noticing a deficit in the number of observed solar neutrinos compared to predictions [DHH68]. The first evidence for the theory of neutrino oscillations came from the Super-Kamiokande experiment in 1998 [FHI$^+$98].

With the flavor eigenstates $\alpha = (e, \nu, \tau)$ and the mass eigenstates $i = (1, 2, 3)$ a weak eigenstate $|\nu_\alpha\rangle$ can be written as

$$|\nu_\alpha\rangle = \sum_{i=1}^{3} U^*_{\alpha i} |\nu_i\rangle \,, \tag{3.1}$$

where $U^*_{\alpha i}$ denotes the unitary Pontecorvo–Maki–Nakagawa–Sakata (PKMS) neutrino mixing matrix [Pon57, Pon68, MNS62]. The probability to observe a neutrino that was produced in the flavor eigenstate α in the flavor eigenstate β at the distance x is then written as

$$P(\nu_\alpha \to \nu_\beta) = |\langle \nu_\beta | \nu_\alpha(x) \rangle|^2 \,. \tag{3.2}$$

If the assumption is made that the different mass eigenstates have the same momentum at

production then after time t each has picked up a phase factor $\exp(-iE_i t)$ and thus

$$|\nu_\alpha(t)\rangle = \sum_{i=1}^{3} U^*_{\alpha i} e^{-iE_i t} |\nu_i\rangle \,. \tag{3.3}$$

The transition probability to observe a state $|\nu_\alpha\rangle$ in state $|\nu_\beta\rangle$ after time t is therefore given by

$$P(\nu_\alpha \to \nu_\beta; t) = \left| \sum_{i=1}^{3} U^*_{\beta i} e^{-iE_i t} U^*_{\alpha i} \right|^2 . \tag{3.4}$$

The Taylor expansion of the energy E_i of a relativistic neutrino with mass $m_i \ll p$ can be written as

$$E_i = \sqrt{p^2 + m_i^2} \simeq p + \frac{m_i^2}{2p} \,. \tag{3.5}$$

Substituting Eq. 3.5 in Eq. 3.4 together with $x \simeq t$ finally yields the probability to observe flavor β after a propagation distance x when flavor α was emitted:

$$P(\nu_\alpha \to \nu_\beta; x) = \left| \sum_{i=1}^{3} U^*_{\beta i} e^{-i \frac{\Delta m^2_{ij}}{2p} x} U^*_{\alpha i} \right|^2 \tag{3.6}$$

where $\Delta m^2_{ij} = m_i^2 - m_j^2$ denote the differences of the squared masses of the mass eigenstates i and j, and j corresponds to any of the mass eigenstates. The magnitude and the frequency of the oscillation therefore depend on the matrix elements $U_{i\alpha}$, the mass square difference Δm^2_{ij} between the mass eigenstates and the energy of the neutrino. The typical length scale of the oscillation is then controlled by m^2_{ij}/p and the distance between two oscillation maxima is given by

$$L_{ij}(E) = \frac{4\pi p}{\Delta m^2_{ij}} = 2.48\,\mathrm{m} \frac{E\,[\mathrm{MeV}]}{\Delta m^2_{ij}\,[\mathrm{eV}^2]} \,. \tag{3.7}$$

If we assume the Standard Model with three neutrino flavors the mixing matrix U can be written as

$$(U_{\alpha i}) = \begin{pmatrix} c_{12}c_{13} & s_{12}c_{13} & s_{13}e^{-i\delta} \\ -s_{12}c_{23} - c_{12}s_{23}s_{13}e^{i\delta} & c_{12}c_{23} - s_{12}s_{23}s_{13}e^{i\delta} & s_{23}c_{13} \\ s_{12}c_{23} - c_{12}s_{23}s_{13}e^{i\delta} & -c_{12}c_{23} - s_{12}c_{23}s_{13}e^{i\delta} & c_{23}c_{13} \end{pmatrix} \tag{3.8}$$

where $c_{ij} = \cos\theta_{ij}$, $s_{ij} = \sin\theta_{ij}$, θ_{ij} the mixing angles and δ a possible CP violating phase. Using the current knowledge about the mixing angles θ_{ij} the mixing matrix U can be approximated as (see [Bec08, GMSS12]):

$$(U_{\alpha i}) = \begin{pmatrix} \frac{\sqrt{3}}{2} & \frac{1}{2} & 0 \\ -\frac{1}{2\sqrt{2}} & \frac{\sqrt{3}}{2\sqrt{2}} & \frac{1}{\sqrt{2}} \\ \frac{1}{2\sqrt{2}} & -\frac{\sqrt{3}}{2\sqrt{2}} & \frac{1}{\sqrt{2}} \end{pmatrix} . \tag{3.9}$$

It is important to note that this mixing behavior is markedly different from the quark sector where

the corresponding mixing matrix is almost diagonal.

The current world average measurements for the mass square differences are given by $\Delta m^2_{21} = (7.50 \pm 0.20) \times 10^{-5}\,\mathrm{eV}^2$ and $|\Delta m^2_{32} = (2.32^{+0.12}_{-0.08}) \times 10^{-3}\,\mathrm{eV}^2|$ [BAB+12]. Note also that these values do not determine the absolute neutrino mass scale! Two different absolute mass hierarchies are possible. The first, where $m_1 < m_2 \ll m_3$ is called the normal hierarchy, while the second possible ordering, where $m_3 \ll m_1 < m_2$ is called the inverted hierarchy.

As the oscillation lengths L_{ij} (Eq. 3.7) are much smaller than the typical distances to astronomical objects and the emission regions are extended, an average probability to observe a certain flavor given the flavor at the production site can be derived:

$$P_{\alpha\beta} := P(\nu_\alpha \to \nu_\beta) = \sum_{i=1}^{3} \|U_{\alpha i}\|^2 \left\|U_{\beta i}\right\|^2 . \tag{3.10}$$

For a flavor production ratio of $\Phi(\nu_e) : \Phi(\nu_\mu) : \Phi(\nu_\tau) = 2 : 1 : 0$ resulting from charged pion decay (see Eq. 2.2) and a propagation in vacuum (thus ignoring the flavor dependent oscillation effects in matter) a flavor ratio of $\Phi(\nu_e) : \Phi(\nu_\mu) : \Phi(\nu_\tau) = 1 : 1 : 1$ will be observed at the Earth [AJY00].

3.2. Neutrino Detection

3.2.1. Neutrino-Nucleon Interaction

Muon neutrinos can interact with nucleons in matter via charged current processes(CC, $W^\pm$ mediates the interaction) and neutral current processes (NC, Z^0 mediates the interaction):

$$\begin{aligned} \overset{(-)}{\nu}_\mu + N &\to \mu^\pm + \text{anything} \qquad \text{(CC)} \\ \overset{(-)}{\nu}_\mu + N &\to \overset{(-)}{\nu}_\mu + \text{anything} \qquad \text{(NC)} . \end{aligned} \tag{3.11}$$

The average scattering angle between the neutrino and the muon in the case of a charged current interaction can be written as (see [GQRS96]):

$$\langle \Psi \rangle = 0.7^\circ \times \left(\frac{E_\nu}{\mathrm{TeV}}\right)^{-0.7} . \tag{3.12}$$

This scattering angle is taken into account in the IceCube Monte Carlo chain (see Sec. 4.8.1). For neutrino energies greater than O(TeV) this scattering angle does not limit the resolution of the reconstruction of the neutrino direction as it is dominated by the intrinsic resolution of the standard muon track reconstruction (see Sec. 4.5.3).

The neutrino-nucleon cross section for neutral current and charged current processes is written as

$$\frac{\mathrm{d}^2\sigma_{\mathrm{NC,\,CC}}}{\mathrm{d}x\,\mathrm{d}y} = \frac{2G_\mathrm{F}^2}{\pi} M_\mathrm{N} E_\nu \left(\frac{M^2_{\mathrm{Z}^0,\mathrm{W}^\pm}}{Q^2 + M^2_{\mathrm{Z}^0,\mathrm{W}^\pm}} \right)^2 \cdot \left(x q_{\mathrm{Z}^0,\mathrm{W}^\pm}(x, Q^2) + x\bar{q}_{\mathrm{Z}^0,\mathrm{W}^\pm}(x, Q^2)(1-y)^2 \right) \tag{3.13}$$

where the Bjorken variables x and y are given by

$$x = \frac{Q^2}{2M_\mathrm{N}(E_\nu - E_{\nu',\mathrm{l}})} \tag{3.14}$$

and

$$y = 1 - \frac{E_{\nu',\mathrm{l}}}{E_\nu} \tag{3.15}$$

and q and $\bar{q}$ are linear combinations of the quark distributions functions for the different flavors (see [GQRS96]). $M_{\mathrm{Z}^0,\mathrm{W}}$ and M_N denote the vector boson masses and nucleon mass respectively.

For neutrino energies $E_\nu < 10^4$ GeV, where the vector boson propagator can be neglected, the cross sections depend approximately linearly on the neutrino energy [KS12]:

$$\sigma_\mathrm{tot} \approx 1.0 \cdot 10^{-38}\mathrm{cm}^2 \frac{E_\nu}{\mathrm{GeV}} \,. \tag{3.16}$$

For $E_\nu > 10^6$ GeV the charged current $\nu_\mu N$ cross section can be approximated by (see [GQRS96]):

$$\sigma_\mathrm{tot} \approx 2.69 \cdot 10^{-36}\mathrm{cm}^2 \left(\frac{E_\nu}{\mathrm{GeV}} \right)^{0.402} \,. \tag{3.17}$$

Similar approximative power laws exists for the $\bar{\nu}_\mu$N cross section as well as the neutral current cross sections. These cross sections are depicted in Fig. 3.1.

As the interaction length of a particle is given by

$$\mathcal{L}_\mathrm{int} = \frac{1}{\sigma_{\nu N}(E_\nu) N_A} \tag{3.18}$$

where $N_\mathrm{A} = 6.022 \cdot 10^{23}\,\mathrm{mol}^{-1}$ is the Avogadro number, the neutrino interaction length scales with the energy as $\mathcal{L}_\mathrm{int} \sim E^{-1}$ for $E_\nu < 10\,\mathrm{TeV}$ and $\mathcal{L}_\mathrm{int} \sim E^{-0.4}$ for $E_\nu > 100\,\mathrm{TeV}$). The resulting neutrino interaction length is shown in Fig. 3.2. The neutrino interaction length becomes smaller than the Earth diameter for energies above $\approx 50\,\mathrm{TeV}$. Therefore neutrinos of higher energies can only be detected close to or above the horizon.

3.2.2. Muon Propagation in Ice

Muons loose energy when they propagate through matter by a number of different mechanisms. Cherenkov radiation losses can be neglected, ionization plays only a minor role for the high-

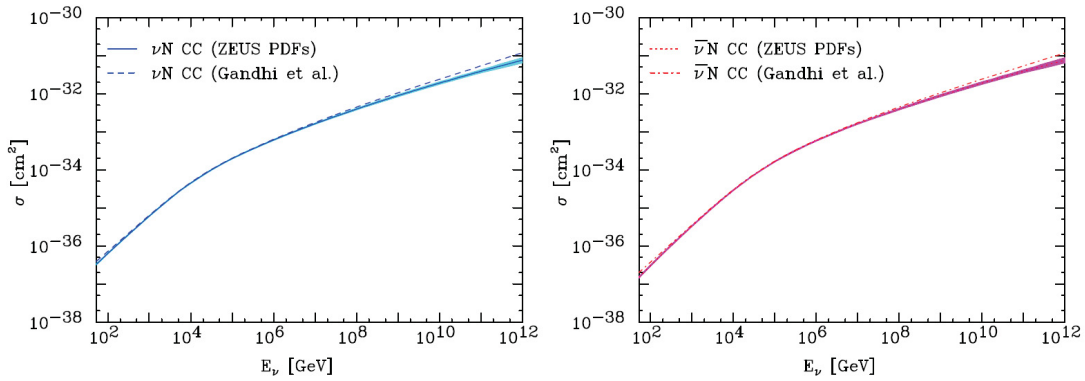

Figure 3.1.: *Neutrino-nucleon cross sections as a function of neutrino energy for neutrinos (left) and anti-neutrinos (right). The neutrino-nucleon cross section is bigger for neutrinos than anti-neutrinos due to the presence of the valence quarks. The two different curves in each plot compare correspond to two different parameterizations of the parton distribution functions. Plot taken from [CS08].*

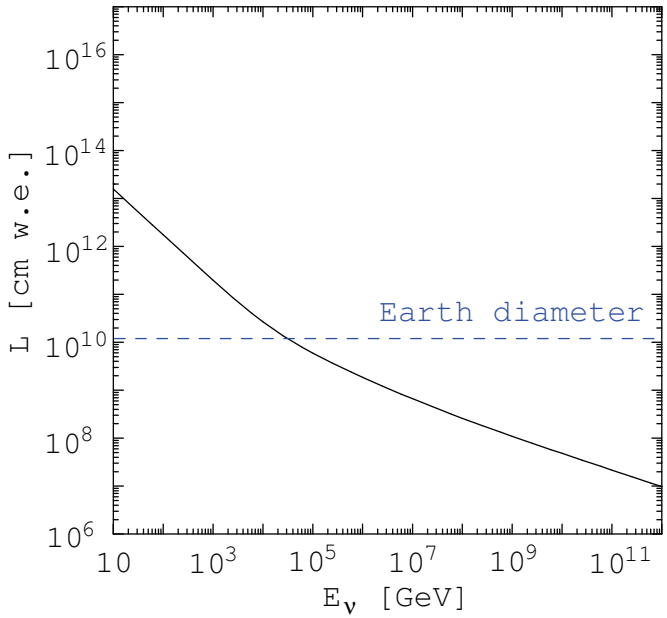

Figure 3.2.: *Neutrino interaction length versus the energy of the neutrino. The Earth diameter is marked by the horizontal line. Neutrinos with $E > 50\,\mathrm{TeV}$ are likely to be absorbed in the Earth if they pass through it.*

energy muons considered here. The energy loss through ionization is almost energy independent and amounts to $a = \frac{\mathrm{d}E_\mu^{textion}}{\rho \mathrm{d}x} = 2.68 \frac{\mathrm{MeV}}{\mathrm{g\,cm^{-2}}}$ in ice.

For muons with energies above several hundred GeV energy losses through direct pair production,

bremsstrahlung and photoproduction dominate over ionization. The energy loss through these processes is approximately proportional to the muon energy. The total energy loss $\mathrm{d}E_\mu/\mathrm{d}x$ can then be written as [BB81]:

$$-\frac{\mathrm{d}E_\mu}{\rho \mathrm{d}x} = a(E_\mu) + b(E_\mu)E_\mu \tag{3.19}$$

where $b \simeq 3.6 \times 10^{-6}\,\mathrm{g}^{-1}\,\mathrm{cm}^2$. Under the assumption that these slowly varying coefficients $a(E_\mu)$ and $b(E_\mu)$ are independent of the muon energy the range of a muon with initial energy E_μ is given by:

$$R(E_\mu, E_\mu^{\min}) = \frac{1}{b} \ln \frac{a + bE_\mu}{a + bE_\mu^{\min}} \tag{3.20}$$

where $E_\mu^{\min}$ is a detector-dependent minimum energy. Equation 3.19 assumes that the losses are continuous. At high energies, however, stochastic losses play a major role. Muons with energies above 1 TeV can loose a large part of their energy in a single interaction (e.g. through a bremsstrahlung photon). Thus a detailed simulation is necessary to obtain the distribution of muon ranges. The survival probability of a muon and the resulting distribution of ranges is shown in Fig. 3.3. A muon with $E_\mu = 10\,\mathrm{TeV}$ has an average range of about 10 km in ice, whereas at

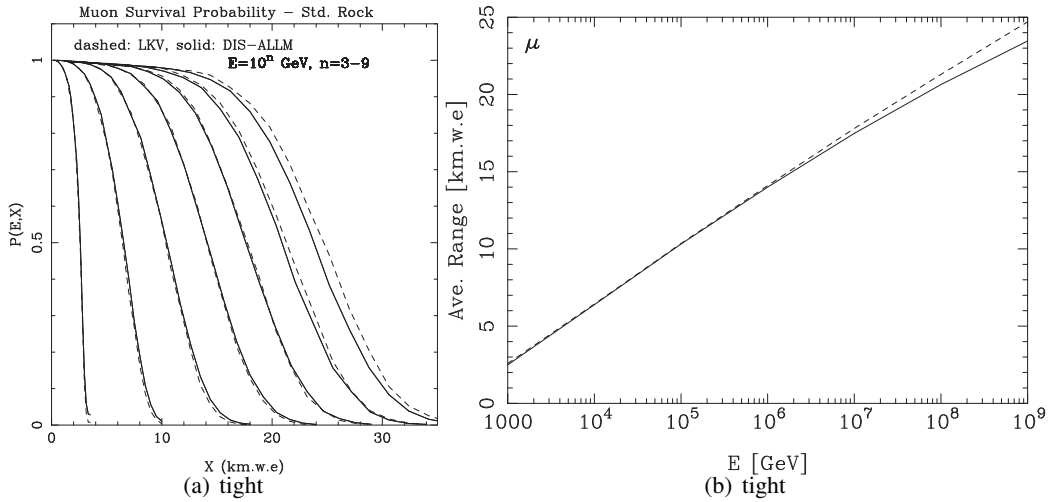

(a) tight (b) tight

Figure 3.3.: *Probability of a muon with a certain energy to survive a given distance without absorption or decay (left). The right plot shows the resulting average muon range for muons with an energy from* 10^3 GeV *to* 10^9 GeV. *The solid and dashed lines show the results from two different models for the parton distribution functions. Plots taken from [IRSS01].*

$E_\mu = 10\,\mathrm{PeV}$ the range increases to about 44 km. This rise of the muon range with energy is very important for neutrino point source searches using high-energy muon neutrinos with neutrino telescopes. While the flux of astrophysical objects decreases with energy, the effective volume of the detector increases due to the increasing muon range.

3.2.3. Cherenkov Radiation

A charged particle that moves faster than the local phase velocity of light in a dielectric medium emits electromagnetic radiation in the form of the so-called Cherenkov radiation [Che34, Vav34, Che37]. The angle θ_C (see Fig. 4.5) under which these photons are emitted is given by

$$\cos\theta_C = \frac{1}{n\beta} \tag{3.21}$$

where n is the index of refraction of the medium and $\beta = v/c$ is the velocity of the particle. The detection medium of IceCube consists of ice with a refractive index at $\lambda = 400\,\text{nm}$ of

$$n \approx 1.32\,. \tag{3.22}$$

This results in a Cherenkov angle of $\theta_C \approx 41°$ for particles with $\beta \approx 1$. The intensity of the radiation is wavelength dependent and peaks in the near-UV region. The differential photon flux of a particle with charge z is given by the Franck-Tamm formula [TF37]:

$$\frac{\mathrm{d}^2N}{\mathrm{d}x\mathrm{d}\lambda} = \frac{2\pi\alpha z^2}{\lambda^2}\left(1 - \frac{1}{\beta^2 n^2(\lambda)}\right) \tag{3.23}$$

where λ is the wavelength of the emitted light and $\alpha \approx 1/137$ the electromagnetic fine structure constant. The spectrum is shown in Fig. 3.4 for the wavelength range where the photomultipliers used in the IceCube detector are most sensitive and where the transmissivity of the glass pressure housing is sufficient (see Sec. 4.2.1). Integrating Eq. 3.23 from 300 nm to 600 nm yields the total light output per unit of track length. Thus a primary Cherenkov photon flux of $2.6 \cdot 10^4$ photons per meter for a high-energy muon is obtained [PW01]. The form of the Cherenkov spectrum

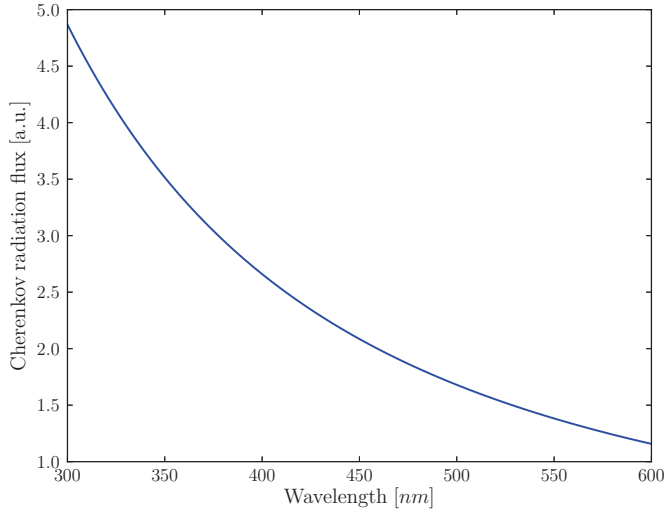

Figure 3.4.: *Cherenkov photon flux (in arbitrary units) of a particle moving with $\beta = 1$ in ice as a function of wavelength in the range of interest for the IceCube detector.*

from particles in ice is almost independent of the energy of the particles. However, the total light output, which comprises both the Cherenkov light from the primary particle as well as the secondary particles, is strongly energy dependent.

3.2.4. Neutrino Detection Methods

This section gives an overviews over methods of neutrino detection that are either currently used or developed. It will not cover techniques that are not in the range of technical feasibility in the foreseeable future like methods to detect the 1.9 K relic neutrinos from the Big Bang (see e.g. [Ebe05]).

Low-Energy Neutrinos

Neutrinos with energies $< O(10\,\mathrm{MeV})$ can be detected via liquid scintillators, radio-chemical methods or Cherenkov radiation employing large detector volumes.

Scintillators Anti-electron neutrinos can react with protons via the inverse β-decay:

$$p + \bar{\nu}_\mathrm{e} \rightarrow n + e^+ \,. \tag{3.24}$$

The threshold energy for this reaction is 1.8 MeV. In order to identify the reaction the two 511 keV annihilation photons of the e^+ have to be detected. For a better background suppression the delayed photon from the capture of the neutron e.g. on cadmium can be exploited:

$$n + {}^{108}Cd \rightarrow {}^{109m}Cd \rightarrow {}^{109}Cd + \gamma \tag{3.25}$$

This technique was used in the first experimental detection of (anti-)neutrinos by Reines and Cowan in 1956 [CRH+56].

Radio-Chemical Methods Charged current ν_x interactions can convert a u-quark into a d-quark in a nucleon. The reaction channel is open to all flavors, but as the electron is the lightest of the three charged leptons, the energy threshold is lowest for ν_e interactions. This method was first established using a chlorine-rich detection fluid by R. Davis in the Homestake Mine in South Dakota to measure the solar neutrino flux. The electron neutrinos interact via

$$\nu_\mathrm{e} + {}^{37}\mathrm{Cl} \rightarrow {}^{37}\mathrm{Ar} + e^- \tag{3.26}$$

with a threshold energy of 814 keV. The produced argon atoms have to be chemically extracted and counted using their radioactive decay. The Homestake experiment provided the first hint of neutrino oscillations as it measured a too low flux of solar electron neutrinos compared to predictions [DHH68].

In order to lower the energy threshold, and thus be able to measure ν_e from the p-p cycle in the Sun, charged current reactions with gallium can be used (e.g. by the GALLEX and SAGE experiments):

$$\nu_e + {}^{71}\mathrm{Ga} \rightarrow {}^{71}\mathrm{Ge} + e^- . \tag{3.27}$$

This reaction has a lower energy threshold of 233.2 keV.

The drawback of the radio-chemical detection method is that it provides no directional information and only very coarse timing, depending on the half-life of the produced isotope (e.g. 11.4 days for ^{71}Ge).

Cherenkov Radiation Charged secondary particles from neutrino induced reactions can produce Cherenkov light, if their energy is high enough (see below). To detect the Cherenkov light emission, a transparent medium is needed. For sufficiently high neutrino fluxes (solar neutrinos, reactor neutrinos, atmospheric neutrinos) artificial bodies of water e.g. in deep underground caverns provide enough target volume to generate fair event rates. Furthermore, in artificial water volumes it is easier to control for impurities causing light absorption or radioactive contaminations that would otherwise increase the background radiation level.

The threshold for the emission of Cherenkov light for an electron in water is 0.26 MeV. Therefore, elastic ν_x-e scattering of sufficiently energetic neutrinos can produce electrons that radiate Cherenkov light in water. This reaction can be initiated by all three neutrino flavors (via an exchange of a Z^0), but is enhanced for ν_e (via an exchange of W^+).

In water that contains deuterium (so-called heavy water) solar ν_e with $E > 1.4$ MeV can react via

$$\nu_e + d \rightarrow p + p + e^- . \tag{3.28}$$

The resulting electron can be detected through its Cherenkov radiation. Detectors employing this detection principle are e.g. SNO [Hal00] and Super-Kamiokande [F$^+$03].

High-Energy Neutrinos

Bubble Chambers A bubble chamber consists of a vessel (usually with a volume of several m^3) filled with a superheated transparent liquid in order to detect charged particles passing through it. The detection principle has first been described by A. D. Glaser in 1952 (see [Gla52]) who was subsequently awarded the Nobel Prize in Physics in 1960. The ionization caused in the superheated liquid by charged particles leads to the formation of microscopic bubbles along their pass that can be photographed. An applied magnetic field bends the paths of charged particles and allows to measure their momenta. Bubble chambers have been used extensively in the early accelerator based neutrino physics. For example experiments at the Gargamelle bubble chamber, filled with the dense CF_3Br to increase the probability of neutrino interactions, discovered the weak neutral currents in 1973 [H$^+$73].

Tracking Calorimeters Tracking calorimeters are build of planes of a detection material interleaved with an absorber material. The detection material provides the tracking information (usually a scintillating plastic, readout with PMTs) while the absorber material increases the target mass. Magnetized steel can be used as an absorber material, to measure the momentum and charge of muons produced by ν_μ charged current interactions. With a high enough detector granularity hadronic showers from neutral current interactions can be distinguished from leptonic showers induced by $e^\pm$. One example of such a detector is the Minos experiment [Nt12] build for the study of neutrino oscillations. The OPERA experiment [ABB+07] employs a finely grained detector using scintillating fibers and photographic emulsions to detect τ-leptons from $\nu_\mu \rightarrow \nu_\tau$ oscillations. The τ-leptons decay almost immediately but can be identified by either detecting the "kink" in the track in the case of a leptonic decay or the three-prong vertex in the case of a decay into pions. Tracking calorimeters are usually used in long-baseline neutrino oscillation experiments with typical neutrino energies below 10 GeV.

Cherenkov Radiation The detection of Cherenkov radiation from secondaries provides the best angular resolution of all neutrino detection methods. Therefore it has the potential to identify astrophysical point sources. Astrophysical neutrinos can be distinguished from atmospheric neutrinos by their presumably harder energy spectrum and their clustering in space and time. As proposed fluxes from astrophysical sources other than the Sun are very low, the target volume needs to be increased by several orders of magnitude compared to solar neutrino experiments. Target volumes of the required size in the km^3-range are no longer financially and technically viable using e.g. excavated caverns. Natural materials providing the required high transparency are water and ice. In order to achieve a good shielding against muons from cosmic ray air-showers, a big material overburden over the instrumented volume is desirable. Therefore deep lakes, the ocean and thick ice shields are natural candidates. While water has the advantage of lower light scattering compared to ice, bio-luminescence and radioactivity from ^{40}K decays pose a challenge to the instruments. The optical properties of glacial ice at the South Pole will be discussed in Sec. 4.7.

Both mediums, water and ice, are currently used for astrophysical neutrino experiments. The Baikal experiment [AAB+09] uses the deep Lake Baikal, ANTARES [AAA+11d] uses the Mediterranean sea and IceCube employs the thick Antarctic glacier at the South Pole.

As the neutrino interaction length decreases with energy (see Sec. 3.2.1) the zenith angle under which neutrinos of a given energy can be detected in deep detectors decreases with energy. Above a neutrino energy on the order of 1 EeV even the shielding material (water or ice) on top of the detector will absorb a sizable fraction of the neutrinos.

Detection of Neutrino Induced Showers For neutrinos of extremely high energies (>100 PeV) the neutrino-nucleon cross section becomes so large (and correspondingly the mean free path so small) that these neutrinos can traverse ~ ten kilometers of rock at maximum. On the other hand, the probability for these neutrinos to interact in the atmosphere and thus to produce a particle shower similar to a cosmic ray air shower is no longer negligible. This provides two ways to detect neutrinos of these energies.

- **Detection of the neutrino-induced air shower** The challenge in detecting neutrino-induced air showers is to discern them from the much more abundant cosmic ray air showers. On average the atmospheric depth of the shower maximum is smaller (i.e. higher up in the atmosphere) for an air shower induced by cosmic-rays than for an air-shower induced by a neutrino. The height of first interaction for a cosmic-ray proton is $h_1 \approx 20.5\,\mathrm{km}$. As the nucleon- nucleon cross-section scales roughly with the mass number A of a nucleus, the mean free path of heavier primary particles is smaller than for protons and consequently the height of first interaction is higher. Neutrinos interact only deeper in the atmosphere due to their smaller cross-section of $\approx 2 \cdot 10^{-32}\ \mathrm{cm}^2$ at 10^{11} GeV (see Fig. 3.1). The AUGER experiment developed techniques to distinguish neutrino induced from cosmic-ray induced air showers and performed a search for these neutrinos. No events were found [Col12] .
- **Detection of Earth skimming neutrinos** At ultra-high energies neutrinos can no longer traverse the whole Earth but there is a region below but close to the horizon where the geometry is such that a neutrino induced shower close to the surface can escape the Earth. The upward-moving shower could then be detected by a fluorescence detector [AIL+05]. Alternatively Imaging Air Cherenkov Telescopes could detect showers originating from neutrino induced horizontal showers in nearby mountains (see e.g. [GBK14]). Due to ν_τ regeneration and the striking τ-decay signature, τ-neutrinos have a much higher probability to be detected in this way [FFWY02, Col12] . The search for Earth skimming neutrinos currently provides the better limit on the ultra-high energy neutrino flux, however at slightly lower energies as the detection of neutrino-induced air showers.

Radio Detection In 1962 the Soviet-Armenian physicist Gurgen Askaryan predicted an effect where a charged particle traveling faster than the phase velocity of light in a dielectric medium produces a shower of charged secondary particles that has a charge anisotropy [Ask62]. The charge asymmetry is caused by the higher prevalence of electrons in the electromagnetic cascade due to Compton scattering of shower photons on electrons from the medium. For wavelengths much larger than the Molière radius of the shower ($\sim 10\,\mathrm{cm}$ in dense materials) the radiations emitted by each charge superimpose coherently. This leads to the emission of a coherent beam (with a power $P \sim$ Number of charged particles^2) of radiation in the radio or microwave range. The effect has first been experimentally verified in the year 2000 [SGW+01]. Natural materials that show dielectric behavior are ice [GBB+07], salt and the lunar regolith [Wil04]. The technique to detect neutrinos via radio signals is supposed to work for energies above 100 PeV.

Experiments employing this effect are RICE [KHS+12], ANITA [GAB+09] and ARA [AAA+12g], all utilizing the Antarctic ice shield as a detection medium. Observations of the moon to detect radio signals caused by the Askaryan effect also yield upper limits on the very high-energy neutrino flux [SBF+11].

Acoustic Detection A fraction of the energy in an electromagnetic shower is converted into heat deposited in the medium. That local heat deposition occurs within $\sim$ several nanoseconds which causes stresses in the medium that are partially relieved via sound waves. This phenomenon has first been described by G. Askaryan in 1957 [Ask57]. First measurements proving the effect

using accelerator beams were reported in 1979 [ADKM79]. Several experiments are investigating the the feasibility of acoustic detection technique as a way to detect neutrinos from the GZK effect ($E_\nu \geq 10\,\mathrm{EeV}$, see Sec. 2.1.1). The experiments SAUND [VGL05] and AMADEUS [LA12] use water as a detection medium whereas SPATS [BBD+08, Tos09, MPRI12] makes use of the Antarctic ice sheet.

3.3. Methods to Identify Neutrino Point Sources

Searches for neutrinos of astrophysical origin must discriminate them against the background of atmospheric neutrinos. Three properties of possible astrophysical neutrino point sources can be exploited to achieve that discrimination:

- **Spatial clustering** Muon neutrinos from an astrophysical point source or an extended source cluster in the direction of the source, whereas atmospheric neutrinos show no such clustering. This feature is used in binned searches for neutrino point sources where the number of detected neutrinos in an on-source bin is compared to the number of neutrinos expected from atmospheric neutrino background alone in a bin at that declination. In an unbinned maximum-likelihood search the directional reconstruction is usually combined with an estimator of the angular reconstruction error, leading to an improved sensitivity.
- **Energy spectrum** Models of neutrino production in astrophysical sources usually predict a harder spectrum than that of atmospheric neutrinos ($\mathrm{d}N/\mathrm{d}E \sim -3.7$). Therefore it is possible to distinguish atmospheric neutrinos from astrophysical neutrinos on a statistical basis based on their energy. This can be exploited in maximum-likelihood point-source searches where the likelihood ratio contains a term corresponding to the probability of the event originating either from the atmospheric neutrino spectrum or a signal spectrum (usually assumed to be a simple power-law).
- **Time clustering** Most emitters of high-energy γ-rays show a strong variability in their emissions in various wavebands. At the same time, these sources are also possible neutrino emitters. As the neutrino and gamma emission might be caused by the same underlying mechanism, a variable neutrino flux with a similar time beavior is likely. Focusing a neutrino search on these periods of interest greatly reduces the background of atmospheric neutrinos and thus increases the discovery potential. Different ways to use the possible time variability of the neutrino signal are explored in the next paragraph.

Methods employing all of these discriminating characteristics are described in [BBD+10].

Time-Dependent Search Methods Several methods can exploit a possible time dependence in the neutrino flux from astrophysical sources. These methods can be divided into two classes:

- Analysis of the neutrino signal alone
- Combination of the neutrino data with photon data

Examples of both methods are described in [AAA+12c].

The neutrino signal alone can be used to search for deviations from a uniform background of atmospheric neutrinos. One possible approach is a search on a list of pre-defined sources using a sliding time window. However, this requires, at least to some approximation, an a-priori knowledge of the length of the neutrino flare. Using several different sliding window sizes would incur a trial factor that reduces the discovery potential. Alternatively, a time-clustering algorithm could be used where the times of the neutrino events themselves define the time windows (see e.g. [BA10]). This approach results in an improved discovery potential compared to the sliding window approach.

The combination of neutrino observations with photon data can happen in different ways. From the photon data (e.g. optical, X-Ray, GeV or TeV) periods of interest can be extracted where the source showed flaring behavior. These time periods define the time windows where a neutrino signal is searched for. Additional model information like e.g. a possible time lag between the photon and the neutrino signal or a prior on the neutrino flux curve (e.g. an emission threshold) can be easily incorporated into this method. However, it relies on the availability of the photon data in the first place! This is especially critical for TeV γ-ray data from Imaging Atmospheric-Cherenkov Telescopes (IACTs, see Sec. 2.5) as these have only a small duty cycle (approximately 10 %) and a small field of view (several square-degree). Thus presently operating Cherenkov telescopes can not monitor all sources of interest continuously. However, once a neutrino flare is discovered, based on an analysis of the neutrino data alone, the TeV γ-ray data would still be of big interest to understand the source behavior, e.g. to assess the opacity of the emission region to TeV photons.

In order to ensure the availability of the simultaneous neutrino and TeV γ-ray data a neutrino flare trigger could provide information to the IACTs when to point at a specific source. This trigger has to be based on an online analysis of the neutrino detector data in order to provide timely alerts. The developments and the first results of such a trigger (the Neutrino Triggered Target of Opportunity) is described in this work. It should be emphasized that γ-ray flares occurring before the accompanying neutrino flare can not be detected with this method. The maximum time lag allowed for the delay between the neutrino flare and the γ-ray flare depends on the observational setup between the partner experiments, e.g. how much observation time of the IACT is committed to each neutrino trigger and what priority these alerts are granted. In the case of delayed photon emission the time lag inherent in such an alert scheme is not a disadvantage.

A discussion of different multi-messenger and multi-wavelength approaches can be found in [Ber11].

4. The IceCube Neutrino Telescope

IceCube is the world's largest neutrino telescope, located at the geographic South Pole. It consists of 5160 photo-multiplier tubes (PMTs) that instrument 1 km^3 of ice. This chapter describes the detector, the data acquisition system and the first level filtering system at the South Pole. Furthermore an overview of the event reconstruction and selection, the optical properties of the South Pole glacier and the Monte Carlo simulation methods is given.

4.1. Detector Layout

Figure 4.1 depicts a schematic view of the IceCube Neutrino Observatory. The in-ice part of the IceCube detector consists of 86 strings of digital optical modules (DOMs). 80 of these strings are instrumented between a depth of 1450 m and 2450 m with a vertical spacing of 17 m between the modules. The strings form a triangular lattice with a horizontal spacing of approximately 125 m. Additional six strings are more closely instrumented with modules that employ PMTs with higher quantum efficiency. These strings form the DeepCore infill array. A pair of purified frozen water tanks with a diameter of 1.8 m is placed on top of every IceCube string. These tanks form the IceTop surface array for the study of cosmic ray air showers in the energy region from about 1 PeV to 80 PeV. The distance of the individual tanks within a tank pair is 10 m. Each tank is equipped with two optical modules, one with a low gain (5×10^5) and one with a higher gain (5×10^6) in order to extend the dynamic range.

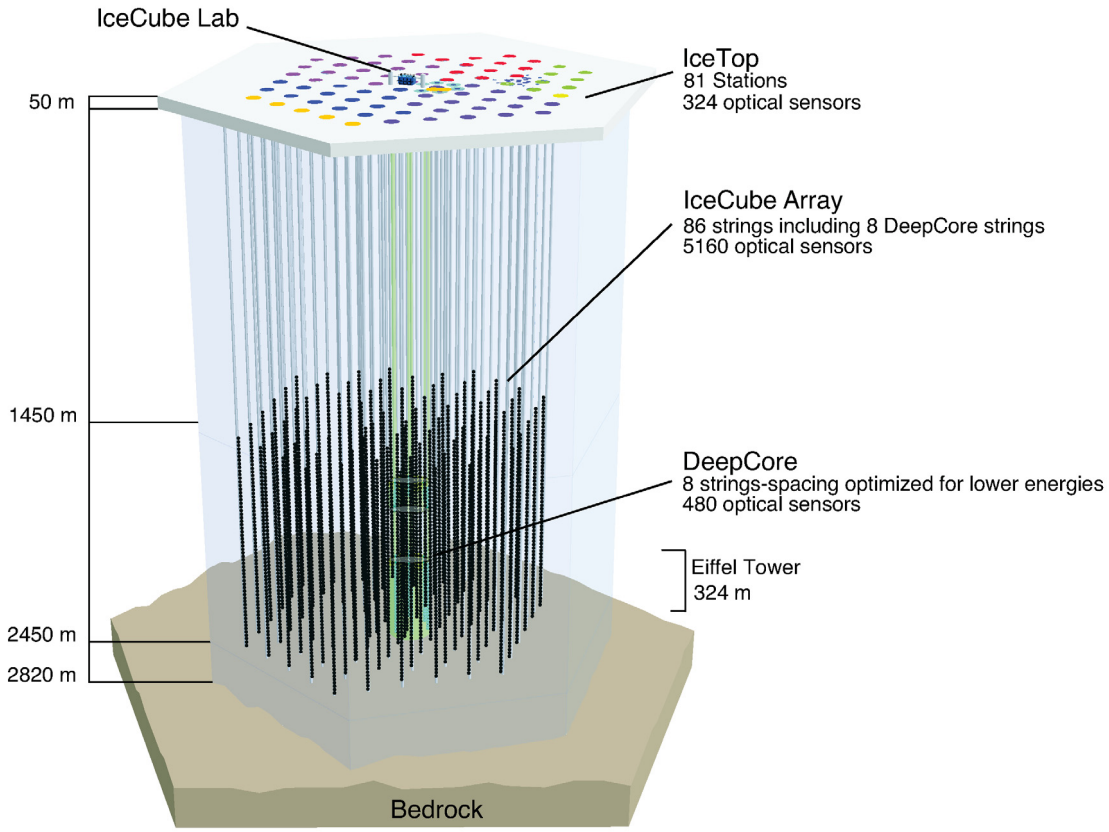

Figure 4.1.: *Schematic layout of the IceCube Neutrino Observatory. See Sec. 4.1 for a description.*

4.2. The Digital Optical Module

The IceCube digital optical module (DOM) consists of a 10-inch diameter photomultiplier housed in a glass pressure sphere together with the associated readout and digitization electronics. A schematic image and a block diagram of the data flow in the DOM can be seen in Fig. 4.2.

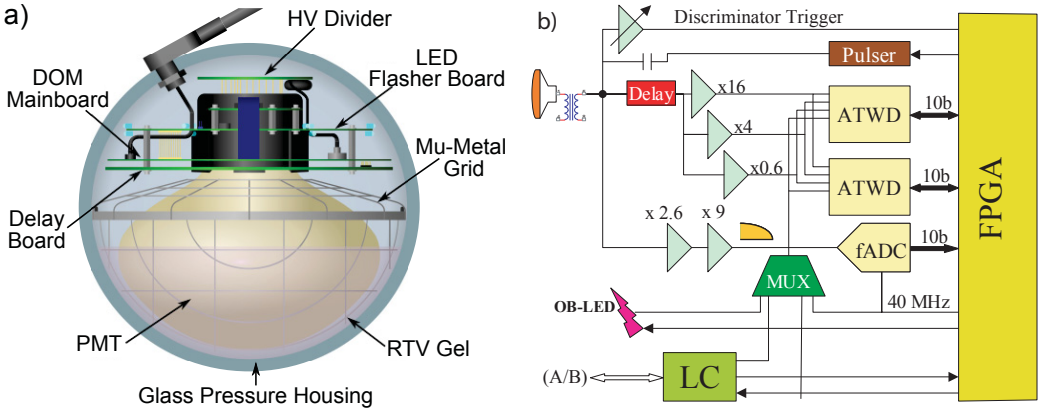

Figure 4.2.: *Schematics of the IceCube digital optical modules (DOMs). Figure (a) shows the PMT and DOM mainboard embedded in the glass pressure sphere. Figure (b) shows the data flow from the analog readout of the photomultiplier to the digitized waveforms transmitted to the surface.*

This description of the DOM is taken from [AAA+10].

4.2.1. The Photomultiplier

The photomultipliers (R7081-02 produced by Hamamatsu Photonics) are sensitive from from 300 to 650 nm, however, the glass pressure sphere that houses them has a lower cutoff in transmissivity at 350 nm. At a wavelength of 390 nm the PMTs have a quantum efficiency of about 25 % (see Fig. 4.3). For single photo-electron pulses the PMT has a transit time spread of 3.2 ns. The PMT is glued to the housing with a flexible, transparent gel for mechanical stability and optical coupling. In order to limit the dark-noise the pressure housing is made of borosilicate glass with extra-low potassium content that lowers the PMT dark-noise rate to ~300 Hz at a temperature of −40 °C. The nominal gain of 10^7 results in single photon pulse amplitudes of around 8 mV. The PMT is coupled inductively to the digitization electronic.

4.2.2. Signal Digitization

The analog signal from the photomultiplier is split into two paths. The first is a 75-ns delay line that is fed into the digitization chain, the second is the trigger logic. The trigger threshold is 0.25 photoelectrons. Signals above that threshold are digitized with two different digitizers,

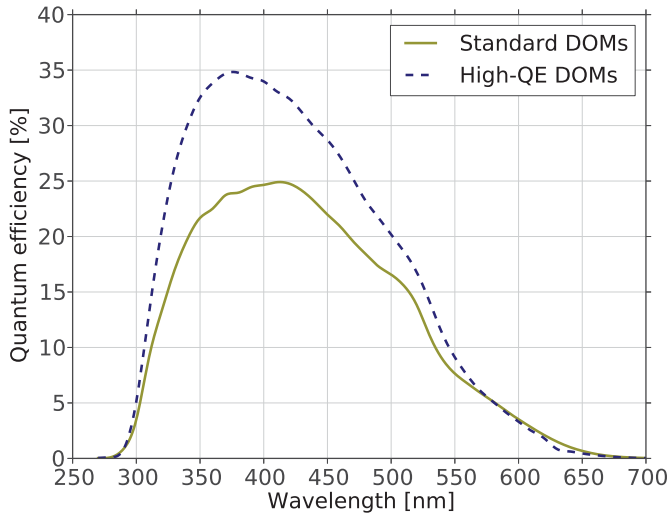

Figure 4.3.: *Quantum efficiency of the PMTs in the IceCube detector as a function of wavelength. The quantum efficiency at a wavelength of 390 nm is about 24 % for the PMTs in the standards DOMs and 34 % for the PMTs in the high quantum-efficiency DOMs used in the DeepCore sub-detector.*

an Analog Transient Waveform Digitizer (ATWD, see [Kle03]) and a Fast Analog to Digital Converter (FADC). The ATWD has four channels, three are fed with the PMT waveform with different amplifications to increase the dynamic range (×0.25, ×2 and ×16), the fourth is reserved for calibration with the light emitting diode (LED) flashers (see Sec. 4.2.3). Each ATWD channel samples 128 bins with a binwidth of 3.3 ns and a resolution per channel of 10 bit. This setup results in a total sampling interval of ~420 ns with a combined dynamic range for the three channels of 15 bit. In order to decrease the dead time resulting from the digitization two independent ATWD circuits are employed that work alternately in a ping-pong fashion. The FADC digitizes data in 256 bins with a bin size of 25 ns (i.e. in a total interval of 6.4 µs) and a resolution per channel of 10 bit.

4.2.3. Calibration

Before being deployed into the ice each optical module went through an extensive commissioning and calibration procedure [AAA+10]. In order to provide an absolute in-situ calibration of the DOMs and assist in the geometry measurement of the IceCube array each optical module is equipped with light emitting diodes (LEDs). Each DOM contains a board with 12 LEDs emitting at a wavelength of 405 nm with an angular emission profile of 30° full-width half-maximum and a light output of 5.7×10^9 photons per pulse for a 50 ns pulse at full brightness. Six of the diodes are pointing horizontally and six upwards at an angle of ~40° to mimic the Cherenkov light emission. The length of the light pulses is variable from 5 to 65 ns. The flashing rate is adjustable from 1.2 to 610 Hz. Dedicated “flasher runs” are performed regularly to measure the

IceCube array geometry and improve the knowledge about the properties of the ice.

Another type of calibration device deployed in the ice are the two "Standard Candles". These two devices consist of pulsed nitrogen lasers emitting at a wavelength of 337 nm and the associated electronics. They are used to calibrate the energy and vertex reconstruction for cascades. To emulate the Cherenkov light profile of electron-neutrino induced cascades, a reflective cone is used. Standard Candle 1 (2) was deployed on 18 January 2006 (16 December 2007) on string 40 (55) pointing upward (downward) between DOMs 22 and 23 (42 and 43) at a depth of approximately 1811 m (2150 m). Standard Candle 2 is thus located just below the big dust layer (see Sec. 4.7) [sta12]. The calibration of the IceCube cascade reconstruction algorithms with the help of the Standard Candles is described in [KDK+08].

Several steps are necessary to convert the readout of the digitizers in each optical module (in raw digitizer counts) to the voltage recorded by the PMT (in mV) and to obtain the absolute photon arrival times at the surface of the PMT. Special calibration runs are performed regularly to obtain the necessary values for these conversions such as the PMT gain as a function of high voltage, the PMT transit time spread, the discriminator thresholds, the time offset of the ATWD and FADC digitizers, the time offset of the two ATWD chips and the digital sampling speeds. In order to convert the digitizer counts to the PMT voltage the digitizer baselines (pedestals) are required as well. The CPU in each DOM triggers a waveform digitization once per second (a "beacon launch") without being triggered by an actual PMT signal. If such a launch happens to fall into a global detector readout window (see Sec. 4.3) it will be included in the data read out from the detector. As this digitized waveform most likely does not contain a PMT signal it can be used to extract the baselines for each DOM. This quantity needs to be known precisely to be able to correct for the droop of the transformer coupling the PMT to the DOM mainboard.

Absolute timing calibration of the clocks on the DOM mainboard is provided by timing pulse that synchronizes the clocks regularly. This timing pulse is derived from the Global Positioning System (GPS).

4.3. Trigger System

The digitization of the waveform is initiated when the PMT signal in a DOM crosses the discriminator threshold of 0.25 photoelectrons. Each optical module is connected to its neighbors on the same string with a dedicated cable. The readout of the full digitized waveform is started only if at least one of the four neighboring DOMs (two modules up or down on the same string) is also triggered within 1000 ns. This is the so-called hard local coincidence (HLC) condition (henceforth referred to as local coincidence). If this condition is fulfilled the digitized ATWD and FADC waveforms are read out and transmitted to the surface. A dedicated computer for each string (the *DOMHub*) forwards the hit information to the global trigger system. Several trigger conditions are defined. The most important one for the purpose of this work is the Simple Multiplicity Trigger which requires eight triggered optical modules (i.e. four local coincidence pairs) anywhere in the detector within 5 µs. Other global trigger conditions concern e.g. lower multiplicities confined to the DeepCore infill array or a certain number of optical modules that

are hit and are located on a single string. When a global trigger is formed the full detector data is read out in a readout window around the trigger (4 µs before the first launch in the trigger till 6 µs after the last launch in the trigger). Once this time window is defined, the DOMHubs request also the data from optical modules that where triggered but where the local coincidence condition was not fulfilled. The information recorded for those so-called Soft Local Coincidence (SLC) hits is limited to a time stamp and the charge in the three highest FADC bins. Triggers with overlapping readout windows are subsequently merged. The stream of triggered events is then sent to the online processing and filtering (PnF) system.

4.4. Online Filtering System

As the data volume produced at trigger level is too big to be transferred via satellite, a first selection has to be applied directly at the South Pole. Triggered events that are deemed interesting for the various physics channels are selected (by "filters") and tagged to be transferred. For events that are not selected by any of the filters only a very small amount of data (the "SuperDST") is transferred. This is useful for studies that require a large sample of atmospheric muons, e.g. studies concerning large scale cosmic ray anisotropies (see [TI12]).

4.4.1. Technical Setup

Figure 4.4 shows the schematics of the online filtering PnF system. Triggered events are picked up and dispatched (by the *DAQDispatch* process) to the central element of the filtering system, the *PFServer*. As a single server process would not be able to handle the full detector event rate, several servers are used (though not shown in the schematics). These servers send each individual event to a filtering client (*PFClient*) that decodes the DAQ data, extracts the pulses from the digitized waveforms and applies reconstruction and filtering algorithms. The events are then sent back to the server where they are reassembled in their original order. The raw and filtered data is then written to disk (by the *PFWriter* process) and handed over to the SPADE system (see Sec. 4.6). Certain selected events can also be sent to so-called "Analysis Clients" that are used to run online alerts systems like the Optical Follow-Up Program (see [AAA$^+$12d]) and the Neutrino Triggered Target of Opportunity Program (*NToO*) described in this work.

4.4.2. The Muon Filter

The filter that forms the basis for the *NToO* is the Muon Filter. It is one of the main filters that runs on the PnF filtering clients selecting events to be transferred to the North via satellite. The aim of the Muon Filter is to select well reconstructed muon tracks at trigger level.

As the main backgrounds are different for the regions $\theta < 90°$ ("down-going" tracks) and $\theta > 90°$ ("up-going" tracks) the filter uses different selection strategies.

The Muon Filter is described in more detail in Sec. 5.1.

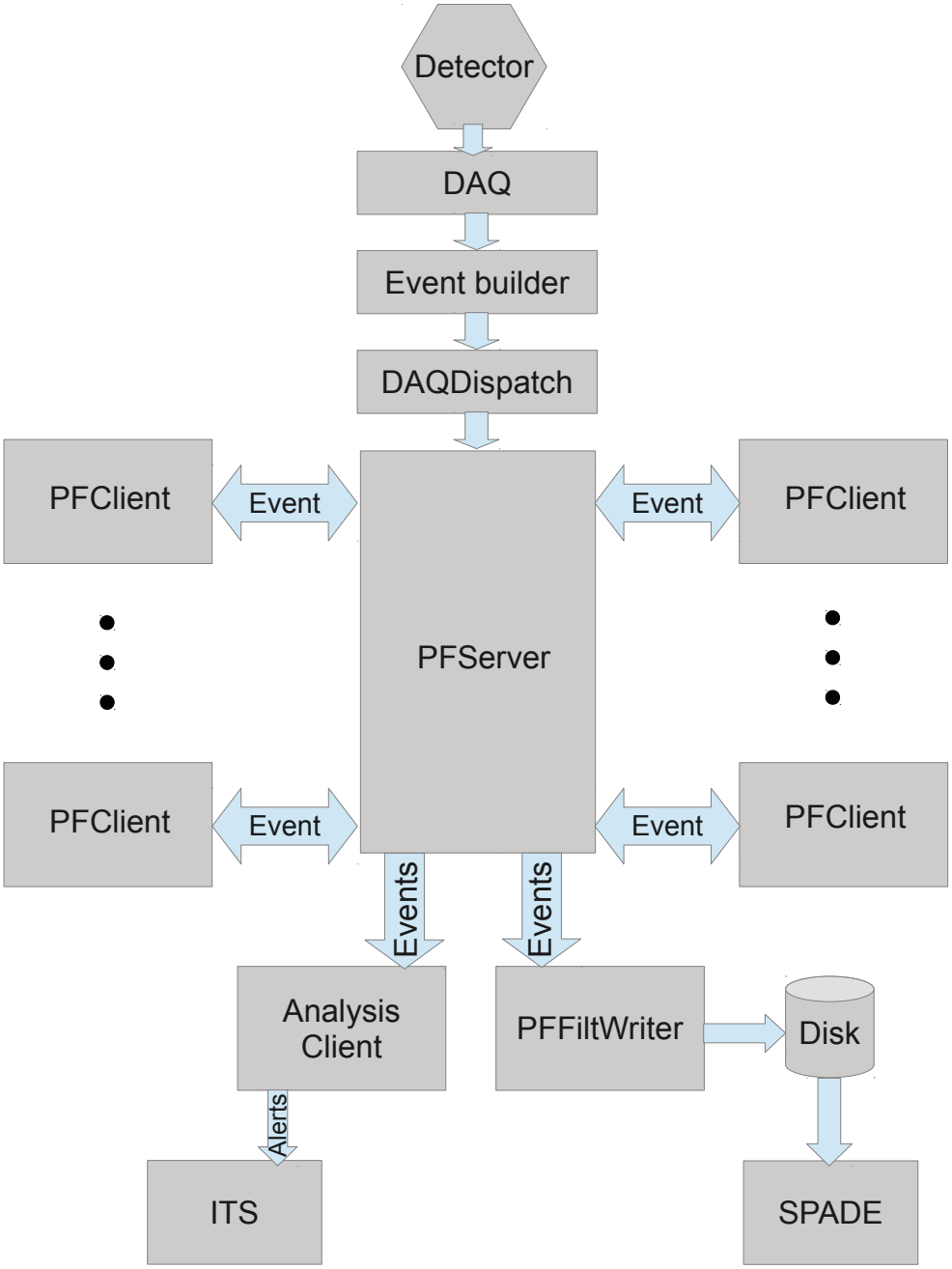

Figure 4.4.: *Schematics of the online processing and filtering (PnF) system for IceCube at the South Pole. The system is described in Sec. 4.4.*

Up-going region In the upgoing region the signal events are muon tracks originating from neutrinos that traversed the Earth and interacted close to the detector whereas the background consists of downgoing muons from cosmic-ray air showers that have been misreconstructed as upgoing. In order to reduce this background a cut on the quality of the SPE likelihood reconstruction is employed for all events reconstructed with $\cos\theta < 0.2$.

Down-going region In the downgoing region the main background consists of muon and muon bundles from air showers. Neutrino-induced muons can therefore not be selected simply based on the quality of the reconstruction. However, the energy spectrum of the air shower muons is very steep ($\frac{dN}{dE} \sim E^{-3.7}$) and a potential neutrino signal may be identified by its flatter spectrum. Therefore, high-energy events are of special interest and are selected by the Muon Filter. A simple energy proxy for a muon is the number of total detected photons summed over all modules participating in the event (Q_{tot}). The Muon Filter cuts on this total charge as a function of the reconstructed zenith angle.

4.4.3. The Online Level 2 Filter

The likelihood fit applied to all events before the Muon Filter has a poor angular resolution (see Fig. 5.1). In order to make an online selection of neutrino candidates feasible with an efficiency comparable to offline analyes, more elaborate reconstructions (like e.g. the MPE fit, see Sec. 4.5.3) are required. These reconstructions are provided by the Online Level 2 Filter that is based on the output of the Muon Filter. Due to constraints on the available processing power at South Pole it was not possible to apply these reconstructions to all events that passed the Muon Filter in the 2011/2012 season. Further cuts had to be applied first. In preparation for the 2012/2013 season the computing capacity at the South Pole was expanded. This enabled the Online Level 2 filter to apply additional, higher quality, reconstructions to all events that passed the Muon Filter. The filter decision is then based on these fits. The filter itself is described in detail in Sec. 5.2.

4.5. Event Reconstruction and Selection

This section describes the most important track reconstruction algorithms and event selection variables used in the *NToO*.

4.5.1. Hit Cleaning

Hit cleaning is the first step in the event processing chain. Its task is to identify noise, pre-pulse and after-pulse hits and remove them from the event while keeping as many hits originating from Cherenkov photons as possible. Two cleaning steps are applied, first causally related hits are identified, then the time window with the highest number of hits is selected.

SeededRT Cleaning

Noise hits are expected to be uncorrelated (between different DOMs) and not clustered in space and time. Hits caused by Cherenkov photons on the other hand are clustered in space and time. This implies a method to identify noise hits. The so called "Seeded R-T Cleaning" is an iterative method that is designed to do that. In the first step it keeps all HLC hits that have at least two other HLC hits close in space and time ($d_{\text{hits}} < R$ and $\delta T_{\text{hits}} < T$). Then it iterates over all hits (HLC and SLC) not yet in the set of kept hits and adds a new hit to the kept hit set if the new hit fulfills the RT-condition with any hit in the set of already kept hits. This process is stopped after an iteration where no hits where added or after a maximum of three iterations (see [Sch10]). The settings used for the online filtering are:

1. $R = 150\,\text{m}$
2. $T = 1000\,\text{ns}$

In the course of implementing the Online Level 2 filter for the 2011/2012 season the SeededRT cleaning algorithm has been reimplemented to increase the speed by a factor of about 400.

Time Window Cleaning

The "Time Window Cleaning" selects the time window of 6000 ns with most detector hits in the event. This selection is based on the hit set provided by the Seeded RT-cleaning. In an event with coincident particles (e.g. a neutrino induced muon event that happens to have a cosmic ray air shower induced muon in the same trigger window) the time window will usually contain the particle that deposited more charge in the detector. If a signal neutrino induced muon is accompanied by an air-shower muon in the same event it is reasonable to assume that the neutrino induced muon has a higher energy due to the harder signal spectrum. However, more sophisticated hit cleaning methods are developed that are designed to split several muons in the same trigger into subevents.

4.5.2. First-Guess Track Reconstruction Algorithm

Linefit The *Linefit* is the simplest and fastest track reconstruction algorithm used in IceCube. It is usually employed as a first-guess algorithm to serve as a seed for more elaborate track reconstructions.

A muon position $\mathbf{r}(t)$ in the detector can be parametrized as

$$\mathbf{r}(t) = \mathbf{r_0}(t_0) + (t - t_0)\mathbf{v}\,, \tag{4.1}$$

where $\mathbf{v}$ denotes the velocity vector and $\mathbf{r}_0(t_0)$ the position at time t_0. The *Linefit* ignores the physics of Cherenkov light emission and assumes a plane wave of light perpendicular to the muon track, moving through the detector with the same velocity as the muon itself. The χ^2 of an assumed track with $\mathbf{r}_0$, t_0 and $\mathbf{v}$ with respect to the observed photon arrival times in the DOMs

can be written as

$$\chi^2 = \sum_{i}^{\text{Hit DOMs}} (\mathbf{r}_0 + (t_i - t_0)\mathbf{v} - \mathbf{r}_i)^2 \,. \tag{4.2}$$

The χ^2 can be minimized analytically to give the velocity

$$\mathbf{v} = \frac{\langle \mathbf{r}_i t_i \rangle - \langle \mathbf{r}_i \rangle \langle t_i \rangle}{\left\langle t_i^2 \right\rangle - \langle t_i \rangle^2}, \tag{4.3}$$

and a point $\mathbf{r}_0$ on the fitted track

$$\mathbf{r}_0(t_0) = \langle \mathbf{r}_i \rangle - \mathbf{v} \langle t_i \rangle \,, \tag{4.4}$$

where $\langle x \rangle$ denotes the average of x.

Improved Linefit Recently several improvements where applied to the linefit algorithm to improve its robustness to noise and handling of coincident events (see [AAA+14]).

4.5.3. Maximum-Likelihood Track Reconstruction Algorithms

Maximum-likelihood methods are very powerful statistical tools for parameter estimation, i.e. fitting a model to data. In the case of track reconstruction, the parameters that are to be estimated are the track parameters, the zenith angle θ, the azimuth angle ϕ, a point along the track $\mathbf{r}_0$, and the time t_0 when the muon passes $\mathbf{r}_0$. All track angles (the zenith θ and the azimuth ϕ) in IceCube are expressed with respect to the origin of the particle. When standing at the South Pole a particle with a zenith angle $\theta = 0$ is moving directly downwards from the sky towards the center of the Earth (declination $\delta = 0$), a particle with a zenith angle $\theta = \pi$ is straight upgoing.

The data used to estimate the track parameters are the measured photon arrival times $t_{i,j}$ at the DOMs and the DOM positions r_i. Given a model of light emission of a muon and photon propagation in the ice the parameters $\theta, \phi, \mathbf{r}_0$ and t_0 can be estimated by maximizing the likelihood to observe the measured photon arrival times given a set of track parameters:

$$(\theta, \phi, \mathbf{r}_0, t_0) = \arg\max_{\{\theta,\phi,\mathbf{r}_0,t_0\}} \mathcal{L}(t_{i,j}, r_i | \theta, \phi, \mathbf{r}_0, t_0) \,, \tag{4.5}$$

where i runs over all DOMs that registered at least one photon, j runs over the photons in each DOM. Generally other parameters like the energy of the muon may be included in the fit. Practically however, this is not very useful and other methods are applied for estimating the energy of a muon.

The knowledge about the Cherenkov light emission and light propagation in ice is encoded in the likelihood function $\mathcal{L}$ which needs to be specified. As the likelihood generally cannot be maximized analytically, numerical minimizers are employed (the minimization of $-\mathcal{L}$ is equivalent to the maximization of $\mathcal{L}$). In order to improve the numerical stability, $-\log \mathcal{L}$ is

minimized. The numerical minimization process can get stuck in a local minimum of the negative log-likelihood as opposed to the desired global minimum. In order to help the minimizer a so-called iterative likelihood fit can be employed where the minimizer is seeded with different first guess tracks. The direction of these seed tracks is usually chosen at random.

Description of Photon Time Residuals

The expected arrival time t_e of an unscattered Cherenkov photon at a position with a perpendicular distance d (see Fig. 3.4) to the track is given by

$$t_{\mathrm{e}} = t_{\perp} + \frac{d}{c_{\mathrm{vac}}} \left(\frac{n_{\mathrm{g}}}{\sin\theta_{\mathrm{C}}} - \frac{1}{n_{\mathrm{p}} \sin\theta_{\mathrm{C}}} \right) \tag{4.6}$$

where n_{g} is the group index of refraction and n_{p} the phase index of refraction. The time residual t_{res} is then defined as the difference of the expected and measured arrival time $t_{\mathrm{res}} = t_{\mathrm{e}} - t_{\mathrm{meas}}$. In [Pan96] the probability density function of photon arrival times was investigated for photons emitted from point-like light sources in water. The resulting *Pandel function* also forms the basis of the description of the time residual distribution in ice. It is defined as

$$p(t_{\mathrm{res}}) = \frac{1}{N(d)} \frac{\tau^{-(d/\lambda)} t_{\mathrm{res}}^{(d/\lambda-1)}}{\Gamma(d/\lambda)} \cdot \exp\left(t_{\mathrm{res}} \cdot \left(\frac{1}{\tau} + \frac{c_{\mathrm{medium}}}{\lambda_{\mathrm{a}}} \right) + \frac{d}{\lambda_{\mathrm{a}}} \right) \tag{4.7}$$

where the normalization $N(d)$ is given by

$$N(d) = e^{-d/\lambda_a} \cdot \left(1 + \frac{\tau \cdot c_{\mathrm{medium}}}{\lambda_a} \right)^{-d/\lambda} . \tag{4.8}$$

This parametrization has several disadvantages. It is not defined for negative t_{res}, does not include the jitter of the PMT, and has a non-physical pole at $t_{\mathrm{res}} = 0$. These problems can be solved by convolving the *Pandel function* with a Gaussian of a given width (usually 15 ns in IceCube), which is denoted P^{conv} in the following. Several approximations are used to speed up the numerical evaluation of the resulting function (see [vFJ07]).

Single Photoelectron Likelihood

The Single Photoelectron (SPE) likelihood takes into account only the arrival time of the first registered photon in each DOM. The motivation is that this is usually the least scattered photon and thus carries most information. The likelihood is given by the product of the individual convoluted *Pandel* functions:

$$\mathcal{L} = \prod_{i \in \text{Hit DOMs}} P^{\mathrm{conv}}(t^i_{\mathrm{res}}) \,. \tag{4.9}$$

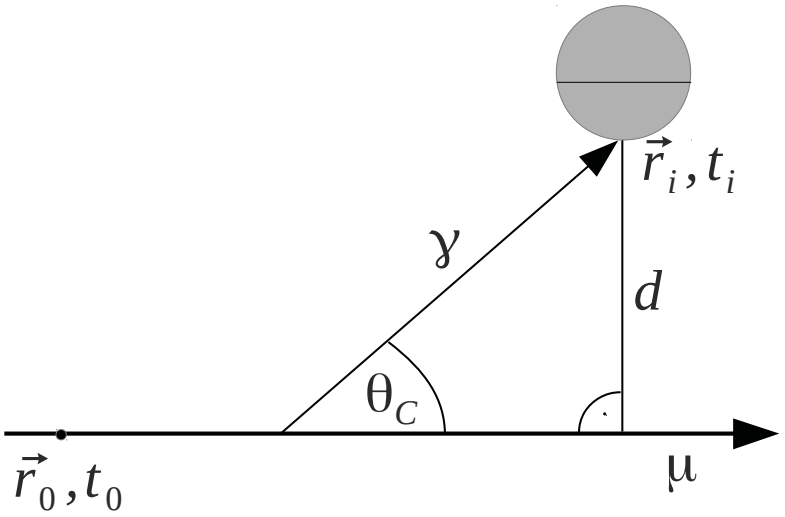

Figure 4.5.: *Geometry of Cherenkov light emission from a muon track, recorded on a DOM at* $\mathbf{r}_i$ *at time* t_i*. The Cherenkov photons are emitted under an angle* θ_C *from the track, in ice* $\theta_C \approx 41°$*.*

Multi Photoelectron Likelihood

The SPE likelihood completely ignores subsequent photons in a given DOM. A better model of the actual measurement process is provided by the Multi Photoelectron (MPE) fit. The probability density function used in this likelihood formulation does not only take into account the time residual of the first of N detected photons in a DOM but also that $N-1$ of these photons have been registered after the first. The likelihood for each optical module is given by the probability to register the first photon at $t_{i,1}$ and all other $N-1$ photons at later times:

$$\mathcal{L}(\{r_i, t_{i,1}, N_i\}|\theta, \phi, \mathbf{r}_0, t_0) = \prod_{i \in \text{Hit DOMs}} N_i P^{\text{conv}}(\mathbf{r}_i, t_{i,1}) \left(\int_{t_{i,1}}^{\infty} P^{\text{conv}}(\mathbf{r}_i, t) dt \right)^{N_i - 1} . \tag{4.10}$$

Track fits based on the MPE likelihood achieve a significantly improved angular resolution compared to fits based on the SPE likelihood.

4.5.4. Resolution Estimation

A critical parameter in a maximum-likelihood based search for neutrino point sources is the error of the reconstruction for each event. As it can only be determined on an event-by-event basis with simulated data, an estimate has to be used for experimental data. [1] Two different approaches are applied in IceCube.

[1] In the absence of a neutrino standard candle the deficit in muons from the direction of the moon is used to establish the absolute pointing accuracy of the detector and of the reconstructions (see [IAA+13a]).

Paraboloid fit The *Paraboloid fit* scans the likelihood space around the minimum determined in the track fit by varying the fit parameters. The resulting points in the likelihood space are fitted with a parabola. From this parametrization the changes in the respective parameter value can be obtained that result in a change of the log likelihood $\log \mathcal{L}$ by $\Delta \log \mathcal{L} = -0.5$. These parameter values are estimates of the error on the fitted track parameters (e.g. the direction) and therefore serve as resolution estimates. Due to the repeated evaluation of the likelihood function this method can be too slow to be used in the online filtering, especially for high-energy events with a large number of hit DOMs.

Since the likelihood used in the track fit does fully describe the Cherenkov light emission and propagation, the angular resolution estimate given by *Paraboloid fit* is biased. The bias can be calibrated using Monte Carlo events to derive a correction factor which is a function of the reconstructed event energy. The calibration will be explained in more detail in Sec. 7.1.

Cramér-Rao Resolution Estimate The Cramér-Rao theorem provides a lower bound on the variance of an estimated parameter. For an unbiased estimator of a multidimensional parameter $\theta = \theta_1, \theta_2, \ldots$ the covariance is at least as high as the inverse of the Fisher information matrix:

$$cov(\theta_m, \theta_k) \geq I(\theta)^{-1} . \tag{4.11}$$

The Fisher information matrix $I_{mk}(\theta)$ is given by

$$I_{mk}(\theta) = -\langle \left[\sum_{i=1}^{\text{modules}} \frac{\partial^2}{\partial\theta_k \partial\theta_m} \ln p(t_i; \theta) \right] \rangle . \tag{4.12}$$

This estimation of parameter variances can be used to obtain an estimate of the angular uncertainty of a muon reconstruction (see [KLS08]). As the calculation involves no minimization of a likelihood it is considerably faster than the *Paraboloid* fit and thus is the preferred method to be used in online analysis.

4.5.5. Energy Reconstruction

The energy reconstruction method used in this work is implemented in the *MuE* software module. It is based on a comparison of the registered number of photons to the number of expected photons for a muon of a specific energy. The number of emitted photons per track length $N_0(E_\mu)$ can be parametrized as $N_0(E_\mu) = 32440 \cdot (1.22 + 1.36 \cdot E_\mu[\text{TeV}])\,\text{m}^{-1}$ [CZ07]. Without scattering and absorption the photon density would decrease as $1/d$ with increasing distance d from the track. However, in the fully diffusive regime, where scattering and absorption dominate, there would be an exponential dependence. The behavior observed in reality lies in between (see [CZ07]) and can be parametrized using Monte Carlo simulations. Taking into account the ice structure and the effective area of the photo multipliers, the number of emitted photons per track length (and thus the energy of the muon track) can then be derived. Recently several improved methods were developed (see e.g. [AAA+13c]). An overview over the energy reconstruction methods used in

IceCube is given in [IAA+13b].

4.6. Data Transfer to the North

Two different systems are used to transfer detector and monitoring data to the North for further analysis.

SPADE SPADE (South Pole Archival and Data Exchange) is the system that is responsible for storing the raw and filtered data coming out of the filtering system and queuing it for satellite transfer. Generally, the data are stored on magnetic tape. In addition, for each type of data (e.g. filtered events or monitoring data) SPADE can be assigned to transfer the data via satellite with a pre-defined priority. The high bandwidth transfer of filtered detector data (~100 GB per day) happens via the GOES 3 (Geodetic Earth Orbiting Satellite) and TDRS (Tracking and Data Relay Satellite) NASA systems.

ITS ITS (IceCube Teleport System) uses the Iridium satellite system to transfer short messages to the northern hemisphere. As a number of Iridium satellites is always visible from the South Pole the system provides a highly available connection [IRI]. However, the amount of data that can be transferred is limited to about 1800 characters per message. Therefore this communication channel is used only to transfer low volume control and monitoring data to and from the northern hemisphere. A dedicated web page (called *I3Live*) enables remote control of the detector, the data acquisition, and the filtering system using these ITS messages. Additionally the system can also be used to transfer alert messages for online analysis programs, like the Optical Follow-up System [AAA+12d] and the Neutrino Triggered Target of Opportunity Program (this work).

4.7. Optical Properties of the South Pole Glacier and their Modeling

Glacial ice is the most transparent solid known for light with a wavelength of 200 nm to 400 nm [ABB+95, ABB+97]. In the South Pole glacier up to a depth of 1500 m the scattering and absorption is mainly caused by air bubbles trapped in the ice. At greater depth these bubbles have transformed from their gas phase into the solid air-hydrate clathrate phase [Mil69]. The scattering and absorption below 1500 m is dominated by dust grains and impurities that originate from old volcanic ash layers [PWC00].

Two processes influence the light propagation in ice: absorption and scattering. Light scattering in ice can be described by the Mie scattering theory that assumes spherical scattering centers. A photon is scattered on average after a step length of λ_s with an average scattering angle $\langle \cos\theta \rangle$. For ice $\langle \cos\theta \rangle$ has been determined to be 0.94. The scattering is therefore strongly forward peaked.

The scattering of photons can be described as a random-walk process. The propagation distance in step $i + 1$ projected on the initial direction is given by $\lambda_s \langle \cos\theta \rangle^i$. By summing all the distances projected onto the first step direction, the effective scattering length

$$\lambda_e(\lambda) = \frac{\lambda_s(\lambda)}{1 - \langle \cos\theta \rangle} \tag{4.13}$$

in the limit of a large number of steps can be obtained. If a photon cloud with a specific direction is injected into the ice, λ_e can be understood as distance from the injection point at which the cloud center comes to a halt. The effective scattering length depends on the wavelength. A typical value for the effective scattering length used in the likelihood-based reconstruction is 33 m.

The absorption in ice is denoted by the absorption length λ_a, which corresponds to the mean free path of a photon in ice before it is absorbed. The absorption length depends on the wavelength and generally comprises absorption by dust particles and the ice itself. However, in the wavelength range from ∼200 nm to ∼500 nm absorption is almost entirely dominated by the depth-dependent dust grain concentration in the ice. The typical value for the absorption length used in the reconstruction is 98 m. This is the average value over depths from 1.5 to 2.5 km.

The properties of the ice have been measured with pulsed and continuous light sources embedded in the AMANDA-II and IceCube detectors. A good account of these measurements and ice description used with the AMANDA-II detector can be found in [AAB+06a]. Further input data come from several sources. During the drilling of several IceCube holes a device called "dust logger" was lowered into the water-filled holes before deploying the instrumented detector strings [W+07]. From these measurements the dust concentration as a function of depth has been extracted with a spatial resolution of about 2 mm. These dust concentration measurement, however, only reaches a maximum depth of about 2100 m. Although no deep ice core has been drilled at the South Pole the data measured elsewhere in Antarctica can be extrapolated to the South Pole to provide dust concentration measurements down to the bottom of the glacier (at a depth of ∼2800 m) [B+10].

Ice Models The optical properties of the South Pole glacier have to be taken into account in the event simulation and reconstruction in the form of modeling the wavelength dependent absorption and scattering in a so-called ice model. Most ice models use a horizontally layered ice structure as this is required by *Photonics* (see Sec. 4.8.3). Only recently a model with a tilted layer structure has been developed [AAA+13b] which can, however, only be used with direct photon propagation codes. Studies on asymmetries in the scattering behavior are also ongoing.

Most of the Monte Carlo simulations in this work uses the SPICE I model [C+10] which is a fit of the ice parameters to the data recorded using the flasher LEDs in the IceCube DOMs (see Sec. 4.2). An earlier ice model, called the AHA model, is described in [AAB+06a]. Both models, together with the older *Millennium* model, are shown in Fig. 4.8.

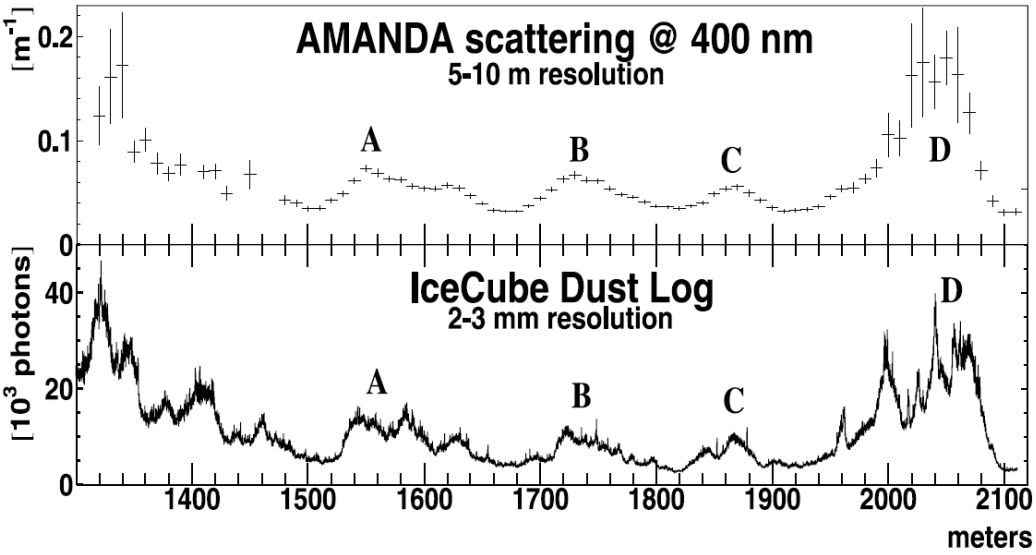

Figure 4.6.: *Scattering coefficient measured with the AMANDA detector (top) and dustlogger data taken before IceCube string deployment (bottom). The number of scattered photons can be used to calculate the dust concentration as a function of depth in the ice. The peaks marked A, B, C and D correspond to historic periods of high dust concentration in the atmosphere caused by volcanic activity. Peak D, at a depth of around* 2000 m*, is the biggest dust layer and is located roughly in the middle of the depth range covered by the IceCube detector.*

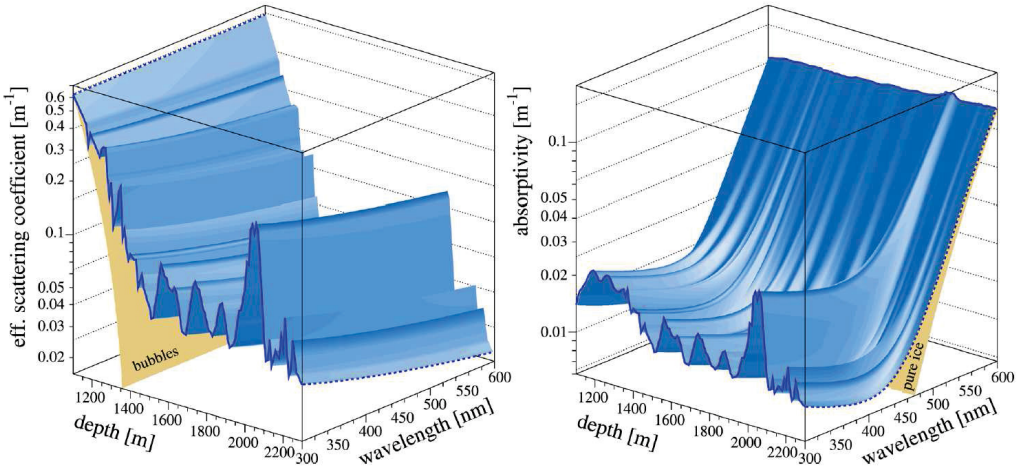

Figure 4.7.: *Ice properties as measured with the AMANDA-II detector as function of depth. The strong depth dependence of scattering and absorption is clearly visible. The layer structure arises from the deposition of volcanic ash on the ice surface at times back to* ~ 70000 *years ago (which corresponds to a depth of* ~ 2200 m *(see [PWC00]). Plot taken from [AAB*$^+$*06a].*

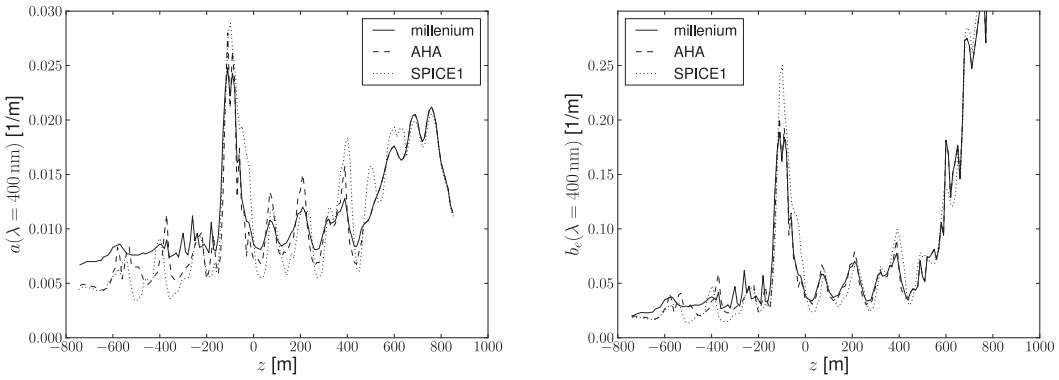

Figure 4.8.: *Absorption coefficient a (left) and effective scattering coefficient b_e (right) for different ice models at a wavelength of $\lambda = 400\,\mathrm{nm}$ in detector coordinates ($z = 0\,\mathrm{m}$ is at a depth of around $1940\,\mathrm{m}$ and denotes the center of IceCube). The millennium model was derived from measurements with the AMANDA detector. To improve its accuracy below $z = -200\,\mathrm{m}$, ice core data obtained at East Dronning Maud Land, Antarctica has been extrapolated to the South Pole, resulting in the AHA model. Measurements with flashing LEDs in IceCube suggest, however, that the peaks and valleys are more pronounced than indicated by this extrapolation. The SPICE I model that incorporates this flasher LED data was employed for most Monte Carlo simulations in this work.*

4.8. Simulation

Monte Carlo event simulations are a very important tool in modern particle and astroparticle physics, especially in the search for new or very rare event signatures. In the absence of a "standard candle" for the type of signal one is looking for, Monte Carlo simulations are needed e.g. to define triggers, to develop event selection schemes, to develop and characterize reconstruction algorithms and to estimate event selection efficiencies and sensitivities. As no beam of high-energy neutrinos is available Monte Carlo studies are used, extensively in IceCube.

4.8.1. Event Generation

Background Events

For neutrino searches, muons produced in cosmic ray induced air showers are the dominant background in IceCube. They trigger the detector with a rate $\sim 10^6$ times higher than atmospheric neutrinos. Cosmic-ray air showers are simulated using a patched version of the CORSIKA program (see [HKC+98]). One of four seasonal atmospheric profiles is randomly selected for each event. The cosmic ray primaries are sampled from the phenomenological *Polygonato* model (see [Hoe03]). The background datasets used in this work where produced with the *Sybill* [EGLS92] hadronic interaction model. A a sizable fraction of events in the IceCube detector include several muons from distinct air showers. These so-called coincident air shower events are simulated as well.

Signal Events

Neutrino events are simulated with a simulation program called *neutrino-generator*, which is a wrapper around the Monte Carlo generator *ANIS* (see [GK05]). *ANIS* generates neutrinos, propagates them through the Earth and finally forces them to interact in a volume around the detector. It can simulate all three neutrino flavors and takes into account regeneration of ν_τ during propagation through the Earth. To make the neutrino event generation more computing-efficient, neutrinos are forced to interact in an interaction volume around the detector. The probability that this happens is taken into account in an event weight. As different primary neutrino spectra are needed by different analyses, one usually simulates a generic primary spectrum $dN/dE_\nu \sim E_\nu^\gamma$ where $\gamma = -1$ or $\gamma = -2$. The events can be re-weighted to the desired spectrum for each analysis. The output of the *neutrino-generator* in the case of a charged current ν_μ interaction are a muon produced at the interaction vertex and the accompanying hadronic cascade. The cascade is not simulated in detail.

Neutrino Monte Carlo generators for high-energies rely on the extrapolation of the measured νN structure functions (see e.g. [LHK+00]) to calculate cross sections resulting in an uncertainty at the highest energies ($\gtrsim 10^{16}$ eV). For the accurate simulation of low energy events (<100 GeV), needed e.g. for neutrino oscillation measurements using the Deep Core array, a dedicated program called *Genie* is used (see [ABB+10]).

4.8.2. Muon Propagation

The simulation of the muon propagation and the muon energy loss is essential to obtain the light distribution in the detector. In IceCube a software package called *MMC* [CR04b] is employed for that purpose. *MMC* calculates the continuous energy loss of the muon as well as the stochastic losses due to bremsstrahlung, pair production, photonuclear interactions and delta electrons (see Sec. 3.2.2). The probabilities for the respective energy losses are sampled from tabulated energy-dependent cross sections. All stochastic losses are recorded. Once the muon energy passes below a user defined threshold (below which it is no longer be detectable by IceCube) the tracking is stopped.

4.8.3. Photon Production and Propagation

The Cherenkov light emission of a muon moving through ice has two different contributions. One is the Cherenkov light emitted by the muon itself. The other is the Cherenkov light emitted by the secondary particles produced in the stochastic energy losses of the muon (e.g. an electromagnetic cascade initiated by an e^+/e^- pair produced by pair- production). The Cherenkov light yield and emission profile of electromagnetic and hadronic cascades have been parametrized from GEANT4 [AAA$^+$03] simulations [Wie95, RW12]. The Cherenkov light yield and emission profile of the bare muon can be calculated from first principles.

To obtain the photon hit times in the individual optical modules from the light emission produced by a certain muon track, different approaches are used. Most IceCube Monte Carlo uses tabulated photon intensities and time distributions produced with the *Photonics* software package (see [LMB$^+$07]). These tables contain the photon arrival time distributions and the mean number of expected photons for a given angle and distance of a DOM to a muon track. During the table generation, the group velocity n_g, the phase velocity n_p, the effective scattering length λ_e, and the absorption length λ_a are taken into account as a function of wavelength and depth. The *Photonics* tables are produced by tracking a huge number of individual photons for a given emission hypothesis. The resulting probability density functions are binned (e.g. as a function of the distance of the receiver to the track) and interpolated when used. *Photonics* assumes a horizontally layered ice structure and thus does not work with tilted ice layers. To reduce the systematic errors caused by the binning used in the tables and to limit the amount of computing memory needed to load these tables, recently smooth spline interpolations have been developed (see [WvL13]).

To circumvent the restriction to horizontally layered ice and to remove the artifacts caused by the binning and interpolation of probability density functions, direct photon propagation software has been developed. This software uses the massive computing capacities of Graphics Processing Units (GPUs) that has become available in recent years. This makes it possible to simulate the propagation of individual photons for each event. It is currently still unfeasible to use this code for the mass production of high-energy neutrino simulation as the number of emitted photons scales roughly with the energy of the muon and the required computing power exceeds event the GPU resources.

4.8.4. Detector Simulation

The detector simulation is concerned with the response of the PMTs to detected photons, the digitization of the PMT waveform in the DOM, and the trigger system.

Simulation of the Photomultipliers The simulation of the PMT response to photons uses a software module called *pmt-simulator*. It takes the individual PMT high voltage into account to simulate the response. It furthermore inserts pre- and after- pulses as well as noise hits and considers saturation of the PMT. The output of this module is a collection of so-called *I3Waveform* objects.

Simulation of the Digital Optical Modules A software module called *DOMsimulator* is concerned with the simulation of the DOM main board response to the waveform generated by the *pmt-simulator*. *DOMsimulator* simulates the main board trigger logic, ATWD and FADC digitization and the local coincidence logic. The waveform droop produced by the inductive coupling of the PMT to the main board is taken into account as well as digitizer saturation. The output of the module is a collection of *I3DOMLaunch* objects.

Simulation of the Trigger System The stream of *I3DOMLaunch* objects produced by the DOM simulation is subjected to the same trigger conditions as the actual detector data. Also, the readout window padding and event merging is implemented with the same logic.

The final result of the simulation chain is a simulated event that provides the same data as an actual event from the IceCube detector.

4.9. Event Signatures in IceCube

The three neutrino flavors and the different interaction types (charged current versus neutral current) will generate different event signatures in the detector. These can be divided into track-like events, cascade-like events and mixed event signatures. They will be described shortly.

Track-like Events Track-like events are generated by charged current ν_μN interactions which produce muons that traverse the detector. The geometry of Cherenkov light emission enables a good directional reconstruction. The achievable angular resolution with respect to the initial neutrino depends on the track geometry (i.e. the length of the track in the detector volume) and the energy of the muon. At low energies the resolution is limited by the scattering angle of the muon with respect to the neutrino.

Depending on the energy of the muon and its point of production it deposits a fraction of its energy inside the detector. Only the lowest energy events with an energy $\gtrsim 10\,\mathrm{GeV}$ can be fully contained inside the detector volume. Measuring $\mathrm{d}E/\mathrm{d}x$ for muons not fully contained inside the

active detector volume provides a lower bound on the energy of the incoming neutrino. However, the resulting energy resolution is limited (see [CZ07]).

Cascade Events Cascade events are produced by charged current $\nu_{e/\tau}$N interactions (electromagnetic and hadronic cascade), ν_x-e scattering (electromagnetic cascade) and neutral current ν_xN interactions (hadronic cascade). The particle cascades deposit their energy in a very small volume. Only at energies > PeV the electromagnetic shower becomes significantly elongated due to the Landau-Pomeranchuk-Migdal (LPM) effect [LP53]. Electromagnetic cascade events that are contained in the fiducial volume of the detector enable a calorimetric energy measurement that results in a very good energy resolution. On the other hand, the isotropization of photons from the almost point-like emission of Cherenkov light severely constrains the angular resolution of these events.

Mixed Event Topologies The charged current interaction of ν_τ can result in event topologies that are a mix of track-like and cascade-like events. Due to the very short lifetime of the τ (2.9×10^{-13} s) even τ's of very high energies are going to decay before they lose all their energy. Only τ leptons with an energy > $O(1\,\text{PeV})$ will propagate far enough to enable the separation of the production and decay vertices. Events for which this separation is not possible are indistinguishable from ν_e-induced cascades.

The τ is the only lepton that can decay hadronically, resulting in a second hadronic cascade at the decay vertex. Decays to charged leptons (either e or μ) result in the production of a new ν_τ. This process is called ν_τ-regeneration. It makes the Earth transparent for ν_τ of the highest energies.

Electrons or positrons from the τ-decay will immediately initiate an electromagnetic cascade, whereas muons will produce a track-like signature in the detector and thereby mimic a ν_μ induced track. The energy of the initial τ-lepton, the relative positions of the primary ν_τ interaction vertex, the secondary decay vertex and the resulting lepton (in the case of a leptonic decay) with respect to the active detector volume result in a multitude of different event signatures.

For the purpose of this work, which is the search for time-dependent emission from neutrino point sources, only track-like signatures are considered as their superior angular resolution is required.

4.10. Statistics

4.10.1. Effective Area

The effective area of a detector is defined as the cross-sectional area of a 100 % efficient detector that would register the same number of events in a given energy interval and zenith region. In the case of the IceCube detector the effective area is strongly energy and zenith angle dependent due to the energy dependence of the neutrino-nucleon cross section (see Sec. 3.2.1). As the effective

area A_{eff} is estimated from weighted neutrino Monte-Carlo simulations it can be calculated as

$$A_{\text{eff}}(E,\theta) = \frac{\sum\limits_{\text{sel}} w_i}{\sum\limits_{\text{gen}} w_i} A_{\text{gen}} \tag{4.14}$$

where the w_i are the event weights of the selected (sel) and generated (gen) events in a certain energy range and zenith region. A_{gen} is the area over which the generated events have been distributed. Figure 5.9 shows the effective area for the final selection level of the analysis presented in this work.

Given the effective area $A_{\text{eff}}(E,\theta)$ the expected event rate from a signal flux $\Phi(E) = \frac{\mathrm{d}N}{\mathrm{d}E\,\mathrm{d}t}$ can be calculated as

$$\dot{N} = \int_{E_{\text{min}}}^{E_{\text{max}}} A_{\text{eff}}(E,\theta)\Phi(E)\mathrm{d}E\,. \tag{4.15}$$

4.10.2. Statistics of Counting Experiments

The ultimate goal of a neutrino point source search is to measure a number of signal events n_{s} from a source. In the binned search method, which is currently used in the Neutrino Triggered Target of Opportunity Program, this number can be derived from the number of detected on-source events n_{obs} and the number of expected background events n_{bg}. As the hypothetical signal contribution is small the number of expected background events can be directly inferred from the data, by averaging the event rate in a zenith band around the on-source bin. This corresponds to the "On-Off" methodology used by γ-ray telescopes. As each measurement is afflicted with a statistical error a confidence interval $[n_{\text{s}}^{\text{l}}, n_{\text{s}}^{\text{u}}]$ for the true value $n_{\text{s}^{\text{true}}}$ is the final outcome of the measurement, when ignoring systematic errors.

Neyman Construction of Confidence Intervals Given a detected number of events n_{obs} and an expected number of background events n_{bg} for each possible value of n_{s} an interval $[n_1, n_2]$ can be found so that

$$P(n_1 < n_{\text{obs}} < n_2 | n_{\text{s}}, n_{\text{bg}}) = \alpha \leq \sum_{n=n_1}^{n_2} \mathcal{P}(n|n_{\text{s}} + n_{\text{bg}}) \tag{4.16}$$

where $\mathcal{P}(n|n_{\text{s}})$ denotes the Poisson distribution

$$\mathcal{P}(k|\lambda) = \frac{\lambda^k}{k!}\exp(-\lambda) \tag{4.17}$$

and α the confidence level. The confidence interval on n_{s} is then given by the interval $[n_{\text{s}}^{\text{l}}, n_{\text{s}}^{\text{u}}]$ so that for all $n_{\text{s}}^{\text{l}} \leq n_{\text{s}} \leq n_{\text{s}}^{\text{u}}$ the number of observed events n_{obs} is contained in the interval $[n_1, n_2]$ when constructed according to Eq. 4.16. A problem arises from the fact that the intervals $[n_1, n_2]$

are not unique, common choices are e.g. the central interval so that $P(n < n_1|n_s, n_{bg}) = P(n > n_2|n_s, n_{bg})$ or the upper confidence limit so that $P(n > n_2|n_s, n_{bg}) = 1 - \alpha$ and $n_1 = 0$.

The central requirement on the confidence interval $[n_s^l, n_s^u]$ is that contains the true value n_s^{true} in a fraction α of cases if the experiment is repeated a lot of times. This property is called proper coverage. However, as n_s is bound to be positive, in the case that $n_s^l \leq 0$, often n_s^u is reported as the upper limit of the measurement. However, deciding after the experiment to report a confidence interval (e.g. if the significance of the measurement crosses some predefined threshold) or an upper limit leads to wrong coverage. This problem is called flip-flopping and can be avoided by the Feldman-Cousins unified approach to confidence intervals described in [FC98]. The method also avoids the problem of empty confidence intervals, e.g. in the case of $n_{obs} = 0$ while $n_{bg} > 0$.

Feldman-Cousins Construction of Confidence Intervals The Feldman-Cousins construction provides a prescription how to construct the intervals $[n_1, n_2]$ defined in Eq. 4.16 for a given n_s. For each n the ratio of the likelihood of obtaining n events, given the actual n_s and the likelihood of observing n events given the best physically allowed mean $n_s^{max} + n_{bg}$

$$\lambda = \frac{\mathcal{P}(n|n_s + n_{bg})}{\mathcal{P}(n|n_s^{max} + n_{bg})} \tag{4.18}$$

is calculated where n_s^{max} is the n_s, which maximizes $\mathcal{P}(n|n_s + n_{bg})$. If n_s is limited to physically allowed values only (i.e. $n_s \geq 0$) we obtain $n_s^{max} = \max(0, n - n_{bg})$. The interval $[n_1, n_2]$ is then expanded to include the values n in decreasing order of λ until the sum $\sum_{i=n_1}^{n_2} \mathcal{P}(i|n_s + n_{bg}) \geq \alpha$. As in the case of the Neyman construction the confidence interval on n_s is then given by the interval $[n_s^l, n_s^u]$ so that for all $n_s^l \leq n_s \leq n_s^u$ the number of observed events n_{obs} is contained in the interval $[n_1, n_2]$ when constructed according to the likelihood ordering principle.

Sensitivity Given an expected number of background events n_{bg}, the number of actually observed events n_{obs} follows a Poisson distribution $\mathcal{P}(n_{obs}|n_b)$ if no signal contribution is present (i.e. $n_s = 0$). For any particular observed n_{obs} drawn from that distribution one obtains an upper limit n_s^u according to the Feldman-Cousins construction. A quantity called the average upper limit (often also called sensitivity) can be defined as the average over the probabilities for the experimental outcomes:

$$\langle n_s^u \rangle = \sum_{n_{obs}=0}^{\infty} n_s^u(n_{obs}, n_{bg}) \mathcal{P}(n_{obs}|n_{bg}) . \tag{4.19}$$

In this work sensitivities are calculated for the confidence level $\alpha = 90\,\%$.

The average upper limit on the number of signal events $\langle n_s^u \rangle$ can be translated into an average upper limit on the signal flux using the event rate $\dot{N} = \mathrm{d}N/\mathrm{d}t$ for a specific neutrino flux $\Phi(E)$ and the observation time t_{obs}:

$$\Phi^{sens} = \frac{\langle n_s^u \rangle}{\dot{N} \cdot t_{obs}} \Phi . \tag{4.20}$$

The sensitivity for a specific flux model is often used as a figure of merit in a neutrino event selection (see e.g. Sec. 5.3.2).

5. Online Neutrino Event Selection

This section describes the online neutrino selection that is the basis for the Neutrino Triggered Target of Opportunity Program (*NToO*). The event selection takes place in several steps, called "levels" in IceCube.

The Muon Filter (see Sec. 5.1) constitutes the first filtering level. It is a standard IceCube filter and not specific to the program presented here. The subsequent Online Level 2 filter (see Sec. 5.2) is based on the input from the Muon Filter and was specifically developed to enable online analyses. Currently the Online Level 2 filter forms the basis of the Optical Follow-Up program (see [AAA$^+$12d]) and the *NToO* program presented in this work. Based on cut variables calculated from the Online Level 2 filter, an online neutrino event selection was implemented (see Sec. 5.3).

5.1. Muon Filter

The Muon Filter is the basis for the standard IceCube muon neutrino analysis, e.g. the searches for neutrino point sources, searches for neutrinos from Gamma-Ray Bursts and measurements of the atmospheric muon neutrino flux. The filter aims to select well reconstructed muon tracks from the full sky. The input of the Muon Filter are all events that trigger the Simple Multiplicity Trigger (see Sec. 4.3). The Simple Multiplicity Trigger has a rate of approximately 2500 Hz, of which about 45 Hz pass the Muon Filter. For analyses which focus on low energy events ($E_\nu < 10^3$ GeV) dedicated filters exist that take advantage of the low-energy capabilities of the DeepCore infill array. These low-energy filters also make use of dedicated trigger conditions (see Sec. 4.3).

The Muon Filter setups for the IceCube 2011/2012 season and the 2012/2013 season are explained in detail in [K$^+$10] and [G$^+$12] respectively. The filter will thus be described only briefly here.

5.1.1. Reconstructions

The track reconstructions and cuts applied in the Muon Filter have been very stable over the last years. Improvements to reconstruction algorithms, changes in the available satellite transfer bandwidth or changes in the data serialization format lead to small adjustments from season to season.

Season 2011/2012

All events triggering the Simple Multiplicity Trigger were reconstructed with the *Linefit* first-guess algorithm as described in Sec. 4.5.2. The result from this track fit formed the input to a SPE track fit (see Sec. 4.5.3). The Muon Filter decision was based on variables calculated from the SPE fit.

Season 2012/2013

In 2012/13 an improved Linefit algorithm was used (see Sec. 4.5.2).

5.1.2. Event Selection Cuts

The Muon Filter divides the sky in two regions where it applies different selection techniques to remove background events. In the up-going region ($\theta \geq 78.5°$) the background events are muons mis-reconstructed as up-going (or slightly above the horizon) which in fact originate from cosmic ray induced air showers. The main handle to remove these events are parameters characterizing the reconstruction quality of the event. In the down-going region ($\theta < 78.5°$) signal and background events have the same signature, namely high energy muon tracks. As the energy spectrum of muons in cosmic ray air-showers ($\Phi(E) \sim E^{-3.7}$) is much steeper than the searched-for signal spectra, cuts on energy related variables are an efficient way to reduce this background. However, as the currently the *NToO* is only implemented for $\theta > 90°$ the event selection cuts in the upgoing region won't be described in detail.

Up-going Region

In the up-going region ($\theta \geq 78.5°$) the Muon Filter uses a cut variable derived from the value of the likelihood of the SPE track fit (see Sec. 4.5.3) The definition of the cut variable is similar to the reduced log-likelihood of the fit. All events which are reconstructed with a zenith angle $\theta_{\mathrm{SPE}} \geq 78.5°$ and that fulfill

$$\max \mathcal{L}_{\mathrm{SPE}}/(N_{\mathrm{DOM}} - 3) \leq 8.7, \tag{5.1}$$

where N_{DOM} denotes the number of hit DOMs in that event, pass the filter. The efficiency of the Muon Filter for atmospheric neutrinos is about 87 %. Neutrinos following a spectrum of the form $\Phi(E) \sim E^{-2}$ are selected with an efficiency of about 93 %. The cuts remained unchanged between the IceCube seasons of 2011/2012 and 2012/2013. The total event passing rate of the Muon Filter amounts to approximately 45 Hz, about 18 Hz are reconstructed with $\theta_{\mathrm{SPE}} > 90°$.

5.2. Online Level 2 Filter

While the Muon Filter provides a sample of neutrino candidate events it is still heavily background dominated (compared to the atmospheric neutrino rate of about 10 mHz at the trigger level). In order to apply further cuts with a high signal efficiency, more elaborate reconstructions with an improved angular resolution are needed. Further reconstructions that e.g. estimate the angular reconstruction uncertainty are also helpful for following analyses. The combination of additional reconstructions and event selection cuts is referred to as the "Online Level 2 Filter".

5.2.1. Reconstructions

The SPE fit used as an input to the Muon Filter has a limited angular resolution compared to an MPE fit. Both fits are compared in Fig. 5.1. During the first season of running the IceCube detector in its full 86-string configuration (from May 2011 till May 2012), the limited CPU resources at the South Pole prohibited applying more resource-intensive reconstructions to all events that passed the Muon Filter. Therefore event selection cuts had to be applied to the events passing the Muon Filter before additional reconstructions could be run. The computing resources at the South Pole were expanded ahead of the second full season of IceCube in its 86-string configuration (from May 2012 till May 2013). This expansion made it possible to run some reconstructions (a two-iteration SPE fit and the MPE fit) before applying the Online Level 2 cuts.

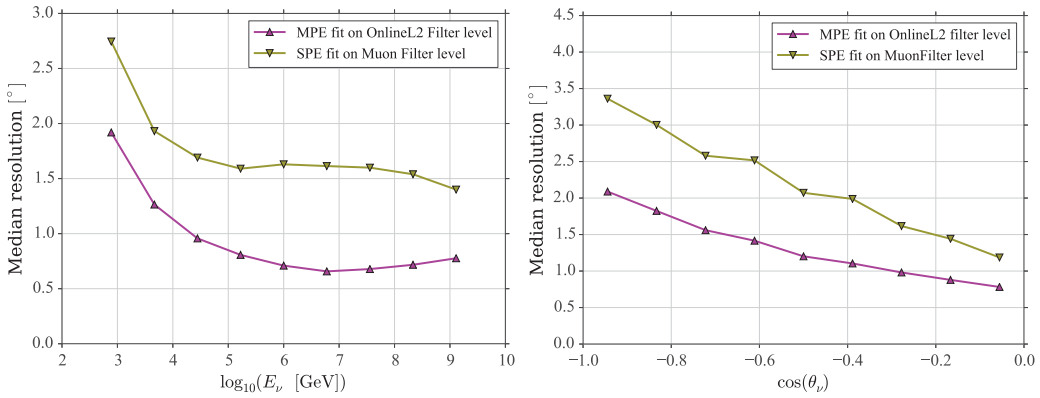

(a) (b)

Figure 5.1.: *Median angular resolutions in the 2011/2012 season for a neutrino sample after the Muon Filter and after the Online Level 2 Filter. The MPE fit which is applied to events passing the OnlineL2 Filter improves the angular resolution.*

5.2.2. Selection Cuts

The cuts of the Online Level 2 filter were designed such that this filter provides a very generic event sample, that could be used for different analyses. Therefore, the cuts chosen should

be simple and stable. The selected events are a strict subset of the Muon Filter events. All reconstructions and cut variables applied before and after the Online Level 2 filter are stored and transferred via satellite to the North for all events that pass the filter.

"Up-going Region"

The main criterion to distinguish the mis-reconstructed atmospheric muon background from the neutrino events are quality parameters of the reconstructed track. Several variables derived from the single-iteration SPE fit have been used to identify these well reconstructed tracks and to suppresses mis-reconstructed air-shower muons during the 2011/2012 season. During the 2013/2013 season these variables have been derived from the MPE fit.

Reduced Log-Likelihood In a maximum-likelihood fit the value of the likelihood at the maximum divided by the number of degrees of freedom of the fit is a measure of the fit quality [BL98]. For the SPE and MPE track fits employed in the Online Level 2 filter the reduced log-likelihood R_{LogL} can be written as

$$R_{\mathrm{LogL}} = \frac{-\log \mathcal{L}_{\max}}{N_{\mathrm{DOM}} - 5} \tag{5.2}$$

where N_{DOM} denotes the number of hit DOMs in the event. It has been shown empirically that this variable, however, is energy dependent for the track fits employed in IceCube. Thus a cut on this variable introduces a bias against well reconstructed low-energy events. In order to reduce the energy dependence a modification is used where the log-likelihood value is instead divided by $N_{\mathrm{DOM}} - 2$:

$$P_{\mathrm{LogL}} = \frac{-\log \mathcal{L}_{\max}}{N_{\mathrm{DOM}} - 2}\,. \tag{5.3}$$

In addition to a smaller energy dependence this cut variable also shows a higher signal efficiency at a fixed background passing rate compared to the traditional reduced log-likelihood.

Number of Direct Hits Another measure of the track quality is the number of DOMs that have registered a hit with a very small time residual $t_{\mathrm{res}} \in [-15\,\mathrm{ns}, 75\,\mathrm{ns}]$ with respect to the arrival time expected for Cherenkov emission from the fitted muon track (see Sec. 4.5.3). Such hits are said to be a "direct hits". The number of direct hits N_{Dir} is calculated using only the first registered photon in each DOM. A photon causing a direct hit has undergone less scattering in the ice and thus can contribute more information to the directional reconstruction. The number of direct hits is therefore related to the quality of the track reconstruction.

Direct Length In a rotated coordinate system where the x-axis is given by the fitted track direction a quantity called "Direct Length" can be defined as

$$L_{\mathrm{Dir}} = |\max_{\text{Direct hits}} x - \min_{\text{Direct hits}} x| \tag{5.4}$$

where the minimum and maximum are calculated over all direct hits as defined in the previous paragraph.

The hits defining the direct length are caused by the least scattered photons and hence contribute the most to the reconstrution. The bigger L_{Dir}, the longer is the lever arm of the reconstruction and the smaller is usually the reconstruction error. Therefore, selecting events with bigger L_{Dir} selects the events most valuable for a point source analysis.

Cut Combination The cut variables described in the previous paragraphs have been combined to achieve a good background rejection as well as a good signal efficiency. Events that are reconstructed as up-going ($\theta_{\mathrm{SPE}} > 85°$) and fulfill

$$P_{\mathrm{LogL}} \leq 7.3 \text{ or } N_{\mathrm{DOM}} > 70 \text{ or } \left(\frac{L_{\mathrm{Dir}}[m]}{180}\right)^2 + \left(\frac{N_{\mathrm{Dir}}}{10}\right)^2 \geq 1 \tag{5.5}$$

are selected by the Online Level 2 filter. The cut on the number of hit DOMs ($N_{\mathrm{DOM}} > 70$) was added to ascertain that high energy events, even when reconstructed with a bigger directional error, always pass the filter. The dependence of the filter rate on the combination of L_{Dir} and N_{Dir} is shown in Fig. 5.2.

Rates and Efficiency Due to seasonal variations in the atmospheric density profile the total rate varies by about 20 % over the course of the year (see Fig. 6.14).

Cut	E^{-1}	E^{-2}	E^{-3}
L2 UpGoing	93 (99)	85 (98)	80 (97)

Table 5.1.: *Efficiency of the Online Level 2 Filter in the 2011/2012 season with respect to the Muon Filter (in %). Number in parenthesis give the efficiencies for events with* $\Delta\Psi_{MPE} < 3°$*).*

The efficiency of the Online Level 2 filter for different signal spectra is listed in Tab. 5.1. It is worthwhile to note that the efficiency is greater than 96 % for well reconstructed events ($\Delta\Psi < 3°$) originating from a soft spectrum with $\Phi(E) \sim E^{-3}$. The filter efficiency with respect to the Muon Filter as a function of the primary neutrino energy is shown in Fig. 5.3. It can be observed that the selection efficiency generally increases with the primary energy. However, events that are reconstructed within 3° of their true direction are selected with more than 90 % efficiency over the whole energy range.

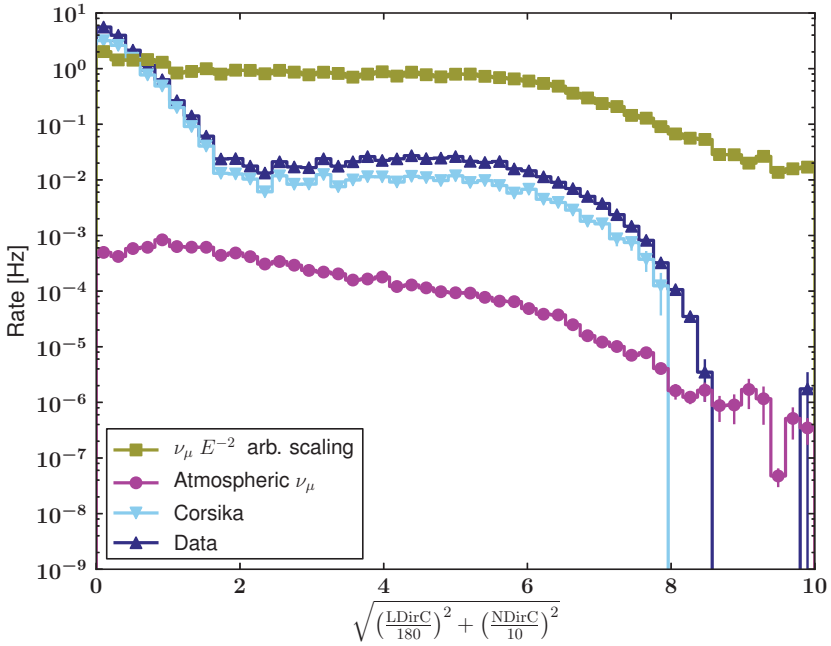

Figure 5.2.: *Histogram of a variable calculated from the direct length and the number of directs hits in an event in order to discriminate between misreconstructed muons and signal events for the Online Level 2 Filter in the 2011/2012 season.*

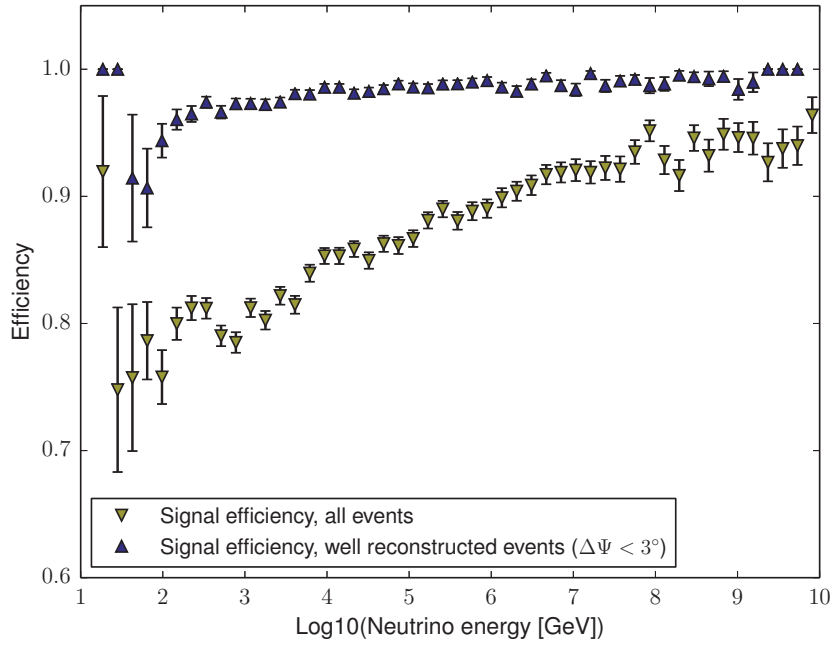

Figure 5.3.: *Efficiency of the Online Level 2 filter during the 2011/2012 IceCube season with respect to the Muon Filter as a function of primary neutrino energy.*

5.2.3. Additional Reconstructions

The event rate of about 5 Hz after the Online Level 2 filter allows to apply additional reconstructions at the South Pole. The following reconstructions (described further down, see Sec. 5.3) have been applied:

- 2-iteration SPE-Fit[1]
- MPE fit, seeded with the 2-iteration SPE-Fit[1]
- Bayesian Fit
- Geometrical and time-based split fits
- MuE energy reconstruction (see Sec. 4.5.5)
- CramerRao resolution estimate

5.2.4. Contraints

The technical setup of the filtering system at the South Pole (see Sec. 4.4) is sensitive to the variance of the event processing times. This rules out the usage of event reconstructions that can occasionally take much longer than ~5 s per event. One consequence is that the number of iterations in the SPE fit is limited to 2. For events with many hit DOMs (>500) more fit iterations would lead to event processing times of more than 10 seconds. As the angular resolution of the SPE reconstruction improves only marginally beyond 2 iterations this does not limit the angular resolution.

Another reconstruction that can not be applied due to these time constraints is the Paraboloid fit (see Sec. 4.5.4). This fit estimates the directional uncertainty of a reconstruction by fitting the likelihood-space around the maximum of the likelihood with a parabola. The resulting event-by-event uncertainty estimate is the de-facto standard in the usual IceCube point-source searches (see e.g. [AAA$^+$11c]). The Paraboloid fit is, however, too slow to be used online. A faster alternative exists, the so-called "CramerRao" method (see Sec. 4.5.4).

Both angular uncertainty estimates, the Paraboloid fit and the CramerRao method, show an energy-dependent bias in the ratios of the estimated to the true angular uncertainty. This bias has been studied more extensively for the Paraboloid fit and can thus be easily corrected for. The behavior of the bias is less well understood for the CramerRao fit, nevertheless the bias can be corrected. The angular uncertainty estimate is not used in the *NToO* as implemented up to now. It plays, however, a crucial role in the maximum-likelihood based search (see Sec. 7.1).

[1] Since the 2012/2013 season this fit is applied before the Online Level 2 filter cuts to all events that passed the Muon Filter

5.3. Neutrino Level Event Selection

This section describes the cut variables and the optimization of the cuts for the neutrino level event selection. First the event variables are described, then the cut optimization procedure is explained and then the final cuts are outlined. The cuts to select neutrino events have been developed using a part of the IceCube 2011/2012 dataset, the first season IceCube ran in its complete 86-string configuration, and a Monte Carlo dataset based on the SPICE I ice model for the neutrino simulation. The cuts have been applied unchanged in the 2012/2013 season, except for the cut on the Bayesian Likelihood ratio following a bug fix in the configuration of that reconstruction (described later in this section).

5.3.1. Cut Variables

Fit Likelihood The scaled likelihood of the track fit was introduced in Sec. 5.2.2. This variable is one of the most powerful cut variables to identify misreconstructed muon tracks. In order to select neutrino events, the different scaling parameters for the fit likelihood value of the MPE fit were investigated. A scaling of the likelihood by $N_{\mathrm{DOM}} - 3.5$ produced the most efficient cut variable to select neutrino events:

$$S_{\mathrm{LogL}} = \frac{-\log \mathcal{L}_{\mathrm{max}}}{N_{\mathrm{DOM}} - 3.5}\,. \tag{5.6}$$

The scaling by $N_{\mathrm{DOM}} - 3.5$ instead of $N_{\mathrm{DOM}} - 2$ as in the Online Level 2 filter showed a higher signal efficiency at the same background rejection in combination with the other cut variables.

Direct Hits The concept of a direct hit has been introduced in Sec. 5.2.2. The cut variable used in the neutrino level event selection is the number of hits with a time residual of $[-15\,\mathrm{ns}, 75\,\mathrm{ns}]$ with respect to the MPE fit.

Direct Length The concept of the direct length has been introduced in Sec. 5.2.2. The cut variable used in the neutrino level event selection is the direct length derived from the MPE track fit with a direct hit time window of $[-15\,\mathrm{ns}, 75\,\mathrm{ns}]$.

Split Fits The track reconstruction for a correctly reconstructed upgoing track should be stable against changes to the set of DOMs used for reconstruction. On the other hand, for two coincident muons wrongly reconstructed as one upgoing track or other cases of misreconstruction, changes to the DOM set should have a much bigger impact on the reconstructed direction. This is the rationale for splitting the DOM set used in the reconstruction in two parts and subsequently performing a maximum-likelihood fit on each part separately. Different criteria can be used to split the DOM set:

- The geometrical splitting splits the hits according to their position with respect to the center of gravity (COG) of all hits. The center of gravity is calculated as

$$\mathbf{x}_{\mathrm{COG}} = \frac{1}{N_{\mathrm{DOM}}} \sum_{i=0}^{N_{\mathrm{DOM}}} \mathbf{x}_i \tag{5.7}$$

  where $\mathbf{x}_i$ are the positions of the individual hit DOMs. The center of gravity $\mathbf{x}_{\mathrm{COG}}$ is then projected on the track obtained with the MPE fit, yielding the point $\mathbf{x}^{\mathrm{proj}}_{\mathrm{COG}}$. Each hit location is then also projected on the track and compared to $\mathbf{x}^{\mathrm{proj}}_{\mathrm{COG}}$. Hits whose projections lie on one side of $\mathbf{x}^{\mathrm{proj}}_{\mathrm{COG}}$ are sorted into one set, hits whose projections lie on the other side are sorted into a second set.

- The time based splitting splits the hits into two sets by comparing each hit to the mean of all hit times t_{mean}. Hits that fulfil $t_i \leq t_{\mathrm{mean}}$ are sorted into one set, hits that fulfil $t_i > t_{\mathrm{mean}}$ are sorted into another set.

For each of the four subsets of hits a standard Linefit (see Sec. 4.5.2) is performed which acts as a seed for a two-iteration SPE maximum-likelihood fit. The zenith angle θ_i resulting from the SPE fit is used to define the cut variable:

$$\Delta_{\mathrm{Split/MPE}} = \max_{i \in \text{split fits}} (\cos\theta_i - \cos\theta_{\mathrm{MPE}}) \,. \tag{5.8}$$

Bayesian Likelihood Ratio The probability that an event selected by the Online Level 2 filter and reconstructed as upgoing (i.e. $\theta_{\mathrm{MPE}} > 90°$) is truly a neutrino induced muon and not a misreconstructed air shower muon is very small ($\sim 10^{-3}$). A useful cut variable can be derived by forcing a down-going track fit and calculating the likelihood ratio to the MPE fit.

The likelihood of this Bayesian fit is calculated as the product of the MPE likelihood of the track and a weight

$$w = 2.49655 \cdot 10^{-7} \cos\theta^{1.67721} \cdot \exp\left(-\frac{0.778393}{\cos\theta}\right). \tag{5.9}$$

The weight w corresponds to the muon air shower flux as a function of zenith. In order to force the numerical minimizer to reconstruct a down-going track ($0 \leq \theta \leq 90°$) a penalty term is multiplied to the likelihood for track hypotheses with $\theta > 90°$. This penalization was wrongly configured in the season 2011/2012 which made the fit less useful. The configuration was fixed in the 2012/2013 season and the cut on this variable was adapted (see Tab. 5.3).

The difference of the logarithms of the Bayesian likelihood fit and the MPE fit

$$\Delta_{\mathrm{Bayesian/MPE}} = \log_{10}(\mathcal{L}_{\mathrm{Bayesian}}) - \log_{10}\mathcal{L}_{\mathrm{MPE}} \tag{5.10}$$

is a useful cut variable especially for events that have been reconstructed with a zenith angle close to the horizon.

Comparisons of Data and Simulation Figure 5.4 and Fig. 5.5 depict the distribution of all cut variables for data, simulated atmospheric neutrinos, simulated air shower muons and a hypothetical signal neutrino flux with $\Phi(E) \sim E^{-2}$ after the Online Level 2 filter. The agreement between the data and the background simulation is generally good.

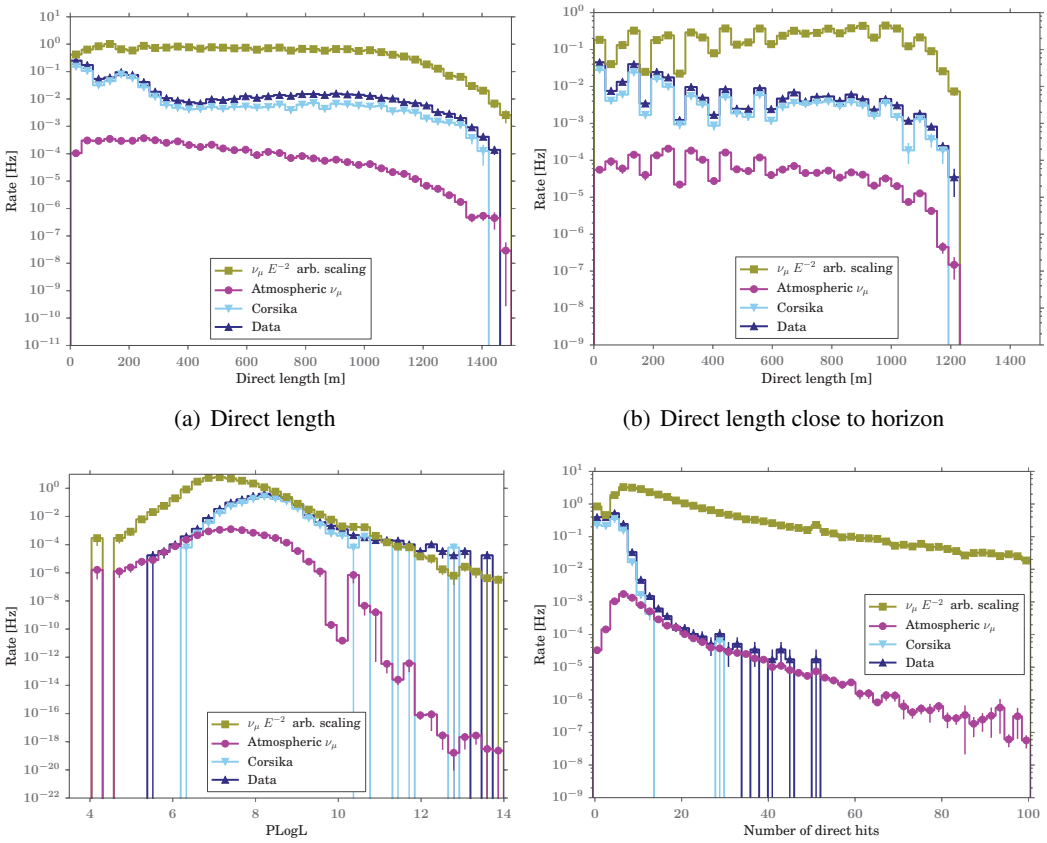

(a) Direct length

(b) Direct length close to horizon

(c) SLogL

(d) Direct hits

Figure 5.4.: *Comparison of the data from the* 2011/2012 *season, atmospheric neutrino simulation and air shower muons of variables used to selected neutrino events after the Online Level 2 filter. The data at this level is still heavily dominated by misreconstructed air shower muons.*

A good agreement between data and simulation on this level justifies to run a cut optimization algorithm to find the best neutrino selection cuts. The corresponding plots for the 2012/2013 season are shown in Appendix A.

5.3.2. Cut Optimization

The scaled likelihood S_{LogL} (see Fig. 5.4(c)) and the number of direct hits N_{Dir} (see Fig. 5.4(d)) show a clear transition from the background dominated regime to the signal dominated regime

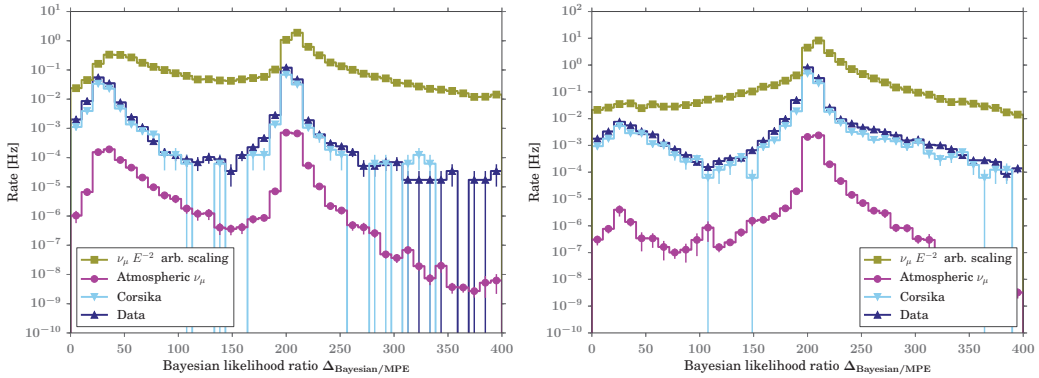

(a) Bayesian likelihood ratio close to the horizon ($\theta_{\text{MPE}} < -0.2$)

(b) Bayesian likelihood ratio

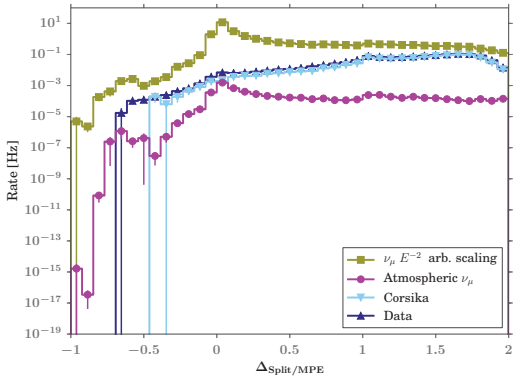

(c) $\Delta_{\text{Split/MPE}}$

Figure 5.5.: *Comparison of the data from the* 2011/2012 *season, atmospheric neutrino simulation and air shower muons of variables used to selected neutrino events after the Online Level 2 filter. The data at this level is still heavily dominated by misreconstructed air shower muons.*

with increasing cut strength (smaller S_{LogL} values, larger N_{Dir}). However, a cut on a single variable would yield a very low signal efficiency and hence a higher neutrino flux would be required for a discovery. One way to improve the signal efficiency while still removing a high percentage of background events would be a machine learning algorithm like Boosted Decision Trees. However, complex machine learning techniques require more signal and background simulation as was available at the start of the first season of IceCube in its 86-string configuration. Furthermore these techniques had not been established at that time for point source searches in the IceCube experiment. Applying them to a novel online analysis would have been ill-advised.

In order to achieve the best sensitivity possible the cuts on the variables described in the previous section have been optimized together in different zenith angle regions. The cuts on all variables were optimized together to achieve the lowest sensitivity (see Eq. 4.19) to neutrino fluxes with a spectral index $\gamma = -2$. For each combination of cut values the rate of remaining data events was used as the approximation for the background rate. The rate of signal events for a given flux was estimated from neutrino Monte Carlo. The cut optimization was repeated for flares of different durations, from flare durations ranging from 1 day to 20 days. As traditional minimizers like Minuit where found to get stuck in local minima a Particle Swarm Optimization Algorithm was used (see [KE95]). For simplicity the minimization assumes that the flare time window is known. In the binned point-source method the radius of the on-source bin is a free parameter. The optimal bin size as a function of zenith depends on the angular resolution and the background rate of atmospheric neutrinos at each zenith angle. The search bin radius has been optimized together with the cut variables to yield the best sensitivity.

Figure 5.6 shows the resulting sensitivities as a function of zenith angle for flares with a duration of 1 day and 10 days.

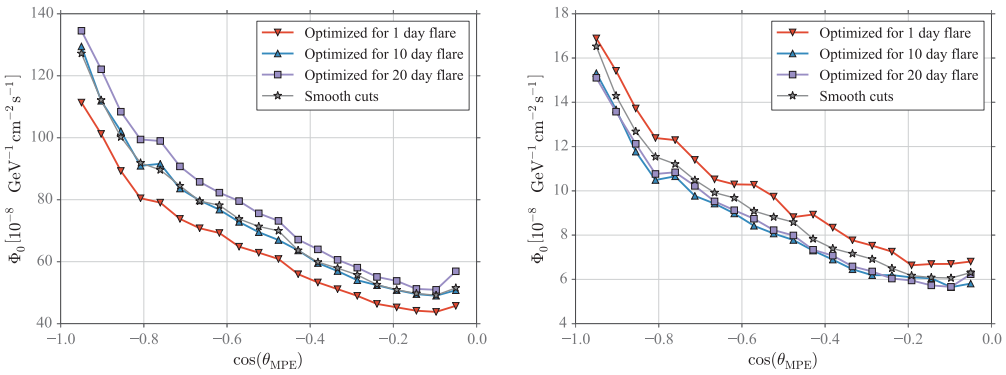

(a) 1 day (b) 10 days

Figure 5.6.: *Sensitivity as a function of zenith to a neutrino flux with $dN/dE \sim E^{-2}$ for a neutrino flare length of 1 day (Fig. (a)) and 10 days (Fig. (b)). Each plot shows the sensitivities achieved for that particular flare length with cuts optimized for different flare durations."Smooth cuts" denote the optimal cuts for different flare durations. The cuts were optimized using the 2011/2012 dataset.*

For each flare duration the optimization results in slightly different optimal cuts. Generally the optimal cuts are softer for shorter flare durations as the sensitivity is improved by increasing the signal passing rate at the cost of a bigger background (atmospheric neutrino) contamination. Applying e.g. the optimal cuts for a 1 day flare to a 10 day flare results in a worse sensitivity (see Fig. 5.6(b)). Figure 5.7 shows the optimal cut values for most employed variables as a function of zenith angle for different flare durations.

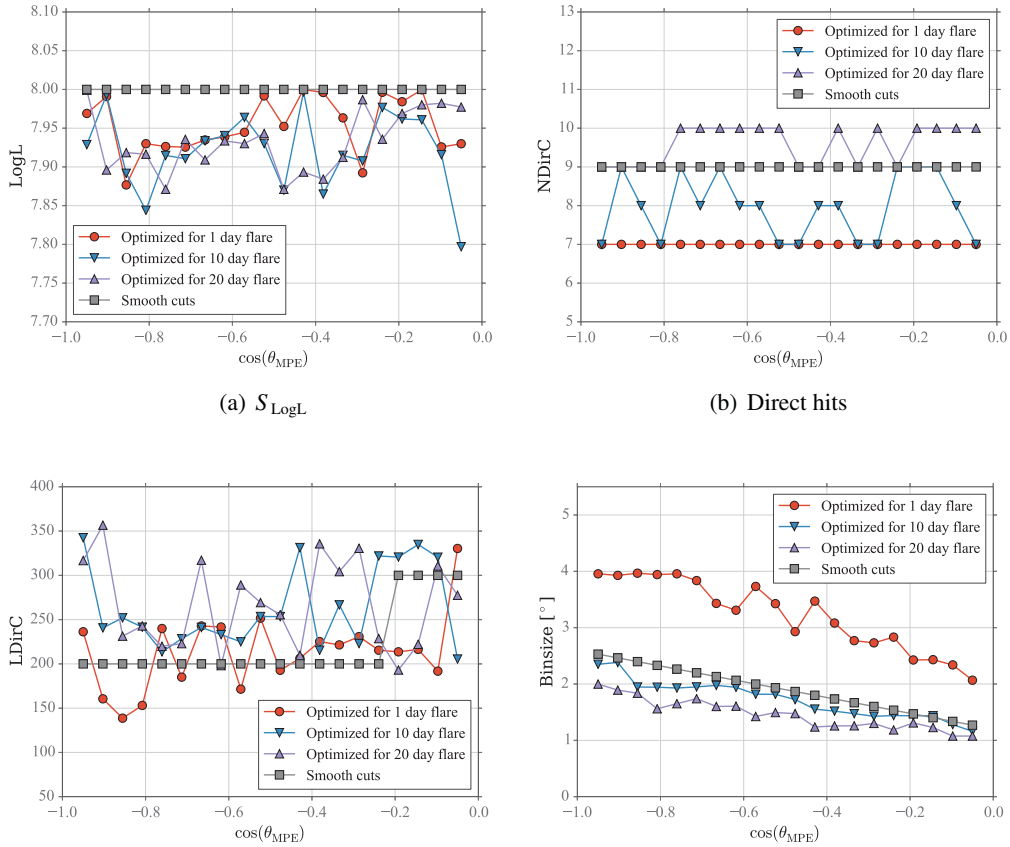

(a) S_{LogL} (b) Direct hits

(c) Direct length (d) Bin radius

Figure 5.7.: *Optimal cut values found by a minimization procedure for different cut variables as a function of zenith angle and different flare durations (1, 10 and 20 days). The smooth cuts depict the final chosen cut values. The cuts were optimized using the 2011/2012 dataset.*

As can be seen from the non-smooth behavior of the cut variables as a function of zenith angle, the minimization procedure is prone to statistical fluctuations in the particular signal and background sample used for the optimization. Thus the final set of cuts should be smooth and should be a compromise between the optimal cuts for different flare durations.

The final set of smooth cuts resulting from the cut optimization is listed in Tab. 5.2 for the

2011/2012 data and plotted in Fig. 5.7. As explained earlier a bug was fixed in the calculation of the Bayesian likelihood ratio prior to the 2012/2013 season. This required changing the cut on this particular variable for the 2012/2013 season. The resulting complete set of cuts used in this season is listed in Tab. 5.3. Note, that only the cut on the Bayesian likelihood ratio has been changed between the two seasons!

Region	**Direct hits**	**SLogL**	**Direct Length**	$\Delta_{\text{Split/MPE}}$	$\Delta_{\text{Bayesian/MPE}}$
$\cos\theta_{\text{MPE}} < -0.2$	≥ 9	≤ 8.0	≥ 200	< 0.5	> 150
$-0.2 \leq \cos\theta_{\text{MPE}} \leq 0$	≥ 9	≤ 8.0	≥ 300	< 0.5	> 40

Table 5.2.: *Neutrino selection cuts resulting from the cut optimization described in Sec. 5.3.2 for different zenith angle regions (first column) for the* 2011/2012 *season. An event has to fulfill all cut criteria to pass the selection (i.e. a logical "and" condition between the cut variables is applied). The cut variables are defined in Sec. 5.3.1.*

Region	**Direct hits**	**SLogL**	**Direct Length**	$\Delta_{\text{Split/MPE}}$	$\Delta_{\text{Bayesian/MPE}}$
$\cos\theta_{\text{MPE}} < -0.2$	≥ 9	≤ 8.0	≥ 200	< 0.5	No cut
$-0.2 \leq \cos\theta_{\text{MPE}} < -0.07$	≥ 9	≤ 8.0	≥ 300	< 0.5	No cut
$-0.07 \leq \cos\theta_{\text{MPE}} < -0.04$	≥ 9	≤ 8.0	≥ 300	< 0.5	> 35
$-0.04 \leq \cos\theta_{\text{MPE}} \leq 0$	≥ 9	≤ 8.0	≥ 300	< 0.5	> 40

Table 5.3.: *Neutrino selection cuts for the* 2012/2013 *season adapted from the cut optimization done for the* 2011/2012 *season. An event has to fulfill all cut criteria to pass the selection (i.e. a logical and condition between the cut variables is applied). The cut variables are defined in Sec. 5.3.1.*

The search bin radius as a function of zenith angle (see Fig. 5.7(d)) has been parametrized as:

$$r = 1.2^\circ + 1.4^\circ \cdot \cos\theta\,. \tag{5.11}$$

5.4. Properties of the Neutrino Sample

This section discusses the properties of the final neutrino sample. As the results of the *NToO* presented in this work are derived from the 2012/2013 dataset, the figures for this data are shown here. Equivalent plots for the 2011/2012 data, that was used for the cut optimization, can be found in Appendix B.

5.4.1. Angular Resolution

Figure 5.8 depicts the median angular resolution of the final neutrino sample for the 2012/2013 season as a function of neutrino energy and as a function of neutrino zenith angle.

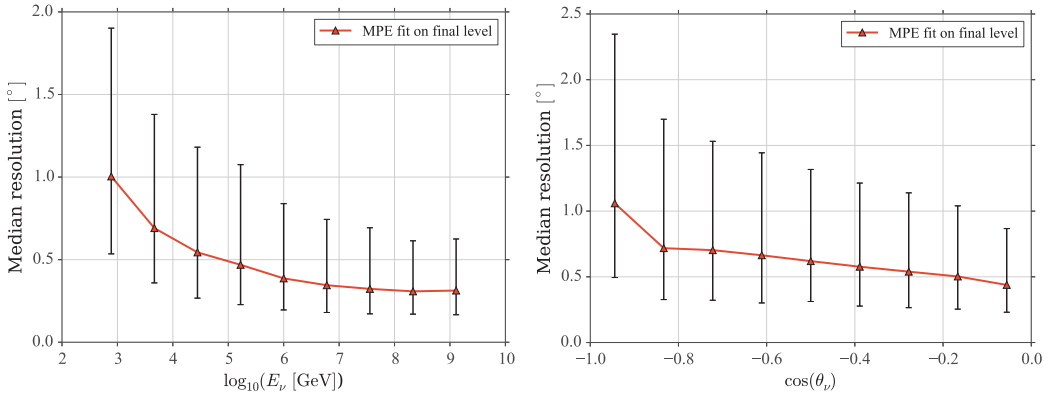

(a) (b)

Figure 5.8.: *Median angular resolutions for the final selected neutrino sample of the 2012/2013 season as a function of neutrino energy (Fig. (a)) and zenith angle (Fig. (b), assuming a primary neutrino spectrum with $\Phi(E) \sim E^{-2}$). The bars depict the 25th and 75th percentile of the resolution.*

5.4.2. Efficiency and Effective Areas

Figure 5.9 depicts the effective area for muon neutrinos as a function of neutrino energy in different declination regions.

It is worthwhile to note that the effective area reaches only about 1 m^2 at 1000 GeV. For events with declination between 10° and 30° the effective area reaches a maximum of about 1000 m^2 at $10^{6.5}$ GeV and begins to drop above $10^{7.5}$ GeV due to absorption of neutrinos in the Earth. Only for neutrinos very close to the horizon ($0° \leq \delta \leq 10°$) and for neutrino energies greater than 10^8 GeV the effective area reaches 10^4 m^2.

The efficiency of the event selection cuts with respect to the Online Level 2 are depicted in Fig. 5.10 for all events (dashed) and events that have been reconstructed within 3° of their true direction. Well-reconstructed events are selected with an efficiency of more than 60 % above 1 TeV, the peak efficiency of about 80 % is reached between 100 TeV and 10 PeV.

E^{-1} ($\Delta\Psi_{\mathrm{MPE}} < 3°$)	E^{-2} ($\Delta\Psi_{\mathrm{MPE}} < 3°$)	E^{-3} ($\Delta\Psi_{\mathrm{MPE}} < 3°$)
54 % (71 %)	54 % (73 %)	32 % (53 %)

Table 5.4.: *Efficiency of the neutrino selection cuts with respect to the Online Level 2 filter (in %) for the 2012/2013 season. The efficiencies for well reconstructed events (defined as events with $\Delta\Psi_{MPE} < 3°$) are given in parantheses.*

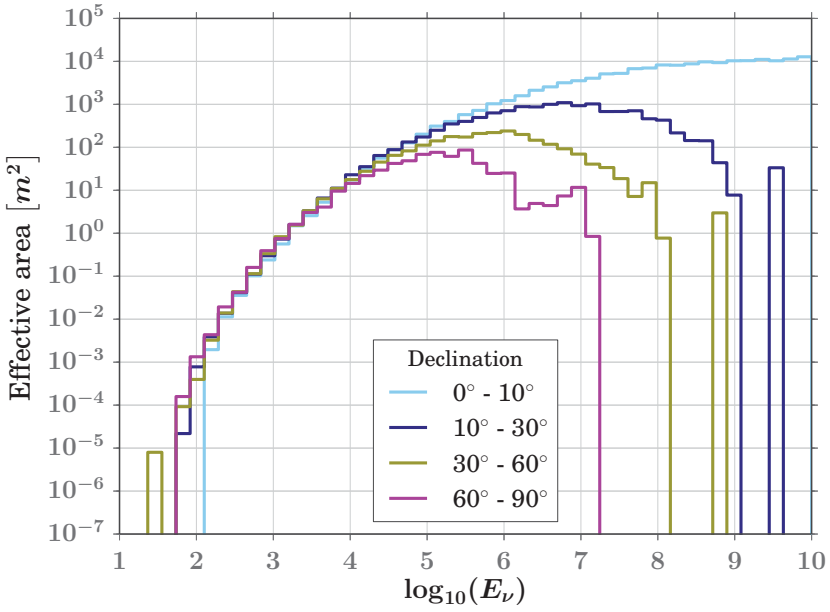

Figure 5.9.: *Effective area of the final neutrino selection for the* 2012/2013 *dataset. The strongly energy dependent neutrino-nucleon cross section leads to the observed behavior of an effective area that is generally increasing with energy, until neutrino absorption becomes too strong. For bigger declinations the effect of neutrino absorption sets in at lower energies due to the longer path through the Earth.*

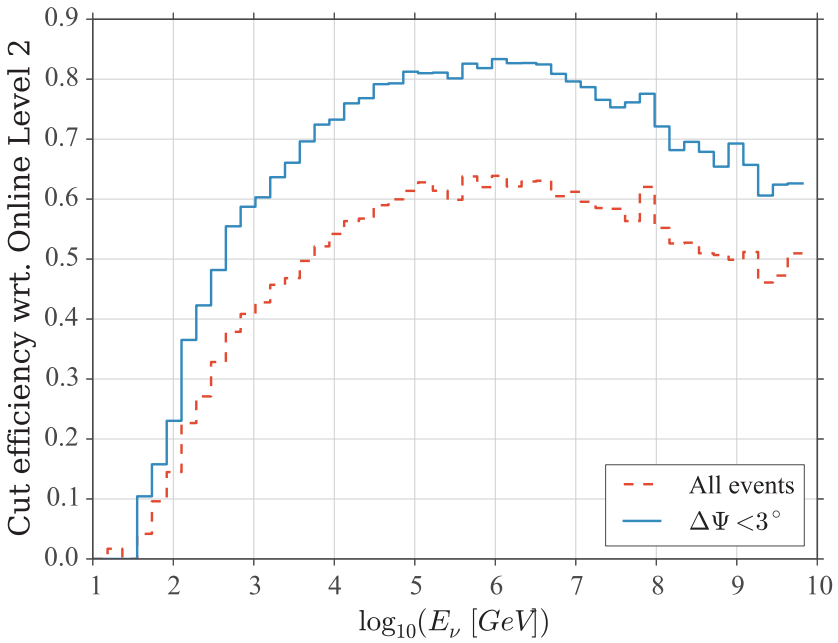

Figure 5.10.: *Efficiency of the neutrino selection cut with respect to Online Level 2 for all events (blue, solid line) and events with* $\Delta\Psi_{MPE} < 3^\circ$ *(red, dashed line).*

5.4.3. Sensitivity and Discovery Potential

Figure 5.11 shows the sensitivity of the final sample for neutrino flares with a spectrum $\Phi(E) \sim E^{-2}$ and flare durations of ten days (Fig. 5.11(b)) and one day (Fig. 5.11(a)). It is important to note that this is not the sensitivity achieved by the Neutrino Triggered Target of Opportunity Program as the sensitivity plotted here requires precise knowledge of the flare time window. Compared to Fig 5.6, which depicts the sensitivity for the 2011/2012 dataset, only small changes in the region $\cos\theta_{\mathrm{MPE}} < -0.8$ are visible.

5.4.4. Data vs. Simulation: Comparison at Neutrino Level

Figure 5.14 shows the distribution of the reconstructed zenith angle (θ_{MPE}) for the neutrino level of the complete 2012/2013 data, compared to simulated atmospheric neutrinos and atmospheric (air shower) muons. The total data rate amounts to 2.06 mHz, while the predicted rate of atmospheric neutrinos is 1.88 mHz. The predicted rate of atmospheric muons at this cut level is 0.08 mHz. The agreement between the data and the atmospheric neutrino prediction is very good in the zenith region $-1 \leq \cos\theta_{\mathrm{MPE}} \leq -0.3$. Closer to the horizon the data rate is systematically higher than the predicted atmospheric neutrino rate, with the disagreement increasing towards the horizon. Muons from air showers surviving to that cut level seem to show up preferentially in the zenith region close to the horizon. The muon contamination from air shower events can also be seen in the plots of the cut variables (Fig. 5.12 and Fig. 5.13). The remaining air shower muons show

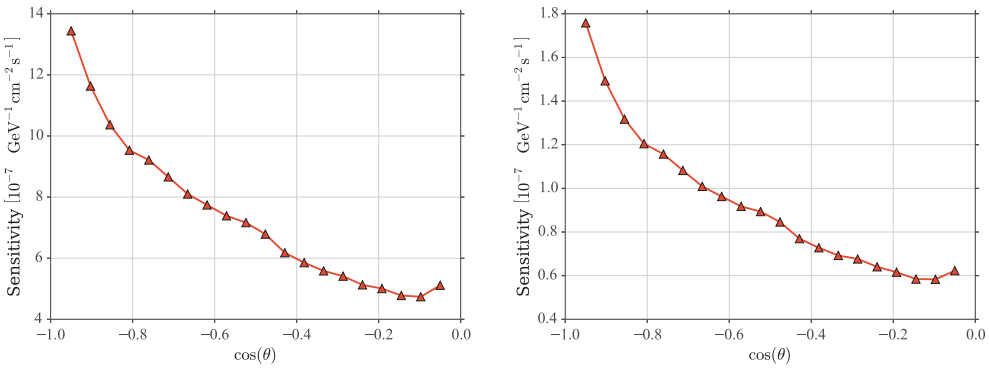

(a) (b)

Figure 5.11.: *Sensitivity to neutrino flares with a spectral index* $\gamma = -2$ *and a duration of* 1 *day (Fig. (a)) and* 10 *days (Fig. (b)) as a function of* $\cos\theta$.

up preferentially close to the cut boundary, e.g. the lower bound of the cut on the direct length (see Fig. 5.12(b) and Fig. 5.12(a)). This region close to the cut boundary also shows the biggest excess of data over expected atmospheric neutrinos.

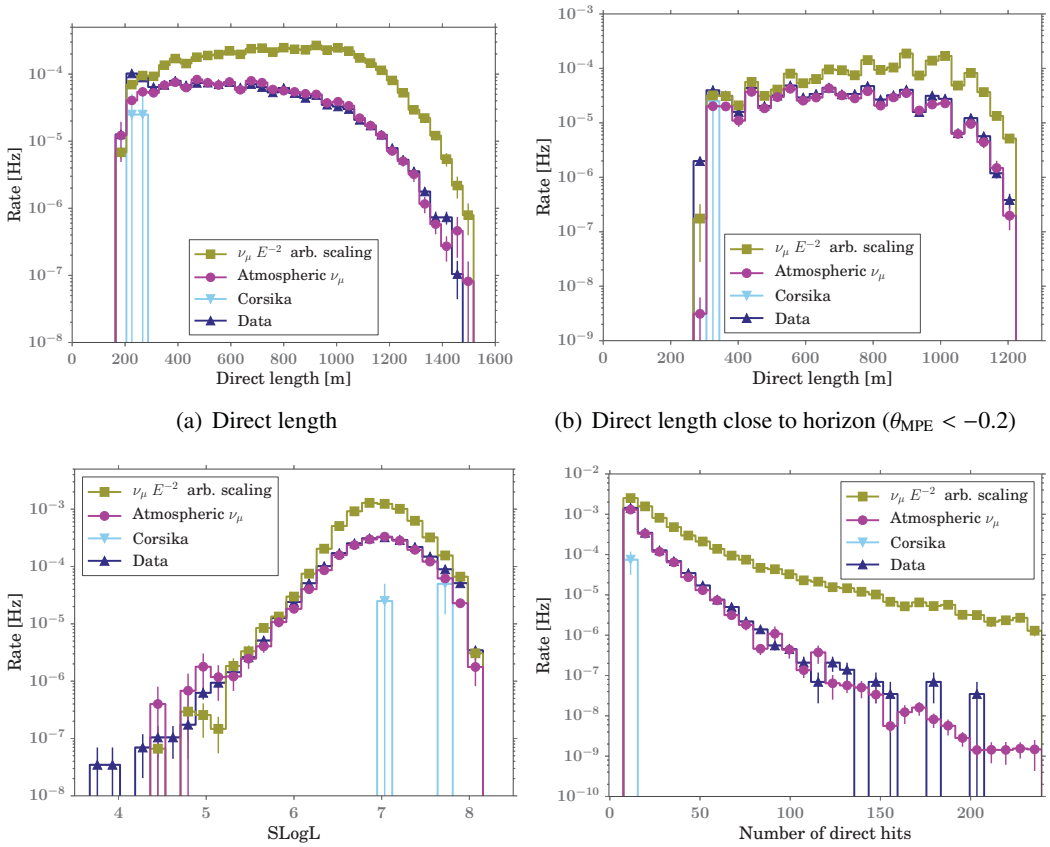

(a) Direct length

(b) Direct length close to horizon ($\theta_{\mathrm{MPE}} < -0.2$)

(c) SLogL

(d) Direct hits

Figure 5.12.: *Comparison at the neutrino level of the distribution of the used cut variables for the complete 2012/2013 dataset, atmospheric neutrino simulation and simulated air show muons (Corsika).*

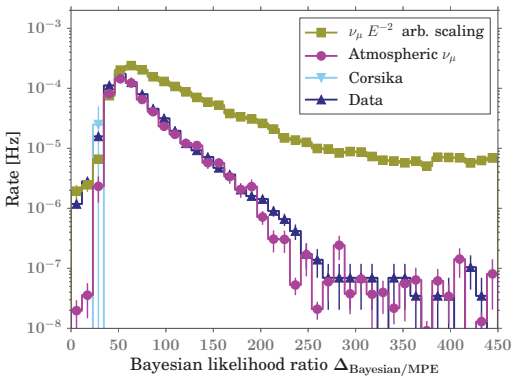

(a) Bayesian likelihood ratio close to the horizon ($\theta_{\text{MPE}} < -0.2$)

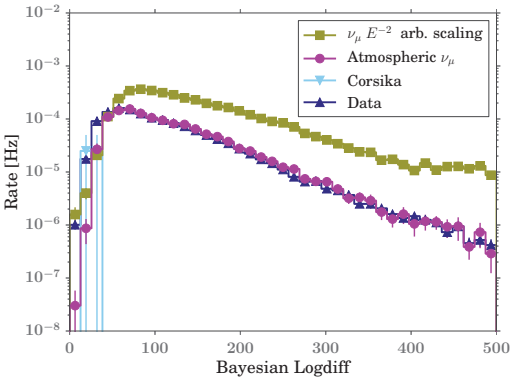

(b) Bayesian likelihood ratio

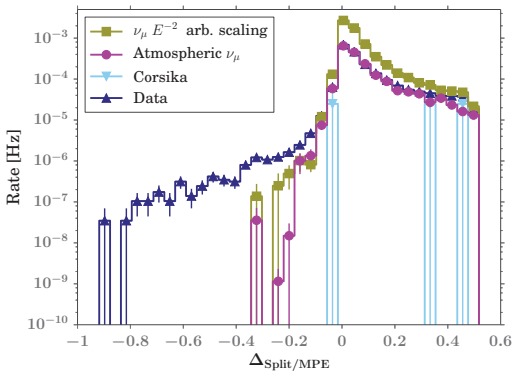

(c) $\Delta_{\text{Split/MPE}}$

Figure 5.13.: *Comparison at the neutrino level of the distribution of the used cut variables for the complete 2012/2013 dataset, atmospheric neutrino simulation and simulated air show muons (Corsika).*

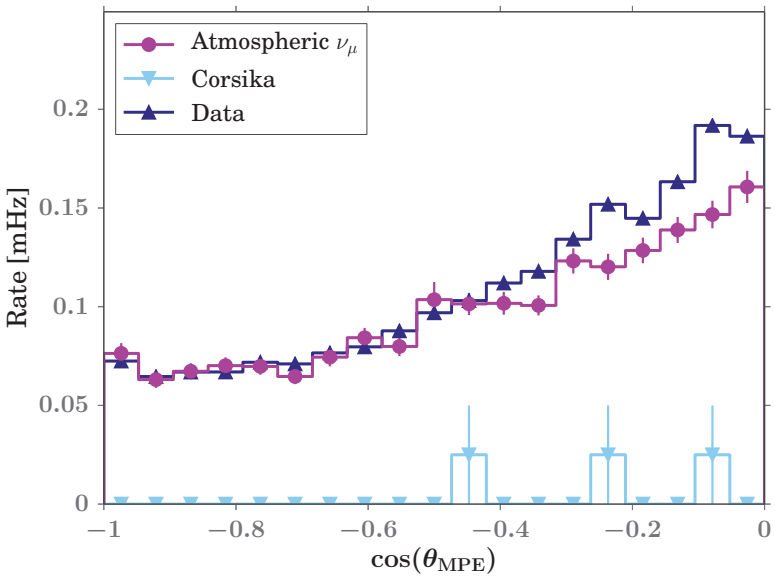

Figure 5.14.: *Comparison of the distribution of the reconstructed zenith angle ($\cos\theta_{MPE}$) for the complete 2012/2013 dataset, atmospheric neutrino simulation and simulated air shower muons (Corsika).*

6. The Neutrino Triggered Target of Opportunity Program

This chapter describes the technical design and implementation of the Neutrino Triggered Target of Opportunity Program. After motivating the program, the technical challenges posed by operating online at the South Pole are described. The technical solutions are explained, special emphasis is put on the monitoring of the detector and the alert system.

6.1. Motivation and Overview

The first and major goal of the Neutrino Triggered Target of Opportunity Program (*NToO*) is to increase the availability of simultaneous neutrino and high-energy γ-ray data for periods of interest. As described in Sec. 2.3.5 periods of elevated emission ("flares"), both in γ-rays and neutrinos, are of particular interest to understand the emission mechanism. Imaging Air-Shower Cherenkov Telescopes (IACT), however, have a small field of view and a limited duty cycle (see Sec. 2.5). These constraints limit the amount of time that these instruments can dedicate to long-term monitoring of variable sources. If a neutrino flare from an astrophysical object (e.g. an AGN) would be detected by IceCube it is unlikely that this source will have been monitored with an IACT at the same time. Thus in this case the chance to better understand the source emission by combining different messengers is lost. In order to ensure the availability of neutrino observations and almost simultaneous high-energy γ-ray data for periods of enhanced source activity, a trigger from a neutrino telescope is needed.

The second goal of the *NToO* is to increase the discovery potential for time-variable point sources of neutrinos with IceCube. The detection of a high-energy γ-ray flare with an IACT triggered by an alert from IceCube can help establishing the neutrino signal even if it is not significant enough on its own to qualify as a discovery. However, this requires a decent knowledge of the a-priori probability to observe the source in a high state of γ-ray emission. Currently the flux state distribution is only reasonably well measured for very few blazars, e.g. Markarian 421 (see [TBS$^+$10]). Monitoring programs with smaller IACTs may cure this handicap (see e.g. [DBB$^+$13]).

In order to be able to send nearly-real-time alerts to high-energy γ-ray telescopes, the search for neutrino flares has to be performed online at the South Pole. As the *NToO* is the first online analysis in IceCube searching for neutrino flares from point sources on timescales longer than a couple of seconds, it has to be proved that such an analysis can be done efficiently and reliably. Simplicity and robustness of implementation should take precedence over novel algorithms.

The Neutrino Triggered Target of Opportunity Program presented in this work uses the IceCube neutrino telescope to monitor a list of predefined source candidates for neutrino flares. As flares in the TeV γ-ray regime last up to a couple of days (see e.g. [TBS+10]), the neutrino flare search is restricted to a maximum duration of 21 days, based on the premise that neutrino and high-energy γ-ray flares are produced by the same physical processes. If the statistical significance of a temporal cluster of neutrinos detected in the vincinity of a monitored source candidate crosses a predefined threshold, an alert message will be forwarded to the IACT partner experiments. It is important to ensure that alerts will only be sent during stable running conditions. Therefore, an effective real-time monitoring of the stability of the data taking and processing is necessary. In addition the alert generation system itself needs to be monitored to ensure its continuous operation and reliability.

6.2. Technical Challenges

Typical IceCube analyses operate on the data well after it has been collected at the South Pole. For example, searches for neutrino point sources are performed or updated in yearly intervals. Thus the analysis tools and techniques can be tuned to the particular analysis. Within an offline analysis computing power is usually not constraining the track reconstructions and statistical methods. An online alert system, like the one described here, however, has a different general setup that requires compromises.

This section describes the technical challenges faced by the *NToO* and discusses how they are addressed.

Computing Capacity The computing capacity available at the South Pole is limited due to constraints on the available electrical power. As described in Sec. 4.4.1, the online processing and filtering system processes individual events on different filter clients. The processing time per event is highly variable and generally increases with the number of hit DOMs in the event. After the processing the *Dispatch* server collects the events from the filtering clients and sorts them into the right time order, before writing them to disk. Therefore, an event which is processed much longer than the following events leads to extensive buffering of those events. With an event rate of about 2500 Hz this becomes unfeasible for processing times beyond a few seconds. Thus the processing time taken by each event needs to be limited. This limits the choice and the number of additional reconstructions that can be run within the Online Level 2 filter (see Sec. 5.2) and the *NToO*. It must be shown that a neutrino selection and a search for flaring sources is possible with sufficient efficiency within these constraints.

Data Storage and Transfer In order to select neutrino induced events efficiently, additional muon track reconstructions have to be applied. Furthermore different cut variables have to be calculated. Ideally these reconstructions and cut variables would be stored and should be accessible in the North for further analysis. This increases the amount of data to be transferred from the South Pole, as well as the necessary storage capacity in the North.

Detector Stability Monitoring An online follow-up program running with little human intervention must be secured against possible problems with its input data. These problems can be e.g. detector malfunctions that result in events that mimic neutrinos. Therefore, the stability of the detector and the components involved in data taking has to be ensured in an automatic way.

Alert Forwarding Alerts should be forwarded to the partner telescopes quickly and reliably. Ideally a follow-up observation should take place during the same night (if the alert arrives during night time at the telescope site) or the following night. As explained in Sec. 4.6 IceCube employs two different systems to transfer data to and from the South Pole. As the amount of data to be transferred in a single alert message is very small (see Sec. 6.6.2), the ITS system, which offers very low latencies (see Sec. 4.6), can be used. However, for a quick follow-up analysis of an alert or a closer inspection of the events contributing to it, access to the original data is needed. This data can currently only be provided with the delay inherent in the transfer of the filtered data. The delay is typically on the order of 24 to 48 hours. This delay is also the reason why the event selection and flare search for the *NToO* has to be implemented at the South Pole.

Alert System Reliability and Monitoring A distributed real-time alert system consisting of different components and running largely unattended needs to be monitored. The monitoring should be largely automated, so that automatic messages are generated in case a problem arises. Note that this concerns different systems that the aforementioned detector stability monitoring!

6.3. Overview of the Technical Design

The *NToO* consists of two main subsystems, the generation of the alerts and the forwarding of those alerts to the partner telescopes. The alert generation includes the neutrino event selection and is implemented completely at the South Pole. The alert forwarding and monitoring system, on the other hand, is divided between the South Pole and the IceCube computing center at the University of Madison/Wisconsin, USA. The basic components of the *NToO* are depicted in Fig. 6.1.

Components at South Pole The following components of the *NToO* run at the South Pole. Each item will be described in more detail later.

- Selection of neutrino candidate events
- Monitoring of the detector stability
- Calculation of the significance of neutrino clusters
- Generation of alert and monitoring messages

Components in the North The components of the *NToO* running in the North are:

- Receiving of the alert
- Forwarding of the alert to the respective parter telescopes
- Monitoring of the alert system

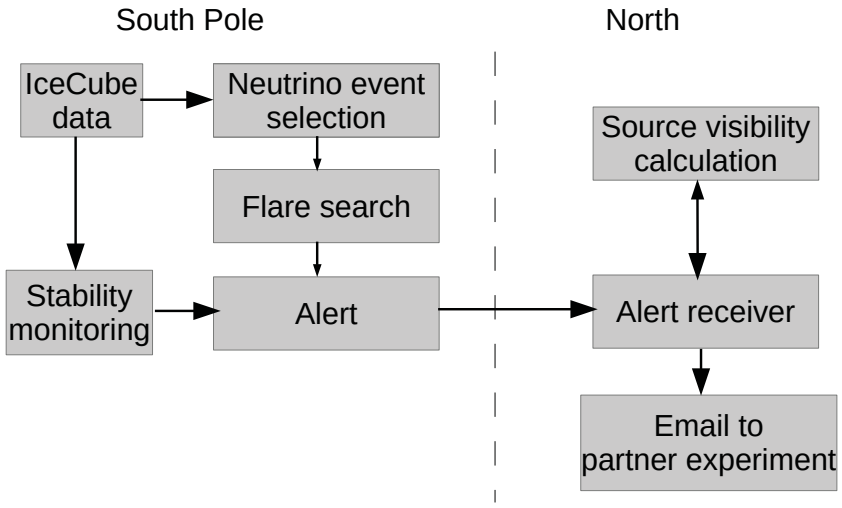

Figure 6.1.: *Schematic of the design of the Neutrino Triggered Target of Opportunity Program.*

6.4. Generation of Alerts

This section describes how the significances of neutrino clusters in the *NToO* are calculated and how the resulting alerts are generated and handled, both at the South Pole and in the northern hemisphere.

6.4.1. Significance Calculation

The timescale of a neutrino flare is not fixed a-priori and thus the simple approach of a rolling-time window approach is not adequate to detect flares. The time clustering approach that was developed for an unbiased neutrino flare search [Sat10] looks for any time frame with a significant deviation of the number of detected neutrinos from the expected background. The simplest implementation uses a binned approach where neutrino candidates within a fixed bin around a source are regarded as possible signal events. In order to exploit the information that can be extracted from the estimated reconstruction error and other event properties like the energy, an unbinned maximum-likelihood method is under development (described in Sec. 7.1).

If a neutrino candidate is detected at time t_i around a source candidate the expected background $N_{\mathrm{bg}}^{i,j}$ is calculated for all other neutrino candidates j with $t_j < t_i$ from that source. To calculate $N_{\mathrm{bg}}^{i,j}$ the detector efficiency as a function of the azimuth angle and the uptime has to be taken

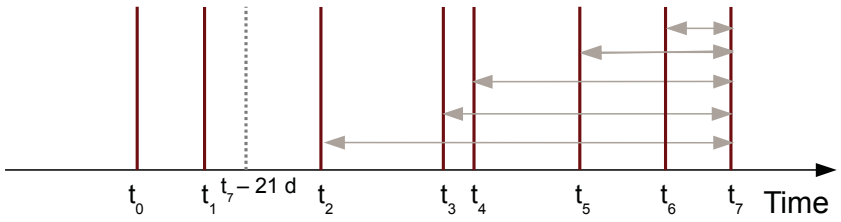

Figure 6.2.: *Schematics of the time-clustering algorithm. For an event in an on-source bin detected at time t_7 the significances of all clusters formed with events detected up to* 21 *days back are calculated.*

into account (see Sec. 6.4.1). The probability to observe the multiplet (i, j) by chance is then calculated according to:

$$p_{\mathrm{obs}} = \sum_{k=N^{i,j}_{\mathrm{obs}}-1}^{\infty} \frac{(N^{i,j}_{\mathrm{bg}})^k}{k!} e^{-N^{i,j}_{\mathrm{bg}}} \tag{6.1}$$

where N_{obs} is the number of detected on-source neutrinos between t_j and t_i. It is reduced by 1 to take into account the bias introduced by the fact that one only does this calculation only right after a signal candidate is detected. As typical flares in high energy gamma rays have a maximal duration of several days we constrain our search for time clusters of neutrinos to 3 weeks at maximum. The clustering scheme is depicted in Fig. 6.2. The probability p_{obs} is often expressed in terms of the distance to the center of a normal distribution measured in units of standard deviations that results in the same cumulative probability in the right tail (e.g. a probability of $\log_{10} p_{\mathrm{obs}} = -2.87$ is often quoted as $3\,\sigma$).

If the cluster with the highest significance exceeds a certain threshold (e.g. corresponding to $3\,\sigma$) the detector stability will be checked and an alert will be sent to a Cherenkov telescope to initiate a follow-up observation.

Calculation of N_{bg}

The number of expected background events N_{bg} in a time window $[t_i, t_j]$ for a source at certain declination is given by

$$N_{\mathrm{bg}} = \sum_{t=t_1}^{t_2} \Delta t^{1,2}_{\mathrm{up}} \dot{N}(\theta) \epsilon(\Phi(t)) \tag{6.2}$$

where $\dot{N}(\theta)$ is the zenith angle dependent rate of background events (see Fig. 5.14) and $\epsilon(\Phi(t))$ the azimuth dependent efficiency of the IceCube detector. The stable detector uptime between t_1 and t_2 is given by $t^{1,2}_{\mathrm{up}}$. During the operation of the *NToO* in the 2012/2013 season the zenith angle dependent background rate $\dot{N}(\theta)$ has been estimated using the data from the 2011/2012 season. The corresponding error is discussed in Sec. 8.4.1.

Azimuth Asymmetry The physical layout of the IceCube detector where the instrumented strings are positioned on a hexagonal grid (Fig. 4.1) results in an increased detection efficiency for events that propagate along the symmetry axes. Therefore the expected number of background events in a time window for a source at a certain right ascension depends on the azimuth angle range covered during that time. The natural azimuth dependence is reinforced by the cut variables that favour events that pass close to a lot of strings (e.g. direct hits and direct length). The azimuth dependent detector efficiency is shown in Fig. 6.3.

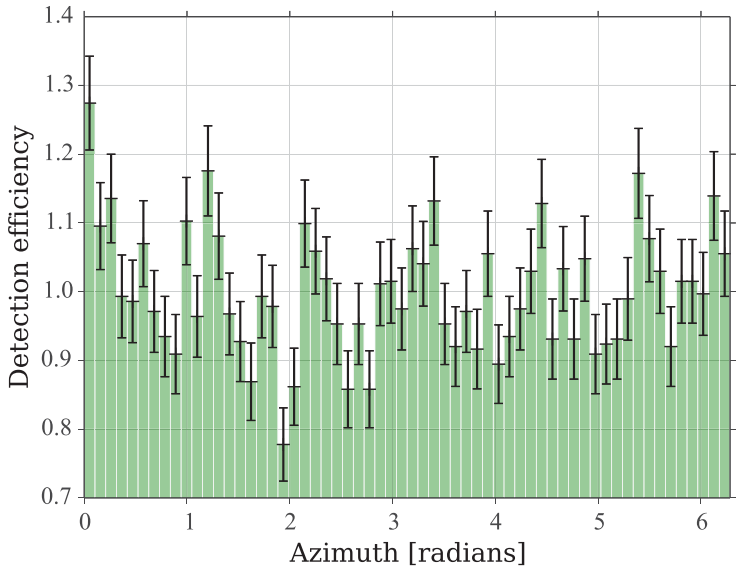

Figure 6.3.: *Azimuth dependent efficiency of the neutrino selection normalized to an average efficiency of* 1*. The dependence is caused by the hexagonal layout of the grid of IceCube strings that produces symmetry axes with increased detection efficiency.*

The efficiency distribution has been estimated using the 2011/2012 dataset. The effect of the azimuth asymmetry is only considered for clusters with $t_i - t_j < 2\,\text{days}$ as the contribution is negligible for longer durations.

Uptime The stable uptime between $t_{\text{up}}^{1,2}$ in a time window $[t_1, t_2]$ is calculated using the online detector stability monitoring (described in Sec. 6.5) and combined with information about the start and stop times of the data taking runs. The technical details are described in Sec. 6.6.1.

6.4.2. Discovery Potential

As the *NToO* aims to discover neutrino flares of astrophysical sources is it important to understand what fluxes are necessary for a detection by this program. The probability to trigger an alert as a function of the neutrino flux assuming a spectral index $\gamma = -2$ and a flare duration of 10 days is

shown in Fig. 6.4 for alert thresholds corresponding to $3\,\sigma$ and $5\,\sigma$ for a source at a declination $\delta = 0.864$.

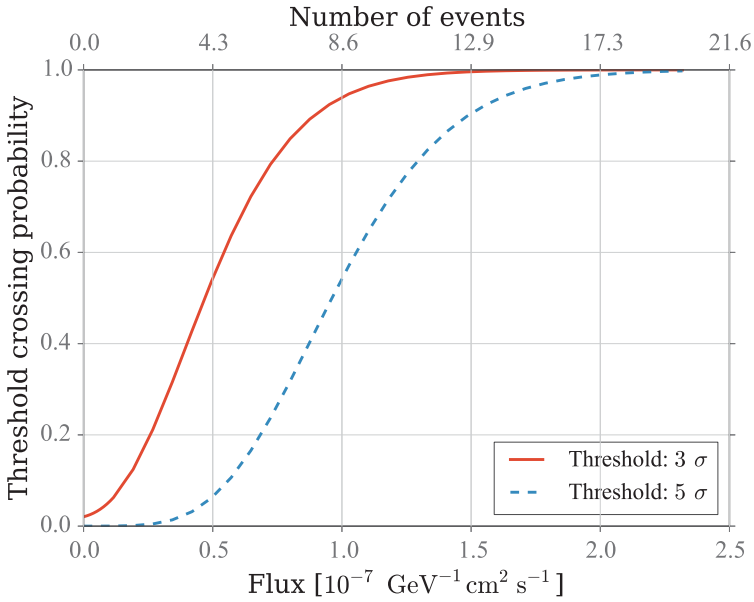

Figure 6.4.: *Probability to trigger an NToO alert as a function of flux for flares with a duration of* 10 *days at a declination* $\delta = 0.864$*, given for alert thresholds of* $3\,\sigma$ *(red, solid line) and* $5\,\sigma$ *(blue, dashed line).*

Figure 6.5 shows the flux as function of declination that results in a trigger probability of 50% for significance thresholds corresponding to $3\,\sigma$ and $5\,\sigma$ for a flare with a duration of 10 days and a spectral index $\gamma = -2$.

One of the underlying assumptions of the *NToO* is that the physical processes that produce flares of high-energy neutrinos also produce flares of high-energy photons with approximately the same evolution in time, i.e. photon and neutrino flares are not significantly delayed with respect to each other. Therefore it is important to know at what point in the development of a neutrino flare the alert is sent to the partner telescopes. Figure 6.6 shows the median alert trigger time for a source at $\delta = 0.864$ for different alert thresholds and flare durations of 1 and 10 days. A signal flux of the form $\Phi(E) = 2.0 \cdot 10^{-7}\mathrm{GeV}^{-1}\mathrm{cm}^{2}\mathrm{s}^{-1}E^{-2}$ will on average trigger an alert about halfway through the flare for an alert threshold of $4.0\,\sigma$. It is important to note that this leaves enough time for the forwarding of the alert to the partner telescopes and the actual execution of the observation, also if the observation can only happen during the following night.

The rate of alerts caused by the atmospheric neutrino background is shown in Fig. 6.7 as a function of the alert threshold. This rate of background alerts is required in order to set a sensible threshold for the forwarding of alerts to the partner telescopes.

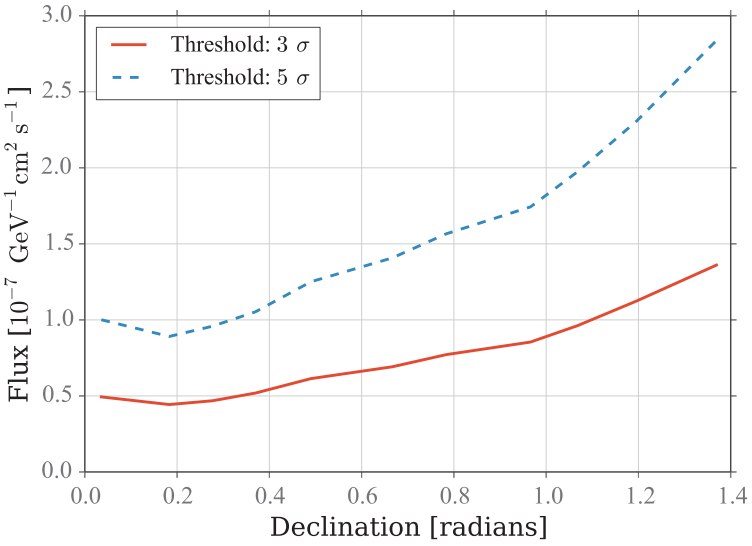

Figure 6.5.: *Neutrino flux needed from a given source declination to trigger a flare with a significance of* $3\,\sigma$ *(solid line) and* $5\,\sigma$ *(dashed line) with a probability of* 50%*. The neutrino spectrum is assumed to be an unbroken power law with a spectral index of* -2*, the flare duration is* 10 *days.*

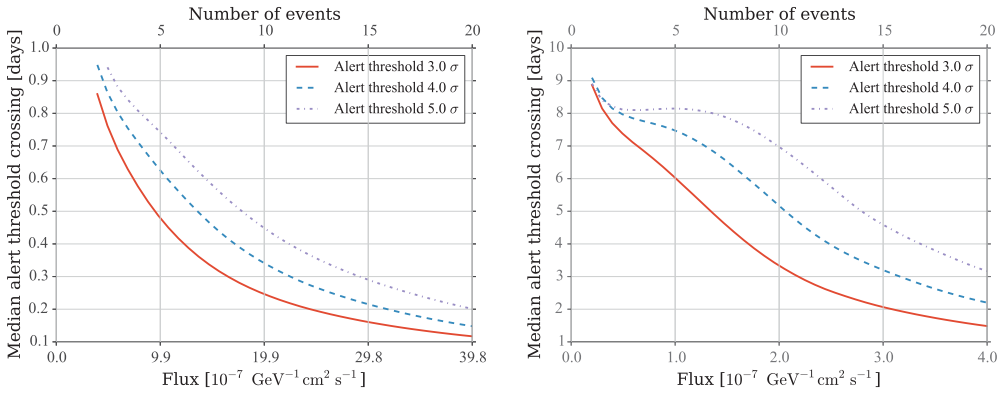

Figure 6.6.: *Fraction of the flare duration when a flare is triggered for different thresholds for flares with a duration of 1 day (Fig. (a)) and a duration of 10 days (Fig. (b))*

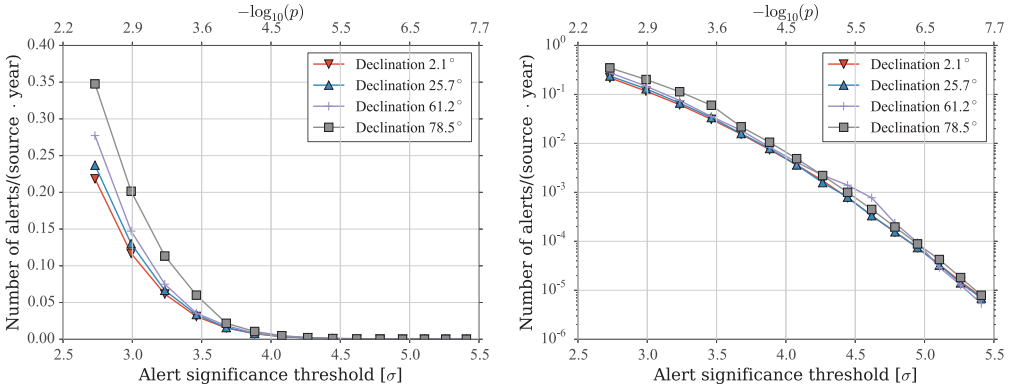

(a) Linear scale

(b) Logarithmic scale

Figure 6.7.: *Expected alert rates for the NToO caused by atmospheric neutrinos for different source declinations as a function of alert significance.*

6.4.3. Sources

Source Selection

The most interesting objects for gamma-ray follow-up observations triggered by IceCube are variable sources of TeV neutrinos, which are either known to exhibit a bright GeV flux in gamma rays and show extrapolated fluxes detectable by IACTs, or are already detected by IACTs. In simple hadronic emission models the GeV flux and the TeV flux are both caused by π^0-decay. Hence a bright and variable GeV flux is a sensible selection criterion. We consider two different target source lists. One list was selected based on the second Fermi point-source catalog [NAA+12]. The following criteria are applied:

- Redshift < 0.6
- Fermi variability index > 41.64 (corresponding to the 99% confidence level of the source being variable)
- Spectral index as observed with Fermi < 2.3 (BL Lacs only)
- Fermi flux $1 - 100$ GeV $> 1 \cdot 10^{-9}$ph cm^{-2} s^{-1} (BL Lacs only)
- Fermi flux $0.1 - 1$ GeV $> 7 \cdot 10^{-8}$ph cm^{-2} s^{-1} (FSRQs only)

These selection criteria (which are discussed in more detail in [CGB+13]) resulted in 36 sources. This list of target sources was combined with lists provided by the partner telescopes covering the northern hemisphere ($\delta > 0$). In total 109 sources were monitored by the *NToO* during the 2012/2013 IceCube season. Each of the two partner telescopes Magic and Veritas only receives alerts for the sources corresponding to its own list and the source selected according to the criteria above. The overlap between the source lists provided by Magic and Veritas is about 50 %. Figure 6.8 shows the declination distribution of the sources.

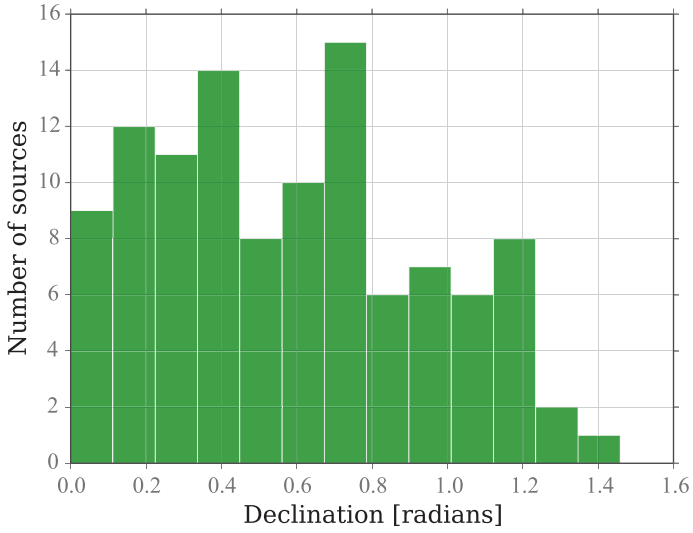

Figure 6.8.: *Declination distribution of the sources monitored by the NToO during the* 2012/2013 *IceCube season.*

6.4.4. Alert Thresholds

The significance thresholds that trigger an alert to the partner telescopes Magic and Veritas have to be set according to the maximum number of agreed alerts.

The alert threshold for the Magic telescopes was set to $-\log_{10}(p_{\text{obs}}) = 3.163$ (corresponding to $3.2\,\sigma$). This threshold results in 7.4 expected alerts per year for the combination of the Magic list and the sources selected according to the criteria in the previous section. Assuming that the source can be observed with a probability of 40 % (see Sec. 6.6.3) this leads to the expectation of 3 follow-up observations per year.

The alert threshold for the Veritas telescope has been set to $-\log_{10}(p) = 3.633$ (corresponding to $3.5\,\sigma$) to reflect the lower number of alerts agreed between IceCube and Veritas. This threshold results 2.4 expected alerts per year, resulting in 1 follow-up observation.

6.4.5. Monitoring

The low rate of accidental background alerts from atmospheric neutrinos (see Fig. 6.7) makes it necessary to add additional monitoring to the system in order to ensure that all components are working as expected. Ideally this monitoring should cover the whole chain from the event selection, stability monitoring, to the generation, sending and receiving of alerts.

Test Alerts

So-called test alerts can be generated at the South Pole, using the same event sample as used by the *NToO*. To achieve a sufficiently large rate of test alerts the number of points that are monitored should be high. 1000 random positions were chosen as test sources, with a flat distribution in $\cos\theta$. The threshold to send a test alert should be lower than the corresponding threshold for the physics alerts in order to achieve a high number of test alerts. Thus the threshold for test alerts was set to $p_{\text{obs}} = 0.1$ (see Eq. 6.1).

Using the original neutrino event sample used for the physics alerts also for the test alerts would unblind additional positions in the sky. The usual way to test point source analyses in a way that preserves blindness are scrambled data sets. The event times are shuffled and new sky coordinates are calculated for each event. Due to the location of the IceCube detector right at the geographic South Pole, only the right ascension is affected by this procedure. In the case of the *NToO*, however, a continuous stream of events needs to be shuffled while preserving properties like the azimuth and time distribution of the events. The simple algorithm developed to realize this is described in Sec. 6.6.1.

Monitoring Web Page

The test alerts generated from the blinded event sample are collected and analyzed. To aid the interpretation of these alerts a web page was created that displays each alert. The web page is automatically updated upon receiving a new alert. In addition to each individual alert, also global properties of all alerts received to date are shown, e.g. the rate of test alerts, their zenith distribution and their significance distribution.

Alert Display Each alert is displayed on a web page showing the distribution of events contributing to the alert both in time and space (see 6.9). In the case of an alert for an astrophysical source this allows for a rapid inspection of the event properties.

Figure 6.9 depicts a high-multiplicity test alert, consisting of 8 events, issued on 7 July 2012. It corresponds to the test alert with the highest significance in the 2012/2013 data taking season with $-\log_{10}(p_{\text{obs}}) = 4.85$. The contributing events were detected over a duration of 10.2 days.

For each alert the weighted average direction of the events is calculated as

$$\mathbf{x}_{\text{avg}} = \sum_i \frac{\sum_i \sigma_i^2}{\sigma_i^2} \mathbf{x}_i \tag{6.3}$$

where the σ_i are the resolution estimates of the individual events and the $\mathbf{x}_i$ are their directions. The weighted average is displayed in the spatial event plot, the individual event weights ($\sum_i \sigma_i^2/\sigma_i^2$) is represented as the heigth of the bars in the temporal plot.

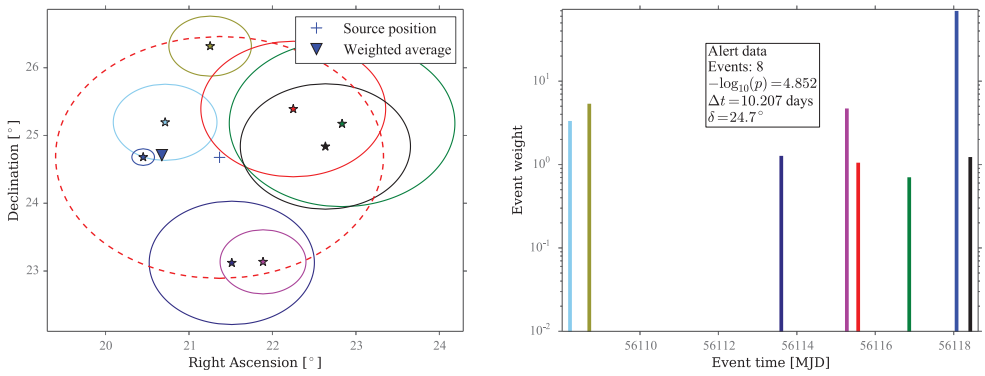

(a) Spatial event distribution

(b) Temporal event distribution

Figure 6.9.: *Spatial (Fig. (a)) and temporal (Fig. (b)) distribution of events contributing to a test alert. The ellipsis describe the estimated angular error for the reconstructed tracks.*

Monitoring Plots of global properties of all monitoring alerts received to date can be used to monitor the stable operation of the whole alert system. For example changes in the total test alert rate can hint to problems with the event selection or uptime calculation, long delays between the detection of the events and the arrival of the test alerts in the North can be a sign of problems with the data processing, the stability monitoring database or the transfer of the test alerts to the North. Figure 6.10 shows some of the quantities derived from the test alerts in order to monitor the alert system.

An important quantity to monitor is the rate of received test alerts (Fig. 6.10(a)). The regular arrival of test alerts in the North is used as a heartbeat of the overall system. If no test alert is received for more than 6 hours a warning email is issued to a list of people so the cause can be investigated. Warning emails are reissued every 2 hours if no new alert has been received in the meantime. This threshold of 6 hours for warning emails is rather conservative, as can be seen in Fig. 6.10(b). This figure shows the histogram of the waiting times between subsequent test alerts. It follows the expected exponential distribution reasonably well. A δt of 6 hours is well in the range of expected waiting times. However, to enable timely interventions, an early warning is preferred. Figure 6.10(d) depicts the distribution of the significances of the test alerts.

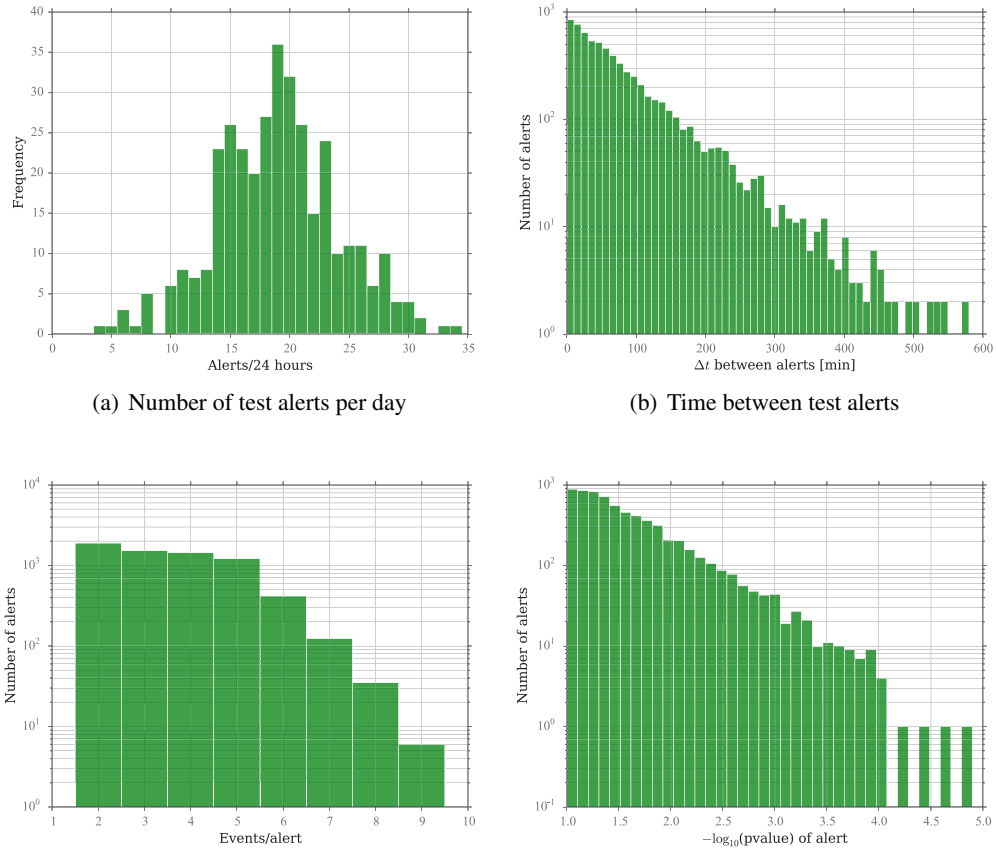

(a) Number of test alerts per day

(b) Time between test alerts

(c) Number of events in alert

(d) Significance of test alerts

Figure 6.10.: *Monitoring information derived from the test alerts for the NToO. See text for a description.*

6.5. Detector Stability Monitoring

This section describes the detector stability monitoring developed to ensure the validity of all alerts sent by the *NToO*.

6.5.1. Motivation

Ensuring the stability of the detector is very important for any online alert program to minimize the rate of false alerts due to problems with the detector itself, the data acquisition (DAQ) or the filtering software. IceCube employs a very extensive monitoring of the DAQ system and South Pole online processing. However, the results of this monitoring are only available with a certain delay after data-taking and thus not useful for an online follow-up program which requires timely alerts. Furthermore, the offline monitoring does not provide information on the detector stability with high granularity but declares a whole run, with a usual duration of eight hours, as either *good* or *bad*. Problems like a few strings of the detector dropping out of the data taking shortly before the end of a run do not render the data taken up to that point invalid. To ensure that alerts are triggered only by neutrino multiplets formed by neutrinos that were detected during stable running conditions, a simple but powerful online stability monitoring scheme based on the continuous monitoring of certain trigger and filter rates has been developed.

6.5.2. Rate Measurements

Quantities that are sensitive to problems affecting the data quality and that are at the same time simple to measure, record and evaluate are the trigger rates of the detector and the filter rates of the online filters (see Sec. 4.3 and Sec. 4.4). Trigger rates, like e.g. the Simple Multiplicity trigger, are sensitive to low level problems, like possible errors in the trigger configuration or an incorrect DOM calibration. Filter rates can also be affected by these issues but additionally give information about the stability of the filtering chain. Problems that affect the event reconstruction or distributions of cut variables used in a filter would also change the corresponding filter rate.

All trigger and filter rates are measured in the central PnF server (see Sec. 4.4.1) using a dedicated software module. Events are counted in time bins of 600 seconds and the corresponding rates and time bin meta data (like start and end of the time bin) is inserted into a relational database. Time bins are not allowed to span run transitions, thus the last rate measurement period in a run is often much shorter than 600 seconds resulting in a correspondingly bigger statistical error.

The database containing the rates date is mirrored to the northern hemisphere to be easily accessible for offline studies. Storing the data in a relational database makes it convenient to retrieve any trigger and filter rate for arbitrary time periods. For each of the trigger and filter rates approximately $5 \cdot 10^4$ measurements are recorded in the database in a full year. Figure 6.11 shows the Online Level 2 Filter rate for run 121283, that took place on 9 December 2012, as an example. This plot also exemplifies a small problem with the system currently in place. Detector runs are often several seconds longer than exactly 8 hours due to technical reasons. The default time bin for the rate monitoring of 600 seconds leads to a last time bin that is very short with

a correspondingly big error. Additionally there is discrepancy of several seconds between the time of the last event in a run and the run end as recorded by the DAQ. This discrepancy usually results in a systematically lower rate in the last time bin. As the relative fraction of the last time bin is very small (< 0.1 %) this does not significantly reduce the uptime of the *NToO*.

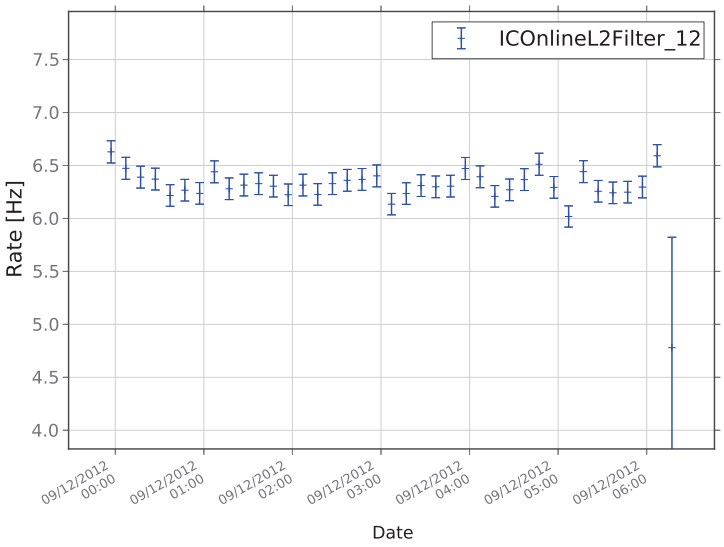

Figure 6.11.: *Data rate of the Muon Filter for detector run* 121283 *that took place on* 9 *December* 2012*. The error bars show the statistical error on the measured rate. The larger error in the last bin before the run ends is caused by the shortness of that bin due to the imperfect alignment of the time bins with the run end (see Sec. 6.5.2).*

6.5.3. Data Quality Decision

The *NToO* selects ν_μ induced muon tracks to detect time-variable point sources of neutrinos. Any problem that affects the detection and reconstruction of these muons would therefore impact this program. Thus the inputs derived from the rate monitoring for the *NToO* should be related to the muon related triggers and filters that form the basis of the neutrino level event selection. The following trigger rates, filter rates and ratios are used to check the stability:

- Simple Multiplicity trigger rate
- Muon Filter rate (*MuonFilter_12* in 2012/2013)
- Online Level 2 filter rate (*ICOnlineL2Filter_12* in 2012/2013)
- Ratio of Online Level 2 filter rate to Muon Filter rate
- Ratio of Online Level 2 filter rate to Simple Multiplicity Trigger rate

The combination of these rates and ratios to form a *stability score* will be described in Sec. 6.5.4. As the final neutrino event selection (see Sec. 5.3) is performed in a different subsystem, this final level event rate is not recorded in the database. Due to the very low atmospheric neutrino rate of about 2 mHz at the final cut level, the statistical error on the rate measurement with the default time binning of 10 minutes would be very large. Recording this rate with a different binning and combining it with the other rates would make the system much more complicated. A higher level monitoring of the alert system that depends on the final level event rate will be described in Sec. 6.4.5. Therefore, the final neutrino level event rate is not used as an input in the rate based detector stability monitoring.

6.5.4. Stability Score Calculation

The atmospheric muon rate depends on the development of the air shower (see Sec. 2.1.2) and thus on the atmospheric density profile. As seasonal temperature changes of the atmosphere influence this density profile, the atmospheric muon rate measured in the detector shows a pattern of seasonal variation. On top of these slow seasonal variations (see Fig. 6.12), faster weather changes (see Fig. 6.13) lead to changes in the IceCube trigger rate on the timescale of hours to days. This background of atmospheric muons dominates all trigger and filter rates used for the online stability monitoring. Therefore, a simple stability decision based on the deviation from fixed reference rates cannot be used.

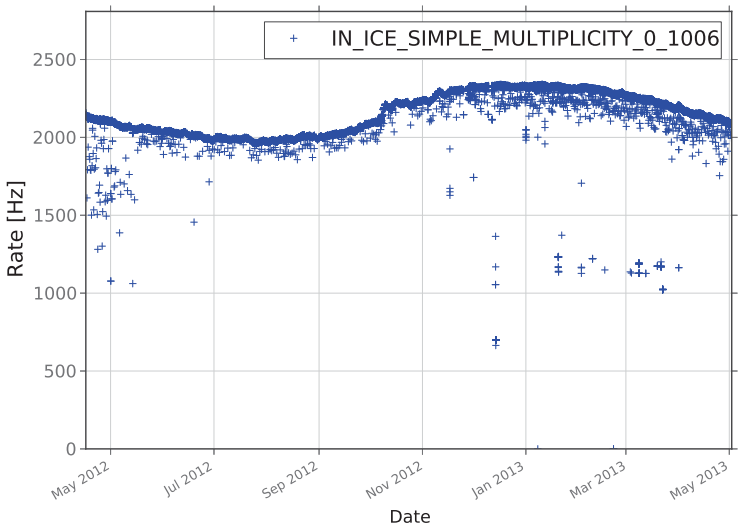

Figure 6.12.: *Rate of the Simple Multiplicity Trigger over the full IceCube season* 2012/2013. *The pattern of solar irradiation at the South Pole causes seasonal changes in the atmospheric density profile. This causes the slow rate variations of approximately* 15 *% over a full year.*

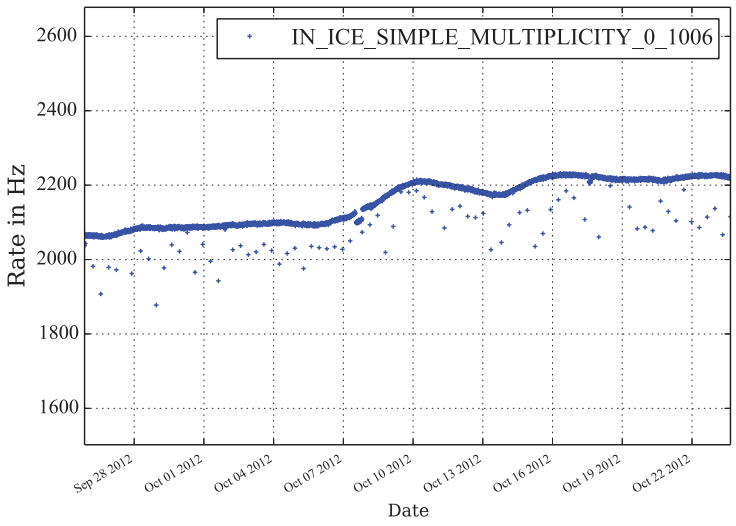

Figure 6.13.: *Fast changes in the weather conditions in the upper atmosphere can lead to quick changes in the IceCube trigger rate as happened between* 7 *October* 2012 *and* 10 *October* 2012.

A common method to predict a time series of (potentially noisy) measurements is a moving average filter. The filter smooths noisy data to either produce smoothed data for presentation purposes or to make forecasts of the time series. Three different averaging methods are usually employed, simple moving averages, weighted moving averages or exponential moving averages (see e.g. [NIS]).

A N-period simple moving average weighs the last N measurements equally to produce the smoothed prediction. Doing that, the average always lags sudden changes in the data. This can be overcome by applying a weight to each measurement in the averaging process depending on how long ago the measurement was taken. This requires two inputs, the number of measurements N to average over and the weight function. In the case of the stability monitoring one would weigh more recent measurements higher than less recent measurements so that the average reacts faster to changes of the rates caused by a changing muon rate. Another way to achieve this fast adaption is an exponential moving average.

Exponential Moving Average Given measurements of a quantity x (e.g. a filter rate) at time steps i (denoted as x_i) the exponential moving average S at time step i is calculated as

$$S_1 = x_1 \tag{6.4}$$

$$S_i = \alpha x_i + (1-\alpha) S_{i-1} \; ; \; \text{for } i > 1 \, . \tag{6.5}$$

The parameter α determines how fast the weight given to past measurements decays, higher α give more weight to recent observations and reduce the impact of past measurements faster. The step width is given by the binwidth of 600 seconds of the rate monitoring.

Analogously to the exponential moving average also an exponential moving standard deviation σ can be defined as

$$\sigma_i = \sqrt{\langle x^2 \rangle - S_i \cdot S_i} \, . \tag{6.6}$$

Here $\left\langle x^2 \right\rangle$ denotes the exponential moving average (see Eq. 6.5) of x^2. To update the exponential moving average only the most recent calculated value of S_i is needed. This is in contrast to the simple and weighted moving averages where the past N data points need to be kept for updates of the average. Therefore, an exponential smoothing has been chosen in the stability monitoring to greatly simplify the implementation of the moving average calculation.

Implementation of the Stability Score Calculation The idea of the stability score is to compare the current detector trigger and filter rates in time bin i to an exponential moving average of these rates up to that point in time. The averages and standard deviations are calculated for the rates and ratios listed in Sec. 6.5.3 with the parameters $\alpha = 0.01$ [1]. In order to judge the detector stability in a time bin i a combined score ξ_i is calculated as

$$\xi_i = \sum_j \frac{|x_i^j - S_{i-1}^j|}{\sigma_{i-1}^j} \tag{6.7}$$

where j enumerates the rates and ratios listed in Sec. 6.5.3 and S_{i-1} and σ_{i-1} are the exponential moving averages and standard deviation prior to the time bin i. This summed deviation ξ_i is referred to as the *badness* of a time bin. If ξ_i is below a certain threshold ξ_{thresh} this time bin i assigned a good quality and the averages and standard deviations are updated according to Eq. 6.5 and Eq. 6.6. If ξ_i is above the threshold the data quality in this time bin is judged as insufficient. In this case all final level events in that time bin are discarded, the time bin is counted as detector dead time and the averages and standard deviations are not updated with the rates from time bin i. The threshold employed in the *NToO* is $\xi_{\text{thresh}} = 8$.

Figure 6.15 shows histograms of the total badness and its subcomponents calculated using Eq. 6.7 for the full 2012/2013.

[1] Until 25 November 2012 $\alpha = 0.005$, which gave more weight to past measurements. In order to be better able to cope with fast rate variation due to weather changes the value of α was changed to 0.01.

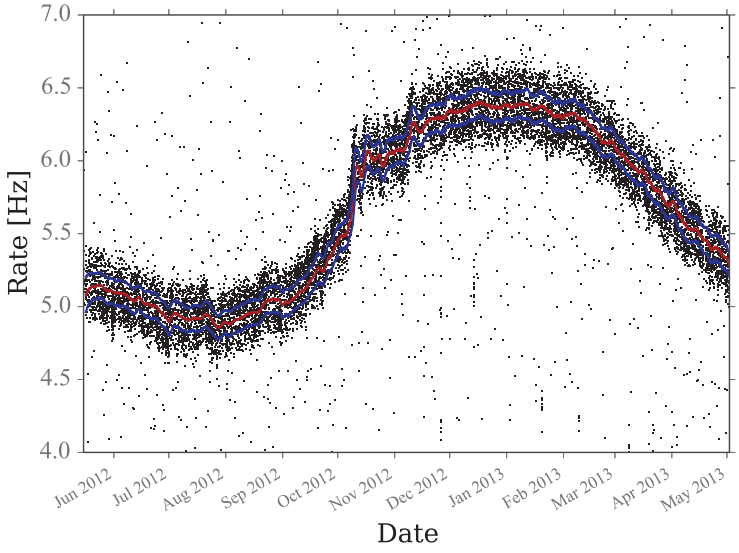

Figure 6.14.: *Rate of events passing the Online Level 2 Filter over the complete 2012/2013 IceCube season. The solid red line depicts the moving average of the Online Level 2 filter rate, the blue lines show the* $1\,\sigma$ *exponential standard deviation around the average.*

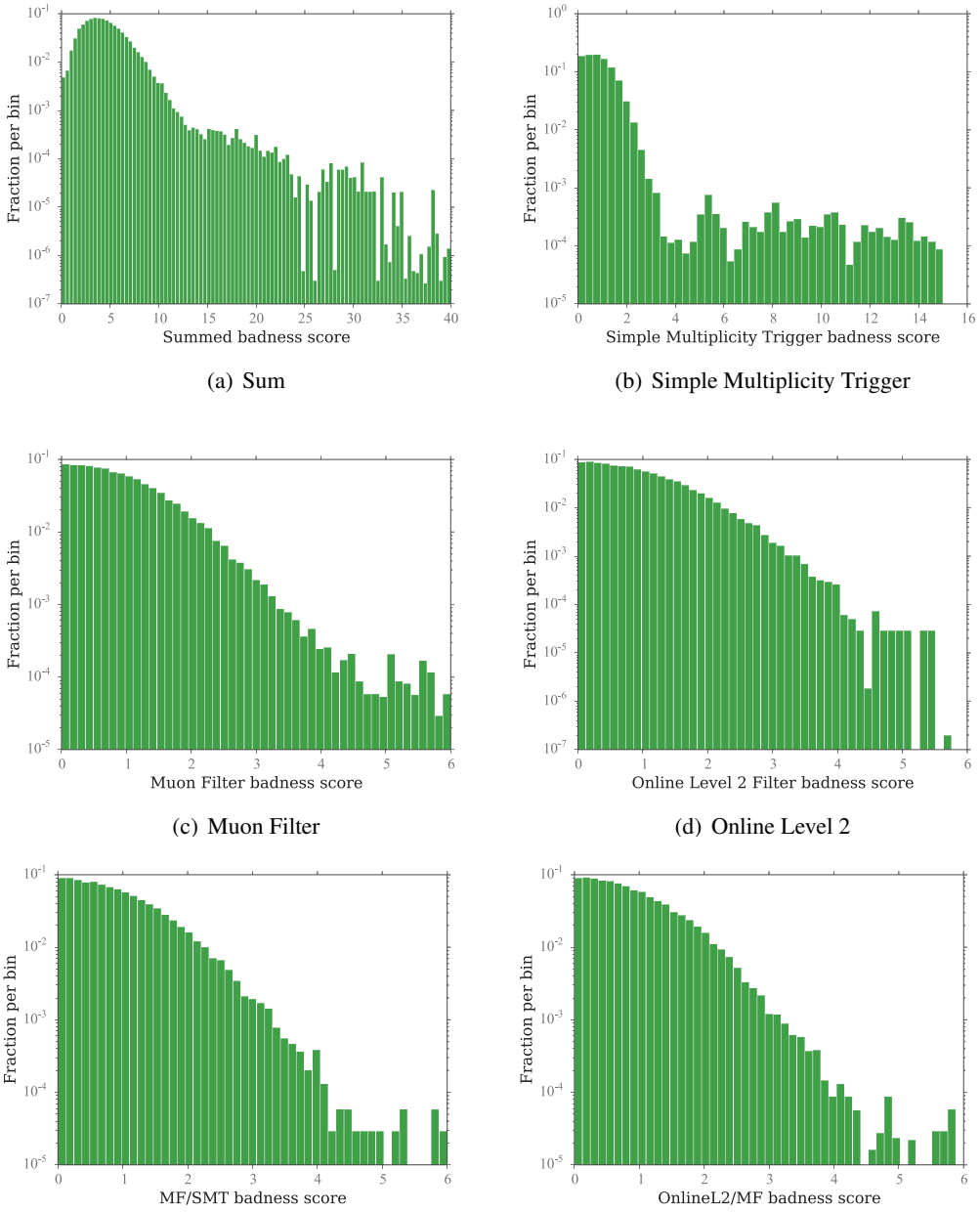

(a) Sum

(b) Simple Multiplicity Trigger

(c) Muon Filter

(d) Online Level 2

(e) Muon Filter/Simple Multiplicity Trigger

(f) Online Level 2/Muon Filter

Figure 6.15.: *Histogram of the total badness (Fig. (a)) calculated using Eq. 6.7 for the full* 2012/2013 *season. Figure (b) to Fig. (f) show the individual badness components.*

Figure 6.16 shows the cumulative clean uptime for the *NToO* in the 2012/2013 season as determined by the detector stability monitoring.

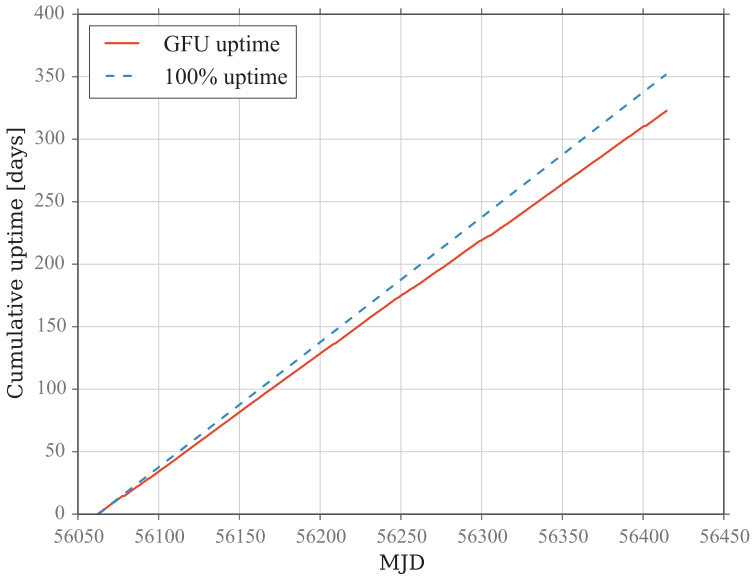

Figure 6.16.: *Cumulative uptime of the NToO system during the* 2012/2013 *IceCube season. The uptime calculation takes into account detector calibration runs and the times marked as bad by the online stability monitoring.*

The IceCube 2012/2013 data taking season started with run 120156 on 15 May 2012 at 10:05:48 UTC and ended after run 122275 on 2 May 2013 at 09:48:49 UTC. Of the 351.98 days between the season start and end, 322.17 days are marked as good by the stability monitoring. This results in a good uptime fraction of 91.5 %. Of the total deadtime of 29.8 days, 1.14 day are due to the various calibration runs and the gaps between detector runs. Typical IceCube offline analyses report uptime fractions of around 95 %.

Comparisons of the Online Stability Monitoring with the more extensive offline quality checks performed by the Detector Verification Group show that the online system reliably identifies unstable detector conditions. However, the Online Stability Monitoring seems to be quite conservative in its quality decision. The inspection of time bins with badness values between 8 and 10 suggest that these also could be used for the *NToO* without increasing the risk of using bad detector data.

6.6. Technical Implementation of the Follow-Up System

This section describes the design of the various parts of the *NToO* system. The main goal of the design was that the system should be robust against failures of any of the different subcomponents

and should not loose data in such an event. Therefore all components have been separated as much as possible and intermediate results are stored frequently.

6.6.1. Setup at South Pole

Event serialization The selection of neutrino candidate events happens inside the PnF system (see Sec. 4.4) and is described in detail in Sec. 5.3. Each selected neutrino candidate event is serialized to JSON format (see [Cro06, JSO13]) and written to a dedicated directory on disk. To facilitate the generation of test alerts (also called "monitoring alerts") each selected event is written twice, once with its actual sky coordinates and a second time with a randomized right ascension for the generation of test alerts.

Randomization of Sky Coordinates The atmospheric neutrino rate at the final event selection level is $\approx 2\,\mathrm{mHz}$. To randomize the event coordinates in right ascension for the blind generation of test alerts one could in principle assign each event a random azimuth angle. This would, however, destroy the pattern due to the azimuth dependent efficiency of the detector (see Fig. 6.3). In order to preserve this pattern in the scrambled dataset the conversion of local coordinates (zenith and azimuth) to sky coordinates (right ascension and declination) for each event is done not with its original event time but the time of the previous neutrino event. The first event after the startup of the event selection process is assigned a random right ascension. As the rate of atmospheric neutrinos is about 2 mHz this results in a random shift of each event by several degrees on average. This randomization scheme is depicted in Fig. 6.17.

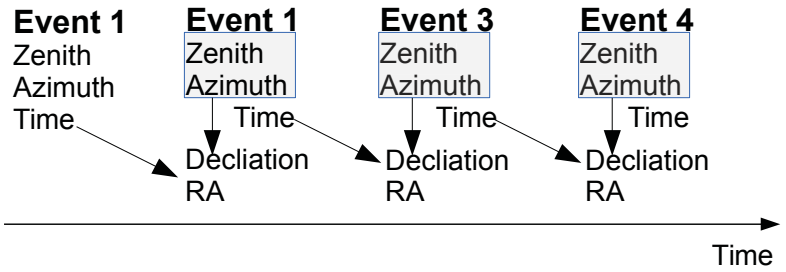

Figure 6.17.: *Scheme to generate a random event sample for monitoring the alert generation system of the NToO.*

Alert Generation The event directory is checked for new events every 30 seconds by the daemon that runs the time-clustering algorithm. First for each detected event the badness score from the detector stability monitoring is calculated in order to decide if the event is kept. Events that do not pass the stability check are discarded from the time-clustering algorithm, but stored on disk for future inspection (see next paragraph).

The program running the clustering algorithm keeps a list of events it has detected in the last 21 days from each of the monitored sources. For each new event that falls into the search bin of one

of the monitored sources, the time-clustering algorithm for that particular source is run. If the significance derived from any cluster of events crosses the alert threshold of a partner experiment, an alert is generated and send to the North where it is processed further.

Uptime Estimation and Stability Monitoring The effective uptime of the *NToO* is determined from two systems, the Detector Stability Monitoring (see 6.5) and a database that records information about each detector run.

The IceCube run database is kept at the South Pole by the PnF system. The database contains information about each detector run, e.g. its start and end time and the type of run. Possible run types are for example "Physics", which describes a normal data taking run, or "LID" (light in the detector), which describes any run where an artificial light source was switched on in the detector (see Sec. 4.2.3). The effective detector uptime between times t_1 and t_2 is calculated by summing the time spent in "Physics" runs between these two times. The run information (except the run end time) is available in the database as soon as the run starts.

Before the time clustering procedure is applied to a selected neutrino event the stability of the detector is checked using the detector stability monitoring described in Sec. 6.5. If the events is accepted, the file is moved to a directory containing the accepted events. If the stability can't be decided upon right now (e.g. as the relevant data is not yet in the database) the event is kept in a staging directory. If the detector is judged to be unstable the event is moved to another location. At any point the file system reflects the status of an event. All internal data in the daemon itself can be restored by re-reading the files. Thus the system is stable against problems with e.g the hardware or a failure of the daemon itself.

6.6.2. Transfer of the Alert Messages

The alert messages are transferred to the northern hemisphere with the help of the IceCube Teleport System (ITS, see Sec. 4.6). However, the amount of data that can be transferred in one message with ITS is limited to 1800 characters. As this limit can be reached by a high-multiplicity alert, a compression scheme was developed to be able to pack at least 30 events in a message (compared to a maximum of 10 events without compression). An alert comprised of more events that can be fitted in a single message is truncated by leaving out event data. In this way the immediately important information like the alert source and the significance is still transferred. Information left out in the alert can be retrieved later. As an alert alert with more than 30 contributing events is very unlikely, a more elaborate scheme where long messages are split into smaller chunks before transmission was not implemented.

The average delay of the message transfer is shown in Fig. 6.18. The delay is generally below 60 seconds, severe delays (up to one day) can occur in case of problems with the ITS system.

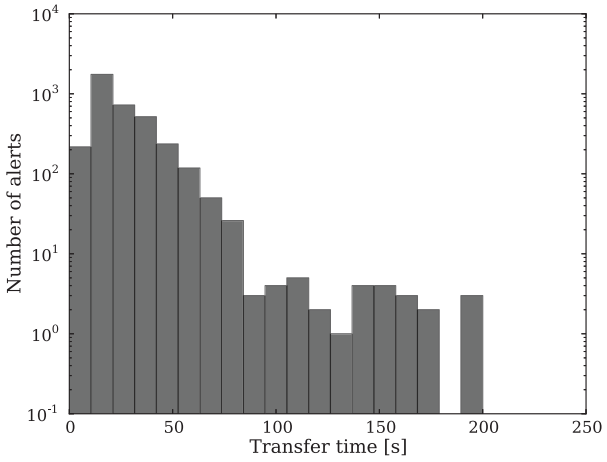

Figure 6.18.: *Histogram of the duration of the message transfer via ITS from the South Pole to the receiving computer in the northern hemisphere.*

6.6.3. Setup in the Northern Hemisphere

All messages transferred with the *ITS* system are received at a central location, the IceCube computing center in Madison, Wisconsin (USA). The *ITS* system is not only used to transfer alert messages for the online analysis programs but mainly to provide remote control of the detector itself via *I3Live* (see Sec. 4.6). Each message transferred via *ITS* has been marked at the South Pole with its destination (e.g. the *NToO*). Each message is forwarded via XML-RPC (see [xml]) to a handler daemon.

After an alert is received by the handler daemon it is immediately stored to disk as a plain text file, as well as into a database. Each type of message (physics alert, test alert or status message) is handled differently.

Status Messages Status messages are send from the South Pole every 12 hours to be able to check if the software components at the South Pole are still operational e.g. during an extended detector outage when no test alerts would be sent. Currently status messages contain little information, only the number of neutrino events ingested by the time-clustering algorithm since the last status message is recorded. In the future this can be extended to include further monitoring information. Status messages are stored in a database, and the time when the last of these messages was received is displayed on the monitoring web page.

Test Alerts Each test alert is immediately displayed on a web page, global statistics like the rate of test alerts over the last 24 hours are updated.

Physics Alerts If an alert concerning a neutrino flare from an astronomical object is received it has to be decided if a follow-up observation can take place and consequently if the alert should be forwarded to the partner experiments. The first question to answer is if the source is visible to the partner experiment. Using the *PyEphem* Python module (see [pye]) the current object coordinates are calculated in the horizontal coordinate system to determine the zenith angle of the source for either Magic or Veritas (or both if the source is on both source lists and the significance crosses both alert thresholds). If all of the following criteria are met the alert is subsequently forwarded to the corresponding experiment(s):

- Source rises at least 30 degrees above the horizon for at least 30 minutes during dark time (when the sun is at least 18 degrees below the horizon) within the 24 hours following the alert
- Current phase of the Moon < 0.5
- Source distance to the Moon > 60 degrees
- Source distance to the anti-Moon > 60 degrees

Averaged of all declinations and right ascensions a source fulfills these criteria about 40 % of the time.

The alert message to the partner experiment contains the alert source, the number of events, the time of the first and last event and the weighted average position of all events (see Sec. 6.4.5). Alerts with a very high significance ($-\log_{10} p \geq 5.0$) contain a special marker, when sent to the Magic telescope.

Irrespective of the source observability the IceCube personnel responsible for the maintenance of the *NToO* is informed of the alert. If the alert satisfies the visibility criteria an email is send to the corresponding partner experiment. As in the case of the test alerts, the alert is also visualized on a dedicated web page.

7. Planned Improvements to the *NToO*

In its current form the Neutrino Triggered Target of Opportunity Program operates at the South Pole since March 2012. It was the first step in establishing the *NToO*, demonstrating its technical feasibility and proving that a time-dependent point source search can be run stably and reliably over long periods of time at the South Pole. Therefore a simple search technique like the binned method has been implemented first. However, current offline searches for neutrino point sources usually employ unbinned maximum likelihood methods to increase the discovery potential.

7.1. Maximum-Likelihood Method

This section describes the maximum-likelihood method which is going to substitute the currently employed binned significance estimation (see Sec. 6.4.1) as it reduces the neutrino flux required for a discovery. It is planned to be deployed at the South Pole for the start of the IceCube season 2014/2015.

7.1.1. Motivation

The binned point-source search method simply counts the number of events in a spatial bin around the investigated source candidate in different time frames. The statistical significance of each observation is calculated by comparing that number to the number of expected background (atmospheric neutrino) events. Each event inside the search bin is weighted equally, events outside the bin do not contribute. However, an event at the boundary of a bin with a very low estimated reconstruction error can be less likely to originate from the source than an event further away with a bigger estimated uncertainty. This is not taken into account in the binned search method.

Besides spatial clustering another feature distinguishing the atmospheric neutrino background from astrophysical neutrinos is the energy spectrum of the events. While the atmospheric neutrino spectrum is rather soft with $\Phi(E) \sim E^{-3.7}$, predicted astrophysical neutrino spectra are much harder (e.g. $\Phi(E) \sim E^{-2}$). As an event-by-event energy estimate of the muon energy is possible (see Sec. 4.5.5) this information can be used to distinguish signal from background events.

7.1.2. Likelihood Formulation

Given a set of observations O and a statistical model with parameters S the conditional probability $\mathcal{L} = P(O|S)$ can be defined. This probability is called the likelihood function. For given

observations it can be maximized with respect to the parameters S so that

$$S_{\max} = \arg\max_{S} \mathcal{L}(O|S)\,. \tag{7.1}$$

The resulting set of parameters $S_{\max}$ is called the maximum-likelihood estimate. It has been shown that maximum-likelihood parameter estimators are efficient and consistent estimators as the sample size increases to infinity [BL98].

In the case of a time-dependent point source search the observations are given by certain parameters of the detected events, like their position $\mathbf{x}_i$ relative to the source at $\mathbf{r}$, their estimated angular reconstruction uncertainty σ_i, their estimated energy E_i and their time t_i. The set of parameters S that are to be estimated typically comprises the number of signal events n_s and the spectral index of the signal γ. For a time-dependent point-source search also the time of emission T and the width σ of the emission period could be added (as described in [BBD+10]). However, a different approach is taken here where the pair of events is found that delimits the time window $[T_\mathrm{s}^\mathrm{sig}, T_\mathrm{e}]$ with the maximum test statistic λ. This approach has been developed in [BA10].

Time-Clustering Algorithm In the same way as in the binned method the search for clusters of astrophysical neutrinos is limited to a duration of 21 days, i.e. to a time window $T_\mathrm{e} - T_\mathrm{s} = 21$ d. An event i inside that time window is called signal-like when the ratio of the signal to background likelihood $S_i/B_i > 1$ (see below for a definition of S_i and B_i), assuming a spectral index $\gamma = -3.0$. Every pair of signal-like events defines a time window $[T_\mathrm{s}^\mathrm{sig}, T_\mathrm{e}^\mathrm{sig}]$ ($T_\mathrm{s} \leq T_\mathrm{s}^\mathrm{sig}, T_\mathrm{e}^\mathrm{sig} \leq T_\mathrm{e}$) for which the likelihood is maximized and the corresponding test statistic value λ is calculated. The final test statistic value is then given by the maximum of the test statics values over all time windows delimited by signal-like events. In the application in the *NToO* S_i/B_i is calculated for each newly detected event. If the event is signal-like the time clustering algorithm is run, however the the last event stays fixed, i.e. $T_\mathrm{e} = T_\mathrm{e}^\mathrm{sig}$. This scheme is depicted in Fig. 7.1.

The likelihood is modeled as a mix of background and signal events as

$$\mathcal{L}(x_i, E_i, t_i|n_s, \gamma) = \prod_{i=0}^{N} \left(\frac{n_\mathrm{s}}{N} \mathcal{S}_i + (1 - \frac{n_\mathrm{s}}{N}) \mathcal{B}_i \right) \tag{7.2}$$

with the signal likelihood $\mathcal{S}_i$ for event i

$$\mathcal{S}_i = \mathcal{E}(E_i|\gamma) \times \frac{1}{2\pi\sigma_i^2} \cdot e^{-\frac{|\mathbf{x}_i - \mathbf{r}|^2}{2\sigma_i^2}} \times \mathcal{T}(t_i)\,. \tag{7.3}$$

The energy likelihood $\mathcal{E}(E_i|\gamma)$ denotes the probability to observe an event with the estimated energy E_i given an injection spectrum with the spectral index γ. The second term describes the probability to observe an event with an estimated angular reconstruction error σ_i at a distance

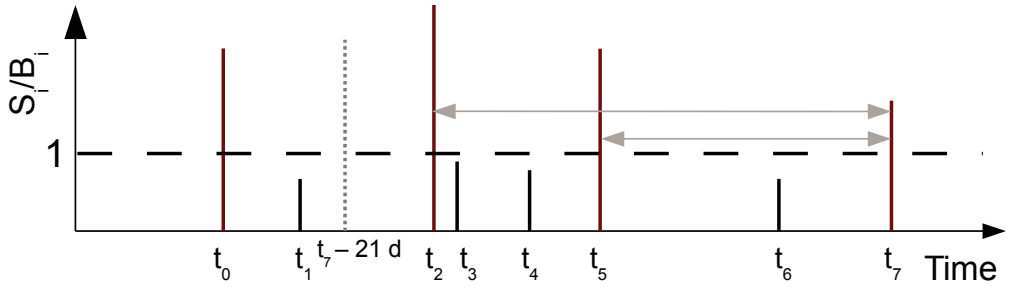

Figure 7.1.: *Schematic of the time-clustering algorithm employed in the maximum-likelihood search for neutrino flares. For each detected event the ratio of the signal to background likelihood S_i/B_i is calculated for all close-by monitored sources (assuming a spectral index $\gamma = -3$). For signal-like events with $S_i/B_i > 1$ the test statistic λ is calculated over all time windows formed by pairs of signal-like events in the last 21 days. Thus in the scenario depicted here (where the last detected event at t_7 is signal-like) the test statistic λ would be evaluated for the time windows $[t_7, t_5]$ and $[t_7, t_2]$.*

$|\mathbf{x}_i - \mathbf{r}|$ from the source position $\mathbf{r}$. The time likelihood $\mathcal{T}(t_i)$ for an event at time t_i is given by

$$\mathcal{T}(t_i) = \begin{cases} \frac{1}{\mathcal{U}(T_\mathrm{s}^\mathrm{sig}, T_\mathrm{e})}, & \text{if } T_\mathrm{s}^\mathrm{sig} \leq t_i \leq T_\mathrm{e} \\ 0, & \text{else} \end{cases} \tag{7.4}$$

where $\mathcal{U}(T_\mathrm{s}^\mathrm{sig}, T_\mathrm{e})$ denotes the effective detector uptime in the signal time window $[T_\mathrm{s}^\mathrm{sig}, T_\mathrm{e}]$.

The background likelihood $\mathcal{B}_i$ for event i is given by

$$\mathcal{B}_i = \frac{1}{\Omega} \times \mathcal{E}(E_i|\nu_\mu^\mathrm{atm}) \times \frac{1}{\mathcal{U}(T_\mathrm{s}, T_\mathrm{e})} \tag{7.5}$$

where $\mathcal{E}(E_i|\nu_\mu^\mathrm{atm})$ describes the probability to observe an atmospheric neutrino with the energy estimate E_i. Ω denotes the space angle of the search area and $\mathcal{U}(T_\mathrm{s}, T_\mathrm{e})$ the effective detector uptime in the time window $[T_\mathrm{s}, T_\mathrm{e}]$.

The test statistic value λ is given by

$$\lambda = -2 \ln \left(\frac{\mathcal{U}(T_\mathrm{s}^\mathrm{sig}, T_\mathrm{e})}{\mathcal{U}(T_\mathrm{s}, T_\mathrm{e})} \frac{\mathcal{L}(\gamma = 0)}{\mathcal{L}(\gamma^\mathrm{max}, n_\mathrm{s}^\mathrm{max})} \right). \tag{7.6}$$

The term inside the logarithm multiplying the likelihood ratio corrects for the correspondingly larger number of smaller signal time windows inside the search time window (for a derivation see [BA10]).

To determine the signal to background likelihood ratio S_i/B_i in the time-clustering algorithm (see

Fig. 7.1), the time terms in $\mathcal{S}_i$ and $\mathcal{B}_i$ are not taken into account, i.e.

$$\frac{S_i}{B_i} = \frac{\mathcal{E}(E_i|\gamma) \times \frac{1}{2\pi\sigma_i^2} \cdot e^{-\frac{|\mathbf{x}_i - \mathbf{r}|^2}{2\sigma_i^2}}}{\frac{1}{\Omega} \times \mathcal{E}(E_i|\nu_\mu^{\mathrm{atm}})} \,. \tag{7.7}$$

The spectral index γ is fixed to -3.

7.1.3. Kernel Density Estimation

In order to estimate the numerous probability densities required in the unbinned maximum-likelihood method, the kernel density estimation (KDE) technique is used.

Given a sample of measurements of a quantity x, a kernel probability density estimate provides a non-parametric, unbinned estimate $\hat{p}(x)$ of the underlying probability density function $p(x)$ [Sco92].[1]

The estimate of the probability density at point x, given the samples $x_i, i = 1 \ldots n$, is given by

$$\hat{p}_h(x) = \frac{1}{nh} \sum_{i=1}^{n} K\left(\frac{x - x_i}{h}\right) \tag{7.8}$$

with the bandwith h and the Gaussian kernel function

$$K(t) = \frac{1}{2\pi} e^{-\frac{1}{2}t^2} \,. \tag{7.9}$$

Other kernel functions are also possible, though Gaussian kernels are most commonly used. The bandwidth h was set to

$$h = 0.9\hat{\sigma}n^{-1/5} \tag{7.10}$$

according to "Silvermans rule of thumb" [Sil86], with $\hat{\sigma}$ denoting the standard deviation of the sample and n the number of measurements in the sample. The formalism is easily extended to weighted samples.

7.1.4. Energy Likelihood

In order to determine the signal energy likelihood function $\mathcal{E}(E_i^{\mathrm{reco}}|\gamma)$, Monte Carlo events within a band of ±5 degrees around a source position are used. The events are reweighed for 1000 equidistant injection spectral indices γ ranging from $\gamma = -6$ to $\gamma = -1$. For each value of γ a kernel density is estimated and stored. During the likelihood maximization, signal energy probability densities for arbitrary spectral indices (in the aforementioned range) are interpolated linearly from the pre-calculated densities. Figure 7.2 shows the estimated probability density of the reconstructed energy for a signal spectrum with $\gamma = -2$ at two different declinations.

[1] The often used histogram is a special case of the kernel probability density estimate using a square kernel.

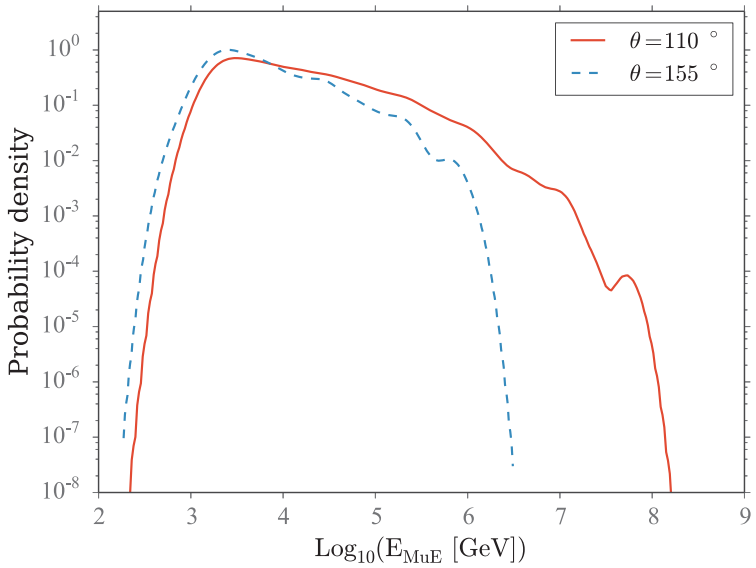

Figure 7.2.: *Kernel density estimate of the MuE energy estimator of simulated signal events with a flux* $\Phi(E) \sim E^{-2}$ *at the zenith angles* $\theta = 110°$ $(\delta = 0.35)$ *and* $\theta = 155°$ $(\delta = 1.13)$.

The background energy probability density $\mathcal{E}(E_i|\nu_\mu^{\mathrm{atm}})$ is estimated using a kernel PDF constructed from the data in a zenith band ±5 degrees around the source position. Figure 7.3 shows the estimated probability density of the reconstructed energy for two different declinations.

A comparison of the estimated probability densities of the reconstructed energies for data and a simulated atmospheric neutrino spectrum can be seen in Fig. 7.4. The agreement between the two PDFs is decent and justifies using the reconstructed energy as a parameter in the maximum-likelihood fit.

7.1.5. Resolution Estimation

The angular resolution of the neutrino events at the final cut level depends strongly on the neutrino energy (see Fig. 5.8(a)) and thus also on the declination (see Fig. 5.8(b)). These dependencies need to be taken into account during the injection of signal events for the estimation of the discovery potential (see Sec. 7.1.6). For each declination where signal events are to be injected kernel density estimates of the angular reconstruction error are generated for different energy bands. The corresponding Monte Carlo events are sampled from a declination band ±10 degree around the source. Figure 7.5 shows an example of the resulting probability density estimated for a source at a declination of $\delta = 0.2768$.

Besides the point spread function a PDF of the event-by-event angular reconstruction error σ_i is required (see Eq. 7.3) in order to simulate maps with injected signal event. This resolution estimate is provided by the Cramér-Rao resolution estimator (see Sec. 4.5.4). Figure 7.6(a) shows

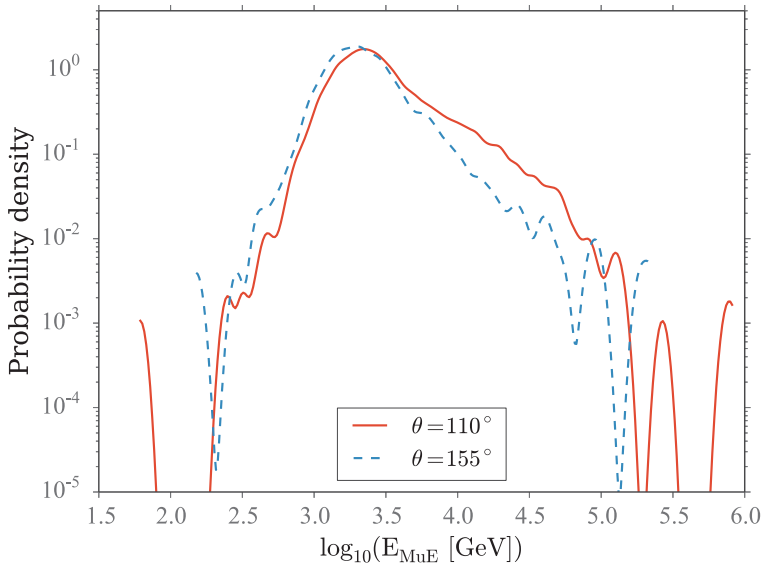

Figure 7.3.: *Kernel density estimate of the MuE energy estimator of data events at the zenith angle* $\theta = 110°$ ($\delta = 0.35$) *and at the zenith angle* $\theta = 155°$ ($\delta = 1.13$).

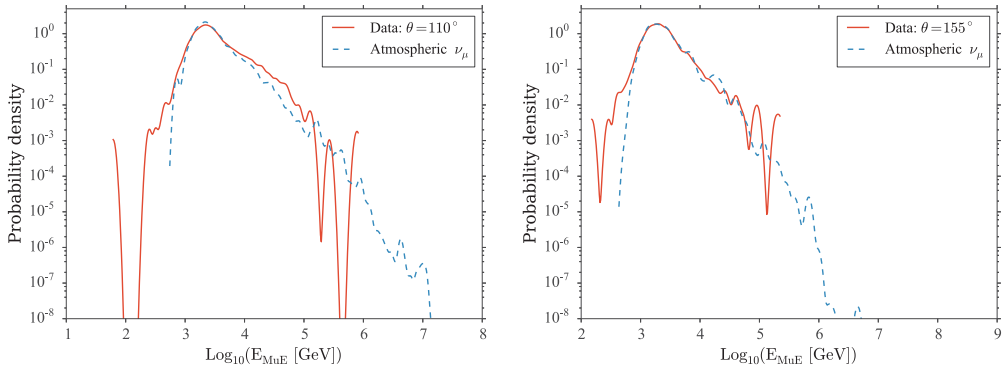

(a) $\theta = 110°$ (b) $\theta = 155°$

Figure 7.4.: *Comparison of the kernel density estimates of the PDFs of the reconstructed energy for data and simulated atmospheric neutrinos at* $\theta = 110°$ ($\delta = 0.35$, *Fig. (a)) and* $\theta = 155°$ ($\delta = 1.13$, *Fig. (b)).*

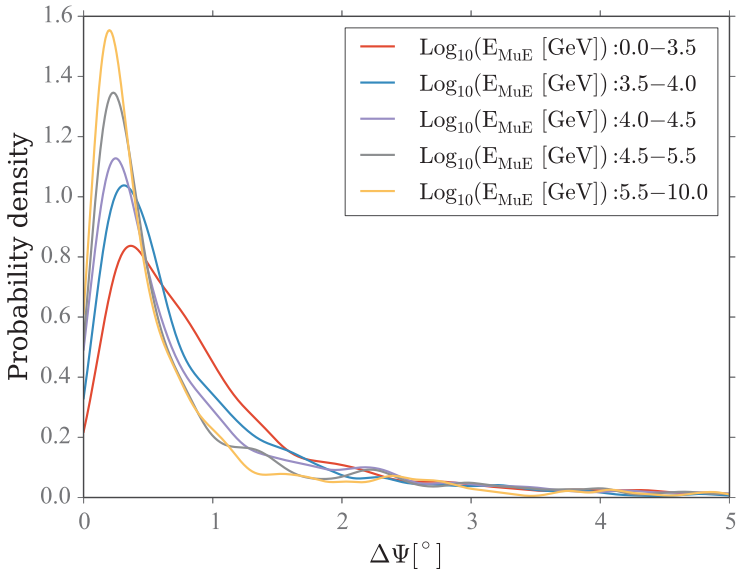

Figure 7.5.: *Kernel density estimates of the point spread function in different energy bands at a zenith angle* $\theta = 106^\circ$ ($\delta = 0.2768$).

the median of the ratio of the true angular reconstruction error to the error estimated with the Cramér-Rao method as a function of estimated neutrino energy. As can be seen this ratio deviates significantly from the desired value of 1, i.e. the estimator is not median-unbiased.

In order to transform the Cramér-Rao angular error estimate into a median-unbiased estimator an energy dependent scaling function is applied. A similar scaling is applied to the angular error estimated from the Paraboloid fit (see Sec. 4.5.4) in all IceCube point-source analyses (see e.g. [AAA+11c]).

The scaling is achieved by applying a polynomial correction as a function of estimated energy E_{MuE} to the estimated reconstruction uncertainty $\sigma_{\text{Cramer-Rao}}$ as follows:

$$\begin{aligned}\sigma^{\text{corrected}}_{\text{Cramer-Rao}} = (&9.59 \cdot 10^{-2} E^4_{\mathrm{MuE}} - 1.66 E^3_{\mathrm{MuE}} + 11.17 E^2_{\mathrm{MuE}} \\ &- 33.26 E_{\mathrm{MuE}} + 37.34) \cdot \sigma_{\text{Cramer-Rao}}\end{aligned} \tag{7.11}$$

The median of the ratio of the true reconstruction error to the estimated resolution after it has been corrected using Eq. 7.11 is shown in Fig. 7.6(b).

The full probability density estimate of the ratio of true angular reconstruction error to estimated error after applying the correction from Eq. 7.11 is depicted in Fig. 7.7(a). This PDF is used to sample a reconstruction error for each signal event injected during the estimate of the discovery potential. Figure 7.7(b) shows that the corrected Cramér-Rao estimator provides a good estimate of the full angular uncertainty PDF.

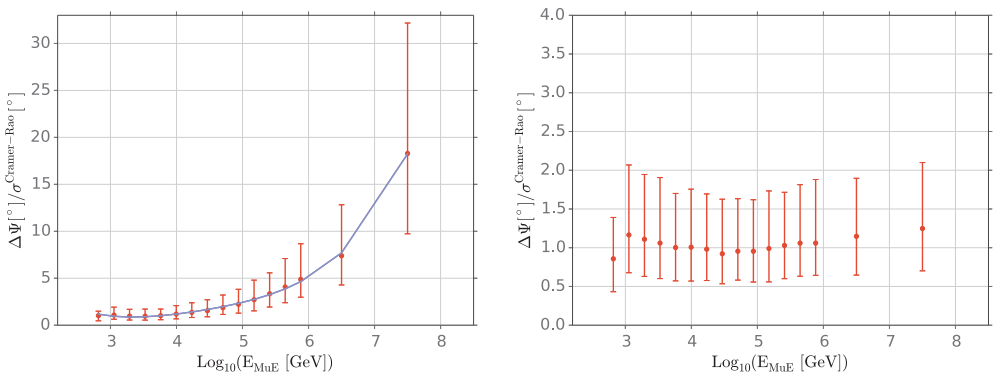

(a) (b)

Figure 7.6.: *Figure (a) shows the median of the ratio of the true angular reconstruction error $\Delta\Psi$ to the event-by-event resolution estimate using the Cramér-Rao estimator as a function of the estimated event energy. This ratio shows an energy dependent bias. The bars show the 25th and 75th percentile of the ratio. The bias can be corrected for by applying a polynomial scaling function to the resolution estimate (solid line in Fig. (a), Eq. 7.11). Figure (b) shows the ratio after the scaling function has been applied.*

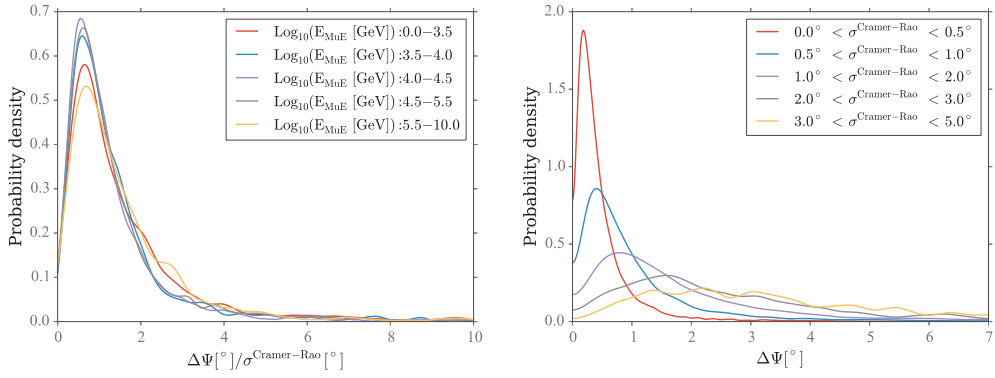

(a) (b)

Figure 7.7.: *Figure (a) shows the kernel density estimate of the ratio between the actual reconstruction error and the error estimated using the Cramér-Rao method in different energy bands after a correction for the energy dependent bias (see Fig. 7.6). Figure (b) shows the distributions of the actual reconstruction error for different ranges of estimated errors.*

7.1.6. Simulation

Generation of Scrambled Maps

In order to estimate the discovery flux correctly at short timescales it is important to preserve the structure in the azimuth distribution of events (see Fig. 6.3) during the generation of random samples. Therefore scrambled maps are generated by scrambling the event times and calculating a new right ascension for each event using

$$\mathrm{RA}_{\mathrm{new}} = (\mathrm{RA}_{\mathrm{orig}} + 2\pi \cdot (\mathrm{MJD}_{\mathrm{orig}} - \mathrm{MJD}_{\mathrm{new}})/0.99726957) \mod 2\pi \tag{7.12}$$

where $\mathrm{RA}_{\mathrm{orig/new}}$ denote the original and new right ascension respectively and the original and the new event time are described by $\mathrm{MJD}_{\mathrm{orig/new}}$. The constant 0.99726957 is the length of the sideral day measured in solar days, i.e. the time (in days) it takes the Earth to turn around itself exactly once with respect to the fixed stars. This approximate expression is exact to within arcsecond precision.

Background Simulation

In order to assess the sensitivity and discovery potential of the maximum-likelihood method simulations were run for five example sources. For each declination 10^8 background maps were generated by scrambling the available data events from the 2012/2013 IceCube season using the procedure described in Sec. 7.1.6.

The time clustering algorithm is applied to each scrambled map and the maximum test statistic value λ over the whole data taking period is stored. Figure 7.9(a) shows the distribution of the value of the test statistic λ at a declination of $\delta = 0.864$.

Signal Simulation

In order to calculate the discovery potential signal-like events have to be injected into the event maps. Simulated signal events are generated by drawing a random reconstructed energy from the distribution corresponding to a source energy spectrum of $\Phi(E_\nu) \sim E^{-2}$. The angular reconstruction error and the ratio of the true to estimated angular reconstruction error are drawn from their respective distributions (see Sec. 7.1.5) corresponding to the declination and the reconstructed neutrino energy. Signal events are injected uniformly over a fixed time window, i.e. the flare is assumed to have a simple block-like time structure. Due to a bug in the software module that provides the MuE energy estimate at the South Pole, wrong energy estimates were calculated in a period of 17.5 days from 21 December 2012 09:42 UTC till 7 January 2013 22:16 UTC. Events from that period were thus excluded from the simulation. Therefore the effective uptime of the dataset used in the simulation is 305.26 days. The cumulative uptime is shown in Fig 7.8, the down time associated with the bug in the energy estimation around MJD 56290 is clearly visible.

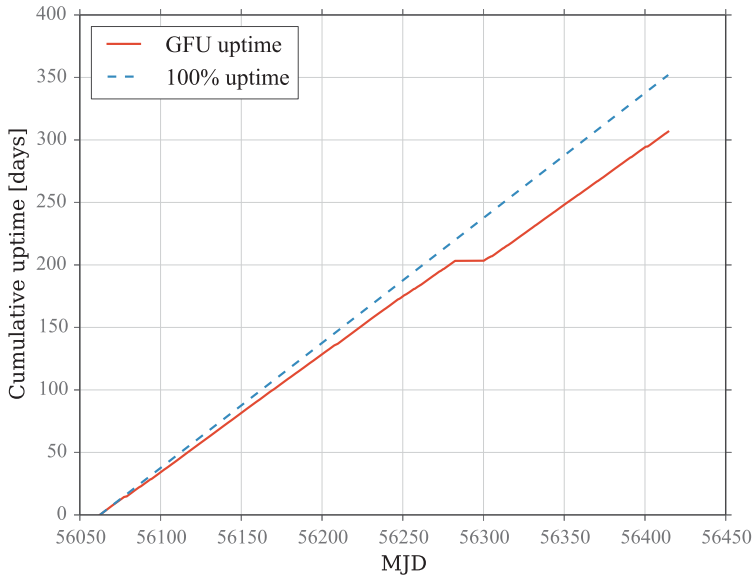

Figure 7.8.: *Cumulative uptime of the data sample derived from the* 2012/2013 *NToO used for the studies of the maximum-likelihood based clustering method. The deadtime of about* 16 *days around MJD* 56290 *results from a bug affecting the MuE energy reconstruction.*

After the generation of the combined background and signal sample the time clustering algorithm is applied the same way as it would be in the *NToO*. For each event at time t_i with $S_i/B_i > 1$ the time clustering algorithm is run over the last 21 days. The maximum test-statistics value λ (see Eq. 7.6) over all time windows is recorded.

The number of injected signal events is varied from 0 to 45, 50000 scrambled maps with injected signal events are simulated for each amount of signal events. Test statistic distributions corresponding to arbitrary fluxes can later be obtained by weighting the simulations according to the Poisson distribution of expected events from that particular flux. The distribution of test statistic values λ at a declination of $\delta = 0.864$ for a Poisson mean number of injected signal events $\mu = 2.0$ and $\mu = 9.0$ over a period of 5 days is shown in Fig. 7.9(b).

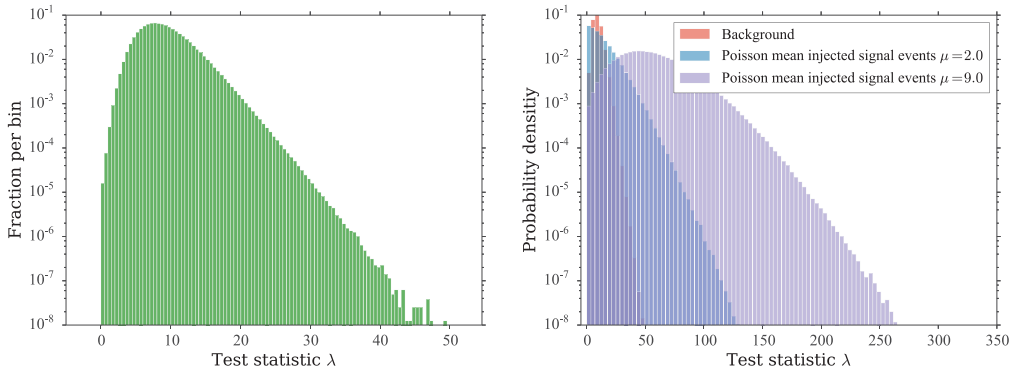

(a) Background

(b) Background with injected signal events

Figure 7.9.: *Distribution of the test statistic value λ of the time-clustering algorithm applied to 10^8 scrambled maps of the IceCube data from the season 2012/2013 at a declination of $\delta = 0.864$ for background only maps (Fig. (a)) and maps with signal events that are injected over a period of 5 days (Fig. (b)).*

Figure 7.10 proves that the maximum-likelihood method succeeds in fitting the injected number of signal events and the spectral index of the injected events.

Calculation of the Discovery Potential

At each examined declination 10^8 scrambled background maps are generated and $\lambda_{5\,\sigma}$, the value of λ correspondig to a significance of $5\,\sigma$ ($-\log_{10} p = 6.5428$) is recorded. The median discovery flux at this significance level is then given by the flux that results in a test statistic distribution whose median is equal to $\lambda_{5\,\sigma}$. A flare with the corresponding flux would be detected with a signifance exceeding $5\,\sigma$ with a probability of 50 %.

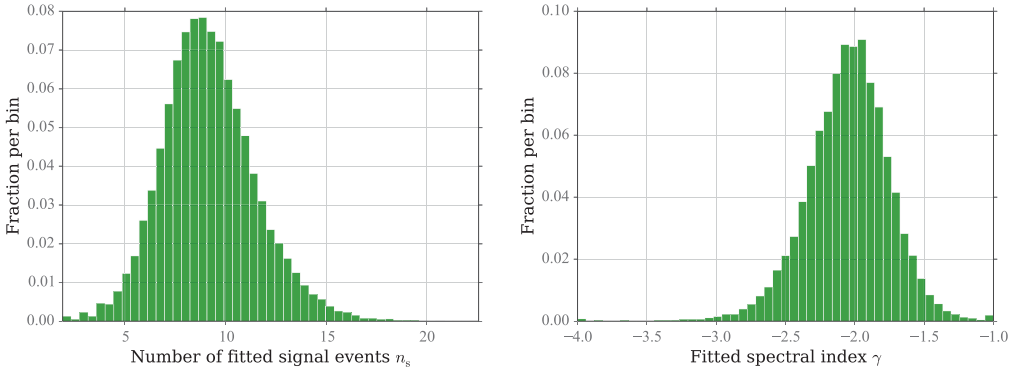

(a) (b)

Figure 7.10.: *Distribution of fitted number of signal events (Fig. (a)) and fitted spectral index (Fig. 7.10(b)) for scrambled maps with a Poisson mean μ of* 8 *injected signal events with a spectral index of* $\gamma = -2.0$.

7.2. Results

Figure 7.11 shows the flux needed for a discovery of a flare with a significance of $5\,\sigma$ as a function of flare duration. The events are assumed to be distributed uniformly inside the flare time window (i.e. no particular time structure is assumed). The discovery significance incorporates the trial factor arising from scanning for a flare over the whole year. It does, however, not incorporate the trial factor incurred by looking for flares at different locations in the sky (i.e. the number of sources is not corrected for).

Comparing the number of events needed for a discovery with a significance of $5\,\sigma$ for the binned and unbinned method in Fig. 7.11 is becomes clear that the unbinned maximum-likelihood method greatly improves the chances for the discovery of a neutrino flare. Closer to the horizon ($\theta = 106°(\delta = 0.277)$) about 40 % more events are required by the binned search to discover a flare with a duration of 1 day compared to the unbinned maximum-likelihood method. The improvement increases to 70 % for flares with a duration of 10 days. The reason for the increasing difference between both methods is the larger trial-factor of the binned method, as the time clustering is done over all events, whereas only the signal-like events are used in the unbinned method. The improvement of the unbinned maximum-likelihood method with respect to the binned method is less strong further away from the horizon ($\theta = 140°(\delta = 0.864)$). At this declination 20 % (45 %) more events are required by the binned method for flares with a duration of 1 day (10 days). The reason for the decreased difference is the increasing absorption of high-energy neutrinos the further one moves away from the horizon. The softening of the observed neutrino spectrum makes it harder for the maximum-likelihood method to discern astrophysical from atmospheric neutrinos.

Figure 7.12 shows the flux necessary to discover a flare with a duration of 10 days with a

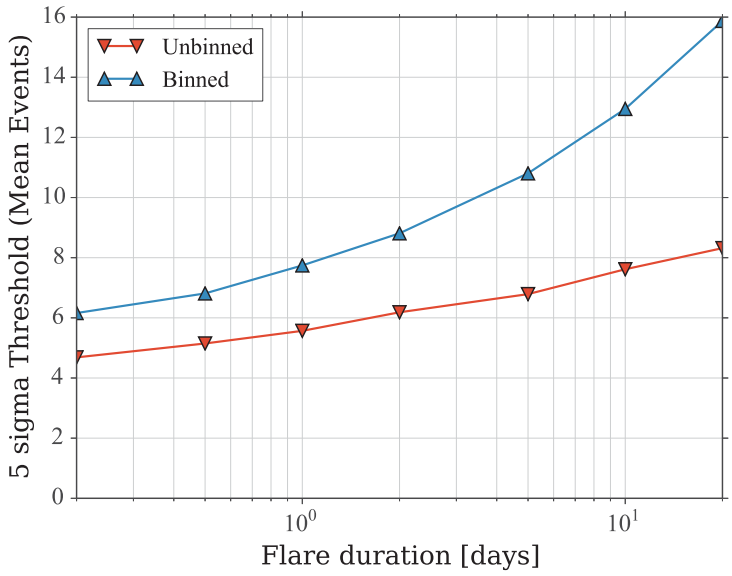

(a) $\theta = 106°$ ($\delta = 0.277$)

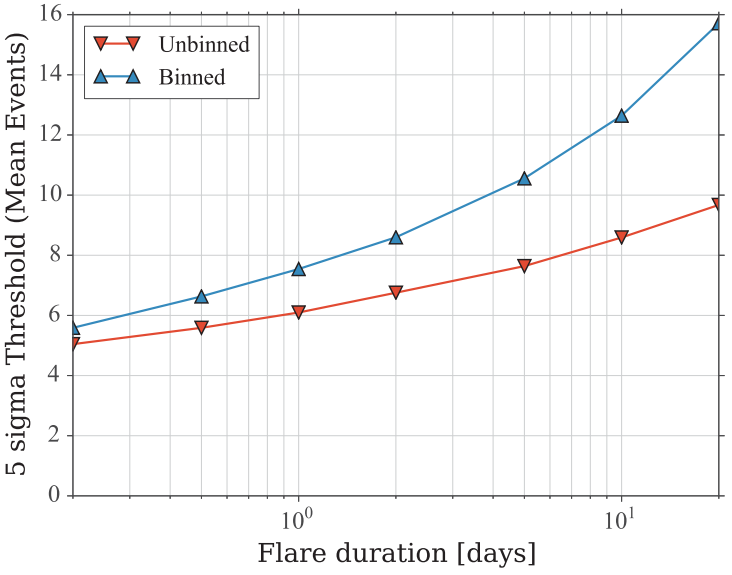

(b) $\theta = 140°$ ($\delta = 0.864$)

Figure 7.11.: *Comparison of the number of events for required for the binned search and the maximum-likelihood based unbinned method to discover neutrino flares of different durations with a significance corresponding to* $5\,\sigma$ *with a probability of* 50 % *at a zenith angle* $\theta = 106°$ ($\delta = 0.277$) *(Fig. (a)) and* $\theta = 140°$ ($\delta = 0.864$) *(Fig. (b)).*

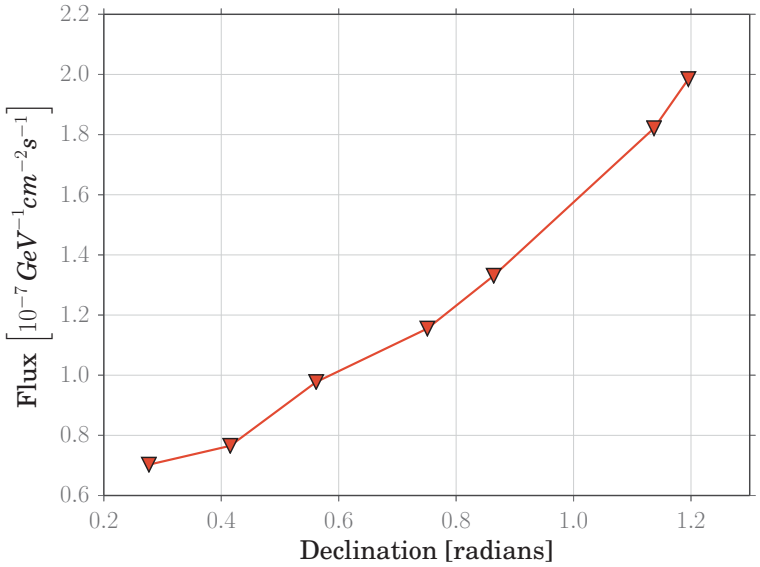

Figure 7.12.: *Flux as a function of declination that is needed to discover a flare with a duration of* 10 *days with a significance corresponding to* $5\,\sigma$ *in* 50 % *of the cases.*

significance corresponding to $5\,\sigma$ as a function of declination. Close to the horizon ($\delta = 0.27$) a flux of $7 \cdot 10^{-8}\,\mathrm{GeV}^{-1}\mathrm{cm}^{-2}\mathrm{s}^{-1}$ is necessary to discover a flare with a duration of 10 days with a probability of 50 %. Due to the neutrino absorption in the Earth and the worse angular resolution the necessary flux increases to $2 \cdot 10^{-7}\,\mathrm{GeV}^{-1}\mathrm{cm}^{-2}\mathrm{s}^{-1}$ at a declination of $\delta = 1.2$.

7.3. Improvements to Track Reconstruction and Event Selection

7.3.1. Improvements to Track Reconstruction

The event reconstruction employed in the *NToO* is the MPE fit described in Sec. 4.5.3. For computational performance it uses constant scattering and absorption lengths throughout the whole detector. For a long time the simulation of the Cherenkov light propagation in the ice used tabulated PDFs of light intensities and arrival times. These tables, however, use several GB of main memory which prohibited their use online at the South Pole. Recently algorithmic advances lead to efficient compression of these tabulated multi-dimensional PDFs by fitting them with splines (see [WvL13]). This decreases both the time and memory requirements of fits that are using these PDFs. Therefore it is planned to deploy in 2014 the so called *SplineFit* online at the South Pole to be applied to all events passing the Online Level 2 Filter. Current studies show that this fit improves the angular resolution by about 20 – 30 %, depending on the event energy.

7.3.2. Improvements to the Event Selection

The currently deployed neutrino event selection in the *NToO* employs straight cuts on a number of variables that discriminate between signal neutrinos and atmospheric muon background. The cuts on these parameters have been optimized to achieve an optimal sensitivity. If one imagines the variables as a multi- dimensional space, straight cuts will always select a hypercube. Events that fall inside are classified as signal, events outside as background. This shape in the space of cut variables, however, is most likely not the most optimal shape in terms of signal-background separation.

Several methods have been developed in the past to improve the discrimination of signal from background in a number of domains. One of the first implementations were the so called neural networks. It can be shown that they can select arbitrary shapes in multiple dimensions. However, neutral networks are quite slow to train and require the optimization of a number of parameters. In recent years a class of classification algorithms derived from decision trees has gained huge grounds, especially in particle and astroparticle physics. One such algorithm is the boosted decision-tree. Its main idea is to train simple decision trees to discriminate signal from background. Each tree itself selects one (or more) hypercube(s) in the parameter space. However, after the training of each tree wrongly classified events are increased in their weight for the next tree, the so called boosting process. Asking a trained ensemble of trees to classify an event results a number between 0 and 1, namely the fraction of trees that classify this event as signal. A cut on this single variable can then be optimized to achieve the desired objective (e.g. maximal sensitivity or discovery potential).

Boosted decision trees are by now routinely used in IceCube point-source analysis. They improve the selection efficiency especially at lower energies compared to straight cuts. This in turn improves the sensitivity for softer spectra.

It is planned to deploy an event selection based on a boosted decision tree for the *NToO* starting in the 2014/2015 season.

8. Results

This section summarizes the results of the first full year of operation of the *NToO*. Section 8.1 gives the essential information for each alert issued during that period, in Sec. 8.2 the significance of the results is presented. The statistical significance of the number of observed alerts is presented in Sec. 8.2. Section 8.4 then discusses the statistical and systematic errors.

Time (UTC)	$-\log_{10}(p_{\mathrm{obs}})$	N_{bg}	N_{obs}	Duration [days]	Weighted RA [°]	Weighted Dec [°]	Follow-up
2012-08-20 09:53	3.747	0.51	6	6.34	198.27	48.48	No
2012-09-13 01:52	4.057	$6.5 \cdot 10^{-5}$	2	$8.33 \cdot 10^{-4}$	240.81	15.14	No
2012-11-09 07:28	4.637	0.35	6	4.17	177.1	49.57	Yes
2013-04-26 05:02	3.726	0.81	7	12.74	27.72	1.77	No
2013-04-29 06:36	4.065	1.02	8	15.80	27.74	1.73	No
2013-09-12 20:01	3.309	0.96	7	11.79	78.5	61.96	Yes
2013-09-14 21:10	3.752	1.13	8	13.84	78.45	61.93	Yes
2013-09-16 00:46	4.301	1.25	9	14.99	78.84	61.74	Yes
2013-09-21 18:31	4.097	1.72	10	20.73	78.84	61.69	No
2014-02-13 22:07	3.765	0.5	6	6.80	356.62	53.14	No
2014-02-14 18:27	4.572	0.56	7	7.65	356.61	53.15	No
2014-02-19 23:10	4.073	1.0	8	12.84	356.61	52.34	Yes
2014-02-23 12:33	4.231	1.28	9	16.40	356.47	51.98	Yes
2014-02-26 18:55	4.590	1.49	10	19.67	356.47	51.99	No
2014-03-09 10:28	3.404	1.70	9	20.94	300.455	64.921	No

Table 8.1.: *Overview over the alerts generated by the NToO in the 2012/2013 and 2013/2014 seasons. Thin horizontal lines separate alerts from different sources, the thick horizontal line separates the two seasons. The alerts from the 2012/2013 season are discussed in detail in Sec. 8.1. Only the first group of alerts from the 2013/2014 season is discussed in Sec. 8.3 due to its particular development.*

Table 8.1 gives an overview over all alerts sent by the *NToO* to date. The alerts from the 2012/2013 season will be discussed in detail. Only the alert for the first source from the currently still ongoing 2013/2014 season is discussed in detail in Sec. 8.3 due to its particular development.

8.1. Alerts During the 2012/2013 Season

In total five (5) alerts have been generated by the *NToO* during the 2012/2013 season for four (4) different sources.

8.1.1. 20 August 2012

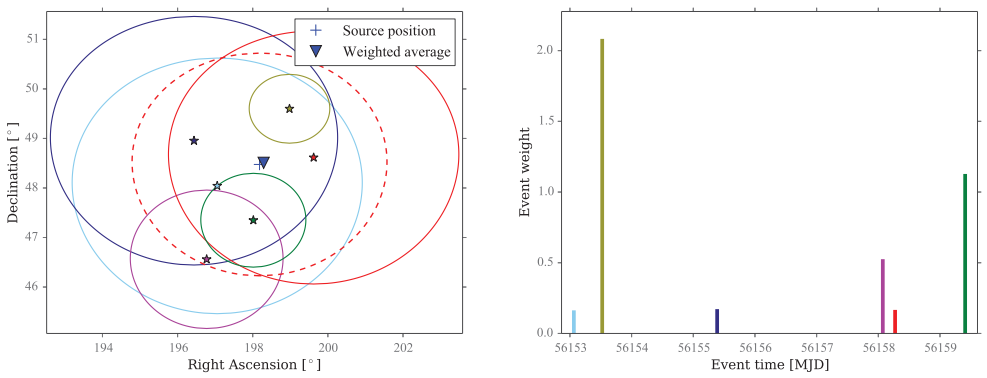

(a) (b)

Figure 8.1.: *Spatial (Fig. (a)) and temporal (Fig. (b)) distribution of the events contributing to the online alert issued on* 20 *August* 2012*. The circles around the events in Fig. (a) depict the individual estimated angular reconstruction uncertainties. The height of the bars in Fig (b) corresponds to the event weights derived from the angular reconstruction uncertainties (see Eq. 6.3). The weights are used to calculate the weighted average direction of the events.*

The first alert during the 2012/2013 IceCube season was generated on 20 August 2012 at 09:53 UTC, originating from the source GB6 B1310+4844 (located at $\theta = 138.49$). The alert comprised six events detected over a duration of 6.344 days resulting in a p-value of $\log_{10} p_{\text{obs}} = -3.747$ (see Eq. 6.1).[1] The spatial distribution of the events in the on-source bin and the temporal distribution of the weighted events are shown in Fig. 8.1. Due to a software bug this alert was not forwarded to a partner experiment.

8.1.2. 13 September 2012

The second alert during the 2012/2013 IceCube season was sent on 13 September 2012 at 01:52 UTC, originating from the source 4C15.54 (located at $\theta = 105.85°$). The alert comprised two events separated by 72 seconds resulting in a p-value of $\log_{10} p_{\text{obs}} = -4.057$. This doublet of neutrino events was also detected by the Optical Follow-Up Program. Figure 8.2 shows the spatial and temporal distribution of the two events. The alert was forwarded to the MAGIC telescopes. However, as the MAGIC telescopes were in a commissioning phase, the alert could not be followed up.

[1] In the following the term significance in the context of a single alert will be understood to be synonymous with $-\log_{10} p_{\text{obs}}$.

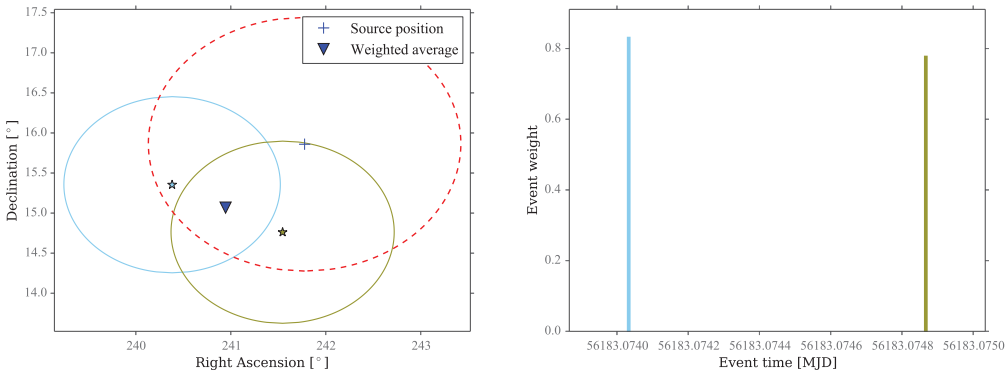

(a) (b)

Figure 8.2.: *Spatial (Fig. (a)) and temporal (Fig. (b)) distribution of the events contributing to the online alert issued alert on* 13 *September* 2012*. See Fig. 8.1 for an explanation.*

8.1.3. 9 November 2012

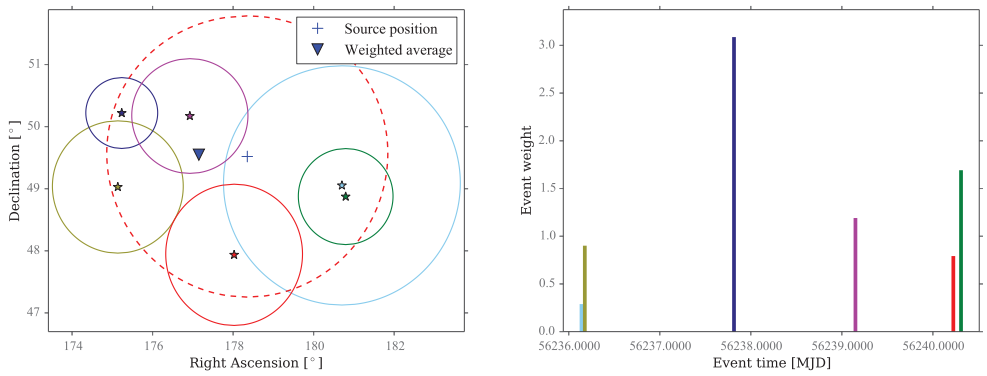

(a) (b)

Figure 8.3.: *Spatial (Fig. (a)) and temporal (Fig. (b)) distribution of the events contributing to the online alert issued alert on* 09 *November* 2012*. See Fig. 8.1 for an explanation.*

The third alert during the 2012/2013 IceCube season was generated on 9 November 2012 at 07:28 UTC originating from the source 1150+497 (located at $\theta = 139.5°$). The alert comprised six events observed during 4.169 days. The p-value for this observation is $\log_{10} p_{\text{obs}} = -4.637$, the highest alert significance of the alerts sent during the 2012/2013 season. The alert was forwarded to the VERITAS telescope and resulted in a follow-up observation.

Results of the Follow-Up Observation The VERITAS team received the alert from IceCube on 9 November 2012 at 07:29 UTC. Poor weather and bright moonlight conditions did not allow VERITAS observations until 12 November 2012, at which point the source was visible at low elevations at the very end of the night. A further observation was made on the following night. The total exposure time amounts to 71.15 min. The observations were performed in "wobble" mode, with the source located 0.5 degrees North or South from the center of the field of view. No statistically significant evidence for gamma- ray emission is seen from the position of the blazar, or from any location within the field of view, which subtends approximately 3 degrees (diameter) around the targeted position. The integral upper limit (99 % confidence) above 300 GeV for an assumed differential spectrum with a spectral index $\gamma = -2.5$ is $3.0 \cdot 10^{-8}\,\mathrm{m}^{-2}\,\mathrm{s}^{-1}$ (see [VER]).

Maximum-Likelihood Offline Analysis In order to test the maximum-likelihood analysis described in Sec. 7.1, the analysis was applied to the alert from 9 November 2012. The time-window for the time-clustering algorithm was restricted to the 21 days before the last event that contributed to the alert. The probability densities for the reconstructed energy of atmospheric neutrinos and signal events for spectral indices ranging from $\gamma = -4$ to $\gamma = -1$ were generated as described in Sec. 7.1. The highest test statistic value $\lambda = 10.09$ was obtained in the same time window as for the binned online search (MJD 56236.1399 to 56240.3092). The number of signal events is fitted as $n_s = 4.57$, the best fit spectral index $\gamma = -4$. The probability to obtain a maximum test statistic value $\lambda \geq 10.09$ in a lifetime of 306.67 days (see Fig. 7.8) for a source at a declination of $\delta = 0.864$ is $p = 0.33$. The distribution of test statistic values λ for the scrambled data sets is shown in Fig. 8.4, the test statistic value λ of this alert is marked by a vertical line. The result obtained with the implemented unbinned maximum-likelihood method has been verified with an independently developed code [Gor].

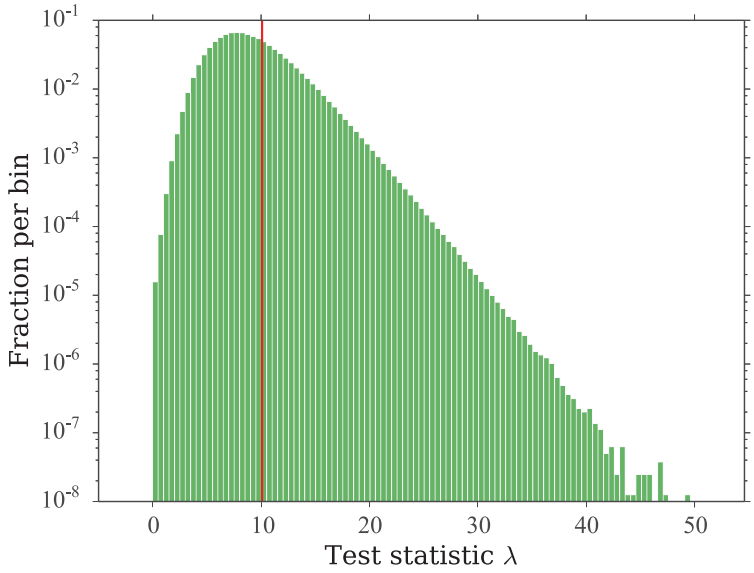

Figure 8.4.: *Distribution of the maximum test statistic value λ (see Eq. 7.6) obtained for scrambled data sets by running the unbinned maximum-likelihood time-clustering algorithm over* 306.67 *days of lifetime. The value obtained in the offline analysis for the alert issued on* 11 *November* 2012 *(λ = 10.09) is marked by the vertical red line. Note that this distribution was generated for this single source, it does not take into account the trial factor from the number of sources.*

8.1.4. 26 and 29 April 2013

The last two alerts of the *NToO* in the 2012/2013 season originated from the source RGB J0152+017 (located at $\theta = 91.77°$) and were generated on 26 April 2013 at 05:02, followed by a second alert on 29 April 2013 at 06:36 UTC. The first alert was triggered by 8 neutrinos observed over a period of 12.74 days and had a p-value of $\log_{10} p_{\text{obs}} = -3.726$. An additional event was observed 3.06 days later, reducing the total p-value to $\log_{10} p_{\text{nobs}} = -4.065$, which resulted in the second alert from the same source. As the source RGB J0152+017 was not visible to any partner experiment the alert was not forwarded. Figure 8.5 shows the spatial and temporal distribution of the contributing events in the second alert from 29 April 2013.

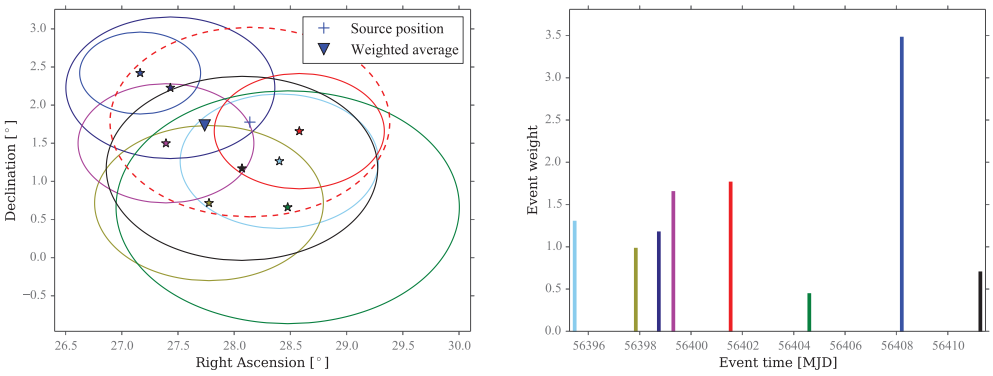

(a) (b)

Figure 8.5.: *Spatial (Fig. (a)) and temporal (Fig. (b)) distribution of the events contributing to the online alert issued alert on* 29 *April* 2013. *See Fig. 8.1 for an explanation.*

8.2. Significance of the Results

During the 2012/2013 season, the first complete season of operating the *NToO*, 5 alerts were generated. Of these, only the alert issued on 09 November 2012 for the source 1150+497 was followed up. The VERITAS observation did not result in the detection of an enhanced state of γ-ray emission from the source.

In order to compare the number and the significance of the generated alerts to expectations, Monte Carlo simulations were run. Artificial data sets were generated by randomizing the event times and calculating new right ascensions according to Eq. 7.12. The time clustering algorithm employed in the *NToO* was run over each data set and the number of alerts as well as the p-value of the most significant alert were recorded. Figure 8.6 shows the distribution of the number of alerts for 50000 scrambled realizations of the complete 2012/2013 dataset. From these simulations the probability to generate more than 5 alerts is inferred to be 80.0 % .

The probability to obtain an alert with a significance higher than the most significant cluster observed in the data ($\log_{10} p = -4.637$ for the alert from 9 November 2012) is estimated to be 35.2 % (see Fig. 8.7) from the same simulation.

Neither the number of observed alerts nor the highest observed significance deviate strongly from the Monte Carlo predictions for alerts caused by background fluctuations alone. Hence no claim on the detection of an astrophysical neutrino flux can be made.

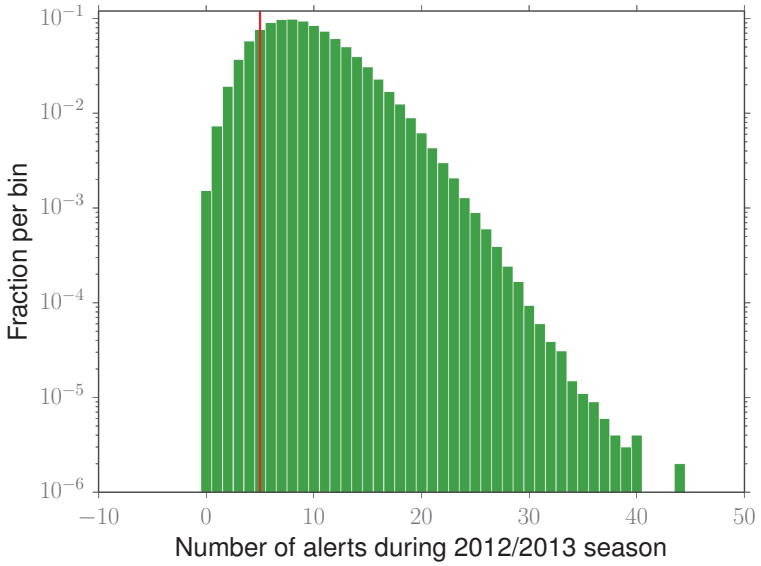

Figure 8.6.: *Probability density of the total number of alerts in scrambled maps of the data set from the* 2012/2013 *season. From this PDF the probability to generate more than* 5 *alerts is inferred to be* 80 %.

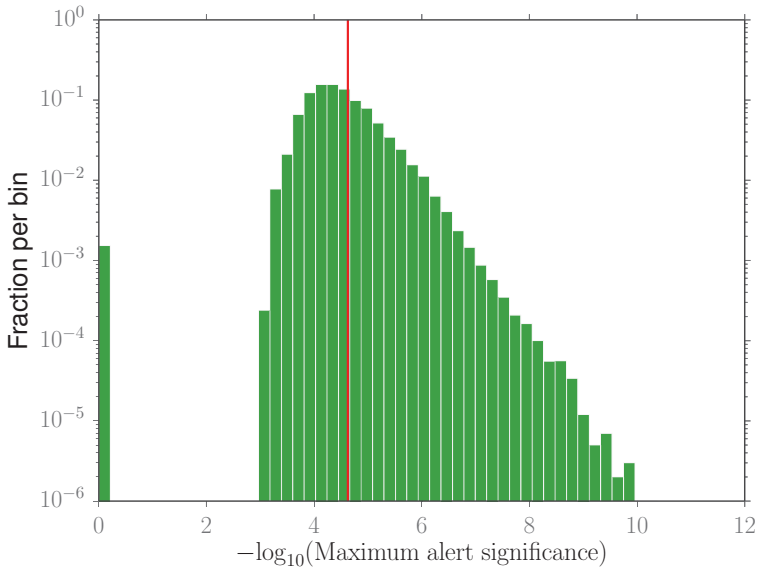

Figure 8.7.: *Probability density of the p-value ($-\log_{10}(p_{obs})$) of the most significant alert from all sources in scrambled maps of the* 2012/2013 *season. In* 35.3 *% of all maps a more significant cluster than observed in the data was caused by background fluctuations in any of the monitored sources. The bin at $-\log_{10}(p_{obs}) = 0$ corresponds to the scrambled maps where no alert was generated (see Fig. 8.6).*

8.3. Alerts during the 2013/2014 season

The Online Level 2 filter and the neutrino event selection of the *NToO* during the 2013/2014 season are very similar to the cuts presented in this work. A comparison between the data at final level (up to September 2013) and neutrino Monte Carlo can be found in Appendix C.

A series of four alerts was issued by the *NToO* from 12 September 2013 till 21 September 2013 for the source RGB 050+612. This sequence of alerts shows some interesting characteristics that make it worth discussing here. The alert resulted in a follow-up observation by MAGIC, however results are not available yet.

Table 8.1 lists the date, the total number of detected events, the expected number of background events, the significance and the weighted direction of each of the four issued alerts. Figure 8.8(a) shows the spatial distribution of the last alert of this series of alerts, Fig. 8.8(b) shows the temporal distribution of the events.

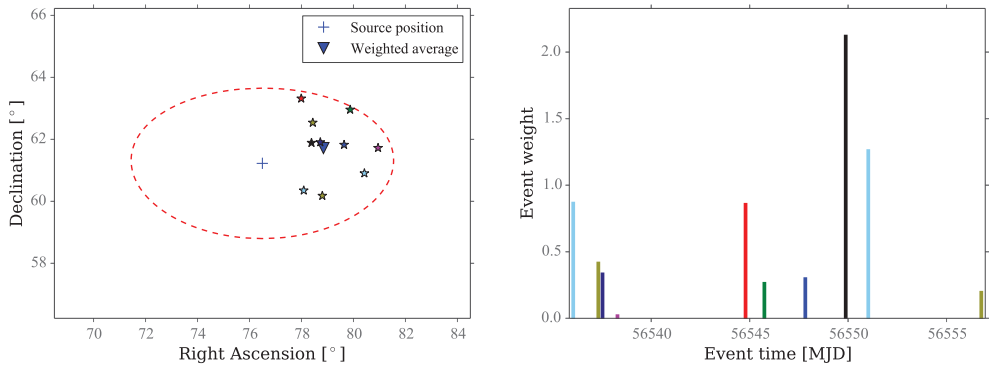

(a) (b)

Figure 8.8.: *Spatial (Fig. (a)) and temporal (Fig. (b)) distribution of the events contributing to the online alert issued alert on* 21 *September* 2013. *The height of the bars in Fig (b) corresponds to the event weights derived from event-by-event estimates of the angular reconstruction. These weights are used to calculate the weighted average direction of the events. The error ellipses are not shown in Fig. (a) to not overcrowd the figure.*

Most of the events that contributed to the alerts cluster around 1.2° away from the source position. This poses a significant challenge for IACTs as their most sensitive field of view is only about 2° wide in diameter. Though the location of the weighted event average is also forwarded to the partner telescopes, their limited experience e.g. the IceCube point spread function makes it almost impossible for their observers to judge if it might be useful to target that point instead of the monitored source. Hence it might be worthwhile to extend the *NToO* to foresee observations of off-source neutrino clusters. This might be especially important for galactic sources, where more than one source might be in the field of view. A much more general approach, however,

would be an *NToO*-like program that covers the full sky without an explicit source list. It would check for statistically significant clusters of neutrinos at any point in the sky and would thus be able to help detect new phenomena in the high-energy γ regime.

The scenario of cluster of neutrinos being set of significantly from a monitored source could also be caused by a systematic bias of the directional reconstruction. However, no such bias has been found in any Monte Carlo study to date. Also the search for the shadow of the Earth's moon on galactic cosmic rays has shown no hints of any systematic pointing error of the detector or the reconstruction software (see [IAA+13a]).

8.4. Discussion of Uncertainties

8.4.1. Statistical Errors

The biggest source of statistical uncertainties is the error on the background rate of atmospheric neutrinos $\mathrm{d}N/\mathrm{d}t$ as a function of the zenith angle θ. During the 2012/2013 season the background rate had to be estimated using data from the previous (2011/2012) season. Figure 8.9 shows the ratio between the background rate used in the online p-value calculation and the background rate derived from the full 2012/2013 data set. The figure shows that over a wide zenith angle range the actual background rates have been underestimated by $5 - 10\,\%$.

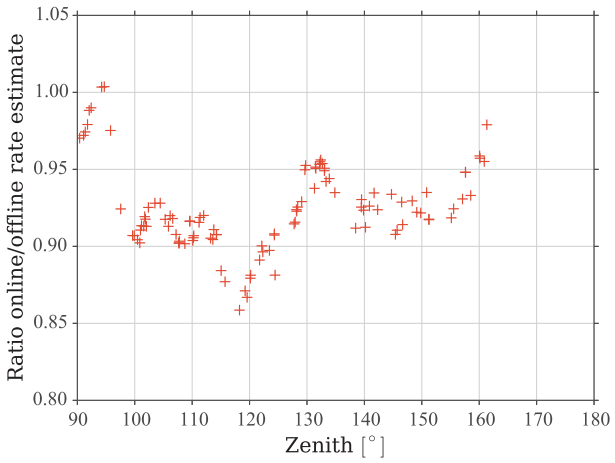

Figure 8.9.: *Ratio of the zenith dependent rate of atmospheric neutrino and muon events estimated from* 2011/2012 *data versus* 2012/2013 *data. The rates estimated from the earlier season have been used online in the* 2012/2013 *season.*

Table 8.2 shows the differences in the alert significances caused by using the two different background rate estimations. Alert significances have been systematically overestimated during the 2012/2013 season with the exception of the alert from 4C 15.54. This alert is special, as

its duration is only 72 seconds. Its significance is affected strongly by the error on the azimuth asymmetry, which has also been estimated using data from the 2011/2012 season.

The actual statistical error on the background rate estimation itself is calculated as $\frac{\sqrt{N}}{N}$, where N is the number of events in the zenith band. Due to the decreasing rate of atmospheric neutrinos the error increases from 0.8 % close to the horizon to 2 % at the nadir. The statistical errors on the background rates estimated from the 2011/2012 dataset (i.e. the rates that have been used in the online significance calculations) are similar.

Source	Zenith [°]	$-\log_{10} p_{\text{obs}}$ online	$-\log_{10} p_{\text{obs}}$ offline
RGB J0152+017	91.77	3.726	3.711
RGB J0152+017	91.77	4.065	4.032
4C 15.54	105.85	4.057	4.189
GB6 B1310+4844	138.5	3.747	3.53
1150+497	139.5	4.637	4.468

Table 8.2.: *Comparison of significance of alerts generated online in the* 2012/2013 *season to significance calculated offline using a more accurate estimate of the background rate of atmospheric neutrinos.*

8.4.2. Systematic Errors

The discussion of systematic errors is based on the numbers given in [AAA+13a], which evaluates the errors for the IceCube detector in its 79-string configuration. Due to the limited availability of Monte Carlo data sets for systematic studies no dedicated studies of systematic uncertainties have been undertaken for the work presented here.

A major strength of the point-source search methods presented in this work is the data-driven background estimation. For the binned search the data is used to estimate the background rate of atmospheric neutrinos, in the maximum-likelihood unbinned search randomized data is used to calculate discovery potentials. Hence the final p-value is unaffected by uncertainties on the flux of atmospheric neutrinos and muons originating from models of air shower development (including the prompt neutrino component from charm decay) or the composition of cosmic rays. Similarly, uncertainties on propagation of Cherenkov light in the ice and the detector simulation do not affect the final p-value.

Light Propagation The two biggest sources of systematic errors are uncertainties on the absolute DOM efficiency and the ice properties affecting the propagation of Cherenkov light. If the absolute DOM sensitivity is varied conservatively by ±10% in the simulation the resulting sensitivity changes by $+6\%/-7\%$. DOM-by-DOM variations of the quantum efficiency with respect to the detector have a negligible effect. The same holds for uncertainties on the quantum efficiency of the DOMs in the DeepCore subarray. Simultaneous scaling of the scattering and absorption in the ice by ±10% resulted in observed changes in the sensitivity of $+5\%/-8\%$.

Theoretical Uncertainties The uncertainties related to modelling of the neutrino interaction and muon propagation are given by:

- Neutrino cross section: $\pm 2\%$,
- Muon propagation: $\pm 3\%$,
- Bedrock density uncertainty: $\pm 3\%$.

The neutrino cross sections at the energies relevant for the work presented here have not been measured directly. As the neutrino-nucleon scattering takes place in the deep-inelastic regime, the cross sections can be calculated from the parton distribution functions. The neutrino Monte Carlo in this work has been produced using cross sections based on the CTEQ5 structure functions. The uncertainties with respect to the CTEQ6 structure functions are determined to be $\pm 2\%$ [Tun02]. Uncertainties in the parametrization of the muon energy losses in the ice result in a theoretical uncertainty of about $\pm 3\%$ [CR04b]. The density of the bedrock below the antarctic glacier is not well measured. A variation of $\pm 10\%$ of the standard value $2.65\,\mathrm{g\,cm^{-3}}$ results in a change of the event rate of $\pm 3\%$.

Uptime Estimation The calculation of the detector uptime is based on the run database, to derive the run start and end times, and detector stability monitoring (see Sec. 6.5). It has been observed that values in the run database can be missing or be modified slightly some time after data taking. This is especially true for the run end times. If a run end time can not be found in the database the current system assumes the start time of the next run to be also to approximate end time of the previous run. This assumption holds true in general, however that have been occasions where detector outages have been missed. A conservative estimate of the resulting over-estimation of the uptime is $+2\%$. This results in an error of -2% in the sensitivity.

Summary Summing in quadrature the different contributions to the systematic uncertainty results in a total value of about 19%. This is in agreement with other, more detailed, studies, e.g. [BA10]. This systematic uncertainty effects the sensitivities and discovery potentials presented in Sec. 6 and Sec. 7. The latter is additionally effected by systematic errors of the energy reconstruction. In [BA10] this is determined to be $\sim 7.5\,\%$. This results in a total systematic uncertainty on the discovery potentials for the maximum-likelihood based analysis of about 21 % for the assumed signal spectrum with $\Phi(E) \sim E^{-2}$.

Contributions from ν_τ The sensitivities and discovery potentials presented here have been calculated assuming that the only neutrino component inducing muon tracks in the ice is ν_μ. However, the branching ratio of a τ (induced by ν_τ interactions) into a μ is about 17%. As detailed in Sec. 3.1 the flavor ratio at the Earth is $1:1:1$ due to neutrino oscillations. This results in a contribution of about $10 - 16\%$ of the ν_τ to the detectable signal flux (see [AAA$^+$11c]).

9. Summary and Outlook

The goal of the Neutrino Triggered Target of Opportunity Program presented in this work is to increase the availability of simultaneous neutrino and high-energy γ-observations for a set of pre-defined sources. The program is based on a multi-step neutrino selection that is applied online at the South Pole. An alert is sent to the partner telescopes MAGIC and VERITAS in case a statistically significant cluster of neutrinos is observed from any of the monitored sources. If the source would be found in an enhanced flux state by the IACT follow-up observation, the combination of the neutrino observation and the high-energy γ-observation could help establish the discovery of neutrino point sources. Furthermore, combining the two observations would increase the potential insight in the physical processes in the source that lead to the flare.

To facilitate the *NToO*, several levels of online event selections were developed (see Chapter 5). Based on the neutrino event selection a time-clustering algorithm has been implemented that searches for statistically significant temporal clusters of neutrinos whose directions are compatible within the typical reconstruction error with a monitored source. The event selection has been optimised to achieve a good discovery probability for flare time scales ranging from ≤ 1 day to 21 days. For example, a source at the declination of Markarian 421 would need to exhibit a flux of $\phi(E) = 0.7 \cdot 10^{-7}\,\mathrm{GeV}^{-1}\mathrm{cm}^{2}\mathrm{s}^{-1}E^{-2}$ during a 10 day flare to be discovered with a probability of 50% at a significance corresponding to $3\,\sigma$ (see Fig. 6.5).

Several technical problems needed to be solved before the *NToO* in its current form could be established. The Online Level2 filter was developed in order to select high-quality muon tracks in the full sky. While retaining almost all well-reconstructed neutrino-induced events it reduces the data rate compared to the previous filter level by about an order of magnitude. Hence it enables the application of more time consuming reconstruction methods on these events. Besides its application in the online follow-up programs the Online Level2 filter also formed the basis of a fast offline follow-up analysis of a GeV γ-ray flare of the Crab nebula detected in 2010 [AAA^{+}12b]. In the future this filter will also be the basis for a fast offline analysis of GRBs in IceCube.

To ensure the validity of the alerts sent by the *NToO* an extensive monitoring system was developed. Different trigger and filter rates where used to determine the detector stability on a very granular level. This stability monitoring system has been proven to work very reliably. In order to monitor the alert generation and forwarding components of the *NToO* a system using test alerts was implemented. This system proved to be vital in the timely discovery of occasional technical problems with the South Pole systems concerned with the *NToO*. The choice of Python (see [Fou]) as an implementation language enabled quick development and easy debugging. The overall software architecture of several small systems interoperating by sending messages, was very successful and runs reliably and stably since more than two years. Due to the quasi-independence of the software components they can be upgraded independently.

The *NToO* is fully operational since March 2012 and monitors 109 sources in the northern sky ($\delta > 0$). During the IceCube season of 2012/2013 five alerts were generated for four different sources. One of the alerts, issued on 9 November 2012 for the source 1150+497, was followed-up by the VERITAS telescope. No significant TeV γ-ray flux was detected from the source and an integral upper limit (99 % confidence) above 300 GeV for an assumed differential spectrum with a spectral index $\gamma = -2.5$ could be set at $3.0 \cdot 10^{-8}\,\mathrm{m}^{-2}\,\mathrm{s}^{-1}$ (see [VER]). The probability to trigger five or more alerts from background fluctuations alone is determined to be 80%. The smallest p-value of any alert was $\log_{10} p = -4.637$ for the alert from November 9, 2012. The probability to observe an alert from any of the monitored sources with this or a smaller p-value caused by background fluctuations in the data set is 35.2%.

The *NToO* is the first realization of a real-time monitoring of likely sources of high-energy neutrino emission in the IceCube experiment. As such the primary goals were to establish the feasibility and prove that such a program can be run stably and reliably over long periods of time. Therefore a simple event selection and search methodology (a time-clustering binned method) were chosen, although more sensitive methods were available. It has been shown in Sec. 7.1 that switching to a maximum-likelihood based time-clustering search lowers the flux needed for a discovery by about 30 – 50%, depending on the declination of the source and the duration of the flare. An improved event selection based on boosted decision trees promises to increase the selection efficiency especially for lower-energy events ($< 10^5$ GeV). This in turn will improve the sensitivity for softer spectra ($\gamma < -2$). It is planned to deploy the maximum-likelihood based analysis and the boosted decision tree based event selection at the start of the 2014/2015 season. In addition an extension of the program to the Southern sky (i.e. $\delta < 0$) is planned. A point-source search in that hemisphere is a regular part of IceCube point-source analyses. Several interesting source candidates, like the galactic center, can be found in that region.

Currently the *NToO* monitors a list of pre-defined sources. In Sec. 8.3 an alert from the 2012/2014 season was discussed that observed a cluster of neutrinos significantly offset from the monitored source. Due to the limited field of view this is hard to handle for current generation IACTs. In general, however, it poses the question of extending the online neutrino point-source search to a full-sky search without a source list. This search would then send alerts for significant temporal clusters of neutrinos anywhere in the sky to partner telescopes. Besides a more complete monitoring of known AGNs and other flaring sources, a program like this would have the chance to discover completely new phenomena.

The program described in this work is a first step to the continuous real-time monitoring of the full sky with neutrinos. It has been proven that an online analysis can be operated reliably and efficiently. Several improvements to the analysis methods used in this program will enhance its sensitivity significantly in the near future. The recent evidence for a diffuse flux of high-energy neutrinos (see [Ice13]) nurtures the hope that the discovery of the first neutrino point source lies not very far in the future.

A. Comparison Data/MC of the 2012/2013 Data after the Online Level2 Filter

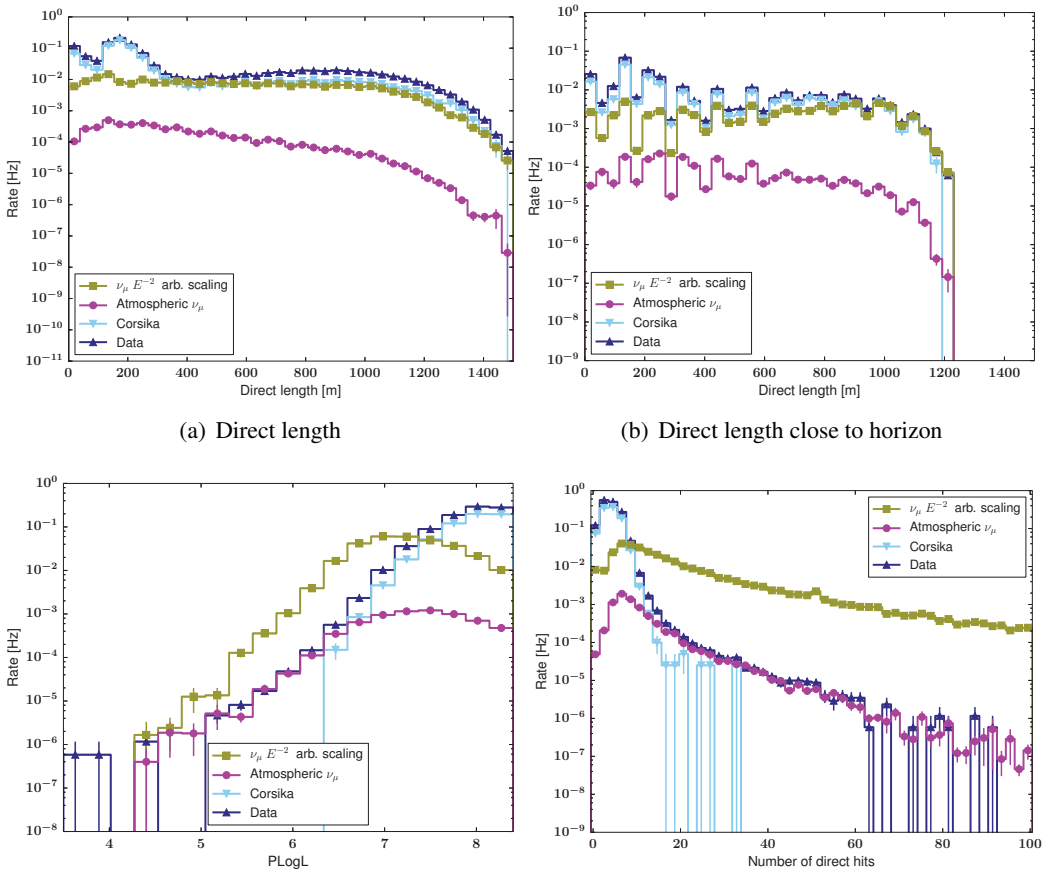

(a) Direct length

(b) Direct length close to horizon

(c) SLogL

(d) Direct hits

Figure A.1.: *Comparison of the data from the* 2012/2013 *season, atmospheric neutrino simulation and air shower muons of variables used to selected neutrino events after the Online Level 2 filter. The data at this level is still heavily dominated by misreconstructed air shower muons.*

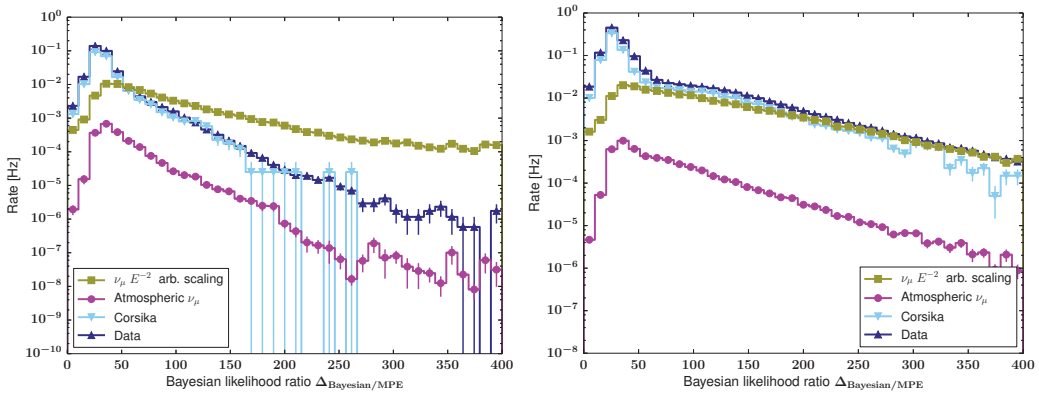

(a) Bayesian likelihood ratio close to the horizon ($\theta_{\text{MPE}} < -0.2$)

(b) Bayesian likelihood ratio

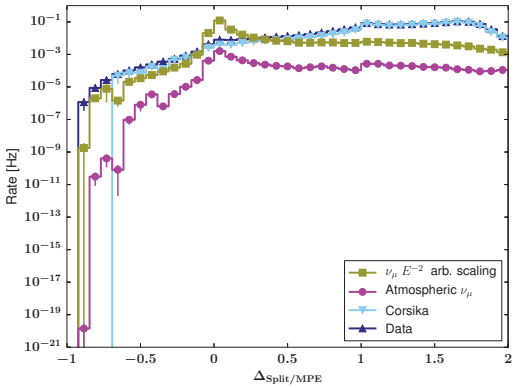

(c) $\Delta_{\text{Split/MPE}}$

Figure A.2.: *Comparison of the data from the* 2012/2013 *season, atmospheric neutrino simulation and air shower muons of variables used to selected neutrino events after the Online Level 2 filter. The data at this level is still heavily dominated by misreconstructed air shower muons.*

B. Properties of the Final Neutrino Sample 2011/2012

Angular Resolution

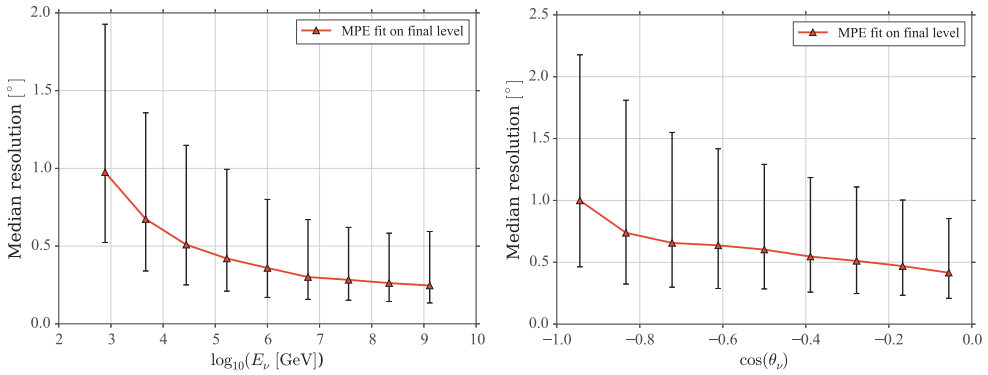

(a) (b)

Figure B.1.: *Median angular resolutions for the final selected neutrino sample of the 2011/2012 season as a function of neutrino energy (Fig. (a)) and zenith angle (Fig. (b), assuming a primary neutrino spectrum with $\Phi(E) \sim E^{-2}$). The bars depict the 25th and 75th percentile of the resolution.*

Effective Area

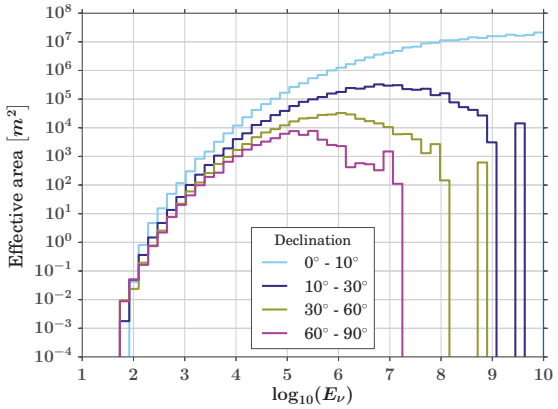

Figure B.2.: *Effective area of the final neutrino sample for the 2011/2012 season in different declination bands as a function of primary neutrino energy.*

Cut Variables: Data/MC Comparison

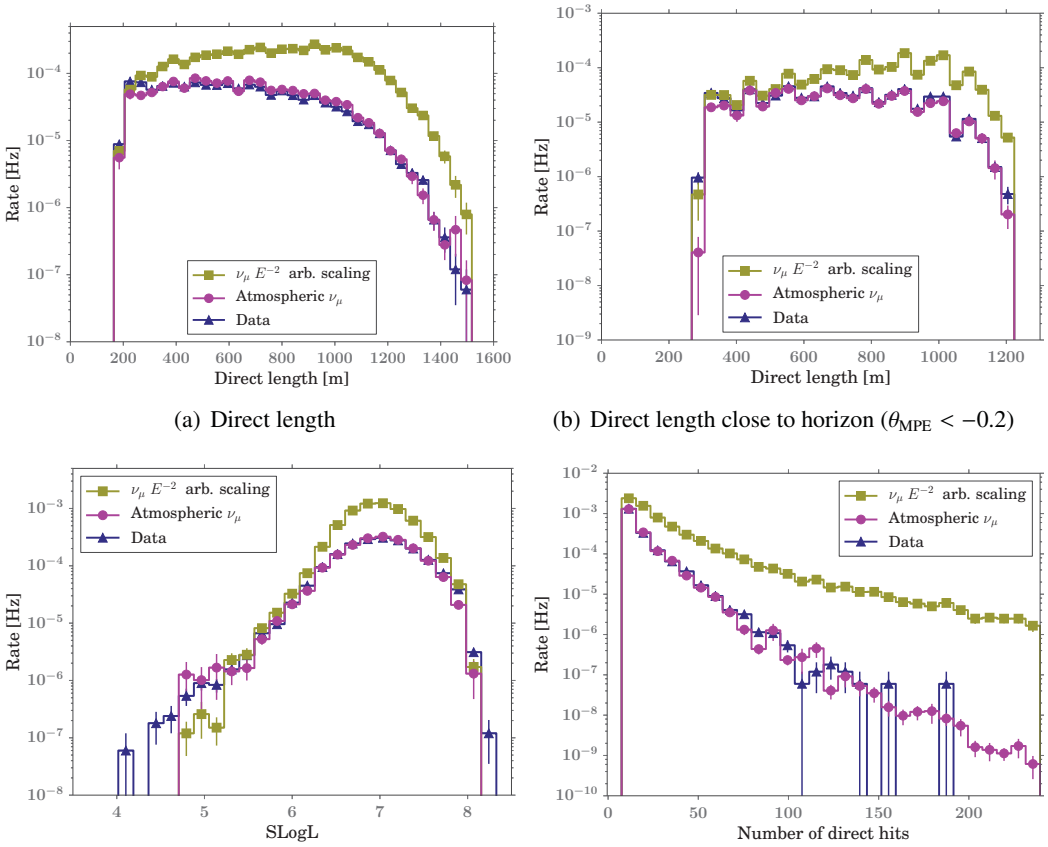

(a) Direct length

(b) Direct length close to horizon ($\theta_{\mathrm{MPE}} < -0.2$)

(c) SLogL

(d) Direct hits

Figure B.3.: *Comparison of data, atmospheric neutrino simulation and a simulated E^{-2} ν_μ-signal flux for the 2011/2012 data set at the final cut level shown for the cut variables used to arrive at this level.*

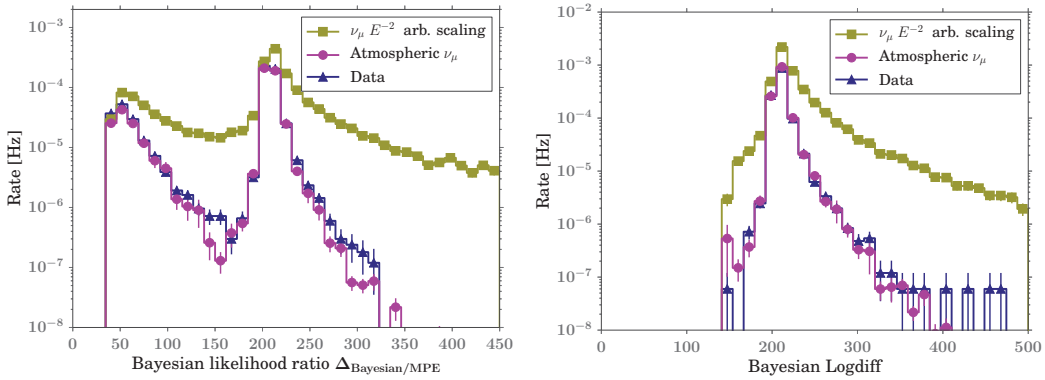

(a) Bayesian likelihood ratio close to the horizon ($\theta_{\text{MPE}} < -0.2$)

(b) Bayesian likelihood ratio

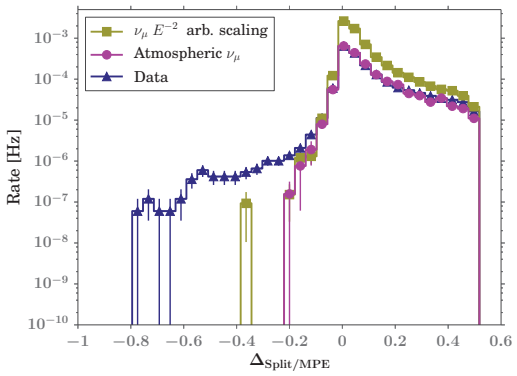

(c) $\Delta_{\text{Split/MPE}}$

Figure B.4.: *Comparison of data, atmospheric neutrino simulation and a simulated E^{-2} ν_μ-signal flux for the 2011/2012 data set at the final cut level shown for the cut variables used to arrive at this level.*

C. Comparsion of Cut Variables for the 2013/14 Season on the Final Cut Level

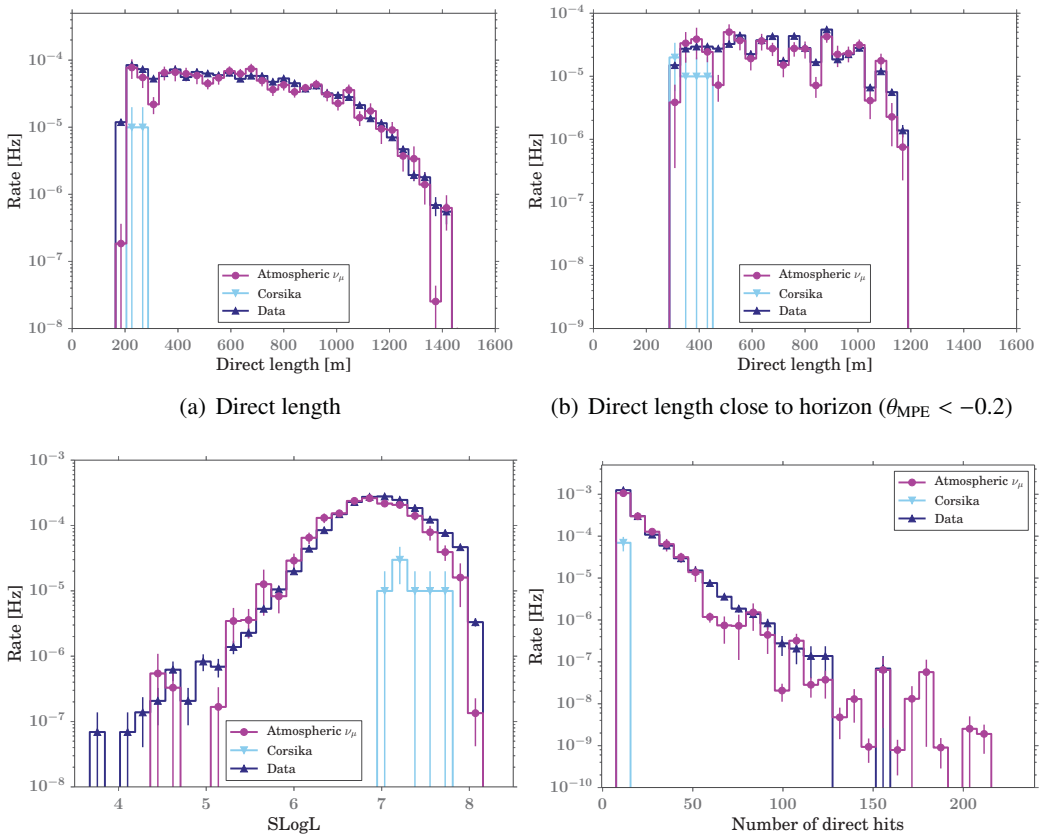

(a) Direct length

(b) Direct length close to horizon ($\theta_{\mathrm{MPE}} < -0.2$)

(c) SLogL

(d) Direct hits

Figure C.1.: *Comparison of the distribution of the cut variables used to arrive at the neutrino level for the partial 2013/2014 dataset, atmospheric neutrino simulation and simulated air show muons (Corsika).*

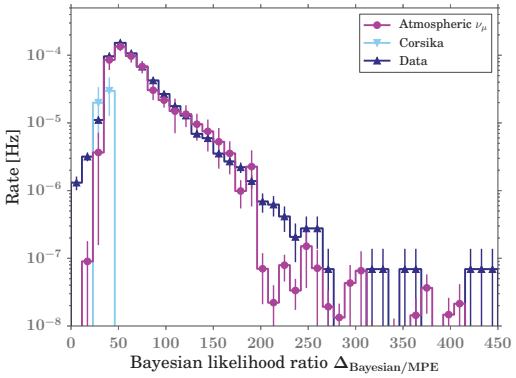

(a) Bayesian likelihood ratio close to the horizon ($\theta_{\text{MPE}} < -0.2$)

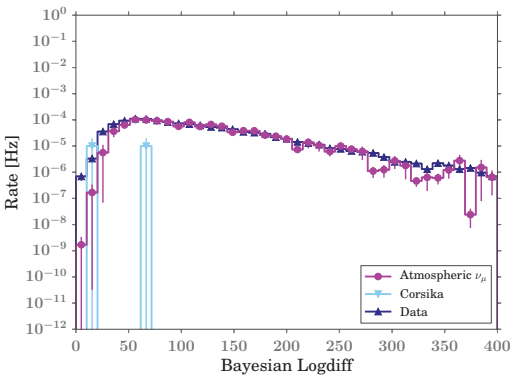

(b) Bayesian likelihood ratio

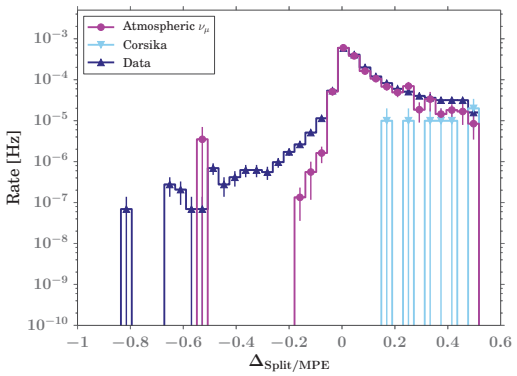

(c) $\Delta_{\text{Split/MPE}}$

Figure C.2.: *Comparison of the distribution of the cut variables used to arrive at the neutrino level for the partial 2013/2014 dataset, atmospheric neutrino simulation and simulated air show muons (Corsika).*

Zenith Angle

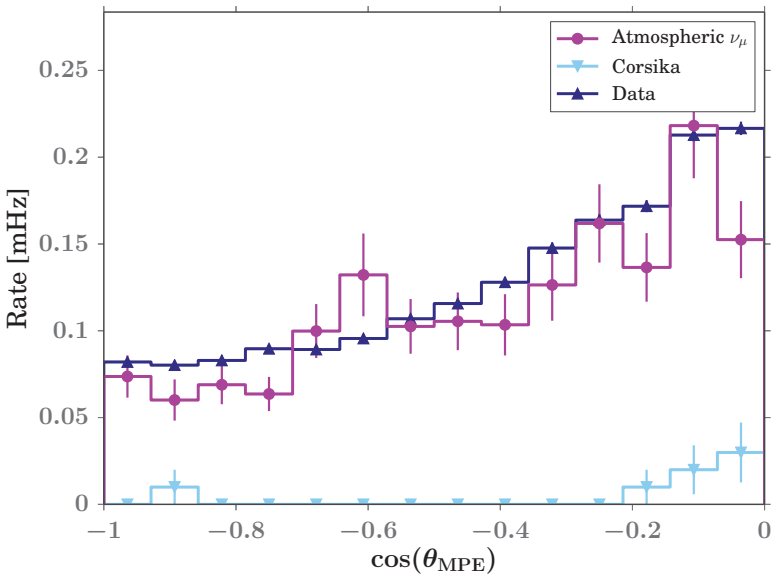

Figure C.3.: *Comparison of the distribution of reconstructed zenith angle* ($\cos\theta_{MPE}$) *for the partial 2013/2014 dataset, atmospheric neutrino simulation and simulated air shower muons (Corsika).*

Bibliography

This work cites several documents that are not publicly accessible, like IceCube Internal Reports and information from the IceCube Wiki. As this is often the only location where certain knowledge is documented it was decided to cite it nevertheless. If you need access to these sources please contact a member of the IceCube collaboration.

[A+00] Andres, E.; et al.: The AMANDA neutrino telescope: principle of operation and first results. In: *Astron. Astrophys.*, volume 13:pp. 1–20, March 2000.

[A+03] Ahrens, J.; et al.: Search for neutrino-induced cascades with the AMANDA detector. In: *Phys. Rev. D*, volume 67(1):pp. 012003–+, January 2003.

[A+13] Abbasi, R.; et al. (IceCube Collaboration): IceTop: The surface component of IceCube. In: *Nucl. Instrum. Methods Phys. Res., Sect. A*, volume A700:pp. 188–220, 2013.

[AAA+03] Agostinelli, S.; et al.: Geant4—a simulation toolkit. In: *Nucl. Instrum. Methods Phys. Res., Sect. A*, volume 506(3):pp. 250 – 303, 2003.

[AAA+04] Aharonian, F. A.; et al.: High-energy particle acceleration in the shell of a supernova remnant. In: *Nature*, volume 432:pp. 75–77, November 2004.

[AAA+06] Albert, J.; et al.: Variable Very-High-Energy Gamma-Ray Emission from the Microquasar LS I +61 303. In: *Science*, volume 312:pp. 1771–1773, June 2006.

[AAA+07a] Achterberg, A.; et al.: Five years of searches for point sources of astrophysical neutrinos with the AMANDA-II neutrino telescope. In: *Phys. Rev. D*, volume 75(10):pp. 102001–+, May 2007.

[AAA+07b] Albert, J.; et al.: Variable very high energy γ-ray emission from markarian 501. In: *Astrophys J.*, volume 669(2):p. 862, 2007.

[AAA+09a] Abbasi, R.; et al.: The IceCube data acquisition system: Signal capture, digitization, and timestamping. In: *Nucl. Instrum. Methods Phys. Res., Sect. A*, volume 601:pp. 294–316, April 2009.

[AAA+09b] Acciari, V. A.; et al.: Radio Imaging of the Very-High-Energy γ-Ray Emission Region in the Central Engine of a Radio Galaxy. In: *Science*, volume 325:pp. 444–, July 2009.

[AAA+10] Abbasi, R.; et al.: Calibration and characterization of the IceCube photomultiplier tube. In: *Nucl. Instrum. Methods Phys. Res., Sect. A*, volume 618:pp. 139–152, June 2010.

[AAA+11a] Abbasi, R.; et al.: Search for a diffuse flux of astrophysical muon neutrinos with the IceCube 40-string detector. In: *Phys. Rev. D*, volume 84(8):082001, October 2011.

[AAA+11b] Abbasi, R.; et al.: Measurement of the atmospheric neutrino energy spectrum from 100 GeV to 400 TeV with IceCube. In: *Phys. Rev. D*, volume 83(1):012001, January 2011.

[AAA+11c] Abbasi, R.; et al.: Time-integrated Searches for Point-like Sources of Neutrinos with the 40-string IceCube Detector. In: *Astrophys J.*, volume 732:18, May 2011.

[AAA+11d] Ageron, M.; et al.: ANTARES: The first undersea neutrino telescope. In: *Nucl. Instrum. Methods Phys. Res., Sect. A*, volume 656:pp. 11–38, November 2011.

[AAA+12a] Abbasi, R.; et al.: Searches for Periodic Neutrino Emission from Binary Systems with 22 and 40 Strings of IceCube. In: *Astrophys J.*, volume 748:118, April 2012.

[AAA+12b] Abbasi, R.; et al.: Neutrino Analysis of the 2010 September Crab Nebula Flare and Time-integrated Constraints on Neutrino Emission from the Crab Using IceCube. In: *Astrophys J.*, volume 745:45, January 2012.

[AAA+12c] Abbasi, R.; et al.: Time-dependent Searches for Point Sources of Neutrinos with the 40-string and 22-string Configurations of IceCube. In: *Astrophys J.*, volume 744:1, January 2012.

[AAA+12d] Abbasi, R.; et al.: Searching for soft relativistic jets in core-collapse supernovae with the IceCube optical follow-up program. In: *Astron. Astrophys.*, volume 539:A60, March 2012.

[AAA+12e] Abramowski, A.; et al.: The 2010 Very High Energy γ-Ray Flare and 10 Years of Multi-wavelength Observations of M 87. In: *Astrophys J.*, volume 746:151, February 2012.

[AAA+12f] Aliu, E.; et al.: Multiwavelength Observations of the AGN 1ES 0414+009 with VERITAS, Fermi-LAT, Swift-XRT, and MDM. In: *Astrophys J.*, volume 755:118, August 2012.

[AAA+12g] Ara Collaboration; et al.: Design and initial performance of the Askaryan Radio Array prototype EeV neutrino detector at the South Pole. In: *Astrop. Phys.*, volume 35:pp. 457–477, February 2012.

[AAA+13a] Aartsen, M. G.; et al.: Search for Time-independent Neutrino Emission from Astrophysical Sources with 3 yr of IceCube Data. In: *Astrophys J.*, volume 779:132, December 2013.

[AAA+13b] Aartsen, M. G.; et al.: Measurement of South Pole ice transparency with the IceCube LED calibration system. In: *Nucl. Instrum. Methods Phys. Res., Sect. A*, volume 711(0):pp. 73 – 89, 2013.

[AAA+13c] Abbasi, R.; et al.: An improved method for measuring muon energy using the truncated mean of dE/dx. In: *Nucl. Instrum. Methods Phys. Res., Sect. A*, volume 703(0):pp. 190 – 198, 2013.

[AAA+13d] Ackermann, M.; et al.: Detection of the characteristic pion-decay signature in supernova remnants. In: *Science*, volume 339(6121):pp. 807–811, 2013.

[AAA+14] Aartsen, M. G.; et al.: Improvement in fast particle track reconstruction with robust statistics. In: *Nucl. Instrum. Methods Phys. Res., Sect. A*, volume 736:pp. 143–149, February 2014.

[AAB+97] Aharonian, F. A.; et al.: Measurement of the flux, spectrum, and variability of tev γ-rays from mkn 501 during a state of high activity. In: *Astron. Astrophys.*, volume 327:p. L5, 1997.

[AAB+99] Aharonian, F. A.; et al.: The time averaged TeV energy spectrum of MKN 501 of the extraordinary 1997 outburst as measured with the stereoscopic Cherenkov telescope system of HEGRA. In: *Astron. Astrophys.*, volume 349:p. 11, 1999.

[AAB+02] Aharonian, F.; et al.: Variations of the TeV energy spectrum at different flux levels of Mkn 421 observed with the HEGRA system of Cherenkov telescopes. In: *Astron. Astrophys.*, volume 393:pp. 89–99, October 2002.

[AAB+03] Aharonian, F. A.; et al.: Is the Giant Radio Galaxy M87 a TeV Gamma-Ray Emitter? In: *Astron. Astrophys.*, volume 403:p. L1, 2003.

[AAB+06a] Ackermann, M.; et al.: Optical properties of deep glacial ice at the South Pole. In: *J. Geophys. Res.(Atm.)*, volume 111(D10):D13203, July 2006.

[AAB+06b] Aharonian, F.; et al.: A low level of extragalactic background light as revealed by γ-rays from blazars. In: *Nature*, volume 440:pp. 1018–1021, April 2006.

[AAB+07] Aharonian, F.; et al.: An Exceptional Very High Energy Gamma-Ray Flare of PKS 2155–304. In: *Astrophys J. L.*, volume 664(2):p. L71, 2007.

[AAB+09] Aynutdinov, V.; et al.: The BAIKAL neutrino experiment - Physics results and perspectives. In: *Nucl. Instrum. Methods Phys. Res., Sect. A*, volume 602:pp. 14–20, April 2009.

[ABB+95] Askebjer, P.; et al.: Optical Properties of the South Pole Ice at Depths Between 0.8 and 1 Kilometer. In: *Science*, volume 267:pp. 1147–1150, February 1995.

[ABB+97] Askebjer, P.; et al.: Optical properties of deep ice at the South Pole: absorption. In: *Appl. Opt.*, volume 36:pp. 4168–4180, June 1997.

[ABB+04a] Ahrens, J.; et al.: Sensitivity of the IceCube detector to astrophysical sources of high energy muon neutrinos. In: *Astrop. Phys.*, volume 20:pp. 507–532, February 2004.

[ABB+04b] Ahrens, J.; et al.: Muon track reconstruction and data selection techniques in AMANDA. In: *Nucl. Instrum. Methods Phys. Res., Sect. A*, volume 524:pp. 169–194, May 2004.

[ABB+07] Adam, T.; et al.: The OPERA experiment Target Tracker. In: *Nucl. Instrum. Methods Phys. Res., Sect. A*, volume 577:pp. 523–539, July 2007.

[ABB+10] Andreopoulos, C.; et al.: The GENIE neutrino Monte Carlo generator. In: *Nucl. Instrum. Methods Phys. Res., Sect. A*, volume 614:pp. 87–104, February 2010.

[ABG+08] Ackermann, M.; et al.: Neutrino Triggered Target of Opportunity (NToO) test run with AMANDA-II and MAGIC. In: *Proceedings of the 30th Int. Cosmic Ray Conf.*, volume 3, pp. 1257–1260. 2008.

[Ack07] Ackermann, Markus: *Searches for signals from cosmic point-like sources of high energy neutrinos in* 5 *years of AMANDA-II data*. Ph.D. thesis, Humboldt Universität zu Berlin, 2007.

[AD01] Atoyan, A.; Dermer, C. D.: High-Energy Neutrinos from Photomeson Processes in Blazars. In: *Phys. Rev. Lett.*, volume 87(22):pp. 221102–+, November 2001.

[ADH+99] Ascher, D.; et al.: *Numerical Python*. Lawrence Livermore National Laboratory, Livermore, CA, ucrl-ma-128569 edition, 1999.

[ADKM79] Askariyan, G. A.; et al.: Acoustic detection of high energy particle showers in water. In: *Nucl. Instrum. Methods*, volume 164(2):pp. 267 – 278, 1979.

[AEM+39] Auger, Pierre; et al.: Extensive cosmic-ray showers. In: *Rev. Mod. Phys.*, volume 11(3-4):pp. 288–291, Jul 1939.

[Aha04] Aharonian, F.: *Very High Energy Cosmic Gamma Radiation*. World Scientific, 2004.

[AIL+05] Aramo, C.; et al.: Earth-skimming UHE tau neutrinos at the fluorescence detector of Pierre Auger Observatory. In: *Astrop. Phys.*, volume 23:pp. 65–77, February 2005.

[AJY00] Athar, H.; Jeżabek, M.; Yasuda, O.: Effects of neutrino mixing on high-energy cosmic neutrino flux. In: *Phys. Rev. D*, volume 62(10):pp. 103007–+, November 2000.

[AS09] Akhmedov, E. K.; Smirnov, A. Y.: Paradoxes of neutrino oscillations. In: *Physics of Atomic Nuclei*, volume 72:pp. 1363–1381, August 2009.

[Ask57] Askaryan, G. A.: Hydrodynamic radiation from the tracks of ionizing particles in stable liquids. In: *Atomic Energy*, volume 3:pp. 921–923, 1957. 10.1007/BF01480076.

[Ask62] Askaryan, G. A.: Excess Negative Charge of the Electron-Photon Shower and Coherent Radiation Originating from It. Radio Recording of Showers under the Ground and on the Moon. In: *J. Phys. Soc. Jpn. Sup.*, volume 17:p. C257, 1962.

[B+10] Bay, R. C.; et al.: South pole paleowind from automated synthesis of ice code records. In: *J. Geophys. Res. (Atmospheres)*, volume 115(D14126), 2010.

[BA10] Bazo Alba, J. L.: *Search for steady and flaring astrophysical neutrino point sources with the IceCube detector*. Ph.D. thesis, Humboldt-Universität zu Berlin, August 2010.

[BAB+03] Barwick, S. W.; et al.: Physics and Operation of the AMANDA-II High Energy Neutrino Telescope. In: Gorham, P. W., editor, *Particle Astrophysics Instrumentation*, volume 4858 of *Presented at the Society of Photo-Optical Instrumentation Engineers (SPIE) Conference*, pp. 79–91. February 2003.

[BAB+12] Beringer, J.; et al. (Particle Data Group): Review of particle physics. In: *Phys. Rev. D*, volume 86:p. 010001, Jul 2012.

[BB81] Bezrukov, L. B.; Bugaev, E. V.: Energy losses of high energy muons in standard rock and water. In: *International Cosmic Ray Conference*, volume 7 of *International Cosmic Ray Conference*, pp. 102–105. 1981.

[BBB+12] Bartoli, B.; et al.: Long-term Monitoring of Mrk 501 for its Very High Energy γ Emission and a Flare in 2011 October. In: *Astrophys J.*, volume 758:2, October 2012.

[BBD+08] Böser, S.; et al.: Feasibility of acoustic neutrino detection in ice: First results from the South Pole Acoustic Test Setup (SPATS). In: *Proceedings of the 30th Int. Cosmic Ray Conf.*, volume 5, pp. 1605–1608. 2008.

[BBD+10] Braun, J.; et al.: Time-dependent point source search methods in high energy neutrino astronomy. In: *Astrop. Phys.*, volume 33:pp. 175–181, April 2010.

[BBR05] Becker, J. K.; Biermann, P. L.; Rhode, W.: The diffuse neutrino flux from FR-II radio galaxies and blazars: A source property based estimate. In: *Astrop. Phys.*, volume 23:pp. 355–368, May 2005.

[Bec08] Becker, J. K.: High-energy neutrinos in the context of multimessenger astrophysics. In: *Phys. Rep.*, volume 458:pp. 173–246, March 2008.

[BEH09] Blümer, J.; Engel, R.; Hörandel, J. R.: Cosmic rays from the knee to the highest energies. In: *Progr. Part. Nucl. Phys.*, volume 63:pp. 293–338, October 2009.

[Ber02] Berger, C.: *Elemententarteilchenphysik*. Springer, 2002.

[Ber11] Bernardini, E.: Astronomy in the Time Domain. In: *Science*, volume 331:pp. 686–, February 2011.

[Bf05] Bernardini, E.; for the IceCube Collaboration: Multi-Messenger Studies with AMANDA/IceCube: Observations and Strategies. In: *ArXiv Astrophysics e-prints*, September 2005. arXiv:astro-ph/0509396.

[BHG+09] Bonnoli, G.; et al.: MAGIC observations of Mkn 421 in 2008, and related optical/X-ray/TeV MWL study. In: *ArXiv e-prints*, July 2009. arXiv:astro-ph/0907.0831.

[BHK12] Böttcher, M.; Harris, D. E.; Krawczynski, H.: *Relativistic Jets from Active Galactic Nuclei*. Wiley, January 2012.

[BL98] Blobel, V.; Lohrmann, E.: *Statistische und numerische Methoden der Datenanalyse*. Teubner Verlag, 1st edition, 1998. ISBN 3519032430.

[Boe06] Boettcher, M.: Modeling the Emission Processes in Blazars. In: *ArXiv Astrophysics e-prints*, August 2006. arXiv:astro-ph/0608713.

[Böt12] Böttcher, M.: Modeling the Spectral Energy Distributions and Variability of Blazars. In: *ArXiv e-prints*, 2012. astro-ph/1205.0539.

[BRM09] Böttcher, M.; Reimer, A.; Marscher, A. P.: Implications of the very High Energy Gamma-Ray Detection of the Quasar 3C279. In: *Astrophys J.*, volume 703:pp. 1168–1175, September 2009.

[BRZ13] Böttcher, M.; Reimer, A.; Zhang, H.: Leptonic and Hadronic Modeling of Fermi-Detected Blazars. Spectral Energy Distribution Modeling and High-Energy Polarization Predictions. In: *European Physical Journal Web of Conferences*, volume 61 of *European Physical Journal Web of Conferences*, p. 5003. December 2013.

[C+10] Chirkin, Dmitry; et al.: Study of ice transparency with IceCube flashers. http://icecube.wisc.edu/~dima/work/WISC/ppc/fit/paper/a.pdf, 2010. Retrieved 2013-01-15.

[CG07] Casandjian, J.-M.; Grenier, I.: A Revised Catalogue of EGRET sources. In: *Proceedings of the 30th Int. Cosmic Ray Conf.* Merida, Mexico, 2007.

[CG08] Celotti, A.; Ghisellini, G.: The power of blazar jets. In: *Mon. Not. R. Astron. Soc.*, volume 385:pp. 283–300, March 2008.

[CGB+13] Cruz, A.; et al.: Search for multi-flares of high energy neutrinos from Active Galactic Nuclei with the IceCube detector. In: *Proceedings of the 33nd Int. Cosmic Ray Conf.* Rio de Janeiro, Brasil, 2013.

[CGSf09] Cortina, J.; et al.: Technical Performance of the MAGIC Telescopes. In: *ArXiv e-prints*, July 2009. arXiv:astro-ph/0907.1211.

[Che34] Cherenkov, P. A.: Vidimoe svechenie chistykh zhidkostei pod deistviem γ-radiatsii (Visible glow of pure liquids under γ-irradiation). In: *Dokl. Akad. Nauk SSSR*, volume 2(8):p. 451, 1934.

[Che37] Cherenkov, P. A.: Visible Radiation Produced by Electrons Moving in a Medium with Velocities Exceeding that of Light. In: *Phys. Rev.*, volume 52:pp. 378–379, Aug 1937.

[Col12] Collaboration, The Pierre Auger: Search for point-like sources of ultra-high energy neutrinos at the pierre auger observatory and improved limit on the diffuse flux of tau neutrinos. In: *Astrophys J. L.*, volume 755(1):p. L4, 2012.

[CP11] Caruso, R.; Pierre Auger Collaboration: General overview of recent results from the Pierre Auger Observatory. In: *Astrophys. Space Sci. Trans.*, volume 7:pp. 445–451, October 2011.

[CP12] Cazon, L.; Pierre Auger Collaboration: Studying the nuclear mass composition of Ultra-High Energy Cosmic Rays with the Pierre Auger Observatory. In: *JPCS*, volume 375(5):p. 052003, July 2012.

[CR+04a] Chen, K.S.; Romero, G.E.; et al.: *Cosmic Gamma-Ray Sources*. Kluwer Academic Publishers, 2004.

[CR04b] Chirkin, D.; Rhode, W.: Propagating leptons through matter with Muon Monte Carlo (MMC). In: *ArXiv High Energy Physics e-prints*, July 2004. `arXiv:hep-ph/0407075`.

[CR05] Chirkin, D.; Rhode, W.: All Lepton Propagation Monte Carlo. In: *Proceedings of the 29th Int. Cosmic Ray Conf.* Pune, India, 2005.

[CRH+56] Cowan, C. L.; et al.: Detection of the free neutrino: a confirmation. In: *Science*, volume 124(3212):pp. 103–104, 1956.

[Cro06] Crockford, D.: The application/json media type for javascript object notation (json), 2006. URL `http://www.ietf.org/rfc/rfc4627.txt`.

[CS08] Cooper-Sarkar, A.; Sarkar, S.: Predictions for high energy neutrino cross-sections from the ZEUS global PDF fits. In: *Journal of High Energy Physics*, volume 1:075, January 2008.

[CZ07] Chirkin, D.; Zornoza, J.: Muon energy reconstruction and atmospheric neutrino spectrum unfolding with the IceCube detector. In: *Proceedings of the 30th Int. Cosmic Ray Conf.* Merida, Mexico, 2007.

[DA81] Dziewonski, A. M.; Anderson, D. L.: Preliminary reference Earth model. In: *Phys. of the Earth and Planet. Int.*, volume 25:pp. 297–356, June 1981.

[DBB+05] Daniel, M. K.; et al.: Spectrum of Very High Energy Gamma-Rays from the blazar 1ES 1959+650 during Flaring Activity in 2002. In: *Astrophys J.*, volume 621:pp. 181–187, March 2005.

[DBB+13] Dorner, D.; et al.: FACT - Long-term Monitoring of Bright TeV-Blazars. In: *ArXiv e-prints*, November 2013. arXiv:astro-ph/1311.0478.

[DHH68] Davis, R.; Harmer, D. S.; Hoffman, K. C.: Search for Neutrinos from the Sun. In: *Phys. Rev. Lett.*, volume 20:pp. 1205–1209, May 1968.

[DHH96] Dubois, P. F.; Hinsen, K.; Hugunin, J.: Numerical python. In: *Computers in Physics*, volume 10(3), May/June 1996.

[DRL07] Dermer, C.; Ramirez-Ruiz, E.; Le, T.: Correlation of Photon and Neutrino Fluxes in Blazars and Gamma Ray Bursts. In: *ArXiv Astrophysics e-prints*, March 2007. arXiv:astro-ph/0703219.

[Dub99] Dubois, P. F.: Extending python with fortran. In: *Computing Science and Engineering*, volume 1(5):pp. 66–73, Sep/Oct 1999.

[Ebe05] Eberle, B.: *Big Bang Relic Neutrinos and Their Detection*. Ph.D. thesis, Universität Hamburg, 2005.

[EGLS92] Engel, J.; et al.: Nucleus-nucleus collisions and interpretation of cosmic-ray cascades. In: *Phys. Rev. D*, volume 46:pp. 5013–5025, December 1992.

[Eic79] Eichler, D.: High-energy neutrino astronomy - A probe of galactic nuclei. In: *Astrophys J.*, volume 232:pp. 106–112, August 1979.

[ERS08] Enberg, R.; Reno, M. H.; Sarcevic, I.: Prompt neutrino fluxes from atmospheric charm. In: *Phys. Rev. D*, volume 78(4):043005, August 2008.

[F+03] Fukuda, Y.; et al. (Super-Kamiokande Collaboration): The Super-Kamiokande detector. In: *Nucl. Instrum. Methods Phys. Res., Sect. A*, volume A501:pp. 418–462, 2003.

[FB+09] Franke, R.; Bernardini, E.; et al.: Neutrino triggered high-energy gamma-ray follow-up with IceCube. In: *Proceedings of the 31st Int. Cosmic Ray Conf.*, volume 4, p. 165. 2009.

[FB+11] Franke, R.; Bernardini, E.; et al.: Neutrino triggered high-energy gamma-ray follow-up with IceCube. In: *Proceedings of the 32nd Int. Cosmic Ray Conf.*, volume 4, p. 165. 2011.

[FC98] Feldman, Gary J.; Cousins, Robert D.: Unified approach to the classical statistical analysis of small signals. In: *Phys. Rev. D*, volume 57(7):pp. 3873–3889, Apr 1998.

[Fer49] Fermi, E.: On the Origin of the Cosmic Radiation. In: *Phys. Rev.*, volume 75:pp. 1169–1174, April 1949.

[FFWY02] Feng, J. L.; et al.: Observability of Earth-Skimming Ultrahigh Energy Neutrinos. In: *Phys. Rev. Lett.*, volume 88(16):161102, April 2002.

[FGLS94a] Fletcher, R. S.; et al.: sibyll: An event generator for simulation of high energy cosmic ray cascades. In: *Phys. Rev. D*, volume 50:pp. 5710–5731, November 1994.

[FGLS94b] Fletcher, R. S.; et al.: sibyll: An event generator for simulation of high energy cosmic ray cascades. In: *Phys. Rev. D*, volume 50:pp. 5710–5731, November 1994.

[FGLS99] Fletcher, R. S.; et al.: Air shower calculations with the new version of SIBYLL. In: *Proc. 26th International Cosmic Ray Conference*, volume 1, p. 415. Salt Lake City, USA, 1999.

[FHI+98] Fukuda, Y.; et al. ((Super-Kamiokande Collaboration)): Evidence for oscillation of atmospheric neutrinos. In: *Phys. Rev. Lett.*, volume 81:pp. 1562–1567, Aug 1998.

[FKR92] Frank, J.; King, A.; Raine, D.: *Accretion power in astrophysics*. Cambridge University Press, 1992.

[Fou] Foundation, Python Software: *Python Language Reference, version 2.7*. URL `http://www.python.org`.

[FR74] Fanaroff, B. L.; Riley, J. M.: The morphology of extragalactic radio sources of high and low luminosity. In: *Mon. Not. R. Astron. Soc.*, volume 167:pp. 31P–36P, May 1974.

[G+96] Gaidos, J.; et al.: Gamma-Ray Variability of the BL Lacertae Object Markarian 421. In: *Astrophys J. L.*, volume 472:p. L9, November 1996.

[G+12] Glüsenkamp, T.; et al.: Muon Filter Proposal IC86-2012. `https://docushare.icecube.wisc.edu/dsweb/Get/Document-59906/MuonFilter2012_v3_with_addendum.pdf`, feb 2012. Retrieved 2013-03-19.

[GAB+09] Gorham, P. W.; et al.: New Limits on the Ultrahigh Energy Cosmic Neutrino Flux from the ANITA Experiment. In: *Phys. Rev. Lett.*, volume 103(5):051103, July 2009.

[Gai04] Gaisser, T.: *Cosmic Gamma-Ray Sources*. Kluwer Academic Publishers, 2004.

[Gai12] Gaisser, T. K.: Spectrum of cosmic-ray nucleons, kaon production, and the atmospheric muon charge ratio. In: *Astrop. Phys.*, volume 35:pp. 801–806, July 2012.

[GBB+07] Gorham, P. W.; et al.: Observations of the Askaryan Effect in Ice. In: *Phys. Rev. Lett.*, volume 99(17):171101, October 2007.

[GBH+07] Grullon, B.; et al.: Reconstruction of High Energy Muon Events in IceCube using Waveforms. In: *Proceedings of the 30th Int. Cosmic Ray Conf.* Merida, Mexico, 2007.

[GBK14] Gora, D.; Bernardini, E.; Kappes, A.: Searching for tau neutrinos with Cherenkov telescopes. In: *ArXiv e-prints*, February 2014. 1402.4243.

[GK05] Gazizov, A.; Kowalski, M.: ANIS: High energy neutrino generator for neutrino telescopes. In: *Comput. Phys. Commun.*, volume 172:pp. 203–213, November 2005.

[Gla52] Glaser, D. A.: Some Effects of Ionizing Radiation on the Formation of Bubbles in Liquids. In: *Phys. Rev.*, volume 87:pp. 665–665, August 1952.

[GmcH11] Gonçalves, V. P.; Hepp, P.: Comparative study of the neutrino-nucleon cross section at ultrahigh energies. In: *Phys. Rev. D*, volume 83:p. 014014, Jan 2011.

[GMSS12] Gonzalez-Garcia, M. C.; et al.: Global fit to three neutrino mixing: critical look at present precision. In: *J. High Energ. Phys.*, volume 12:p. 123, December 2012.

[Gor] Maximum-likelihood code for time-clustering analysis. Gora, D., DESY Zeuthen, private communication.

[GQRS96] Gandhi, R.; et al.: Ultrahigh-energy neutrino interactions. In: *Astrop. Phys.*, volume 5:pp. 81–110, August 1996.

[GQRS98] Gandhi, R.; et al.: Neutrino interactions at ultrahigh energies. In: *Phys. Rev. D*, volume 58(9):pp. 093009–+, November 1998.

[Gre66] Greisen, K.: End to the Cosmic-Ray Spectrum? In: *Phys. Rev. Lett.*, volume 16:pp. 748–750, April 1966.

[GS64] Ginzburg, V. L.; Syrovatskii, S. I.: *The Origin of Cosmic Rays*. Macmillan, 1964.

[GS66] Gould, R. J.; Schréder, G.: Opacity of the Universe to High-Energy Photons. In: *Phys. Rev. Lett.*, volume 16:pp. 252–254, February 1966.

[H+73] Hasert, F.J.; et al. (Gargamelle Neutrino Collaboration): Observation of Neutrino Like Interactions Without Muon Or Electron in the Gargamelle Neutrino Experiment. In: *Phys. Lett.*, volume B46:pp. 138–140, 1973.

[Hal00] Hallin, A. L.: The Sudbury Neutrino Observatory. In: *Nucl. Phys. A*, volume 663:pp. 787–787, January 2000.

[Hal09] Halzen, F.: IceCube: The Rationale for Kilometer-Scale Neutrino Detectors. In: *ArXiv e-prints*, October 2009. arXiv:astro-ph/0910.0436.

[Haz76] Hazard, C.: 4.6. Lunar Occultation Measurements. In: Meeks, M. L., editor, *Astrophysics Radio Observations*, volume 12, Part C of *Methods in Experimental Physics*, pp. 92 – 117. Academic Press, 1976.

[HBB+03] Holder, J.; et al.: Detection of TeV Gamma Rays from the BL Lacertae Object 1ES 1959+650 with the Whipple 10 Meter Telescope. In: *Astrophys J. L.*, volume 583(1):p. L9, 2003.

[HBGM07] Hague, J. D.; et al.: Power laws and the cosmic ray energy spectrum. In: *Astrop. Phys.*, volume 27:pp. 455–464, June 2007.

[Hes65] Hess, V.: *Nobel Lectures, Physics 1922-1941*, chapter Nobel Lecture 1936: Unsolved Problems in Physics: Tasks for the Immediate Future in Cosmic Ray Studies. Elsevier Publishing Company, 1965. http://nobelprize.org/nobel_prizes/physics/laureates/1936/hesslecture.html.

[HH05] Halzen, F.; Hooper, D.: High energy neutrinos from the TeV Blazar 1ES 1959 + 650. In: *Astrop. Phys.*, volume 23:pp. 537–542, July 2005.

[HH09] Hinton, J. A.; Hofmann, W.: Teraelectronvolt Astronomy. In: *Ann. Rev. Astron. Astrophys.*, volume 47:pp. 523–565, September 2009.

[Hil06] Hillas, A. M.: Cosmic Rays: Recent Progress and some Current Questions. In: *ArXiv Astrophysics e-prints*, July 2006. astro-ph/0607109.

[HKC+98] Heck, D.; et al.: Corsika: A monte carlo code to simulate extensive air shower. Wissenschaftliche Berichte FZKA 6019, Forschungszentrum Karlsruhe, 1998. http://www-ik.fzk.de/corsika/.

[HKK+07] Honda, M.; et al.: Calculation of atmospheric neutrino flux using the interaction model calibrated with atmospheric muon data. In: *Phys. Rev. D*, volume 75(4):043006, February 2007.

[HLK+11] Hogan, B. S.; et al.: Chandra Discovery of 10 New X-ray Jets Associated with FR II Radio Core-selected AGNs in the MOJAVE Sample. In: *Astrophys J.*, volume 730:92, April 2011.

[HM84] Halzen, F.; Martin, A. D.: *Quarks and Leptones: An Introductory Course in Modern Particle Physics*. J. Wiley & Sons, January 1984.

[HMS63] Hazard, C.; Mackey, M. B.; Shimmins, A. J.: Investigation of the Radio Source 3C 273 By The Method of Lunar Occultations. In: *Nature*, volume 197:pp. 1037–1039, March 1963.

[Hoe03] Hoerandel, J. R.: On the knee in the energy spectrum of cosmic rays. In: *Astrop. Phys.*, volume 19:pp. 193–220, May 2003.

[Hoe12] Hoerandel, J. R.: The Composition of Cosmic Rays at the Knee. In: *ArXiv e-prints*, December 2012. arXiv:astro-ph/1212.0739.

[Hun99] Hundertmark, S.: AMASIM Neutrino Detector Simulation Program. In: Spiering, C., editor, *Proceedings of the Workshop on Simulation and Analysis Methods for Large Neutrino Telescopes*. Zeuthen, Germany, 1999. DESY-Proc-1999-01.

[HZ97] Halzen, F.; Zas, E.: Neutrino Fluxes from Active Galaxies: A Model-independent Estimate. In: *Astrophys J.*, volume 488:pp. 669–+, October 1997.

[IAA+13a] IceCube Collaboration; et al.: Observation of the cosmic-ray shadow of the Moon with IceCube. In: *ArXiv e-prints*, May 2013. arXiv:astro-ph/1305.6811.

[IAA+13b] IceCube Collaboration; et al.: Energy Reconstruction Methods in the IceCube Neutrino Telescope. In: *ArXiv e-prints*, November 2013. arXiv:physics/1311.4767.

[Ice13] IceCube Collaboration: Evidence for High-Energy Extraterrestrial Neutrinos at the IceCube Detector. In: *Science*, volume 342, November 2013.

[Ina07] Inaba, M.: General performance of the icecube detector and the calibration results. In: *International workshop on new photon-detectors PD07*. June 2007. URL http://pos.sissa.it//archive/conferences/051/031/PD07_031.pdf.

[IRI] Iridum satellite constellation. URL http://en.wikipedia.org/wiki/Iridium_satellite_constellation.

[IRSS01] Iyer Dutta, S.; et al.: Propagation of muons and taus at high energies. In: *Phys. Rev. D*, volume 63(9):pp. 094020–+, May 2001.

[Jac96] Jackson, J.D.: *Classical Electrodynamics*. Wiley, New York, USA, 3rd edition, 1996.

[JR03] Japaridze, G.; Ribordy, M.: Photon arrival time distribution convoluted to a gaussian time measurement uncertainty. AMANDA Internal Report 20031201, Clark Atlanta University and UMH Mons, 2003. http://internal.icecube.wisc.edu/reports/amanda/data/20031201-Reco.pdf.

[JSO13] The json data interchange format, 2013. URL http://www.ecma-international.org/publications/files/ECMA-ST/ECMA-404.pdf.

[K+10] Kurahashi Neilson, N.; et al.: IceCube Muon Filter for 2011 Pole Season. https://docushare.icecube.wisc.edu/dsweb/Get/Document-56581/MuonFilterProposal.pdf, dec 2010. Retrieved 2013-03-19.

[KAB06] Kelner, S. R.; Aharonian, F. A.; Bugayov, V. V.: Energy spectra of gamma rays, electrons, and neutrinos produced at proton-proton interactions in the very high energy regime. In: *Phys. Rev. D*, volume 74(3):034018, August 2006.

[Kar99] Karle, A.: Monte Carlo Simulation of Photon Transport and Detection in Deep Ice: Muons and Cascades. In: *DESY-PROC-1999-1*, p. 174. 1999.

[KDK+08] Kiryluk, J.; et al.: IceCube Performance with Artificial Light Sources: the Road to Cascade Analyses. In: *Proceedings of the 30th Int. Cosmic Ray Conf.*, volume 3, pp. 1233–1236. 2008.

[KE95] Kennedy, J.; Eberhart, R.: Particle swarm optimization. In: *Neural Networks, 1995. Proceedings., IEEE International Conference on*, volume 4, pp. 1942–1948 vol.4. 1995.

[Kf13] Kieda, D. B.; for the VERITAS Collaboration: The Gamma Ray Detection sensitivity of the upgraded VERITAS Observatory. In: *ArXiv e-prints*, August 2013. 1308.4849.

[KHH+04] Krawczynski, H.; et al.: Multiwavelength Observations of Strong Flares from the TeV Blazar 1ES 1959+650. In: *Astrophys J.*, volume 601:pp. 151–164, January 2004.

[KHS+12] Kravchenko, I.; et al.: Updated results from the RICE experiment and future prospects for ultra-high energy neutrino detection at the south pole. In: *Phys. Rev. D*, volume 85(6):062004, March 2012.

[Kle03] Kleinfelder, S.: Advanced transient waveform digitizers. In: Gorham, P. W., editor, *Society of Photo-Optical Instrumentation Engineers (SPIE) Conference Series*, volume 4858 of *Society of Photo-Optical Instrumentation Engineers (SPIE) Conference Series*, pp. 316–326. February 2003.

[KLS08] Köpke, L.; Lünemann, L.; Sander, H.-G.: Muon track reconstruction resolution (note in progress), 2008. Retrieved on 2013-01-15, URL http://www.staff.uni-mainz.de/koepke/Fisher1.pdf.

[Klu97] Klug, J.: *Enhancement of the Up/Down Signal Ratio and Crosstalk Studies in AMANDA*. Master's thesis, Uppsala University, 1997.

[KMPT07] Kranich, D.; et al.: Observations of 3C279 with the MAGIC telescope. In: *Proceedings of the 30th Int. Cosmic Ray Conf.* Merida, Mexico, 2007.

[Kol06] Kolanoski, H.: *Skript "Einführung in die Astroteilchenphysik"*. Humboldt Universitä zu Berlin, 2006.

[KS12] Katz, U. F.; Spiering, C.: High-energy neutrino astrophysics: Status and perspectives. In: *Prog. Part. Nucl. Phys.*, volume 67:pp. 651–704, July 2012.

[KT06] Kusunose, M.; Takahara, F.: A Structured Leptonic Jet Model of the "Orphan" TeV Gamma-Ray Flares in TeV Blazars. In: *Astrophys J.*, volume 651:pp. 113–119, November 2006.

[LA12] Lahmann, R.; ANTARES Collaboration: Status and recent results of the acoustic neutrino detection test system AMADEUS. In: *Nucl. Instrum. Methods Phys. Res., Sect. A*, volume 662:p. 216, January 2012.

[Lan05] Lang, D.: *Search for Point Sources of High-Energy Neutrinos with the AMANDA Detector*. Master's thesis, Universitä Ulm, at DESY Zeuthen, 2005.

[Lf09] Latino, G.; for the TOTEM Collaboration: The TOTEM Experiment at the LHC. In: *ArXiv e-prints*, May 2009. 0905.2936.

[LH74] Lawson, C. L.; Hanson, R. J.: *Solving Least Squares Problems*. Prentice Hall, 1974.

[LHK+00] Lai, H. L.; et al.: Global QCD analysis of parton structure of the nucleon: CTEQ5 parton distributions. In: *European Physical Journal C*, volume 12:pp. 375–392, February 2000.

[LMB+07] Lundberg, J.; et al.: Light tracking for glaciers and oceans – Scattering and absorption in heterogeneous media with Photonics. In: *ArXiv Astrophysics e-prints*, February 2007. arXiv:astro-ph/0702108.

[Lon11] Longair, M.: *High energy astrophysics*. Cambridge University Press, 2011.

[LP53] Landau, L. D.; Pomeranchuk, I.: Electron cascade process at very high energies. In: *Dokl. Akad. Nauk. Ser. Fiz.*, volume 92:pp. 735–738, 1953.

[Mei03] Meier, D. L.: The theory and simulation of relativistic jet formation: towards a unified model for micro- and macroquasars. In: *New Astronomy Reviews*, volume 47:pp. 667–672, October 2003.

[Mil69] Miller, S. L.: Clathrate hydrates of air in antarctic ice. In: *Science*, volume 165:pp. 489–490, August 1969.

[MNS62] Maki, Ziro; Nakagawa, Masami; Sakata, Shoichi: Remarks on the unified model of elementary particles. In: *Progr. Theor. Phys.*, volume 28(5):pp. 870–880, 1962.

[MPE+03] Mücke, A.; et al.: BL Lac objects in the synchrotron proton blazar model. In: *Astrop. Phys.*, volume 18:pp. 593–613, March 2003.

[MPRI12] Meures, T.; et al.: Research and calibration of acoustic sensors in ice within the SPATS (South Pole Acoustic Test Setup) project. In: *Nucl. Instrum. Methods Phys. Res., Sect. A*, volume 662:p. 230, January 2012.

[MR07] Mazin, D.; Raue, M.: New limits on the density of the extragalactic background light in the optical to the far-infrared from the spectra of all known TeV blazars. In: *ArXiv Astrophysics e-prints*, January 2007. arXiv:astro-ph/0701694.

[MRE+99] Mücke, A.; et al.: Photohadronic processes in astrophysical environments. In: *Publications Astronomical Society of Australia*, volume 16:pp. 160–6, August 1999.

[NAA+12] Nolan, P. L.; et al.: Fermi large area telescope second source catalog. In: *Astrophys. J. Suppl.*, volume 199(2):p. 31, 2012.

[Neu03] Neunhöfer, Till: *Die Entwicklung eines neuen Verfahrens zur Suche nach kosmischen Neutrino-Punktquellen mit dem AMANDA-Neutrinoteleskop*. Ph.D. thesis, Johannes-Gutenberg-Universität in Mainz, 2003.

[Nf11] Nepomuk Otte, A.; for the VERITAS Collaboration: The Upgrade of VERITAS with High Efficiency Photomultipliers. In: *ArXiv e-prints*, October 2011. 1110.4702.

[NIS] NIST/SEMATECH e-Handbook of Statistical Methods. http://www.itl.nist.gov/div898/handbook/. Retrieved 2013-11-15.

[NOP07] Niemiec, J.; Ostrowski, M.; Pohl, M.: The inefficiency of the first-order Fermi process in UHECR production at relativistic shocks. In: *ArXiv e-prints*, volume 705, May 2007. arXiv:0705.4453.

[NP06] Narsky, I.; Prosper, H. B.: Optimization of Signal Significance by Bagging Decision Trees. In: Lyons, L.; Karagöz Ünel, M., editors, *Statistical Problems in Particle Physics, Astrophysics and Cosmology*, pp. 143–+. 2006.

[NS02] Neronov, A. Y.; Semikoz, D. V.: Which blazars are neutrino loud? In: *Phys. Rev. D*, volume 66(12):pp. 123003–+, December 2002.

[NSAK02] Neronov, A.; et al.: Large-Scale Extragalactic Jets Powered by Very-High-Energy Gamma Rays. In: *Phys. Rev. Lett.*, volume 89(5):pp. 051101–+, 2002.

[Nt12] Naples, D.; the Minos Collaboration: Oscillation results from MINOS. In: *JPCS*, volume 375(4):p. 042073, July 2012.

[Oli06] Oliphant, Travis E.: *Guide to NumPy*. Provo, UT, March 2006. URL http://www.tramy.us/.

[PAA+07] Pierre Auger Collaboration; et al.: Correlation of the Highest-Energy Cosmic Rays with Nearby Extragalactic Objects. In: *Science*, volume 318:pp. 938–, November 2007.

[PAA+08a] Pierre Auger Collaboration; et al.: Correlation of the highest-energy cosmic rays with the positions of nearby active galactic nuclei. In: *Astrop. Phys.*, volume 29:pp. 188–204, April 2008.

[PAA+08b] Pierre Auger Collaboration; et al.: Upper limit on the cosmic-ray photon flux above 10^{19} eV using the surface detector of the Pierre Auger Observatory. In: *Astrop. Phys.*, volume 29:pp. 243–256, May 2008.

[PAA+11] Pierre Auger Collaboration; et al.: Anisotropy and chemical composition of ultra-high energy cosmic rays using arrival directions measured by the Pierre Auger Observatory. In: *JCAP*, volume 6:022, June 2011.

[PAC+92] Punch, M.; et al.: Detection of TeV photons from the active galaxy Markarian 421. In: *Nature*, volume 358:p. 477, 1992.

[Pan96] Pandel, D.: *Bestimmung von Wasser- und Detektorparametern und Rekonstruktion von Myonen bis* 100 *TeV mit dem Baikal-Neutrinoteleskop NT-72*. Master's thesis, Humboldt Universität zu Berlin, 1996.

[Pan11] Panknin, S.: *Search for Neutrino-Induces Cascade Events in the IceCube Detector*. Ph.D. thesis, Humboldt Universität zu Berlin, 2011.

[PDR03] Protheroe, R. J.; Donea, A. C.; Reimer, A.: Tev gamma rays and cosmic rays from the nucleus of M87, a mis-aligned BL Lac object. In: *Astrop. Phys.*, volume 19:pp. 559–568, 2003.

[Pie08] Pierre Auger Collaboration: Erratum to "Correlation of the highest-energy cosmic rays with the positions of nearby active galactic nuclei" [Astroparticle Physics 29(3) (2008) 188 204]. In: *Astrop. Phys.*, volume 30:pp. 45–45, August 2008.

[PMY+12] Palanque-Delabrouille, N.; et al.: New approach to measure the Quasar Luminosity Function in $0.7 < z < 4.0$ from dedicated SDSS-III and MMT data. In: *ArXiv e-prints*, September 2012. 1209.3968.

[Poh03] Pohl, M.: Particle Acceleration in AGN Jets (Invited Talk). In: Takalo, L. O.; Valtaoja, E., editors, *High Energy Blazar Astronomy, ASP Conference Proceedings*, pp. 133–+. Piikkio, Finland, July 2003.

[Poh04] Pohl, A.: *A Statistical Tool for Finding Non-Particle Events from the AMANDA Neutrino Telescope*. Ph.D. thesis, Uppsala Universitet, 2004.

[Pon57] Pontecorvo, B.: Mesonium and anti-mesonium. In: *Sov. Phys. JETP*, volume 6:p. 429, 1957.

[Pon68] Pontecorvo, B.: Neutrino Experiments and the Problem of Conservation of Leptonic Charge. In: *Sov. Phys. JETP*, volume 26:p. 984, May 1968.

[Pri81] Pringle, J. E.: Accretions disks in astrophysics. In: *Ann. Rev. Astron. Astrophys.*, volume 19:pp. 137–162, 1981.

[Pri06] Price, P. B.: Attenuation of acoustic waves in glacial ice and salt domes. In: *J. Geophy. Res. (Solid Earth)*, volume 111(B10):pp. 2201–+, February 2006.

[PS00a] Pohl, M.; Schlickeiser, R.: (Erratum) On the conversion of blast wave energy into radiation in active galactic nuclei and gamma-ray bursts. In: *Astron. Astrophys.*, volume 355:p. 829, March 2000.

[PS00b] Pohl, M.; Schlickeiser, R.: On the conversion of blast wave energy into radiation in active galactic nuclei and gamma-ray bursts. In: *Astron. Astrophys.*, volume 354:pp. 395–410, February 2000.

[PW65] Penzias, A. A.; Wilson, R. W.: A Measurement of Excess Antenna Temperature at 4080 Mc/s. In: *Astrophys J.*, volume 142:pp. 419–421, July 1965.

[PW01] Price, P. B.; Woschnagg, K.: Role of group and phase velocity in high-energy neutrino observatories. In: *Astrop. Phys.*, volume 15:pp. 97–100, March 2001.

[PWC00] Price, P. B.; Woschnagg, K.; Chirkin, D.: Age vs depth of glacial ice at South Pole. In: *Geophys. Res. Lett.*, volume 27:pp. 2129–+, July 2000.

[pye] Pyephem library. Retrieved 2013-08-19, URL `http://rhodesmill.org/pyephem/`.

[RB07] Rosswog, S.; Brüggen, M.: *Introduction to High-Energy Astrophysics*. Cambridge University Press, 2007.

[RBP05] Reimer, A.; Böttcher, M.; Postnikov, S.: Neutrino Emission in the Hadronic Synchrotron Mirror Model: The "Orphan" TeV Flare from 1ES 1959+650. In: *Astrophys J.*, volume 630:pp. 186–190, September 2005.

[Rei12] Reimer, A.: On the physics of hadronic blazar emission models. In: *JPCS*, volume 355(1):p. 012011, 2012.

[Res94] Resvanis, L. K.: The Birth of High Energy Neutrino Astronomy and Astrophysics. In: *Particles and the Universe*, pp. 165–+. 1994.

[RMF96] Ralston, J. P.; McKay, D. W.; Frichter, G. M.: The Ultra High Energy Neutrino-Nucleon Cross Section. In: *ArXiv Astrophysics e-prints*, June 1996. `arXiv:astro-ph/9606007`.

[RNTN07] Ridky, J.; et al.: Prompt muons in extended air showers. In: *ArXiv e-prints*, volume 706, June 2007. `0706.2145`.

[Rob92] Roberts, A.: The birth of high-energy neutrino astronomy: A personal history of the DUMAND project. In: *Rev. Mod. Phys.*, volume 64:pp. 259–312, January 1992.

[RW12] Rädel, L.; Wiebusch, C.: Calculation of the Cherenkov light yield from electromagnetic cascades in ice with Geant4. In: *ArXiv e-prints*, October 2012. `1210.5140`.

[SAB07] Satelecka, K.; Ackermann, M.; Bernardini, E.: Cluster Search for Neutrinos from Predefined Directions. In: *Proceedings of the 30th Int. Cosmic Ray Conf.* Merida, Mexico, 2007.

[Sat10] Satalecka, K.: *Multimessenger studies of point-sources using the IceCube neutrino telescope and the MAGIC gamma-ray telescope*. Ph.D. thesis, Humboldt Universität zu Berlin, 2010.

[SBF+11] Scholten, O.; et al.: Ultra-high-energy cosmic ray and neutrino detection using the Moon. In: *Nucl. Phys. B (Proc. Suppl.)*, volume 212:pp. 128–133, March 2011.

[SBT+07] Stål, O.; et al.: Prospects for Lunar Satellite Detection of Radio Pulses from Ultrahigh Energy Neutrinos Interacting with the Moon. In: *Phys. Rev. Lett.*, volume 98(7):pp. 071103–+, February 2007.

[SCC+13] Sitarek, J.; et al.: Physics performance of the upgraded MAGIC telescopes obtained with Crab Nebula data. In: *Proceedings of the 33nd Int. Cosmic Ray Conf.* Rio de Janeiro, Brasil, 2013.

[Sch02] Schlickeiser, R.: *Cosmic Ray Astroparticle Physics*. Springer, 2002.

[Sch10] Scholz, O.: *The Design Study of IceCube DeepCore: Characterization and Veto Studies*. Master's thesis, Ruperto-Carola University of Heidelberg, 2010.

[Sco92] Scott, D. W.: *Multivariate Density Estimation*. John Wiley & Sons, Inc., 1992.

[SdS92] Stecker, F. W.; de Jager, O. C.; Salamon, M. H.: TeV gamma rays from 3C 279 - A possible probe of origin and intergalactic infrared radiation fields. In: *Astrophys J.*, volume 390:pp. L49–L52, May 1992.

[SDSS91] Stecker, F. W.; et al.: High-energy neutrinos from active galactic nuclei. In: *Phys. Rev. Lett.*, volume 66:pp. 2697–2700, May 1991.

[SDSS92] Stecker, F. W.; et al.: Erratum: "High-energy neutrinos from active galactic nuclei" [Phys. Rev. Lett. 66, 2697 (1991)]. In: *Phys. Rev. Lett.*, volume 69:pp. 2738–+, November 1992.

[Sf13] Schukraft, A.; for the IceCube Collaboration: A view of prompt atmospheric neutrinos with IceCube. In: *ArXiv e-prints*, February 2013. 1302.0127.

[SGW+01] Saltzberg, D.; et al.: Observation of the Askaryan Effect: Coherent Microwave Cherenkov Emission from Charge Asymmetry in High-Energy Particle Cascades. In: *Phys. Rev. Lett.*, volume 86:pp. 2802–2805, March 2001.

[Sil86] Silverman, B. W.: *Density Estimation for Statistics and Data Analysis*. Chapman & Hall, 1986.

[Spi12] Spiering, C.: Towards high-energy neutrino astronomy. A historical review. In: *Eur. Phys. J. H*, volume 37:pp. 515–565, August 2012.

[SS98] Salamon, M. H.; Stecker, F. W.: Absorption of High-Energy Gamma Rays by Interactions with Extragalactic Starlight Photons at High Redshifts and the High-Energy Gamma-Ray Background. In: *APJ*, volume 493:p. 547, January 1998.

[SSB12] Subramanian, P.; Shukla, A.; Becker, P. A.: TeV blazar variability: the firehose instability? In: *ArXiv e-prints*, March 2012. 1203.5727.

[Sta03] Stanev, T.: *High Energy Cosmic Rays*. Springer, 2003.

[sta12] https://wiki.icecube.wisc.edu/index.php/Standard_Candle, November 2012.

[TA+13] The Fermi-LAT collaboration; et al.: Detection of the Characteristic Pion-Decay Signature in Supernova Remnants. In: *Science*, volume 339, February 2013.

[TAA+12] The TOTEM Collaboration; et al.: Measurement of the forward charged-particle pseudorapidity density in pp collisions at $\sqrt{s}$ = 7 TeV with the TOTEM experiment. In: *Europhys. Lett.*, volume 98:p. 31002, May 2012.

[TAA+13a] The IceCube Collaboration; et al.: Cosmic ray composition and energy spectrum from 1-30 PeV using the 40-string configuration of IceTop and IceCube. In: *Astrop. Phys.*, volume 42:pp. 15–32, February 2013.

[TAA+13b] The IceCube Collaboration; et al.: Cosmic ray composition and energy spectrum from 1-30 PeV using the 40-string configuration of IceTop and IceCube. In: *Astrop. Phys.*, volume 42:pp. 15–32, February 2013.

[TBG+11] Tavecchio, F.; et al.: On the origin of the γ-ray emission from the flaring blazar PKS 1222+216. In: *Astron. Astrophys.*, volume 534:A86, October 2011.

[TBS+10] Tluczykont, M.; et al.: Long-term lightcurves from combined unified very high energy γ-ray data. In: *Astron. Astrophys.*, volume 524:A48, December 2010.

[TF37] Tamm, I. E.; Frank, I. M.: Coherent radiation of fast electrons in a medium. In: *Dokl. Akad. Nauk SSSR*, volume 14:p. 107, 1937.

[Tho74] Thorne, K. S.: Disk-Accretion onto a Black Hole. II. Evolution of the Hole. In: *Astrophys J.*, volume 191:pp. 507–520, July 1974.

[TI12] Toscano, S.; IceCube Collaboration: Observation of anisotropy in the arrival direction distribution of cosmic rays above TeV energies with IceCube. In: *Nucl. Instrum. Methods Phys. Res., Sect. A*, volume 692:pp. 165–169, November 2012.

[TKH03] Tonello, N.; Kranich, D.; HEGRA Collaboration: Study of the VHE Gamma Ray Emission from the AGN 1ES1959+650 with the HEGRA Cherenkov Telescope CT1. In: *Proceedings of the 28th Int. Cosmic Ray Conf.*, volume 5, p. 2615. Tsukuba, Japan, July 2003.

[Tos09] Tosi, D.: Acoustic neutrino detection at the South Pole: latest results from SPATS. In: *TeV Particle Astrophysics 2009*. July 2009.

[Tri12] Tricomi, A.: Results from LHCf Experiment. In: *European Physical Journal Web of Conferences*, volume 28 of *European Physical Journal Web of Conferences*, p. 2003. June 2012.

[Tun02] Tung, W.-K.: New Generation of Parton Distributions with Uncertainties from Global QCD Analysis. In: *Acta Physica Polonica B*, volume 33:p. 2933, October 2002.

[UP95] Urry, C. M.; Padovani, P.: Unified schemes for radio-loud active galactic nuclei. In: *Publications of the Astronomical Society of the Pacific*, volume 107:p. 803, 1995.

[Urr94] Urry, C. M.: Jets in Active Galactic Nuclei. In: Wamsteker, W.; Longair, M. S.; Kondo, Y., editors, *Frontiers of Space and Ground-Based Astronomy*, volume 187 of *Astrophysics and Space Science Library*, p. 335. 1994.

[Vav34] Vavilov, S. I.: O vozmozhnykh prichinakh sinego γ-svecheniya zhidkostei (On the possible causes of blue γ-glow of liquids). In: *Dokl. Akad. Nauk SSSR*, volume 2(8):p. 457, 1934.

[VER] Results of VERITAS observation of SBS 1150+497. VERITAS Collaboration, private communication.

[vFJ07] van Eijndhoven, N.; Fadiran, O.; Japaridze, G.: Implementation of a Gauss convoluted Pandel PDF for track reconstruction in Neutrino Telescopes. In: *ArXiv e-prints*, volume 704, April 2007. arXiv:0704.1706.

[VGL05] Vandenbroucke, J.; Gratta, G.; Lehtinen, N.: Experimental Study of Acoustic Ultra-High-Energy Neutrino Detection. In: *Astrophys J.*, volume 621:pp. 301–312, March 2005.

[W+07] Woschnagg, Kurt; et al.: Dust logger. http://wiki.icecube.wisc.edu/index.php/Dust_logger, Jannuary 2007. Retrieved 2013-01-15.

[W+08] Woschnagg, Kurt; et al.: New ice model. http://wiki.icecube.wisc.edu/index.php/New_ice_model, May 2008. Retrieved 2013-01-15.

[Wag04] Wagner, Wolfgang: *Design and Realisation of a new AMANDA Data Acquisition System with Transient Waveform Recorders*. Ph.D. thesis, University Dortmund, 2004.

[Wal10] Walraff, M.: *Design, Implementation and Test of a New Feature Extractor for the IceCube Neutrino Observatory*. Master's thesis, Rheinisch-Westfälische Technische Hochschule Aachen, 2010.

[WBS07] Wittek, W.; Bartko, H.; Schweizer, T.: Comments on the Unified approach to the construction of Classical confidence intervals. In: *ArXiv e-prints*, volume 706, June 2007. arXiv:0706.3622.

[Wie95] Wiebusch, Christopher: *The Detection of Faint Light in Deep Underwater Neutrino Telescopes*. Ph.D. thesis, Rheinisch-Westfälische Technische Hochschule zu Aachen, 1995.

[Wil04] Williams, D. R.: *The Askar'yan effect and detection of extremely high energy neutrinos in the lunar regolith and salt*. Ph.D. thesis, University of California, Los Angeles, December 2004.

[Wis] Wissing, H.: http://web.physik.rwth-aachen.de/~hwissing/unblind/unblind/.

[WU02a] Woo, J.-H.; Urry, C. M.: Active Galactic Nucleus Black Hole Masses and Bolometric Luminosities. In: *Astrophys J.*, volume 579:pp. 530–544, November 2002.

[WU02b] Woo, J.-H.; Urry, C. M.: The Independence of Active Galactic Nucleus Black Hole Mass and Radio Loudness. In: *Astrophys J. L.*, volume 581:pp. L5–L7, December 2002.

[WvL13] Whitehorn, N.; van Santen, J.; Lafebre, S.: Penalized splines for smooth representation of high-dimensional Monte Carlo datasets. In: *Comput. Phys. Commun.*, volume 184:pp. 2214–2220, September 2013.

[xml] Xml-rpc. Retrieved 2013-08-19, URL `http://en.wikipedia.org/wiki/XML-RPC`.

[YRZ05] Yang, H.-J.; Roe, B. P.; Zhu, J.: Studies of Boosted Decision Trees for MiniBooNE Particle Identification. In: *ArXiv Physics e-prints*, August 2005. `arXiv:physics/0508045`.

[YRZ07] Yang, H.-J.; Roe, B. P.; Zhu, J.: Studies of stability and robustness for artificial neural networks and boosted decision trees. In: *Nucl. Instrum. Methods Phys. Res., Sect. A*, volume 574:pp. 342–349, May 2007.

[ZK66] Zatsepin, G. T.; Kuz'min, V. A.: Upper Limit of the Spectrum of Cosmic Rays. In: *Sov. J. Exp. and Theo. Phys. Lett.*, volume 4:pp. 78–+, August 1966.

List of Figures

List of Tables

Abbreviations

Abbreviation	Explanation
AGN	Active Galactic Nuclei
AHA	Additionally Heterogeneous Absorption
AMANDA	Antarctic Muon and Neutrino Detector Array
ANIS	All Neutrino Interaction Simulation
ANTARES	Astronomy with a Neutrino Telescope and Abyss Environmental Research
ATWD	Analog Transient Waveform Digitizer
CC	Charged Current
COG	Center of Gravity
CORSIKA	Cosmic Ray Simulation for Cascade
DOM	Digital Optical Module
FADC	Fast Analog to Digital Converter
FPGA	Field Programmable Gate Array
FSRQ	Flat Spectrum Radio Quasar
GPS	Global Positioning System
GPU	Graphics Processing Unit
GRB	Gamma-Ray Burst
IACT	Imaging Atmospheric Cherenkov Telescope
ITS	IceCube Teleport System
KDE	Kernel Density Estimate
MAGIC	Major Atmospheric Gamma-Ray Imaging Cherenkov
MJD	Modified Julian Date
MMC	Muon Monte Carlo
MPE	Multi Photoelectron
NC	Neutral Current
NToO	Neutrino Triggered Target of Opportunity Program
PDF	Probability Density Function
PMT	Photomultiplier Tube
SED	Spectral Energy Distribution
SMT	Simple Multiplicity Trigger
SPADE	South Pole Archival and Data Exchange
SPATS	South Pole Accoustic Test Setup
SPE	Single Photoelectron
SPICE	South Pole Ice model
TDRSS	Tracking and Data Relay Satellite System
VERITAS	Very Energetic Radiation Imaging Telescope Array System

Danksagung

Zuallererst möchte ich mich bei Dr. Elisa Bernardini für die Betreuung meiner Doktorarbeit bedanken. Ihre Ermunterung und Unterstützung haben erheblich dazu beigetragen, das Neutrino Triggered Target of Opportunity zu realisieren. Weiterhin bin ich besonders dankbar, die Möglichkeit erhalten zu haben, am MAGIC-Teleskop auf La Palma sowie am Südpol zu arbeiten.

Vielen Dank auch an Dr. Marek Kowalski und Dr. Alexander Kappes, die als weitere Gutachter meiner Arbeit fungierten, sowie an Dr. Peter Uwer, als Vorsitzenden und Dr. Andreas Jankowiak als weiteres Mitglied der Prüfungskommission.

Mein Dank gilt auch Dr. Christian Spiering für seine Unterstützung, insbesondere in der Endphase der Arbeit und das unermüdliche Korrekturlesen. Zu Dank verpflichtet bin ich auch Dr. Markus Ackermann, der, zusammen mit Dr. Elisa Bernardini, die ursprüngliche Idee zum hier vorgestellten Neutrino Triggered Target of Opportunity hatte.
Die Zeit am DESY wäre nicht vorstellbar ohne die Vielzahl von Doktoranden und Post-Docs, von denen ich viele zu meinen Freunden zähle. Danke an das Kaskaden-Büro, Arne, Eike und Achim, dass ihr immer Zeit für einen Tee oder eine Diskussion zu einer kniffligen Software-Frage hattet. Danke Arne und Sebastian, für die vielen Gespräche am See über unsere Arbeit, Politik und das Leben im Allgemeinen, sowie die vielen Abende beim gemeinsamen Kochen. Vielen Dank auch an Gessica, Rebecca, Konstancja, Robert L., Pepe, Lotfi, Heike, Emanuel, Fabian und Delia für viele Diskussionen und nette Abende in Berlin! Gedankt sei auch den vielen Mitgliedern der IceCube-Kollaboration, die die Kollaborationstreffen motivierend und spannend gemacht haben. Bei Dr. Michael Walter möchte ich mich bedanken für die Reisen zur Oden und zur Polarstern im Rahmen des DESY Outreach-Programms.

Ohne technische Unterstützung aus der IceCube-Kollaboration, insbesondere durch Torsten Schmidt und Erik Blaufuss würde das NToo heute nicht so reibungslos am Südpol funktionieren, vielen Dank dafür! Auch den Mitarbeitern des DESY-Rechenzentrums, die für den durchgängigen Betrieb der IT-Infrastruktur sorgen, möchte ich meinen Dank aussprechen!

Ganz besonders möchte ich mich auch bei meiner Familie für den Rückhalt und die Unterstützung während der gesamten Promotion bedanken. Juliane und Tim, ihr musstet, insbesondere während des Schreibens, viel auf mich verzichten. Danke für jedes Lächeln und ermunternde Wort, das mir Kraft gegeben hat!

Selbständigkeitserklärung

Ich erkläre, dass ich die vorliegende Arbeit selbständig und nur unter Verwendung der angegebenen Literatur und Hilfsmittel angefertigt habe. Ich habe mich nicht anderweitig um einen Doktorgrad beworben und besitze keinen Doktorgrad. Die Promotionsordnung der Mathematisch-Naturwissenschaftlichen Fakultät I der Humboldt-Universität zu Berlin ist mir bekannt.

Berlin, den 20.03.2014 Robert Franke